Imaging and Control of Engineered Cells using Magnetic Fields

Thesis by

Pradeep Ramesh

In Partial Fulfillment of the Requirements for
the degree of Doctor of Philosophy
in Bioengineering

CALIFORNIA INSTITUTE OF TECHNOLOGY
Pasadena, California

2019
(Defended May 17, 2019)

Pradeep Ramesh
ORCID: 0000-0001-6243-8145

ACKNOWLEDGEMENTS

> *"The truth is rarely pure and never simple. Modern life would be very tedious if it were either…"*
> Oscar Wilde

In the summer of 2017, a group of us went white-water rafting on the American river near Sacramento, CA. Since 2016 was a particularly strong El Niño year, the river banks were bursting at their seams and the rapids were at their strongest in nearly 7 years. Being an adventurous lot, we naturally chose one of the toughest runs and spent the day rafting down the river, experiencing our share of tumbles, flops, and the occasional boulder along the way. We emerged sopping wet, grinning and laughing about our collective fumbles, while basking in that feeling of having conquered a challenge.

As cliché as it sounds, that trip is a good analogy for this PhD, now approaching 7 years in the making. I am forever grateful to my thesis advisor, Dr. Mikhail G. Shapiro, who has been the proverbial raft along this journey. Thank you for your trust and faith that you placed in me when you asked me to join you in starting your lab at Caltech. Thank you for an inspiring problem, which proved to be a fascinating puzzle to work out. Thank you for giving me a richly adorned scientific playground, full of toys that kept me busy. Thank you for your generous support and burning the midnight oil with me when I was stuck. Finally, thank you for your sunny optimism and humor, which made the lab a fun place to learn.

I am likewise indebted to Bhawna Motwani. Thank you for diving into our adventure with your game-face on. You have been both the proverbial paddle, as well as the life-jacket, and I could not have completed this journey without you. Thank you for your unflagging encouragement and intellectual support, especially in those moments when my knees buckled, and I doubted myself. Thank you for being my metronome, and for having kept me true to my highest ideals.

Thank you to Dr. Dianne Newman and Dr. Victoria Orphan, who indulged my intellectual curiosity with financial support through CEMI, as well as providing a patient ear to hear out my thoughts and ideas on topics ranging from NV centers to phage and atmospheric life. Thank you for welcoming me into the geobiology fold and challenging me to think deeper about my work. Likewise, thank you to Dr. Joe Kirschvink, Dr. David Tirrell, Dr. Frances Arnold, Dr.

Geoff Blake, Dr. Paul H. Oyala, Dr. Andres Collazo, and Dr. Alasdair McDowall for scientific advice, as well as opening up your respective labs for my experiments. Thank you to Dr. Rob Phillips and Dr. David Baltimore for serving as my undergraduate thesis advisors, as well as serving on my graduate thesis committee. Thank you, Rob and David, for having taught me to do bottom-up science and to always calculate before jumping into the melee.

Thank you to Hunter C. Davis and Marjorie Buss who have been such willing partners and enablers throughout our shared scientific adventures. I could only plumb such great intellectual depths with your support, and I hope to have such genial collaborators in the future. Thank you to Dan I. Piraner and Mohamad Abedi for being such good sports and joining me on so many of my impromptu adventures. A Hindu, a Muslim, and a Jew sounds like the perfect setup for a joke, and that is precisely what our office was. Thank you to Di Wu for having created such a fun and carefree environment. Thank you to Dr. George J. Lu and Dr. David Maresca, who have been such genial friends and mentors, and for patiently working through ideas with me. Thank you to Arash Farhadi and Anupama Lakshmanan for all the laughs, and to the rest of the Shapiro Lab for one of the most memorable experiences of my lifetime.

Thank you to my family, to whom I dedicate this work. To my parents, Jayashree Ramesh and Ramesh Ramakrishna, thank you for having instilled a passion for learning, and for all those intellectually enriching experiences as a child. Thank you for having worked tirelessly to ensure that I get the best education I could ever have hoped to receive. To my aunt, R. Seethalakshmi, thank you for having taught me to leave no stone unturned in search of a solution. Your stoic grit has been an inspiration for me. To Kamla Morandani and Naresh Motwani, thank you for your unflagging support and positive encouragement, which has buoyed me through some especially difficult times. And finally to my wife and ultimate collaborator, Bhawna Motwani, whose curiosity propels me to go out and learn every day – thank you for making each day interesting.

ABSTRACT

Making cells magnetic is a long-standing goal of synthetic biology, aiming to enable the separation of cells from complex biological samples and their non-invasive visualization *in vivo* using Magnetic Resonance Imaging (MRI). Previous efforts towards this goal, focused on engineering cells to biomineralize superparamagnetic or ferromagnetic iron oxides, have largely been unsuccessful due to the stringent required chemical conditions. In this thesis, we introduce an alternative approach to making cells magnetic, focusing on biochemically maximizing cellular paramagnetism. Here, we show that a novel genetic construct combining the functions of ferroxidation and iron-chelation enables engineered bacteria to accumulate iron in 'ultraparamagnetic' macromolecular complexes, which subsequently allows for these cells to be trapped using strong magnetic field gradients and imaged using MRI *in vitro* and *in vivo*. We characterize the properties of these cells and complexes using magnetometry, an array of spectroscopic techniques, biochemical assays, and computational modeling to elucidate the unique mechanisms and implications of this 'ultraparamagnetic' concept.

In addition to making cells magnetic, remote control of cellular localization in deep tissue is another long-standing goal of synthetic biology. Such an ability to non-invasively direct cells to sites of interest will not only improve therapeutic outcomes by minimizing off-target activity, but more broadly enable new research on complex cellular communities, such as the gut microbiome, in living animals. Given their deep penetrance through tissues, magnetic fields are ideally suited for facilitating non-invasive targeting of cells; however, the rapid decay of magnetic flux density from its source currently limits the depths to which magnetic targeting can be employed to within 1-2 mm from the surface. Here, we demonstrate a new approach wherein the retention of orally-administered and synthetically magnetized cell-like-particles is selectively enhanced within the murine intestinal tract to depths of up to 13 mm from the surface. Our cellular localization assisted by magnetic particles (CLAMP) strategy can potentially be generalized to any cell (bacterial, mammalian) or drug-containing nanoparticle of interest, and can be combined with existing non-invasive imaging modalities thereby facilitating remote environmental sensing at sites of interest.

Finally, while magnetic fields in MRI scanners are widely used today to safely and non-invasively image anatomical structures in living animals, much of the image contrast in MRI is the result of microscale magnetic-field variations in tissues. However, the connection between these microscopic patterns and the appearance of macroscopic MR images has not been the subject of direct experimental studies due to a lack of methods to map microscopic fields in biological samples under ambient conditions. Here, we *optically* probed magnetic fields in mammalian cells and tissues with submicron resolution and nanotesla sensitivity using nitrogen-vacancy (NV) diamond magnetometry and combined these measurements with simulations of nuclear-spin precession to predict the corresponding MRI contrast. Additionally, we demonstrate the broad utility of this technology for imaging an *in vitro* model of cellular iron uptake, as well as imaging histological samples from a mouse model of hepatic iron overload. Taken together, our approach bridges a fundamental intellectual gap between a macroscopic MRI voxel and its microscopic constituents.

PUBLISHED CONTENT AND CONTRIBUTIONS

Ramesh, P.[†] Buss, M.[†] et. al. (2019). "Remote Control of Cellular Localization in the G.I. Tract Assisted by Magnetic Particles." *In preparation.*

(† Equal contribution)

P.R. conceived the study. P.R. and M.B. designed the experiments, as well as collected and analyzed the resulting data. P.R. conducted the *in silico* studies on magnetic capture. P.R., M.B., and M.G.S prepared the manuscript.

Ramesh, P. et al. (2018). "Ultraparamagnetic Cells Formed through Intracellular Oxidation and Chelation of Paramagnetic Iron". In: Angewandte Chemie Internation Edition 57, pp. 12385-12389. doi: 10.1002/anei.201805042

P.R. conceived, planned, and conducted experiments, analyzed the resulting data, and prepared the manuscript.

Davis, H.[†], **Ramesh, P.**[†] et al. (2018). "Mapping the microscale origins of MRI contrast with sub-cellular NV magnetometry". In: Nature Communications 9, 131. doi: 10.1038/s41467-017-02471-7

(†Equal contribution)

P.R. and H.D. co-conceived and planned the study. P.R. assisted in building the magneto-microscope and preparing the *in vitro* and *in vivo* specimens. H.D. acquired and processed the NV data, and conducted the *in silico* studies on relaxation. P.R. and H.D. performed the MRI measurements and analyzed the resulting data. P.R. also participated in the preparation of the manuscript.

Mukherjee, A, Davis, H.C, **Ramesh, P.** et al. (2017). "Biomolecular MRI reporters: evolution of new mechanisms". In: Progress in Nuclear Magnetic Resonance Spectroscopy, 102-103, pp. 32-42. doi: 10.1016/j.pnmrs.2017.05.002

P.R. participated in the preparation of the manuscript.

TABLE OF CONTENTS

LIST OF TABLES AND ILLUSTRATIONS

Number *Page*

Tables

Figures

NOMENCLATURE

Symbol	**Definition**	**Units (SI)**	**Value**
$\mathbf{B}$	Magnetic flux density	T	Commonly referred to as the magnetic field
$\mathbf{H}$	Magnetic field strength	$\mathrm{A/m}$	Magnetic field produced by ‘free’ currents
$\mathbf{M}$	(Volume) Magnetization	$\mathrm{A/m}$	Magnetic dipole moment per unit volume
$\mathbf{M_s}$	Saturation Magnetization	$\mathrm{A/m}$	Bulk magnetite ~ 4.46×10^5
$\mathbf{M_0}$	Initial or remnant magnetization	$\mathrm{A/m}$	Volume magnetization of the material in the absence of a field
$\mathbf{m}$	Magnetic dipole moment	$\mathrm{A \cdot m^2}$	
$\boldsymbol{m_p}$	Proton rest-mass	kg	1.67×10^{-27}
$\boldsymbol{m_e}$	Electron rest-mass	kg	9.11×10^{-31}
$\boldsymbol{\mu_0}$	Permeability of free space	$\mathrm{H/m}$	$4\pi \times 10^{-7}$
$\boldsymbol{e}$	Electric charge	C	1.60×10^{-19}
$\boldsymbol{\chi}$	Volume magnetic susceptibility	Dimensionless	By convention, $\chi = \frac{\mathrm{M}}{\mathrm{H}}$
$\boldsymbol{\gamma_{I,e}}$	Gyromagnetic ratio	$\mathrm{MHz/T}$	γ_I: Nuclear gyromagnetic ratio γ_e: Electron gyromagnetic ratio
N	Particle density	$\mathrm{m^{-3}}$	
$\boldsymbol{k_B}$	Boltzmann constant	$\mathrm{J/K}$	1.38×10^{-23}
Z	Atomic number	Dimensionless	
$\boldsymbol{g_{I,e}}$	Landé g factor	Dimensionless	$g_e \sim -2.00$ $g_I \sim 5.59$
$\boldsymbol{T_1, T_2}$	Relaxation times	s	
$\boldsymbol{T_E, T_R}$	MRI pulse-sequence parameters	s	
D	Apparent diffusion coefficient of nuclei in MRI	$\mathrm{m^2/s}$	
$\boldsymbol{\eta}$	Dynamic viscosity	$\mathrm{Pa \cdot s}$	$\eta_{water} \approx 10^{-3}$
$\boldsymbol{\mu_B}$	Bohr magneton	$\mathrm{J/T}$	9.27×10^{-24}
$\mathbf{J}$	Total angular momentum operator	$\mathrm{kg/(m^2 \cdot s)}$	
$\boldsymbol{\hbar}$	Planck’s constant	$\mathrm{J/s}$	1.05×10^{-34}
$\mathbf{S}$	Total electron spin operator	$\mathrm{J/s}$	$\hbar\sqrt{S(S+1)}$
$\mathbf{I}$	Total nuclear spin operator	$\mathrm{J/s}$	$\hbar\sqrt{I(I+1)}$
$\boldsymbol{m_s}$	Spin quantum number	Dimensionless	

$\boldsymbol{\epsilon_{i,j,k}}$	Lattice strain constant	$1/\mathrm{s}$	Electric-field coupling constant for an NV-axis. Typical values are of order GHz.
$\boldsymbol{A_{hf}}$	Hyperfine coupling constant		Electron-Proton coupling strength between NV center and ^{13}C or ^{14,15}N within the diamond lattice. Typical values are of order MHz.

Vector quantities are denoted using regular, **bold** symbols whereas scalars are *italicized*.

Chapter 1

NON-INVASIVE BIOLOGICAL IMAGING USING MRI

1.1 Motivations

"When scientists develop methods to help them see things that were once invisible, research always takes a great leap forward." Nobel Prize Committee in 2008

The development of genetically encoded optical reporters has revolutionized the study of cell-biology by directly coupling changes in optical contrast to the expression and activity of molecular targets within the cell. Despite the technological advances in optical imaging, however, all optical contrast agents are fundamentally limited in their utility for studying cell-biology *in vivo* in opaque animals. This is primarily because the amplitude of electromagnetic radiation in the visible (and near infra-red) spectrum is rapidly attenuated ($\mathrm{I} \sim \mathrm{e}^{-\mathrm{z}}$) due to photon scattering and absorption by tissue.[1] Consequently, fundamental questions in mammalian biology pertaining to animal development, neuroscience, and immunology for example, remain unanswered because of our inability to observe cellular biology *in vivo*.

On the other hand, magnetic fields can permeate through the body unencumbered – a feature which arises from the fact that tissue only weakly interacts with magnetic fields. Magnetic Resonance Imaging (MRI) scanners therefore exploit these subtle interactions to form 3D anatomical images of living animals in a safe manner, without the use of ionizing radiation such as X-rays (CT) or γ-rays (PET).[2] However, there are at present few sensitive and genetically encoded reporter genes for MRI – a fundamental technological bottleneck that limits its utility for studying cell and tissue biology *in vivo*.[2] Among the most sensitive and widely used contrast agents in MRI, superparamagnetic iron oxide nanoparticles (SPIONs) act by shifting the local magnetic susceptibility of an MRI voxel ($\sim 1\ \mathrm{mm}^3$) by several parts per million (ppm); consequently, voxels that contain SPIONs, as well as their nearest neighbors, appear darker relative to background in T_2 weighted MRI. While SPIONs have enabled successful cell-tracking and tissue discrimination *in vivo*, their synthetic nature broadly limits their utility for biosensing or studying biology within dividing cells.[3] If magnetic nanoparticles could be genetically encoded and biomineralized, they would arguably remove one of the largest barriers to the widespread use of MRI for studying cell biology in large, living animals. Lastly, such genetically encoded magnetic nanoparticles would also enable remote control of biological function using magnetic fields.

However, despite extensive efforts by the MRI and synthetic biology community, there has been scant progress in engineering a biosynthetic pathway that is truly capable of biomineralizing superparamagnetic iron oxides in model cells (gut microbes, mammalian cells) of interest to human health. Faced with these hurdles, we set out to develop an alternative approach to making cells magnetic. Although our 'ultraparamagnetic' cells are less magnetic than naturally magnetotactic microbes, their strong paramagnetism is sufficient to enable more sensitive detection *in vivo* using MRI, and magnetic capture *ex vivo* using strong magnetic field gradients.

In this thesis, I will first cover the physical principles of MRI and how they broadly inspired our efforts to engineer ultraparamagnetic cells. I will then extend the concepts learned through our cellular engineering efforts to highlight a new method for localizing magnetized therapeutic cells in the GI tract noninvasively. Lastly, again motivated by our efforts to engineer paramagnetic cells, I will introduce a new modality for optical magnetic field imaging, which we used to experimentally study the microscopic origins of MRI contrast.

1.2 Physical principles of Magnetic Resonance Imaging (MRI)

All Magnetic Resonance Imaging (MRI) scanners exploit the phenomenon of Nuclear Magnetic Resonance (NMR) in order to construct 3D images of living animals non-invasively. NMR, as originally described by Isidor Isaac Rabi, occurs whenever an atomic nucleus with non-zero total spin is first placed in a magnetic field.[4] These nuclei effectively act as infinitesimal magnetic dipoles ($\boldsymbol{\mu}$) and preferentially align with an external magnetic field, which results in a population imbalance between their spin eigenstates (Zeeman effect). Parallel spin alignment with the external magnetic field is energetically favored (Eq. 1.1), and its population density (also known as spin polarization) increases in proportion with the energy gap between the two spin eigenstates.

$$\Delta E = m_s \hbar \gamma_I \mathbf{B_0} = \frac{\hbar \gamma_I}{2} \mathbf{B_0} \tag{1.1}$$

Within any MRI voxel at any given time, there is an excess of nuclear spins ($\mathbf{M_0} = \frac{N}{V}\boldsymbol{\mu}$) that are aligned with the magnetic field of the MRI scanner ($\mathbf{B_0}\,\hat{k}$), as described by the Boltzmann distribution (Eq. 1.2a).

$$\frac{N_{\text{aligned}}}{N_{\text{anti-aligned}}} = e^{\Delta E / k_B T} \tag{1.2a}$$

However, the Zeeman coupling between the nuclear magnetization ($\mathbf{M_0}$) and $\mathbf{B_0}$ is weak when compared with thermal energy, and therefore results in a spin polarization of approximately a few parts per million (Eq. 1.2b) under ambient conditions in typical field strengths ($20\ ^\circ\mathrm{C}, 7$ T).

$$\frac{N_{\text{aligned}}}{N_{\text{anti-aligned}}} \sim e^{3.9\times10^{-6}} \rightarrow 3.9\ \text{ppm}\ {}^{1}_{1}\text{H polarization} \tag{1.2b}$$

In addition to creating a population imbalance, $\mathbf{B_0}$ also exerts a torque on $\mathbf{M_0}$, which results in its nutation about $\mathbf{B_0}$ at a nuclei-specific frequency called the Larmor frequency (ω_L).[5] Nuclear magnetic resonance occurs upon *transient* application of a secondary *oscillating* magnetic field ($\mathbf{B_1} = B_1 e^{i\omega_L t}$) in the plane *perpendicular* (*i-j*) to $\mathbf{B_0}\,\hat{k}$. Immediately after resonant excitation by $\mathbf{B}_1$, $\mathbf{M_0}$ tips into the transverse (*i-j*) plane while precessing at the Larmor frequency ($\mathbf{M}_\perp = \mathbf{M_0} e^{i(\omega_L t + \phi)}$). The rotating magnetization vector subsequently induces a current in detection coils that receive signals only from the transverse plane. While the frequency of the induced current is the Larmor frequency, its corresponding phase ($\cos\phi$) decays from one to zero as a result of spatiotemporal inhomogeneities in the magnetic field. Unless the spins are 'refocused' using another resonant excitation pulse ($\mathbf{B_1}$), the MRI signal is effectively lost due to decoherence of nuclear spins. All the information needed to construct an MR image is obtained by recording the restoration of thermal polarization ($\mathbf{M_0}$) along $\mathbf{B_0}$, the dynamics of which are elegantly summarized by the Bloch-Torrey equation (Eq. 1.3).[6]

$$\frac{d\mathbf{M}}{dt} = \mathbf{M} \times \gamma_I \mathbf{B} - D\nabla^2\mathbf{M} - \frac{\mathbf{M}_x\mathbf{i} + \mathbf{M}_y\mathbf{j}}{T_2} - \frac{(\mathbf{M}_z - \mathbf{M_0})\mathbf{k}}{T_1} \tag{1.3}$$

The solution to this first-order coupled differential equation (neglecting the role of spin diffusion) serves as the basis for understanding nuclear spin relaxation and the origins of image contrast in MRI (Eq. 1.4a-1.4b).

$$\mathbf{M_z}(\mathrm{t}) = \mathbf{M_0}\left(1 - e^{-t/T_1}\right) \tag{1.4a}$$

$$\mathbf{M}_\perp(\mathrm{t}) = \mathbf{M_0}e^{-t/T_2} \tag{1.4b}$$

The nuclear magnetization vector ($\mathbf{M}_\perp$) in the transverse plane decays to zero due to two simultaneous processes: *spin-lattice* relaxation and *spin-spin* relaxation, which will be covered in depth to guide rational contrast agent design. The *spin-lattice* relaxation time (T_1) characterizes the time needed for $\mathbf{M_z}$ to recover approximately 63% of its initial longitudinal value ($\mathbf{M_0}$) following resonant excitation with $\mathbf{B_1}$. Meanwhile, the *spin-spin* relaxation time (T_2) characterizes the time needed for the transverse magnetization ($\mathbf{M}_\perp$) to simultaneously decay by approximately 37% of its initial value ($\mathbf{M_0}$). These relaxation time constants are heavily influenced by the spins' local environment, and therefore serve as useful proxies for identifying and characterizing tissue subtypes using MRI.[7] In the following sections, I will summarize the microscopic factors that affect nuclear spin relaxation following resonant excitation, and highlight the mechanisms of various classes of MRI contrast agents using the Bloembergen-Purcell-Pound (BPP) framework.[6]

1.3 Overview of magnetism and its role in MRI contrast

To understand the various factors that influence nuclear spin relaxation, we must first develop an intuition for how matter interacts with an external magnetic field. With the exception of superconducting materials (Meissner effect), magnetic fields permeate through all matter, albeit with varying efficacy. The magnetic field at any given point within a material can be described by the constitutive relation given in Eq. 1.5.

$$\mathbf{B} = \mu_0(\mathbf{M} + \mathbf{H}) \tag{1.5}$$

The total magnetic flux density ($\mathbf{B}$) within a material exposed to a magnetic field includes contributions from both 'free' sources, $\mathbf{H}$, and from 'bound' sources, $\mathbf{M}$, within the material itself. For the purposes of MRI, the external electromagnet acts as the 'free' $\mathbf{H}$ source, whereas $\mathbf{M}$ results from the interaction of the sample with $\mathbf{H}$. With the exception of ferromagnetic materials and superconductors, the magnetization of both diamagnetic and paramagnetic materials can be described to first-order (Eq. 1.6).

$$\mathbf{M} = \mathbf{M_r} + \chi\mathbf{H} \tag{1.6}$$

In the absence of a magnetic field, the initial, or remnant magnetization ($\mathbf{M_r}$), of all diamagnetic and paramagnetic materials is zero. Therefore, magnetic susceptibility (χ) serves as a useful quantity for characterizing the responsiveness of a material to an external magnetic field. I will summarize four relevant types of magnetism that are relevant to understanding MRI and MRI contrast agents.

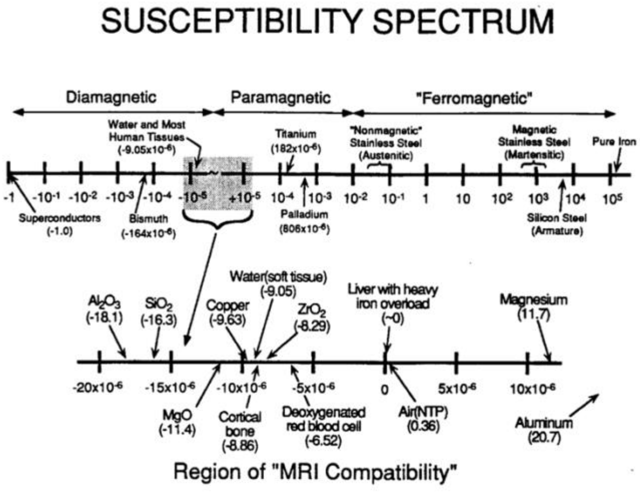

Fig. 1.1 Susceptibility spectrum. | The upper diagram uses a logarithmic scale to indicate the full range of observed magnetic susceptibility values. The bottom diagram uses a linear scale (in ppm) to indicate the properties of some materials with $|\chi| < 20\ \text{ppm}$. The susceptibilities of most human tissues are in the range from -7.0 ppm to – 11.0 ppm. Adapted from Ref.[8]

1.3.1 Langevin diamagnetism ($-1 \leq \chi \leq 0$)

Langevin diamagnetism, which is present in all non-superconducting matter, results from distortions in the orbital motion of electrons as a result of placing an atom in an external magnetic field. Diamagnetism can be approximated classically using Lenz's law of electromagnetic induction. The orbital motion of an electron around its nucleus can be idealized as an infinitesimal current loop that produces an orbital magnetic dipole moment (Eq. 1.7).

$$\boldsymbol{\mu} = -\frac{1}{2}e\mathbf{v}r\,\hat{\mathbf{k}} \tag{1.7}$$

When an external magnetic field ($\mathbf{B}\,\hat{\mathbf{k}}$) is turned on, according to Lenz's law, the resulting change in magnetic flux across the infinitesimal current loop induces the creation of a circumferential *electric* field – which causes the electron to *speed up*. This increase in orbital velocity causes a corresponding *antiparallel* (with respect to the magnetic field) change in the orbital dipole moment (Eq. 1.8).

$$\Delta\boldsymbol{\mu} = -\frac{1}{2}e(\Delta\mathbf{v})r\,\hat{\mathbf{k}} = -\frac{e^2r^2}{4m_e}\mathbf{B}\,\hat{\mathbf{k}} \tag{1.8}$$

In any atom however, its constituent electron orbits are randomly oriented, thus averaging out all orbital magnetic dipole moments. On the other hand, in the presence of a magnetic field, each electron acquires an extra orbital magnetic dipole moment (Eq. 1.8) that is *antiparallel* to the applied field. Consequently, Langevin diamagnetism refers to this collective weak repulsion that all matter exhibits when placed in a magnetic field. The diamagnetic susceptibility (Eq. 1.9) of a material is independent of its temperature and purely a function of its average electron orbital radius $\langle r^2 \rangle$.

$$\chi = -\frac{\mu_0 e^2 NZ\langle r^2 \rangle}{6m_e} \tag{1.9}$$

1.3.2 Curie paramagnetism ($\mathbf{0} < \boldsymbol{\chi} \leq \mathbf{10^{-2}}$)

When an atom is placed in a magnetic field, all of its constituent electron and proton spins are motivated to preferentially align with the external field, since parallel alignment produces the lowest energy configuration (Zeeman effect – Eq. 1.1). The external magnetic field exerts a torque on orbital and spin magnetic dipole moments, but a considerable amount of energy is needed to tilt the orbital magnetic dipole moment, compared with the spin magnetic dipole moment; therefore, contributions to paramagnetic susceptibility from *orbital* angular momenta are negligible to a first order. Since the mass of an electron is small when compared with that of a proton ($m_p/m_e \approx 1836$), its corresponding spin polarization is also considerably higher at a given magnetic field and temperature. Indeed, for electrons, this preferential alignment of *spin* with the applied field is also significantly stronger than their respective *orbital* diamagnetic response.

However, Pauli's exclusion principle curtails the complete alignment of all electron spins in filled atomic orbitals, since spins are necessarily paired in an anti-parallel manner; therefore, these paired electrons have no net spin angular momentum. Consequently, only atoms with *unpaired* electrons or electrons in *partially-filled* orbitals, are responsible for paramagnetism. The magnetic field ($\mathbf{B}$) within a paramagnetic material is in fact *amplified* by the alignment of free electron spins, which produce co-directional magnetic fields. The strength of paramagnetism, meanwhile, is influenced by temperature, since thermal energy randomizes spin alignment. The magnetic susceptibility of paramagnetic materials is therefore inversely correlated with their temperature, as given by the Curie-law (Eq. 1.10a)

$$\chi = \frac{\mu_0 N \boldsymbol{\mu}^2}{3k_B T} \tag{1.10a}$$

Here, the magnetic dipole moment of a paramagnetic substance is computed using its total spin (Eq. 1.10b).

$$\boldsymbol{\mu} = g_e \mu_B \sqrt{S(S+1)} \tag{1.10b}$$

1.3.3 Ferromagnetism ($10^{-2} < \chi < 10^{6}$)

Ferromagnetism is in fact the earliest known type of magnetism, having originally been described by the Greek philosopher Thales of Miletus around the 6th century BCE. Ferromagnetic materials, such as magnetite (Fe_3O_4), possess a permanent, non-zero magnetic moment even in the absence of a magnetizing field. This fundamental property, as elegantly formalized by Charles Kittel, results from the existence of microscopic domains within the bulk ferromagnetic material.[9] Each domain consists of atomic paramagnets ($N \sim 10^5/\text{domain}$), whose individual spin angular momenta are collectively aligned in the same direction. This occurs because of a powerful quantum-mechanical effect called the exchange interaction, in which unpaired valence-electron spins between neighboring atoms are spin-coupled. The exchange interaction is *not* the result of magnetic dipolar coupling between neighboring electron spins, which at-most amounts to a local field of (≈ 0.1 T). Instead, the exchange interaction fundamentally originates from the overlap between electron wavefunctions ($\Psi(i)$) in multi-electron systems. When electronic wavefunctions overlap between two or more atoms, as is often the case for crystalline materials, there is a non-zero probability of electron exchange between atomic nuclei. However, since electrons are fermions, their wavefunctions must be anti-symmetric with respect to electron exchange (i.e. $\Psi(i,j) = -\Psi(j,i)$), according to Pauli's exclusion principle. The likelihood of spin exchange is in turn dictated by the exchange energy, which is given by the Hamiltonian,

$$\hat{H}_{ex} = -2J_{ex}\mathbf{S_i} \cdot \mathbf{S_j} \tag{1.11}$$

where J_{ex} refers to the overlap between two spin wavefunctions ($\mathbf{S_i}$ and $\mathbf{S_j}$) and is calculated by integrating across the space occupied by both atoms (Eq. 1.12).

$$J_{ex}(i,j) = \langle \Psi_i(r_i)\Psi_j(r_j) | \hat{H}_{ex} | \Psi_i(r_j)\Psi_j(r_i) \rangle \tag{1.12}$$

Consequently, materials for which the exchange energy is minimized through *parallel* alignment between neighboring spins ($J_{ex} > 0$) are *ferromagnetic*, and consequently exhibit spontaneous magnetization even in the absence of an external magnetic field. On the other hand, materials for which the exchange energy is minimized through *anti-parallel* alignment between neighboring spins ($J_{ex} < 0$) are *anti-ferromagnetic*, and consequently have *zero* net magnetization below a critical ordering temperature referred to as the Neel temperature. Magnetite is in fact *ferrimagnetic*, a distinction intended to categorize materials for which *anti-parallel* alignment between neighboring spins is favored, but nonetheless have a non-zero spontaneous magnetization due to imperfect cancellation of anti-parallel moments. Magnetite has an inverse spinel structure in which the ferric ions occupy tetrahedral positions within the magnetite unit lattice and are anti-coupled. The non-zero magnetization of magnetite ($4\ \mu_B/\text{lattice}$) therefore results from the ferrous ions that occupy the octahedral position within the unit lattice.[10] Accordingly, considerable efforts have been spent on engineering strongly magnetic materials by substituting the transition metals in the octahedral coordination to create crystals with higher mass magnetizations.[11]

To summarize, the exchange interaction can effectively be understood as a strong, local magnetic field ($\approx\ 10^3$ T) that stabilizes collective spin-polarization against the randomizing effects of thermal motion. At temperatures equivalent to or above the ordering temperature of both ferromagnetic and antiferromagnetic materials, thermal energy is sufficient to overcome the strong spin-spin coupling and the material behaves as a bulk paramagnet. If its constituent domains are randomly aligned, as is the case for polycrystalline ferromagnetic minerals, then it effectively has a net magnetization of zero. By applying an external magnetic field, one can quickly saturate the magnetization of ferro- and ferri- magnetic materials even at relatively weak fields (< 1 T), which explains their utility for magnetic control applications. That said, given their extremely large magnetic susceptibilities ($\chi \gg 10^2$), ferromagnetic materials are not practically useful for MRI, since their presence produces large susceptibility artefacts.

1.3.4 Superparamagnetism

Superparamagnetism is a special case of ferromagnetism and refers to single-domain ferromagnetic materials. For ferromagnetic materials such as magnetite, its single-domain size limit is between 20 – 30 nm in diameter, and magnetite nanoparticles of this size or smaller have no remnant magnetization in the absence of a magnetic field. Because they spontaneously magnetize, even under weak magnetic fields, single domain magnetic nanoparticles are extremely useful as imaging contrast agents for MRI. The magnetic susceptibility of an MRI voxel that contains superparamagnetic iron-oxide nanoparticles (SPIONs) is orders of magnitude larger than what it would be if an equivalent quantity of paramagnetic iron is uniformly distributed throughout the voxel.[12] Another advantage of using SPIONs as contrast agents for MRI is that their magnetization saturates at relatively low fields ($\mathbf{B_0} < 1\ T$). Consequently, one achieves relaxivities on the order of $R_2 \sim 10^2\ \text{mM}^{-1}\text{s}^{-1}$ using SPIONs compared with paramagnetic T_1 contrast agents ($R_2 \sim 10^0\ \text{mM}^{-1}\text{s}^{-1}$) under typical clinical imaging conditions (1.5 T – 3 T). The susceptibility of an MRI voxel that contains SPIONs also follows the Curie Law (Eq. 1.13).

$$\chi = \frac{\mu_0 N \mathbf{m}^2}{3k_B T} \tag{1.13}$$

Here, the magnetic dipole moment of a SPION is described using the Brillouin function (Eq. 1.14a – 1.14b).

$$\mathbf{m} = N g J \mu_B \left(\frac{2J+1}{2J}\coth\left(\frac{2J+1}{2J}\cdot x\right) - \frac{1}{2J}\coth\frac{x}{2J}\right) \tag{1.14a}$$

$$x \equiv \frac{g J \mu_B \mathbf{B}}{k_B T} \tag{1.14b}$$

Lastly, in addition to their utility for enhancing image contrast in T_2 weighted MRI, SPIONs have also been used extensively for magnetic hyperthermia, in which RF pulses tuned to the magnetization flip-flop frequency of a SPION produce local heating.[13] Accordingly, given these useful properties of superparamagnetic nanoparticles, there is considerable interest within the broader MRI community for engineering SPION biosynthetic pathways.

1.4 Mechanisms of nuclear spin relaxation in MRI

Having understood the various types of magnetism in matter, we can now build an understanding of how magnetism drives nuclear spin relaxation in an MRI scanner. Resonant excitation of nuclear magnetization ($\mathbf{M_0}$) which is polarized along $\mathbf{B_0}$ with $\mathbf{B_1}$, forces its cone of precession exclusively into the transverse plane (*i-j*), thus creating a phase-coherent magnetization vector ($\mathbf{M}_\perp$). Once the resonant perturbation is switched off, nuclear magnetization will return to its energetically favored polarization along $\mathbf{B_0}$. This return to axial magnetization, referred to as *spin relaxation*, is fundamentally driven by a combination of dipolar coupling between spins (nuclear and electronic), molecular motion (rotations, vibrations, translations), and spatial fluctuations in the magnetic field (spatial variations in χ).

1.4.1 Spin-lattice relaxation

Spin-lattice relaxation (T_1) refers to the process by which nuclear magnetization returns to its equilibrium polarization along $\mathbf{B_0}$. At any given time, an arbitrarily chosen nuclear spin within an MRI voxel experiences a random time-varying magnetic field ($\mathbf{B}(t) = \mathbf{B_0} + \Delta\mathbf{B}(t)$), as a result of interacting with its randomly moving neighbors, where $|\Delta\mathbf{B}| \ll |\mathbf{B_0}|$. Upon resonant excitation of $\mathbf{M_0}$ with $\mathbf{B_1}$, any transverse components of this randomly fluctuating magnetic field accelerates spin-lattice relaxation, provided that the field fluctuations are resonant with the motion and precession of the spins themselves. This is because only transverse fields can produce an axial torque, which is needed to accelerate T_1 relaxation. More fundamentally, T_1 relaxation occurs as a result of energy exchange between the excited spins and their surrounding environment (the lattice), as described by the BPP solution (Eq. 1.15).[14]

$$R_1 = \frac{1}{T_1} \sim \left[\frac{\gamma_I^4 I \cdot (I+1)}{r^6}\right]\left[\frac{\tau_c}{1+\tau_c^2\omega_L^2} + \frac{4\tau_c}{1+4\tau_c^2\omega_L^2}\right] \tag{1.15}$$

The term in the left set of brackets arises from dipolar-coupling between adjacent nuclei, whereas the term in the right set of brackets is the spectral density function, which provides a complete description of molecular motion. This fundamental relationship between molecular motion and nuclear relaxation suggests that optimal spin-lattice relaxation is achieved when field fluctuations occur at the same temporal frequency as the Larmor frequency of the spin (i.e. $\frac{1}{\tau_c} = \omega_L$). It is also worth noting that $R_1 \to 0$ as $\mathbf{B_0}$ increases, because molecular motion becomes off-resonant with the Larmor frequency at high magnetic fields.

1.4.2 Spin-spin relaxation

Spin-spin relaxation (*T₂*), on the other hand, refers to the complete destruction of phase-coherence between spins in the transverse plane, and is not driven by energy exchange with the lattice. Resonant excitation with $\mathbf{B_1}$ not only tips the magnetization vector into the transverse plane, but also synchronizes the precession phase (ϕ) of the spin ensemble ($\mathbf{M}_\perp$). While all spins continue to precess close to the Larmor frequency, differences in their phase of precession grows with differences in their local field (Eq. 1.16).

$$\Delta\phi = \gamma\mathbf{B}\Delta t \tag{1.16}$$

The BPP solution for spin-spin relaxation is structurally similar to that for spin-lattice relaxation with the exception of an extra term in the spectral density function (Eq. 1.17).

$$R_2 = \frac{1}{T_2} \sim \left[\frac{\gamma_I^4 I \cdot (I+1)}{r^6}\right]\left[\frac{5\tau_c}{1+\tau_c^2\omega_L^2} + \frac{2\tau_c}{1+4\tau_c^2\omega_L^2} + 3\tau_c\right] \tag{1.17}$$

In addition to field fluctuations in the transverse plane, T_2 relaxation is also driven by field fluctuations along $\mathbf{B_0}$. Dipolar interactions between nuclear spins and axial field fluctuations fundamentally broadens the proton resonance frequency linewidth, which manifests itself through accelerated T_2 relaxation. While phase decoherence broadly results from spatiotemporal field inhomogeneities, it is partially reversible. Decoherence that results from molecular motion induced field fluctuations is not reversible, whereas decoherence that results from slowly varying spatial field inhomogeneities can be reversed. This distinction between reversible and irreversible phase loss forms the basis of T_2 and T_2^* imaging in MRI respectively.

1.4.3 Chemical-shift imaging

One principle advantage of MRI over other non-invasive imaging modalities is that it can be used to glean insight about metabolism and soft-tissue physiology even without the administration of any contrast agents. To do so, one exploits the fact that the total magnetic field a nuclear spin experiences is intimately connected with its local chemical environment. For example, by virtue of being covalently bonded to an electronegative atom, protons belonging to hydroxyl or amide groups experience a slightly different magnetic field than water protons. This corresponding shift in the proton Larmor frequency is referred to as chemical shift, and it results from shielding of the proton spin by the orbital motion of its surrounding electrons (Eq. 1.18).

$$\omega_{eff} = \omega_L(1-\delta) \tag{1.18}$$

Here, δ refers to the frequency offset from the bulk proton Larmor frequency and is usually written in parts per million (ppm) since the shielding effects are very small. Chemical exchange saturation transfer (CEST) MRI exploits the fact that protons are labile and have varying chemical shifts.[15]

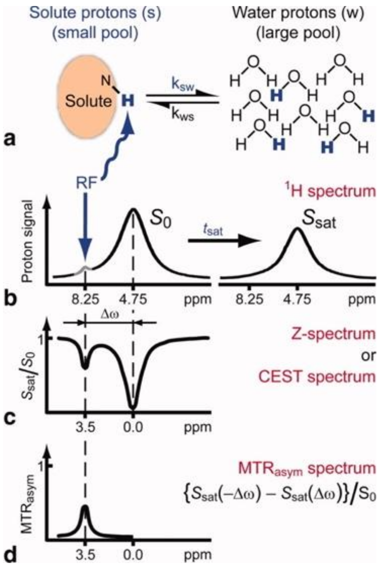

Fig. 1.2 Chemical Exchange Saturation Transfer (CEST). | Principles and measurement approach for pure exchange effects. Adapted from Ref.[15]

In a typical CEST imaging experiment, there are at-least two unique proton frequency pools. The water proton usually forms the 'bulk' spin pool, whereas protons associated with other organic groups such as hydroxy, amide, or imine, constitute the second, chemically shifted (δ) pool. A typical CEST sequence consists of first 'destroying' the MR signal from the second pool through selective irradiation, and concomitantly recording the diminishment of the MR signal from the bulk water pool, as a result of exchange into the secondary pool. As long as the exchange rate of protons between the two chemical pools is equivalent or comparable to the chemical shift between the two resonances, there will be an appreciable loss of 'bulk' magnetization signal. As such, CEST MRI is particularly useful for noninvasive imaging of metabolism, tissue composition, and pH.

1.5 Contrast agents in MRI

Despite its unprecedented power and utility for non-invasive anatomical imaging, MRI is fundamentally limited in its sensitivity by a) density and polarization efficacy of nuclear spins, b) diffusion of spins, and c) molecular motion and resulting fast fluctuations in the magnetic field. Contrast agents in MRI, as with other imaging modalities, are therefore used to improve detection of specific molecular processes relative to background.

1.5.1 T_1 contrast agents: mechanism of action

One of the principal advantages of T_1 – weighted MRI over T_2 – weighted, Diffusion-weighted, and CEST MRI is that voxels which contain T_1 contrast agents appear brighter on T_1 – weighted images. This 'positive' contrast fundamentally results from an acceleration in the T_1 of nuclear spins due to the transient coordination with paramagnetic compounds within the voxel.[16] Since the electron's gyromagnetic ratio ($\gamma_e = 28.02\ \mathrm{GHz/T}$) is approximately three orders of magnitude stronger than that of the proton ($\gamma_I = 42.57\ \mathrm{MHz/T}$), its corresponding thermal polarization is equivalently higher under the same conditions ($20°\mathrm{C}, 7\mathrm{T}$).

$$\frac{N_{\mathrm{aligned}}}{N_{\mathrm{anti-aligned}}} \sim e^{0.0025} \rightarrow 25000\ \mathrm{ppm\ electron\ polarization} \qquad (1.19)$$

Equation 1.19 implies that the electron spins of paramagnetic compounds are by-and-large aligned with magnetic field ($\mathbf{B_0}$) in an MRI scanner. Consequently, any nuclear spins that coordinate with such paramagnetic compounds experience a significantly stronger magnetic field, which in turn accelerates their spin-lattice relaxation, as summarized by the SBM equation (Eq. 1.20).

$$R_{1\,(\text{C.A.})} = \frac{1}{T_1} \sim \left[\frac{\gamma_I^2 \gamma_e^2 S \cdot (S+1)}{r^6}\right]\left[\frac{3\tau_C}{1 + 4\tau_C^2 \omega_L^2}\right] \tag{1.20}$$

The correlation time for fluctuations in the local fields, as experienced by the nuclear spin, is a function of the rotational correlation time of the paramagnetic molecule, the exchange rate at which spins coordinate and dissociate with the paramagnetic molecule, and the longitudinal relaxation time for the electron spin(s) on the paramagnetic compound (Eq. 1.21a).

$$\frac{1}{\tau_C} = \frac{1}{\tau_R} + \frac{1}{\tau_M} + \frac{1}{T_{1e}} \tag{1.21a}$$

The optimal nuclear spin relaxation in the presence of a paramagnetic T_1 contrast agent occurs when the correlation frequency ($\frac{1}{\tau_C}$) is equivalent or comparable to the Larmor frequency. Typical small-molecule paramagnetic T_1 contrast agents have correlation times which are dominated by molecular tumbling (Eq. 1.21b).

$$\frac{1}{\tau_R} \sim 2 - 20\text{ GHz}, \frac{1}{\tau_M} \sim 100\text{ MHz, and } \frac{1}{T_{1e}} \sim 35\text{ MHz at 1.5 T} \tag{1.21b}$$

We can infer from Eq. 1.21a and Eq. 1.21b that the rotational correlation time and exchange rate have the largest influence on the relaxivity of a T_1 contrast agent. Previous strategies for engineering high relaxivity T_1 contrast agents have focused on 1) reducing molecular tumbling, 2) engineering ligands around the paramagnetic ion that affect both the proton exchange rate, as well as 3) total electron spin. While all T_1 contrast agents also produce T_2 effects, these are modest when compared with T_1 contrast. Lastly, while T_1 contrast agents continue to be actively studied in the field, they are not the primary focus of this thesis.[17]

1.5.2 T_2 contrast agents: mechanism of action

The principal advantage of T_2 – weighted imaging is that its corresponding MRI pulse sequences are among the fastest imaging schemes, when compared with other MRI pulse sequences, such as T_1 or CEST; consequently T_2 imaging has been extensively used for functional *in vivo* studies. Additionally, T_2 contrast agents are among the most sensitive contrast agents that have been developed and can be detected *in vivo* at $\mathrm{pg\ Fe/cell}$, approaching sensitivities achieved with PET.[18] Given their sensitivity, as well as speed of detection, the rest of this thesis is focused on engineering and applying T_2 contrast agents to imaging and controlling cellular function non-invasively.

Unlike T_1 contrast agents which primarily relax water protons through direct coordination with paramagnetic centers (inner-sphere relaxation), T_2 contrast agents act by changing the magnetic susceptibility of the voxel itself; consequently, the effects on MRI contrast of T_2 contrast agents can be felt far beyond the voxel that contains them. As such, any water molecules that diffuse through and around such voxels experience fundamentally different magnetic fields.[19–21] The strongest T_2 contrast agents are SPIONs, which introduce significant spatial inhomogeneity in the local magnetic field due to their strong magnetic properties, with saturation magnetization up to ($M_{sat} \sim 120\ \mathrm{emu/g}$).

The influence of SPIONs on T_2 relaxation depends on both their number density within a voxel (N/V), and the characteristic diffusion timescales of the spins themselves (τ_D).[22] To gain deeper insight into how these factors affect T_2 contrast, we start by modeling the phase accrued by a nuclear spin as it diffuses past a SPION of radius R with magnetization **M**. The equatorial z-component of the magnetic field of a SPION of radius R is given by Eq. 1.22.

$$\mathbf{B}_{\text{SPION}} = \frac{\mu_0 \mathbf{M}}{3}\left(\frac{R}{r}\right)^3 (3\cos^2\theta - 1) \tag{1.22}$$

We can define the volume fraction of a voxel occupied by SPIONs as f, wherein

$$f = \frac{Nv}{V} \tag{1.23}$$

Here, $\frac{N}{V}$ corresponds to the number density of SPIONs per voxel, and v is the volume of a SPION. Assuming that the SPIONs are spherical particles of radius R, the characteristic separation distance (l_{sep}) between such particles within a voxel at number density $\frac{N}{V}$ is given by Eq. 1.24.

$$l_{sep} = \left(\frac{v}{f}\right)^{1/3} = \left(\frac{\frac{4}{3}\pi}{f}\right)^{1/3} R \tag{1.24}$$

Over some time τ, nuclear spins diffuse a characteristic distance (l_{diff}) as determined by the 3D diffusion equation, where *D* is the bulk diffusion coefficient of water at room temperature.

$$l_{diff} = \sqrt{6D\tau} \tag{1.25}$$

If the SPIONs are large enough that the characteristic diffusion distance is small when compared with the average inter-particle spacing ($\frac{l_{diff}}{l_{sep}} \ll 1$) at a fixed volume fraction, then the majority of spins only experience a single magnetic environment. In this scenario, the inhomogeneous relaxation rate (R_2^*) is unaffected by spin diffusion and near its theoretical maximum. This 'single-environment' regime is classically referred to as the static dephasing regime since field fluctuations are approximately constant across an MR echo. That said, the loss of phase coherence can be partially reversed by applying a gradient with opposite polarity (spin-echo pulse sequence), which explains why the homogeneous relaxation rate is smaller than the inhomogeneous relaxation rate ($R_2 < R_2^*$) in the static dephasing regime.

On the other hand, if the characteristic diffusion distance is large when compared with the inter-particle separation distance ($\frac{l_{diff}}{l_{sep}} \gg 1$) at a fixed volume fraction, then spins will sample multiple magnetic fields, including those with opposite polarity, within an MR echo. This scenario is referred to as the motional averaging regime, in which the inhomogeneous relaxation rate (R_2^*) can be analytically solved (Eq. 1.26a) from the SBM equations. Additionally, nuclear spin relaxation by SPIONs is referred to as Outer-sphere (OS) relaxation since it requires no direct coordination between the nuclei and the nanoparticle, which also explains how T_2 contrast agents exert their influence across large distances.

$$R_2^* = \frac{4}{9} f(\Delta\omega_0)^2 \tau_D \tag{1.26a}$$

$$\Delta\omega_0 = \gamma \mathbf{B}_{\text{SPION}} \tag{1.26b}$$

$$\tau_D = R^2/D \tag{1.26c}$$

Here, $\Delta\omega_0$ refers to the shift in proton Larmor frequency at the equator of the SPION and τ_D is the characteristic time needed for spins to diffuse into a new magnetic environment. Since the MRI signal is effectively lost when its phase discrepancy exceeds $90°$, ($|\Delta\phi| \geq \pi/2$), we can deduce the effective timescale of spin coherence (τ_R) as follows.

$$\frac{\pi}{2} = \gamma\langle|\mathbf{B}_{\mathbf{SPION}}|\rangle\tau_R \tag{1.27}$$

We can estimate the average magnitude of the magnetic field (z-component) produced by a SPION by integrating out all its angular components at a fixed radius *r* and obtain:

$$\langle|\mathbf{B}_{\mathbf{SPION}}|\rangle \approx \frac{\mu_0\mathbf{M}}{6}\left(\frac{R}{r}\right)^3 \tag{1.28}$$

We can then estimate the characteristic timescale of spin coherence to be[23]

$$\tau_R \approx \frac{3\pi}{\mu_0\gamma\mathbf{M}}\left(\frac{r}{R}\right)^3 \tag{1.29}$$

Equating the time needed for a spin to diffusively sample the field profile of a SPION (τ_D) with the time taken for spin-phase to become completely incoherent (τ_R), enables us to estimate the distance over which a SPION influences the phase of all nuclear spins (Eq. 1.30). Spins outside this 'boundary' remain coherent, whereas those that diffuse into this region will experience field inhomogeneities and faster T_2^* relaxation.

$$l_{boundary} \approx \frac{\mu_0\gamma\mathbf{M}}{3\pi D}R^3 \tag{1.30}$$

Subsequently, equating this boundary length-scale to SPION size yields a critical particle radius (Eq. 1.31). For SPIONs smaller than R_{crit}, nuclear spins will effectively diffuse out of their zone of influence ($l_{boundary}$) *before* being fully dephased, whereas particles larger than this size will fully relax spins within a single encounter.

$$R_{crit} \approx \sqrt{\frac{3\pi D}{\mu_0 \gamma \mathbf{M}}} \quad (1.31)$$

Using typical values for the volume magnetization and water diffusion coefficient, Eq. 1.38 suggests that the critical particle size is approximately around 20 nm. For SPIONs much larger than this critical size, such as 200 nm SPIONs, their zone of influence scales as the cube of particle radius ($l_{boundary} \sim 10\ \mu\text{m}$), which suggests that protons have to diffuse quite far before encountering a new magnetic environment. Unless spins are close to the large SPION surface, they will experience relatively shallow field inhomogeneities whose effects on signal phase can be reversed using a refocusing pulse. Consequently, these simple scaling arguments suggest that the optimal T_2 contrast is achieved using SPIONS that are approximately 20 – 50 nm in size.[24] It is therefore unsurprising that SPIONs within this size regime are the most extensively used contrast agents for *in vivo* imaging studies.

1.5.3 Genetically encoded T_2 contrast agents

Given their superior contrast, there has been considerable interest in developing genetically encoded SPIONs that are between 20 – 50 nm in size. The principle advantage of any genetically encoded contrast agent is that its expression and contrast mechanism can be directly coupled to the biochemical process of interest.[25 - 26] Furthermore, such genetically encoded reporters are useful for longitudinal studies since the contrast agent is continuously synthesized by the cell, as opposed to synthetic agents which lose their contrast potency due to cell division. While there are magnetotactic microbes that naturally biosynthesize SPIONs which are 30 – 50 nm large, there has been scant progress in transferring the microbial biosynthetic machinery into other model prokaryotes or eukaryotes.[27 – 31] This is in part due to the complexity of the microbial machinery which drives magnetosome biogenesis, since it consists of at-least 27 genes distributed across multiple operons spanning a total of ~ 100 kbp in size.[32 – 34] While efforts to achieve heterologous expression of the magnetosome island are ongoing, there have been parallel efforts to exploit other endogenous metalloproteins that can also produce T_2 contrast *in vivo*, albeit weakly.[35 – 41]

Accordingly, one popular chassis for engineering has been the metalloprotein ferritin, which is an 8nm particle that can hold up to 4500 Fe atoms under optimal iron-loading. Ferritin is thought to have evolved as atmospheric concentrations of oxygen rose, and acts as an iron storage and ferrous-iron detoxification vehicle for cells (prokaryotes, archaea, and eukaryotes).[42 - 43] Unlike microbial magnetosomes which biosynthesize superparamagnetic iron oxides such as magnetite, iron in ferritins is stored as a mixture of weakly paramagnetic and antiferromagnetic iron oxides under ambient conditions.[44 – 47]

Furthermore, unlike SPIONs whose relaxivity saturates at fields higher than 1 Tesla, ferritins exhibit a linear increase in relaxivity with increasing field strength. This interesting deviation from conventional outer-sphere relaxation theory (Sec. 1.5.2) is thought to arise from proton-exchange driven dephasing.[48 – 50] Freely diffusing water protons weakly adsorb onto the paramagnetic ferrihydrite surface within the ferritin core, and lose phase through dipolar interactions with paramagnetic ferric ions. Since the ferrihydrite mineral is intrinsically disordered, protons experience a broad (Lorentzian) distribution of magnetic fields.[51 – 53] Lastly, the relaxivity of ferritins is fundamentally limited by 1) water access to the ferrihydrite mineral and 2) the net paramagnetic moment of the mineral itself, which scales as $\sqrt{N_{\mathrm{Fe}}}$.[54]

The ferroxidase center of all known ferritins sits at the interface of two alpha-helical subunits, and uses molecular oxygen as the terminal electron acceptor to oxidize ferrous iron into ferric iron, which is then shuttled into the nanoparticle's interior using an electrostatic potential gradient.[55 – 58] The residues which line the interior surface of ferritins act as nucleation sites for the ferric ion. The oxidation of ferrous iron by the ferroxidase center also produces free protons as a byproduct, and these must be removed to avoid dissolution of the nucleated mineral. Since ferritins are porous and exist within a buffered cytoplasmic environment, any excess protons that are produced as a byproduct of ferroxidase reaction diffuse out of the ferritin core and are subsequently neutralized by endogenous phosphates and bicarbonates. Additionally, the presence of aqueous phosphates within the cytoplasm and the ferritin core contaminates the nascent iron-oxide mineral within the nanoparticle, thus producing mixed valence and intrinsically disordered phospho-ferrihydrite. The bulk of this mineral, however, is antiferromagnetically spin-coupled, and any paramagnetism that results can be accounted for by the incomplete cancellation of canted, surface electrons. As such, only 5% (at most) of the total iron contained within ferritins contributes to its overall paramagnetic moment.[54]

Ferritins are fundamentally unable to mineralize superparamagnetic iron-oxides in living cells due to 1) passive control of interior pH, 2) unsuitable control of iron redox stoichiometry, and 3) unstructured mineralization of iron-oxides. Interestingly, initial experiments with apo-ferritin demonstrated that if the pH, concentration of oxygen, and concentration of ferrous iron could be controlled, then ferritins were indeed capable of nucleating magnetite within their cores, thereby producing a 8 nm SPION with ~ 40 fold improvement in T_2 relaxivity.[59 – 61] Accordingly, over the last three decades, considerable efforts have been directed towards engineering and evolving ferritins to generate variants that are capable of nucleating magnetite in living cells. While such studies have produced ferritin variants with slightly different oxidation rates and mineralization capacity, they have not been successful in producing a truly superparamagnetic nanoparticle under typical cellular conditions.

This is primarily because the rate-limiting criteria for magnetite synthesis are redox-potential and pH.[62] In this light, it is unsurprising that magnetotactic bacteria first create lipid-enclosed nano-compartments in which the pH and redox properties of iron can be tightly controlled, prior to iron import and mineral nucleation.[63-64] The conditions within these magnetosome compartments are thermodynamically permissive for the spontaneous nucleation and growth of magnetite, once a critical amount of ferrous and ferric iron is introduced.[65–67] On the other hand, the typical redox and pH conditions within the mammalian or even most aerobic prokaryotic cytoplasm favor the formation of mixed valence ferrihydrites and non-magnetic iron-oxides.[68]

1.5.4 Engineering paramagnetic cells as T_2 contrast agents

Given the fundamental thermodynamic and chemical constraints that prevent the biomineralization of magnetite and other ferromagnetic iron oxides within the mammalian and *E. coli* cytoplasm, we asked if there was an alternate approach to engineer strongly magnetic cells.

Previous efforts towards engineering strongly paramagnetic ferritins[69 – 74] demonstrated that if a cell had enough paramagnetic metalloproteins, then it could be 1) visualized *in vivo* using MRI and 2) captured *in vitro* using strong magnetic field gradients.[71,72,75] This is unsurprising given that the magnetic susceptibility of most tissues is within $\pm 10 - 20\%$ of that of water; consequently, the paramagnetism wrought by even a single paramagnetic ion, such as Fe^{3+}, is sufficient to overcome the diamagnetic contribution from hundreds of thousands of water molecules. In the case of ferritins, if one assumes an ideal, fully loaded particle with 4500 Fe^{3+} high-spin iron atoms ($S = \frac{5}{2}$) and a diamagnetic protein shell, the magnetic susceptibility of a voxel with a single particle is significantly more paramagnetic (Eq. 1.32).

$$\chi_{ferritin} \sim 520 \times 10^{-6} \tag{1.32}$$

While it is unlikely to observe this high degree of loading and spin-state in cells given the high concentration of endogenous iron chelators, the susceptibility of liver tissue in instances of iron-overload disease was calculated to be approximately $\chi_{hemachromatosis} \sim 10^{-5}$, based on iron levels of approximately 6.6 mg Fe/g.[8] This reinforces the notion that a reasonable quantity of paramagnetic material is sufficient to shift an MRI voxel's magnetic susceptibility by a few ppm, thus enabling more sensitive MRI detection, as well as magnetic capture.

Previous studies on magnetic capture of ferritin expressing cells necessarily incubated cells with high-iron loads (5 mM Fe) in order to maximize its paramagnetic susceptibility. We hypothesized that if we could engineer a protein wherein the iron oxidation activity was decoupled from its iron mineralization phenotype, then we could independently optimize each catalytic step to obtain a much more paramagnetic metalloprotein.[76,77] Then, if these metalloproteins could be expressed in cells in sufficient quantities, doing so would appreciably shift the bulk magnetic susceptibility of the cell towards an ultraparamagnetic phenotype, thereby enabling more sensitive detection *in vivo* using MRI and magnetic capture *ex vivo* using strong magnetic field gradients.

BIBLIOGRAPHY

1. Piraner, D. I. *et al.* Going Deeper: Biomolecular Tools for Acoustic and Magnetic Imaging and Control of Cellular Function. *Biochemistry* **56,** 5202–5209 (2017).
2. Mukherjee, A., Davis, H. C., Ramesh, P., Lu, G. J. & Shapiro, M. G. Biomolecular MRI reporters: Evolution of new mechanisms. *Prog. Nucl. Magn. Reson. Spectrosc.* **102,** 32–42 (2017).
3. Thorek, D. L. J., Chen, A. K., Czupryna, J. & Tsourkas, A. Superparamagnetic iron oxide nanoparticle probes for molecular imaging. *Ann. Biomed. Eng.* **34,** 23–38 (2006).
4. Kellogg, J. M. B., Rabi, I. I. & Zacharias, J. R. The gyromagnetic properties of the hydrogens. *Phys. Rev.* **50,** 472–481 (1936).
5. Bloch, F. Nuclear Induction. *Phys. Rev. Lett.* **70,** 127–127 (1946).
6. Bloembergen, N., Purcell, E. M. & Pound, R. V. Relaxation Effects in Nuclear Magnetic Resonance Absorption. *Phys. Rev. Lett.* **73,** (1947).
7. Plewes, D. B. & Kucharczyk, W. Physics of MRI: a primer. *J. Magn. Reson. Imaging* **35,** 1038–54 (2012).
8. Schenck, J. F. The role of magnetic susceptibility in MRI. *Med. Phys.* **23,** (1996).
9. Kittel, C. Physical Theory of Ferromagnetic Domains. *Rev. Mod. Phys.* **21,** (1949).
10. Szotek, Z. *et al.* Electronic structures of normal and inverse spinel ferrites from first principles. *Phys. Rev. B - Condens. Matter Mater. Phys.* **74,** 1–12 (2006).
11. Lee, J.-H. *et al.* Artificially engineered magnetic nanoparticles for ultra-sensitive molecular imaging. *Nat. Med.* **13,** 95–99 (2007).
12. Lu, X. *et al.* Ultrashort Echo Time Quantitative Susceptibility Mapping (UTE-QSM) of Highly Concentrated Magnetic Nanoparticles: A Comparison Study about Different Sampling Strategies. *Molecules* **24,** 1143 (2019).
13. Chen, R., Christiansen, M. G. & Anikeeva, P. Maximizing hysteretic losses in magnetic ferrite nanoparticles via model-driven synthesis and materials optimization. *ACS Nano* **7,** 8990–9000 (2013).
14. Keeler, J. & Pell, A. J. *Understanding NMR Spectroscopy, Second Edition.* (Wiley, 2010).
15. Van Zijl, P. C. M. & Yadav, N. N. Chemical exchange saturation transfer (CEST): What is in a name and what isn't? *Magn. Reson. Med.* **65,** 927–948 (2011).
16. Lauffer, R. E. Paramagnetic Metal Complexes as Water Proton Relaxation Agents for NMR Imaging : Theory and Design. *Chem. Rev.* **87,** (1987).
17. Shapiro, M. G. *et al.* Directed evolution of a magnetic resonance imaging contrast agent for noninvasive imaging of dopamine. *Nat. Biotechnol.* **28,** 264–270 (2010).
18. Heyn, C., Bowen, C. V., Rutt, B. K. & Foster, P. J. Detection threshold of single SPIO-labeled cells with FIESTA. *Magn. Reson. Med.* **53,** 312–320 (2005).
19. Mills, P. H. & Ahrens, E. T. Theoretical MRI contrast model for exogenous T2 agents.

Magn. Reson. Med. **57,** 442–447 (2007).

20. Brooks, R. A. T2-Shortening by Strongly Magnetized Spheres: A Chemical Exchange Model. *Magn. Reson. Med.* **47,** 257–263 (2002).
21. Brown, K. A. *et al.* Scaling of transverse nuclear magnetic relaxation due to magnetic nanoparticle aggregation. *J. Magn. Magn. Mater.* **322,** 3122–3126 (2010).
22. Vuong, Q. L., Gossuin, Y., Gillis, P. & Delangre, S. New simulation approach using classical formalism to water nuclear magnetic relaxation dispersions in presence of superparamagnetic particles used as MRI contrast agents. *J. Chem. Phys.* **137,** 0–13 (2012).
23. De Haan, H. W. Mechanisms of proton spin dephasing in a system of magnetic particles. *Magn. Reson. Med.* **66,** 1748–1758 (2011).
24. Vuong, Q. L., Berret, J. F., Fresnais, J., Gossuin, Y. & Sandre, O. A universal scaling law to predict the efficiency of magnetic nanoparticles as MRI T2-contrast agents. *Adv. Healthc. Mater.* **1,** 502–512 (2012).
25. Shapiro, M. G., Atanasijevic, T., Faas, H., Westmeyer, G. G. & Jasanoff, A. Dynamic imaging with MRI contrast agents: quantitative considerations. *Magn. Reson. Imaging* **24,** 449–62 (2006).
26. Shapiro, M. G., Szablowski, J. O., Langer, R. & Jasanoff, A. Protein nanoparticles engineered to sense kinase activity in MRI. *J. Am. Chem. Soc.* **131,** 2484–2486 (2009).
27. Rahn-Lee, L. & Komeili, A. The magnetosome model: insights into the mechanisms of bacterial biomineralization. *Front. Microbiol.* **4,** 352 (2013).
28. Arakaki, A., Nakazawa, H., Nemoto, M., Mori, T. & Matsunaga, T. Formation of magnetite by bacteria and its application. *J. R. Soc. Interface* **5,** 977–99 (2008).
29. Lefèvre, C. T. *et al.* Monophyletic origin of magnetotaxis and the first magnetosomes. *Environ. Microbiol.* **15,** 2267–2274 (2013).
30. Uebe, R. & Schüler, D. Magnetosome biogenesis in magnetotactic bacteria. *Nat. Rev. Microbiol.* **14,** 621–637 (2016).
31. Komeili, A. Molecular Mechanisms of Compartmentalization and Biomineralization in Magnetotactic Bacteria. *FEMS Microbiol. Rev.* **36,** 232–255 (2012).
32. Murat, D., Quinlan, A., Vali, H. & Komeili, A. Comprehensive genetic dissection of the magnetosome gene island reveals the step-wise assembly of a prokaryotic organelle. *Proc. Natl. Acad. Sci. U. S. A.* **107,** 5593–8 (2010).
33. Kolinko, I. *et al.* Biosynthesis of magnetic nanostructures in a foreign organism by transfer of bacterial magnetosome gene clusters. *Nat. Nanotechnol.* **9,** 193–197 (2014).
34. Lohsse, A. *et al.* Functional analysis of the magnetosome island in Magnetospirillum gryphiswaldense: the mamAB operon is sufficient for magnetite biomineralization. *PLoS One* **6,** e25561 (2011).
35. Sigmund, F. *et al.* Bacterial encapsulins as orthogonal compartments for mammalian cell engineering. *Nat. Commun.* **9,** 1990 (2018).
36. Patrick, P. S. *et al.* Development of Timd2 as a reporter gene for MRI. *Magn. Reson. Med.* **00,** n/a-n/a (2015).

37. Iordanova, B., Hitchens, T. K., Robison, C. S. & Ahrens, E. T. Engineered Mitochondrial Ferritin as a Magnetic Resonance Imaging Reporter in Mouse Olfactory Epithelium. *PLoS One* **8,** (2013).
38. Pereira, S. M. *et al.* Evaluating the effectiveness of transferrin receptor-1 (*TfR1*) as a magnetic resonance reporter gene. *Contrast Media Mol. Imaging* n/a-n/a (2016). doi:10.1002/cmmi.1686
39. Bartelle, B. B., Szulc, K. U., Suero-Abreu, G. a, Rodriguez, J. J. & Turnbull, D. H. Divalent metal transporter, DMT1: A novel MRI reporter protein. *Magn. Reson. Med.* **000,** 1–9 (2012).
40. Genove, G., DeMarco, U., Xu, H., Goins, W. F. & Ahrens, E. T. A new transgene reporter for in vivo magnetic resonance imaging. *Nat. Med.* **11,** 450–4 (2005).
41. Iordanova, B. & Ahrens, E. T. In vivo magnetic resonance imaging of ferritin-based reporter visualizes native neuroblast migration. *Neuroimage* **59,** 1004–1012 (2012).
42. Chasteen, N. D. & Harrison, P. M. Mineralization in ferritin: an efficient means of iron storage. *J. Struct. Biol.* **126,** 182–194 (1999).
43. Bou-Abdallah, F. The iron redox and hydrolysis chemistry of the ferritins. *Biochim. Biophys. Acta - Gen. Subj.* **1800,** 719–731 (2010).
44. Pan, Y. H. *et al.* 3D morphology of the human hepatic ferritin mineral core: New evidence for a subunit structure revealed by single particle analysis of HAADF-STEM images. *J. Struct. Biol.* **166,** 22–31 (2009).
45. García-Prieto, A. *et al.* On the mineral core of ferritin-like proteins: structural and magnetic characterization. *Nanoscale* **8,** 1088–1099 (2016).
46. Lid, S., Carmona, D., Maas, M., Treccani, L. & Colombi Ciacchi, L. Anchoring of Iron Oxyhydroxide Clusters at H and L Ferritin Subunits. *ACS Biomater. Sci. Eng.* **4,** 483–490 (2018).
47. Brem, F., Stamm, G. & Hirt, A. M. Modeling the magnetic behavior of horse spleen ferritin with a two-phase core structure. *J. Appl. Phys.* **99,** (2006).
48. Gossuin, Y., Roch, A., Muller, R. N., Gillis, P. & Lo Bue, F. Anomalous nuclear magnetic relaxation of aqueous solutions of ferritin: An unprecedented first-order mechanism. *Magn. Reson. Med.* **48,** 959–964 (2002).
49. Brooks, R. A. *et al.* Relaxometry and magnetometry of ferritin. *Magn. Reson. Med.* **40,** 227–235 (1998).
50. Brooks, R. A., Moiny, F. & Gillis, P. On T2-shortening by weakly magnetized particles: The chemical exchange model. *Magn. Reson. Med.* **45,** 1014–1020 (2001).
51. Michel, F. M. *et al.* The Structure of Ferrihydrite, a Nanocrystalline Material. *Science (80-.).* **316,** 1726–1729 (2007).
52. Murad, E. & Schwertmann, U. The Mössbauer spectrum of ferrihydrite and its relations to those of other iron oxides. *Am. Mineral.* **65,** 1044–1049 (1980).
53. Michel, F. M. *et al.* Ordered ferrimagnetic form of ferrihydrite reveals links among structure, composition, and magnetism. *Proc. Natl. Acad. Sci. U. S. A.* **107,** 2787–2792

(2010).

54. Harris, J. G. E., Grimaldi, J. E., Awschalom, D. D., Chiolero, a. & Loss, D. Excess Spin and the Dynamics of Antiferromagnetic Ferritin. **60,** 4 (1999).
55. Douglas, T. & Ripoll, D. R. Calculated electrostatic gradients in recombinant human H-chain ferritin. *Protein Sci.* **7,** 1083–1091 (1998).
56. Bradley, J. M. *et al.* Three aromatic residues are required for electron transfer during iron mineralization in bacterioferritin. *Angew. Chemie - Int. Ed.* **54,** 14763–14767 (2015).
57. Behera, R. K. *et al.* Fe2+ substrate transport through ferritin protein cage ion channels influences enzyme activity and biomineralization. *JBIC J. Biol. Inorg. Chem.* **20,** 957–969 (2015).
58. Bou-Abdallah, F. *et al.* Functionality of the three-site ferroxidase center of Escherichia coli bacterial ferritin (EcFtnA). *Biochemistry* **53,** 483–95 (2014).
59. Clavijo Jordan, V., Caplan, M. R. & Bennett, K. M. Simplified synthesis and relaxometry of magnetoferritin for magnetic resonance imaging. *Magn. Reson. Med.* **64,** 1260–1266 (2010).
60. Meldrum, F. C., Heywood, B. R. & Mann, S. Magnetoferritin: in vitro synthesis of a novel magnetic protein. *Science* **257,** 522–523 (1992).
61. Martínez-Pérez, M. J. *et al.* Size-dependent properties of magnetoferritin. *Nanotechnology* **21,** 465707 (2010).
62. Baumgartner, J. *et al.* Nucleation and growth of magnetite from solution. *Nat. Mater.* **12,** 310–314 (2013).
63. Baumgartner, J. *et al.* Magnetotactic bacteria form magnetite from a phosphate-rich ferric hydroxide via nanometric ferric (oxyhydr)oxide intermediates. *Proc. Natl. Acad. Sci. U. S. A.* **1,** (2013).
64. Moisescu, C., Ardelean, I. I. & Benning, L. G. The effect and role of environmental conditions on magnetosome synthesis. *Front. Microbiol.* **5,** 1–12 (2014).
65. Murat, D. *et al.* The magnetosome membrane protein, MmsF, is a major regulator of magnetite biomineralization in Magnetospirillum magneticum AMB-1. *Mol. Microbiol.* **85,** 684–99 (2012).
66. Arakaki, A., Yamagishi, A., Fukuyo, A., Tanaka, M. & Matsunaga, T. Coordinated functions of Mms proteins define the surface structure of cubo-octahedral magnetite crystals in magnetotactic bacteria. *Mol. Microbiol.* **93,** 1–30 (2014).
67. Fdez-Gubieda, M. L. *et al.* Magnetite Biomineralization in Magnetospirillum gryphiswaldense: Time-Resolved Magnetic and Structural Studies). *ACS Nano* **7,** 3297–3305 (2013).
68. Kosman, D. J. Iron metabolism in aerobes: Managing ferric iron hydrolysis and ferrous iron autoxidation. *Coord. Chem. Rev.* **257,** 210–217 (2013).
69. Matsumoto, Y., Chen, R., Anikeeva, P. & Jasanoff, A. Engineering intracellular biomineralization and biosensing by a magnetic protein. *Nat Commun* **6,** 8721 (2015).
70. Liu, X. *et al.* Engineering Genetically-Encoded Mineralization and Magnetism via

Directed Evolution. *Sci. Rep.* **6,** 1–10 (2016).

71. Kim, T., Moore, D. & Fussenegger, M. Genetically programmed superparamagnetic behavior of mammalian cells. *J. Biotechnol.* **162,** 237–45 (2012).

72. Nishida, K. & Silver, P. a. Induction of biogenic magnetization and redox control by a component of the target of rapamycin complex 1 signaling pathway. *PLoS Biol.* **10,** e1001269 (2012).

73. Radoul, M. *et al.* Genetic manipulation of iron biomineralization enhances MR relaxivity in a ferritin-M6A chimeric complex. *Sci. Rep.* **6,** 1–9 (2016).

74. Iordanova, B., Robison, C. S. & Ahrens, E. T. Design and characterization of a chimeric ferritin with enhanced iron loading and transverse NMR relaxation rate. *J. Biol. Inorg. Chem.* **15,** 957–965 (2010).

75. Xie, H. *et al.* A quantitative study of susceptibility and additional frequency shift of three common materials in MRI. *Magn. Reson. Med.* **00,** n/a-n/a (2015).

76. Vuong, Q. L. *et al.* Paramagnetic nanoparticles as potential MRI contrast agents: Characterization, NMR relaxation, simulations and theory. *Magn. Reson. Mater. Physics, Biol. Med.* **25,** 467–478 (2012).

77. Ma, J. *et al.* Non-superparamagnetic iron-oxide architectures with controlled T 2 contrast ability in magnetic resonance imaging. *Appl. Phys. Lett.* **107,** 0–5 (2015).

Chapter 2

ULTRAPARAMAGNETIC CELLS AS MRI CONTRAST AGENTS

Ramesh, P. et. al. (2018). "Ultraparamagnetic Cells Formed through Intracellular Oxidation and Chelation of Paramagnetic Iron". In: *Angewandte Chemie International Edition* 57, pp. 12385-12389. doi: 10.1002/anei.201805042

2.1 Introduction

Inspired by magnetotactic bacteria, chemical and synthetic biologists have attempted to impart ferromagnetism or superparamagnetism onto non-magnetic microbial and eukaryotic cell types to enable their localization and isolation from complex samples using magnetic fields and visualization with magnetic resonance imaging (MRI).[1–4] Such capabilities would facilitate, for example, the study of commensal and pathogenic microbes inside mammalian hosts and the development of magnetically engineered microbial diagnostic and therapeutic agents.[5,6] However, because of the stringent pH, iron concentrations and redox potentials required for the synthesis of magnetosomal magnetite and other forms of superparamagnetic or ferromagnetic iron oxides, attempts to engineer the formation of these minerals in natively non-magnetic species such as *E. coli* have had limited success.[7–11]

Here, we introduce an alternative paradigm for producing magnetic cells that is focused on maximizing cellular paramagnetism rather than forming superparamagnetic or ferromagnetic deposits. This approach arises from the recognition that many applications of magnetic cells, including MRI and cellular separation, involve multi-Tesla magnetic fields, in which sufficiently paramagnetic cells would be expected to act as microscale magnets, capable of producing MRI contrast and experiencing magnetic gradient forces for localization and separation (Fig. 2.1A).[12,13] With such "ultraparamagnetism" as the stated goal, ferritin – the main iron storage protein in most cells and the focal point of previous efforts in magnetic cell engineering – represents a relatively poor iron host because most of the electron spins in its ferrihydrite core are cancelled by antiferromagnetic partners, such that its net paramagnetic moment equates to only ~5% of the available spin at 37 °C.[14,15]

We hypothesized that better use of intracellular iron could be made by cells expressing a protein construct specifically designed to nucleate and chelate iron in a paramagnetic configuration. In this work, we engineer such a construct, characterize it physically and biochemically, and show that *E. coli* expressing it have 8-fold stronger paramagnetism than ferritin-overexpressing controls. This allows these cells to be localized via magnetic field gradients, visualized with MRI, and isolated from complex biological samples.

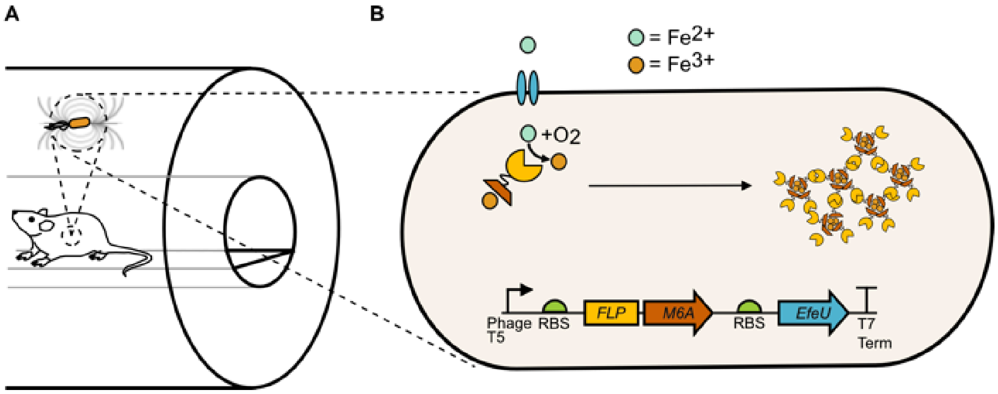

Fig. 2.1 Ultraparamagnetic gene circuit. | A. Paramagnetic cells produce magnetic fields and experience force when placed inside a strong magnetic field, such as in an MRI scanner. **B.** UPMAG gene circuit, comprising a ferroxidase (FLP) fused to a magnetite nucleating peptide (M6A), and a ferrous iron transporter (EfeU). The circuit is driven using an IPTG-inducible T5 phage promoter. The ferrous iron transporter increases the intracellular iron content available to FLPM6A. FLPM6A subsequently forms macromolecular assemblies with oxidized iron.

2.2 Results

To produce and store intracellular iron in a paramagnetic state, we created a fusion protein combining the decameric ferroxidase FLP from *Rhodospirillum Rubrum* with the iron-binding peptide M6A derived from the last 20 C-terminal residues of the Mms6 protein from *Magnetospirillum magneticum* (Fig. 2.1B).[16,17] Iron can be imported into *E. coli* as Fe^{2+}, but must be oxidized to avoid the production of toxic radicals via the Haber-Weiss reaction.[18] We specifically chose FLP for this purpose because it can effectively oxidize ferrous iron, but does not on its own mineralize the iron into potentially poorly magnetic iron oxides.[16] This stands in contrast to ferritin, which both oxidizes iron and stores it as an antiferromagnetic mineral. The second component, M6A, was previously shown to promote and stabilize the nucleation of magnetic iron species *in vitro*.[17,19] We hypothesized that, after FLP oxidizes iron to Fe^{3+}, M6A would bind any available ferrous iron as well as oxidized ferric iron and promote the nucleation of small iron oxide minerals, stabilized by multiple M6A binding interactions (Fig. 2.1B).[20] We predicted that this iron would remain in a loosely ordered, strongly paramagnetic state (Fig. 2.1B). As control constructs, we generated *E. coli* overexpressing bacterioferritin (BFR) or fluorescent proteins (FP: mRuby2 or eGFP). BFR was chosen as our standard for comparison based on its previous use as a genetically encoded contrast agent for MRI.[21] All vectors also included the iron transporter EfeU from *E. coli* Nissle 1917 to facilitate the uptake of ferrous iron from the growth medium. These constructs were expressed in a model strain of *E. coli* (BL21 DE3) with no additional alterations to endogenous iron-handling genes. The complete genetic circuit consisting of FLPM6A and EfeU is hereafter referred to as UPMAG, for UltraParaMagnetic Genes.

2.2.1 Bulk magnetometry of UPMAG cells

As a first step in characterizing the magnetism of UPMAG expressing *E. coli* relative to controls, we measured their magnetic susceptibility at room temperature. As expected, control cells expressing FP were weakly diamagnetic, with a bulk susceptibility ($\Delta\chi$) of -0.05 ± 0.05 ppm. In contrast, cells expressing UPMAG exhibited strong paramagnetism, with a $\Delta\chi$ of 4.68 ± 0.08 ppm (Fig. 2.2A). This magnetic susceptibility was approximately 8-fold stronger than in weakly paramagnetic cells overexpressing BFR ($\Delta\chi = 0.61 \pm 0.06$ ppm). Using the ferrozine assay, we found that cells expressing UPMAG contained 3.33 ± 0.20 fg iron per cell (Fig. 2.2B), such that the measured $\Delta\chi$ represents 50.7% of the theoretical maximum for high-spin iron (Supplementary Table 1). In contrast, BFR cells contained 1.89 ± 0.09 fg iron, such that their 8-

fold lower susceptibility means they derive less than ¼ of the per iron-atom magnetism of UPMAG.

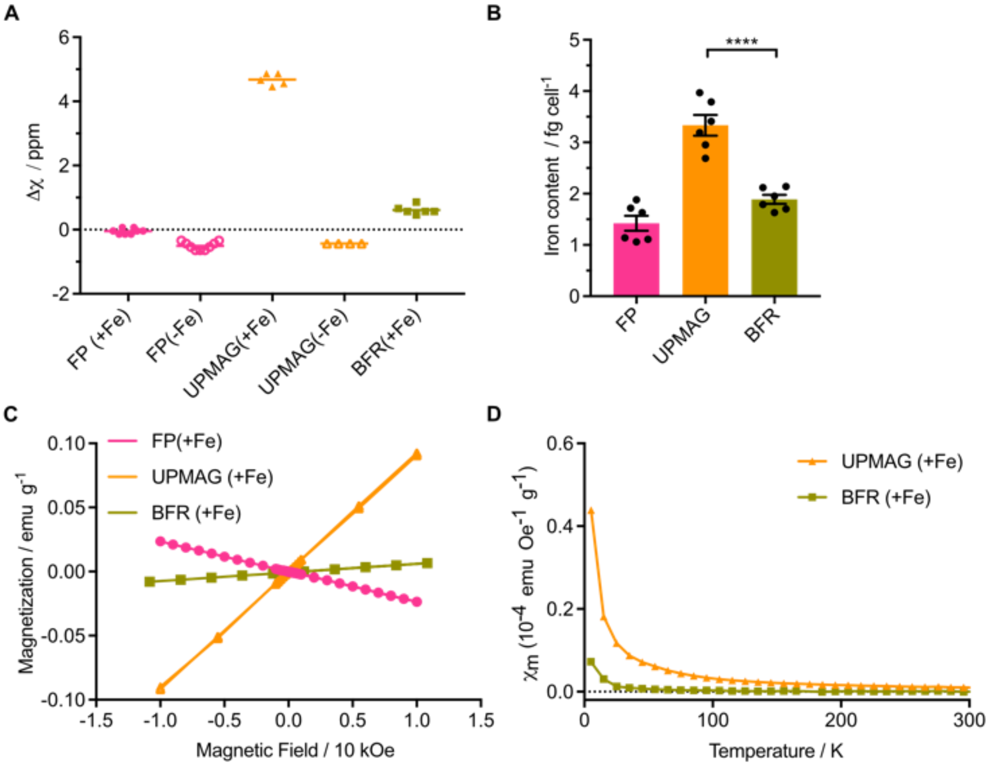

Fig. 2.2 UPMAG cells are strongly paramagnetic. | A. Bulk volume susceptibility measurements of *E. coli* at room temperature. **B**. Quantification of intracellular iron in *E. coli* expressing UPMAG, FP or BFR. **C**. SQUID MPMS measurement of the magnetic moment at constant temperature of 30K while the magnetic field was swept. **D**. SQUID MPMS zero-field cooled measurement of the magnetic susceptibility under a bias field of 500 Oe while the temperature was swept.

In a superconducting quantum interference device (SQUID) magnetometer, the magnetic moment of UPMAG cells had a positive linear dependence on the applied magnetic field and a Curie-Weiss dependence on temperature (Fig. 2.2, C-D) indicative of paramagnetism.[14] In comparison, BFR cells showed weaker paramagnetism and no evidence of ferrimagnetism at 30K, consistent with the literature, while FP cells were diamagnetic.[14] Together, these results indicate that the expression of UPMAG causes intracellular iron to accumulate in a much more strongly paramagnetic state than controls. Mössbauer spectroscopy on UPMAG cells at 80K indicated a composition of mainly high-spin ferric iron (96.5%), in a state consistent with intracellular ferrihydrite (Supporting Data, Fig. 2.7).[22]

To assess the impact of UPMAG expression on cell viability, we monitored cell culture density after induction to express either UPMAG or FP controls, in the presence of ferrous ammonium sulfate. We found that both the growth rate and the final density were similar in both cases (Supporting Data, Fig. 2.14 A-D).

2.2.2 *In vitro* magnetic capture of UPMAG cells.

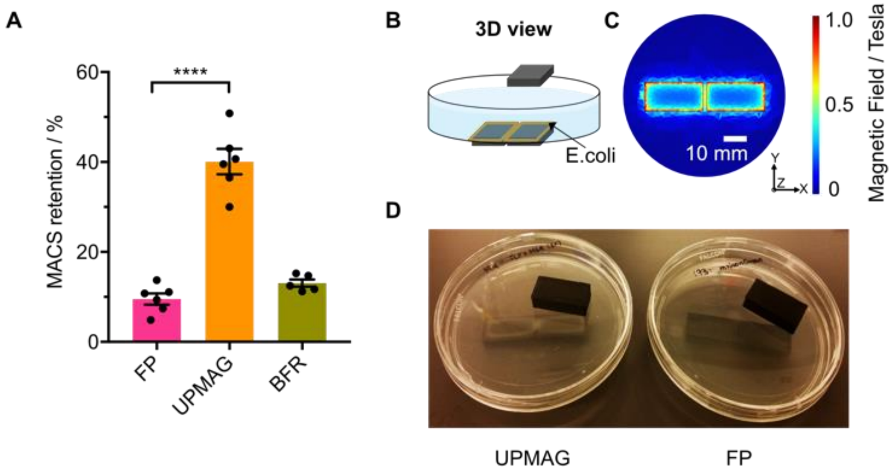

Fig. 2.3 UPMAG cells can be magnetically captured| A. Magnetic column retention of UPMAG expressing *E. coli* relative to controls in a MACS LD column. **B.** N52 NdFeB magnets were placed above and below a petri dish containing *E. coli* expressing either UPMAG or FP in M9 base media and left overnight. **C.** Simulated magnetic field of the bar magnets used in the experiment, showing sharp field gradients at the edges of the magnet (~ 100 T/m). **D.** Photos taken after overnight incubation of *E. coli* expressing UPMAG or controls in Petri dishes placed above the magnets.

To determine whether an enhanced paramagnetic phenotype can enable the manipulation of UPMAG cells using magnetic fields, we first assessed their ability to be retained in magnetically actuated cell sorting (MACS) separation columns.[23,24] We found that *E. coli* expressing UPMAG were retained in MACS columns with 40 ± 2.8 % efficiency – much greater than either FP or BFR cells (Fig. 2.3A). To visualize how UPMAG *E. coli* could be spatially manipulated with strong magnetic fields, we incubated a suspension of UPMAG cells overnight in a petri dish sitting on top of N52 NdFeB magnets (Fig. 2.3B). The estimated 100 T/m magnetic field gradients 1 mm away from the magnet surface (Fig. 2.3C) caused the bacteria to become concentrated in areas of maximal field strength (Fig. 2.3D).

2.2.3 T_2 relaxivity of UPMAG cells

To assess whether the cellular paramagnetism conferred by UPMAG could be used for noninvasive cellular imaging in addition to magnetic actuation, we imaged cells expressing this construct with MRI. When imaged in agarose phantoms at 7 Tesla, UPMAG cells produced T_2 contrast relative to both background and controls at densities as low as 1×10^{10}, colony forming units (cfu) per ml, corresponding to a cellular volume fraction of 3.6 % (Fig. 2.4A).[25] In contrast, cells expressing FP required at least 3-fold higher concentrations to be comparably visualized relative to background. Overexpression of BFR led to only a modest increase in T_2 contrast relative to FP, as expected based on the fact that *E. coli* cultured in iron-rich media also upregulate the expression of endogenous ferritins such as ftnA, ftnB, and BFR.[26–28]

Quantitative NMR measurements at 11.7 Tesla showed that solutions of *E. coli* expressing UPMAG had 70% faster relaxation rates compared to controls at cell optical density OD10 (Fig. 2.4B), with a cellular T_2 relaxivity of approximately $3.4\ \frac{\text{sec}^{-1}}{\text{OD}_{600}}$, or equivalently a per-iron relaxivity of $20.7\ \text{mM}^{-1}\text{sec}^{-1}$, as determined by linear fit. Monte Carlo simulations of water diffusion and spin precession in media containing ultraparamagnetic bacteria further revealed that most of the observed T_2 relaxation enhancement can be explained by diffusional water exchange between the bulk and the $\Delta\chi$-shifted cell interior (Fig. 2.4, C-D, Supporting Data Fig. 2.13A). T_1 relaxivity was similar between UPMAG cells and controls (Supporting Data, Fig. 2.13B).

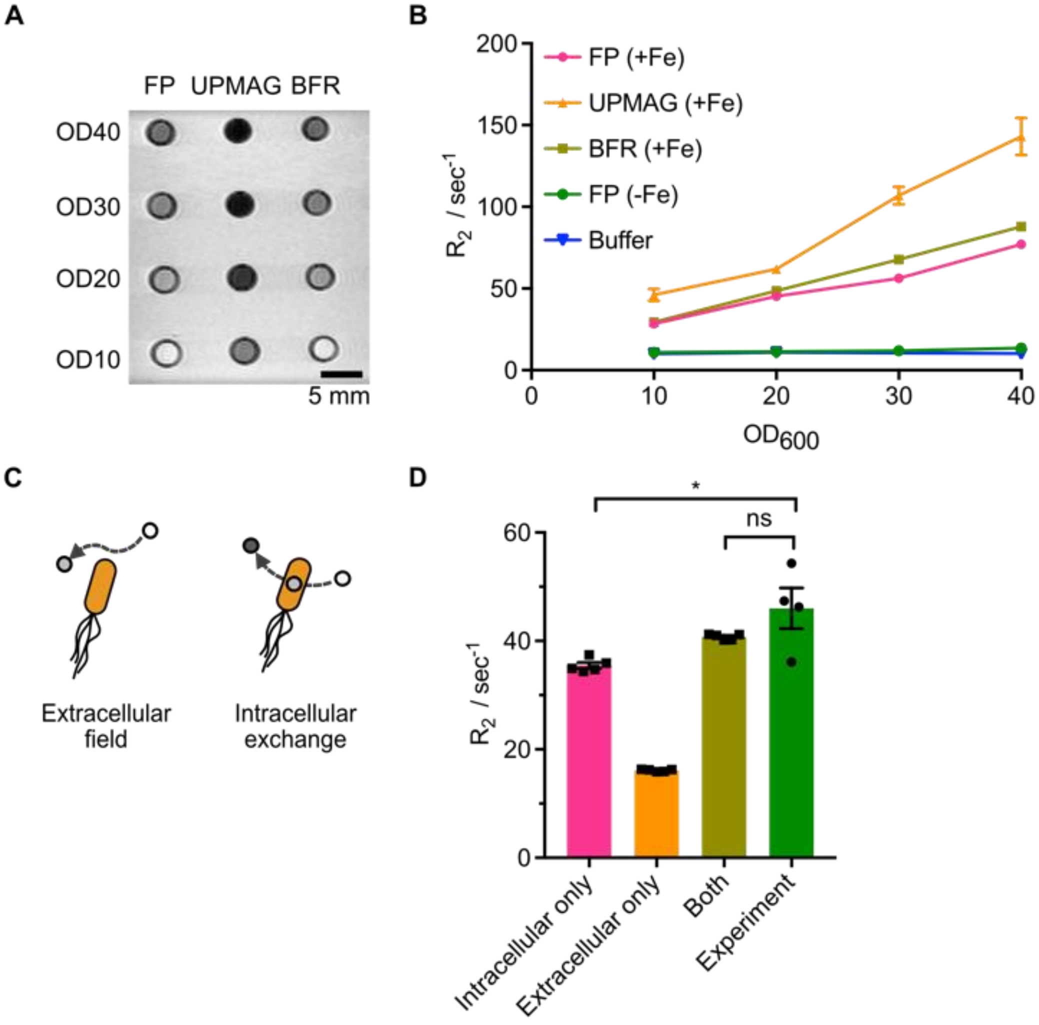

Fig. 2.4 UPMAG cells produce enhanced MRI contrast. | A. A T_2 weighted image of *E. coli* in an agarose phantom, acquired at 7 Tesla using a spin echo sequence with T_R = 2500 ms and T_E = 11 ms. **B.** R_2 vs. OD_{600} for *E. coli* expressing either UPMAG or controls in a Bruker 500 MHz NMR spectrometer with a spin echo sequence and T_E = 0.5 ms. **C.** Schematic of two potential mechanisms of T_2 contrast, one in which water relaxes due to extracellular outer-sphere dipole relaxation, and a second in which water relaxes via diffusional exchange into the intracellular compartment. **D.** Monte Carlo simulation results for cells at OD_{600} = 10, in comparison with experimental data.

2.2.5 *In vivo* MRI detection and *ex vivo* magnetic capture of UPMAG cells

After establishing the basic capabilities of UPMAG expressing cells *in vitro*, we proceeded to test them in proof-of-concept *in vivo* applications. First, to test whether UPMAG enables cellular imaging in the context of a living animal, we injected *E. coli* expressing either UPMAG or control constructs in a hydrogel subcutaneously into the hind flanks of mice (Fig. 2.5A). T_2 weighted images at 7 Tesla showed clear contrast in regions containing UPMAG cells compared to controls (Fig. 2.5B), and T_2 in regions of interest containing these cells was significantly shorter than in regions containing control cells (Fig. 2.5C).

In addition to imaging, a major challenge in studying the *in vivo* function of host-associated bacteria is their isolation from host materials and other microbes. We hypothesized that magnetic fields could be used to rapidly isolate ultraparamagnetic microbes from mixed fecal samples after passage through the gastrointestinal (GI) tract (Fig. 2.5D). Such a capability is relevant for the study of GI-resident microbial populations and the development of sentinel cells engineered to sense and report on the presence of GI pathology, providing a fast way to separate engineered cells from native gut microbes and other fecal contents, compared to conventional alternatives such as growth on selective media.[29]

To provide a proof of concept for this approach, we mixed UPMAG cells with a 10-fold excess of control FP microbes and gavaged the mixture into BALB/c mice. A subset of the gavage mixture was also subjected to MACS *in vitro* to corroborate the *in vivo* experiments (Supporting Data Fig. 2.15 A-B). After allowing time for bacterial passage through the GI tract, we collected feces, homogenized them, and performed MACS – the effectiveness of which was assessed by plating on selective media (Fig. 2.5E). We found that UPMAG cells were enriched 315 ± 48 fold in the MACS eluate relative to their initial abundance (Fig. 2.5F). The genetic identity of each cell type was confirmed using DNA sequencing in a subset of colonies. These results suggest that the magnetic functionality of UPMAG cells can be employed in complex biological samples.

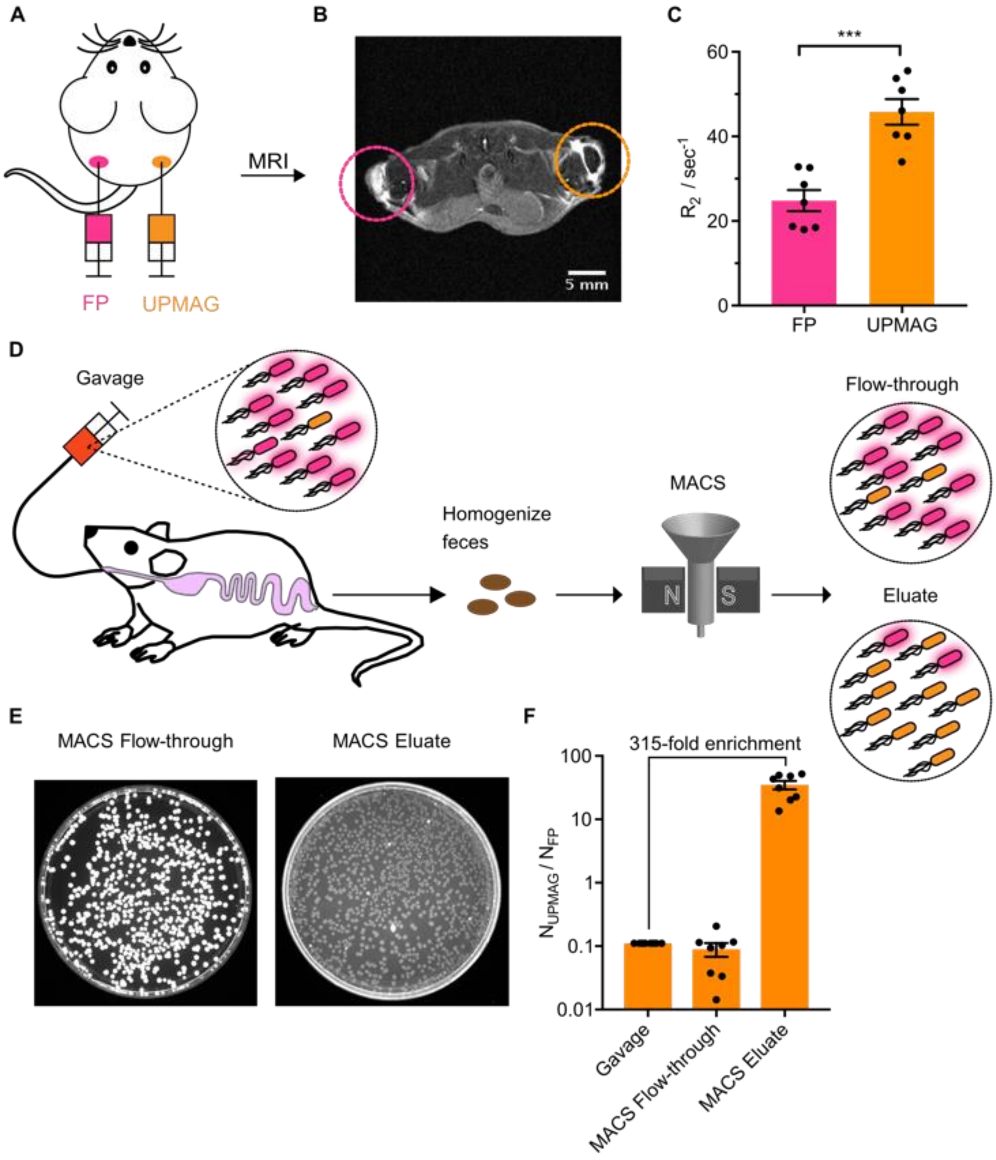

Fig. 2.5 UPMAG cells can be magnetically isolated from *ex vivo* specimens. | A. Schematic of subcutaneous contralateral injections of *E. coli* expressing either control or UPMAG into the hind flanks of NU/J mice. **B.** Representative MRI image of mouse at 7 Tesla using a T_2 RARE sequence (T_R = 5000 ms, T_E = 11 ms, RARE factor = 2). **C.** *In vivo* relaxation rates obtained from pixelwise fitting in Matlab and averaging over the relevant ROIs. **D.** Schematic of the *in vivo* gavage experiment. **E.** Representative image of plates containing the flow-through and eluted fractions. Non-fluorescent colonies contain the UPMAG vector, as confirmed by DNA sequencing. **F.** Ratio of UPMAG to FP cells in the respective MACS fractions.

2.2.6 Biophysical characterization of FLPM6A

Finally, to gain insight into both FLPM6A and the nature of the paramagnetic material formed inside UPMAG cells, we performed biochemical assays on purified FLPM6A, which was augmented with an N-terminal hexa-histidine tag for affinity purification. When expressed in *E. coli* in the absence of iron supplementation, FLPM6A could be found in the soluble fraction of the cell lysate, allowing us to purify it using Ni-NTA affinity purification (Fig. 2.6A, Supporting Data Fig 2.16A). Purified FLPM6A migrates similarly to its expected molecular weight of ~ 160 kDa in size-exclusion chromatography (Supporting Data Fig. 2.16 B) and appears alpha-helical in circular dichroism spectroscopy (Supporting Data Fig. 2.18). This molecular weight corresponds to ten units of FLPM6A, as expected based on the FLP being a decamer.[16] A western blot against denatured FLPM6A indicates the presence of the dimer at ~32 kDa, which is also consistent with the published behavior of FLP in SDS electrophoresis.[16]

Strikingly, when expressed in the presence of 1 mM ferrous iron, FLPM6A moved to the insoluble inclusion body fraction of the lysate (Fig. 2.6A), together with approximately 98% of the total cellular iron (Fig. 2.6B), suggesting that this protein and iron form a stable intracellular complex. To investigate the nature of this complex, we incubated purified FLPM6A with ferrous iron at different molar ratios. At iron:protein ratios above 160, the protein formed a visible "ferrogel" (Fig. 2.6C). Dynamic light scattering (DLS) confirmed the formation of large macromolecular assemblies under these conditions (Fig. 2.6D). Control samples containing a purified hexa-histidine-tagged fluorescent protein, and iron by itself, did not exhibit the same assembly behavior (Supporting Data Fig. 2.17). Native gel electrophoresis revealed a reduction in protein mobility with increasing iron concentrations, with complexes formed at an iron:protein ratio of 320 failing to migrate into the gel (Fig. 2.6E). Prussian Blue iron staining of the same gel indicated that iron was co-localized with the large protein complexes (Fig. 2.6F). Brightfield images of such complexes showed an amorphous macromolecular aggregate. Transmission electron micrographs of these complexes likewise showed an amorphous, electron dense structure (Supporting Data Fig. 2.19 A-B). Notably, the approximate ratio of intracellular iron and FLPM6A in our cellular experiments was 304, explaining why UPMAG cells contain iron-rich macromolecular complexes.

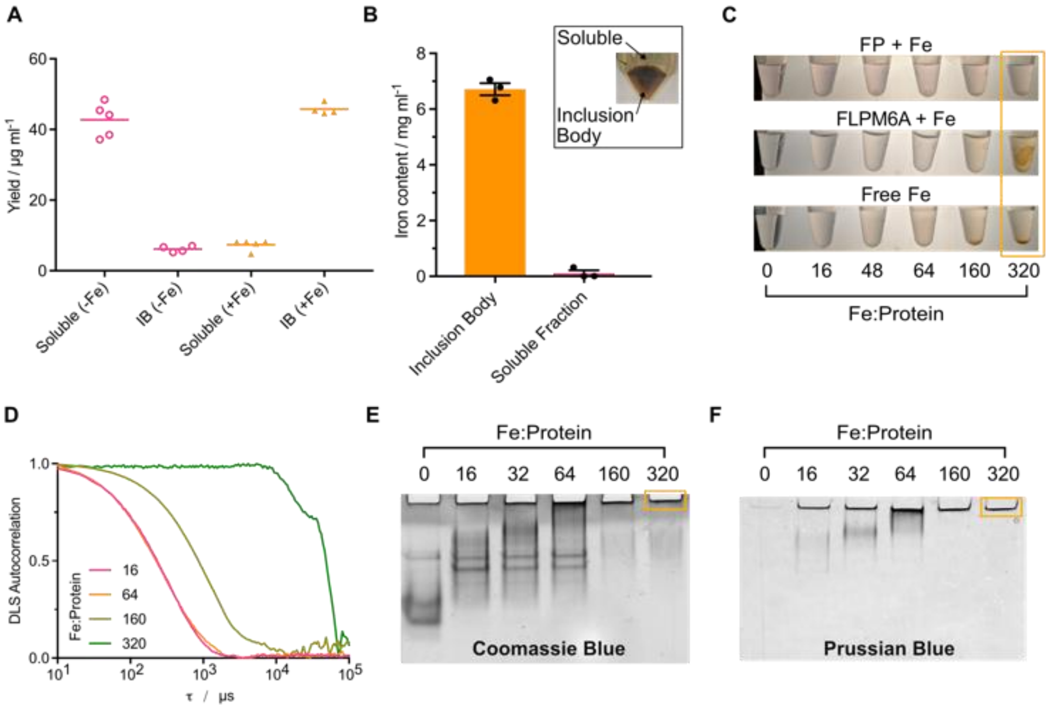

Fig. 2.6 FLPM6A forms a ferrogel. | A. Quantity of FLPM6A in the soluble and insoluble fractions of cell lysates after culture in the absence or presence of iron supplementation (1 mM Fe), quantified per ml of bacterial culture. **B.** Iron quantification of cell lysate compartments when cells expressing UPMAG are grown in iron-rich medium (1 mM Fe), quantified per ml of lysis buffer. **C.** Photo of tubes containing 100 µg/ml (6.5 µM) of purified FLPM6A with iron in molar ratios ranging from 0:1 to 320:1 [Fe]:[FLPM6A]. **D.** DLS autocorrelation plots corresponding to the sample conditions in (C). **E.** Native-PAGE gel of FLPM6A samples corresponding to the conditions in (C). **F.** Prussian Blue staining of the same Native-PAGE gel.

2.3 Supporting Data

Supplementary Table 1 – Measured and Theoretically Available Magnetic Susceptibility

Genetic Construct	Measured Susceptibility $\Delta\chi_{\text{measured}}$	Intracellular Iron concentration (fg/cell)	Theoretically available Susceptibility $\Delta\chi_{\max}$	Magnetic Efficiency $(\Delta\chi_{\text{measured}}/\Delta\chi_{\max})$
UPMAG	4.68×10^{-6}	3.33	9.24×10^{-6}	50.7%
BFR	0.61×10^{-6}	1.89	5.29×10^{-6}	11.5%

This table lists the measured magnetic susceptibility and iron contents of UPMAG and BFR cells (from Figure 2 of the main text), together with the theoretically available susceptibility assuming all the cellular iron is in a high spin state (S=5/2). The last column lists the "Magnetic Efficiency" of the construct, defined as the fraction of the maximally available susceptibility it provides.

2.3.1 Mössbauer spectroscopy of UPMAG cells

Having discerned that FLPM6A stores iron in a disordered ferrogel (Fig. 6), we were interested in understanding the spin state of iron coordinated by the protein, and more broadly the spin state of iron within UPMAG cells themselves. To that end, we pursued three complementary spectroscopic techniques: Mössbauer spectroscopy, Electron Paramagnetic Resonance (EPR) spectroscopy, and Chemical Exchange Saturation Transfer (CEST) spectroscopy to assay the spin state of iron within UPMAG cells, as well as their effects on nuclear spin relaxation.

One of the principle advantages of Mössbauer spectroscopy over EPR is that Mössbauer spectroscopy is not limited to half-integer spin species ($S = \frac{1}{2}, \frac{5}{2}$) such as high-spin and low-spin Fe^{3+}. Integer spin species (S = 1, 2) such as low-spin and high-spin Fe^{2+} cannot be detected using conventional perpendicular mode X-band EPR techniques, but can be accurately quantified using Mössbauer spectroscopy.[30] Furthermore, the narrow linewidths of γ-rays (5×10^{-9} eV) typically used in Mössbauer spectroscopy ensures a spectral resolution exceeding 1 ppt (parts per trillion), which renders this technique extremely sensitive and therefore useful for probing chemical structure and composition of materials.

Mössbauer spectroscopy works on the principle of recoilless emission and subsequent resonant absorption of γ-rays by atomic nuclei. Analogous to electronic transitions between shells of varying angular-momenta which produce photons ranging from X-rays to NIR, transitions between various nuclear angular momentum states produce γ-rays. When such a transition occurs in a 'free' atomic nucleus, the energy of the emitted γ-ray (E_R) is less than the energy needed to excite the transition (E_T), due to conservation of momentum – the emission of a γ-ray causes the atomic nucleus to recoil, akin to a gun recoiling after a bullet is fired. However, if the atomic nucleus is enmeshed in a crystal lattice and the energy of the γ-ray is sufficiently low, then the mass of the recoiling nucleus effectively becomes the mass of the whole lattice (*M*), and the recoil energy ($E_R' = \frac{E_R}{2Mc^2} \to 0$) vanishes. In this scenario, a γ-ray emitted by one atomic nucleus can be resonantly absorbed by a neighboring nucleus, provided that both nuclei are in identical electronic and magnetic environments. Using a moving γ-ray source, one can efficiently sweep across a narrow band of γ-ray energies to probe for optimal, resonant absorption; the effect of moving the source relative to the nucleus produces a relativistic doppler shift on the order of $\Delta E \sim \frac{v_{source}}{c} E_T$, from the perspective of the stationary nucleus.

In typical Mössbauer experiments, decay of ^{57}Fe in the source from $I = \frac{3}{2} \to I = \frac{1}{2}$ produces a 14.4 keV γ-ray that is directed towards the target that also contains ^{57}Fe, albeit in a different chemical environment; in our experiments, the target of interest is a lyophilized powder of UPMAG cells cultured in iron-rich (1 mM Fe^{2+}) growth medium. In most biochemical Mössbauer experiments, the sample of interest is first grown in medium containing ^{57}Fe; however, given that the natural abundance of ^{57}Fe is ~ 2.1% of all Fe, we were able to sufficiently enrich our sample's concentration of ^{57}Fe through lyophilization of a large *E. coli* culture (100 ml). A typical Mössbauer spectrum consists of fractional γ-ray transmission through the target as a function of the ^{57}Fe source's velocity (mm/s). The dip in transmission at a specific velocity, as well as the spectrum's linewidth, are subsequently fit to models of the nuclear environment to ascertain the oxidation state and crystalline structure of iron within the sample.

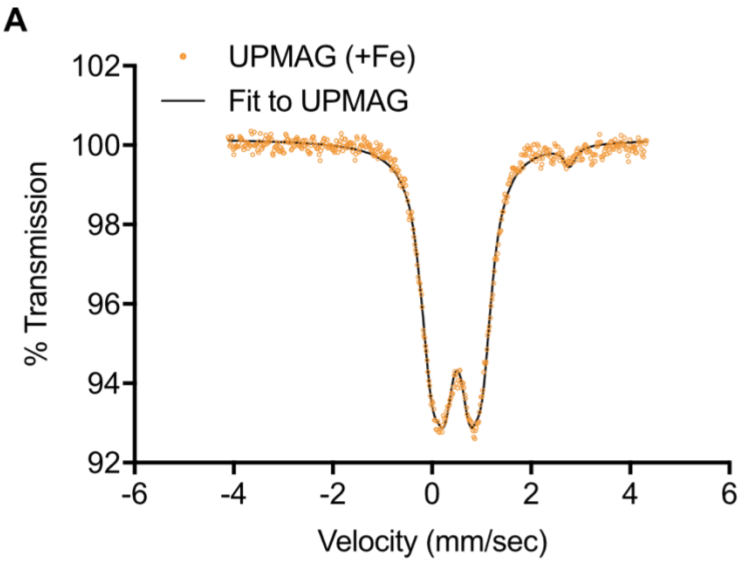

Fit component	Isomer shift δ (mm/s)	Quadrupole splitting ΔE_Q (mm/s)	Relative area
Fe^{3+} site 1	0.5063	1.032	0.4240
Fe^{3+} site 2	0.5074	0.4976	0.5409
Fe^{2+}	1.281	2.991	0.0351

Fig. 2.7 Mössbauer spectroscopy of UPMAG *E.coli* at 80K. | A. The three component fit parameters are listed in the table below the spectrum.

To interpret our Mössbauer spectrum, we must first understand the physical basis for the Isomer shift and Quadrupole splitting respectively. The local electronic and magnetic environment around the nucleus affects the energy gap between various nuclear transitions through dipolar coupling. The spherically symmetric *s* orbitals, especially the *1s* electronic orbital, are centered at the atomic nucleus and therefore have a non-zero probability of interacting with atomic nuclei through Coulombic interactions. Changes in the valence electron shells of an iron atom, such as changes in its oxidation state, perturb its *1s* orbital's wavefunction, which in turn affects nuclear transitions. This monopolar interaction between atomic nuclei and the electron cloud shifts the absorption energy and is referred to as the Isomer shift (IS), given by Eq. 2.1.

$$\mathrm{IS} = \frac{2\pi}{5} Ze^2[|\psi_A|^2 - |\psi_S|^2](E_{ex}^2 - E_g^2) \tag{2.1}$$

Here, $|\psi_A|^2$ and $|\psi_S|^2$ refer to electronic wavefunctions of the absorber and source respectively, whereas E_{ex} and E_g refers to energy of the excited and ground nuclear angular momentum states respectively.

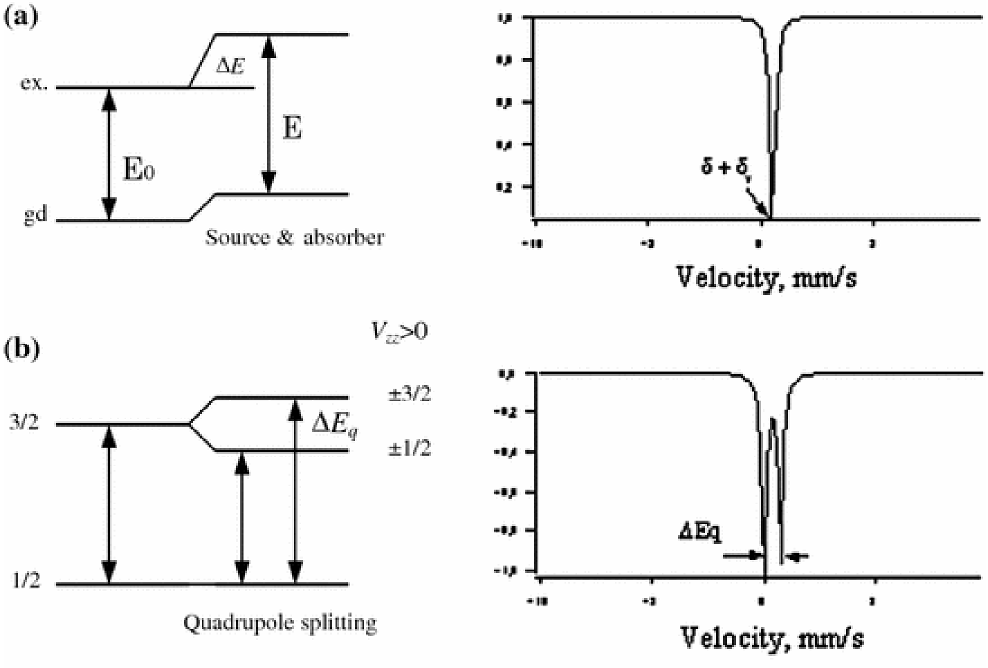

Fig. 2.8 Shift and splitting of nuclear levels of ^{57}Fe nucleus in Mössbauer spectra. | A. Center shift of the observed absorption line; the observed shift in this case is the sum of the isomer shift and second order Doppler shift. **B.** Electric quadrupole splitting ΔE_q. Adapted from Ref.[31]

The charge distribution within the nucleus, however, is not always spherically symmetric. Electric field gradients produced by other charges in the atom and more broadly the material itself, can deform the nuclear charge distribution in its excited state. This nuclear quadrupole moment manifests itself in the form of additional splitting (ΔE_Q) in the Mössbauer spectra.

The IS and quadrupole splitting observed in our Mössbauer spectra are characteristic of ferrihydrite.[32,33] Given the high signal-noise ratio in our measurement, we can reliably conclude that 97% of intracellular iron is in the ferric state and approximately 3% of iron is stored in the ferrous state. This is to be expected given the redox conditions of the *E. coli* cytoplasm which favors the formation of Fe(III)-hydroxides. Lastly, we did not observe any appreciable absorption at source velocities corresponding to the IS and quadrupole splitting of bacterial magnetite ($\mathrm{IS} = 1.32\ \frac{\mathrm{mm}}{\mathrm{s}}, \Delta E_Q = 3.17\ \frac{\mathrm{mm}}{\mathrm{s}}$), suggesting that UPMAG cells are not forming ferrimagnetic minerals.

2.3.2 EPR spectroscopy of FLPM6A

Given that the preponderance of iron in UPMAG cells is in the ferric oxidation state, we were interested in determining the spin state of FLPM6A bound iron. To do so, we turned to EPR spectroscopy, which can sensitively assay the electronic spin-state of paramagnetic compounds. Analogous to NMR (Chapter 1), the EPR effect is only observed upon resonant absorption of RF by unpaired electrons within the sample. That said, given the large gyromagnetic ratios of electrons, EPR spectroscopy uses RF that falls in the microwave spectrum (10 – 100 GHz); however, unlike NMR spectroscopy, the magnetic field in EPR spectroscopy is continuously modulated while the RF irradiation frequency is held constant. Resonant absorption, in turn, is affected by the electron's local environment, which shapes the magnetic field effectively felt by the electron within the EPR probe. The local magnetic field's deviation from the external field ($\Delta\mathbf{B}$) can be understood in terms of deviation from the 'free' electron's gyromagnetic ratio, akin to chemical shift in NMR (Chapter 1). All the information about the unpaired electron's local chemical environment and spin-state can therefore be deduced from an understanding of its effective gyromagnetic ratio. The Hamiltonian for such an unpaired electron in its valence orbital when exposed to $\mathbf{B}$, is given by:

$$H = \mu_B[(g_e\mathbf{S} + \mathbf{L}) \cdot \mathbf{B}] + [\mathbf{S} \cdot D \cdot \mathbf{S}] + [\mathbf{S} \cdot A \cdot \mathbf{I}] \tag{2.2}$$

Here, g_e refers to the 'free' electron gyromagnetic ratio, **S** refers to the total spin-angular momentum of the electron, whereas **L** refers to its total orbital angular momentum. The term in the first set of brackets is the electron-Zeeman interaction, analogous to the nuclear-Zeeman interaction (Chapter 1) that enables NMR spectroscopy. D refers to the zero-field splitting, which arises from spin-orbit coupling ($\mathbf{S} \cdot \mathbf{L}$) and A refers to the hyperfine interaction between the electron and its corresponding atomic nucleus. The spin and orbital terms can be grouped, and the Hamiltonian can be re-written using an effective g tensor for simplicity.

$$H = \mu_B[\mathbf{S} \cdot \mathrm{g}_{\mathrm{eff}} \cdot \mathbf{B}]_{\mathrm{Zeeman}} + [\mathbf{S} \cdot \mathrm{D} \cdot \mathbf{S}]_{\mathrm{zfs}} + [\mathbf{S} \cdot \mathrm{A} \cdot \mathbf{I}]_{\mathrm{hyperfine}} \tag{2.3}$$

Here, $\mathrm{g}_{\mathrm{eff}}$ is a 9-component tensor, which upon diagonalization of the Hamiltonian yields:

$$\mathrm{g}_{\mathrm{eff}} = \begin{bmatrix} g_x & 0 & 0 \\ 0 & g_y & 0 \\ 0 & 0 & g_z \end{bmatrix} \tag{2.4}$$

Fitting an EPR absorption spectrum to the simplified Hamiltonian (Eq. 2.3) yields $\mathrm{g}_{\mathrm{eff}}$, and deviations of $\mathrm{g}_{\mathrm{eff}}$ from g_e are the result of electronic fine structure (spin-orbit, hyperfine, etc.). The g value at any particular absorption peak can be calculated as follows:

$$g = \frac{714.484 \cdot \nu}{\mathbf{B}} \tag{2.5}$$

Here, ν is the MW frequency in GHz and **B** is the EPR magnetic field in Gauss. Another coupling of particular interest for metalloprotein EPR spectroscopy is spin-orbit coupling (**LS**), which arises from synergistic interactions between the spin angular momentum and orbital angular momentum. **LS** interactions break the degeneracy between spin eigenstates, even in the absence of an external magnetic field (zero-field splitting) and can heavily influence the paramagnetic state of the molecule.[34] For example, **LS** interactions account for hemoglobin's transition from paramagnetic to diamagnetic upon oxygen binding. One can obtain information about the magnitude of spin-orbit coupling by fitting the zero-field splitting term in the electron Hamiltonian (Eq. 2.3).

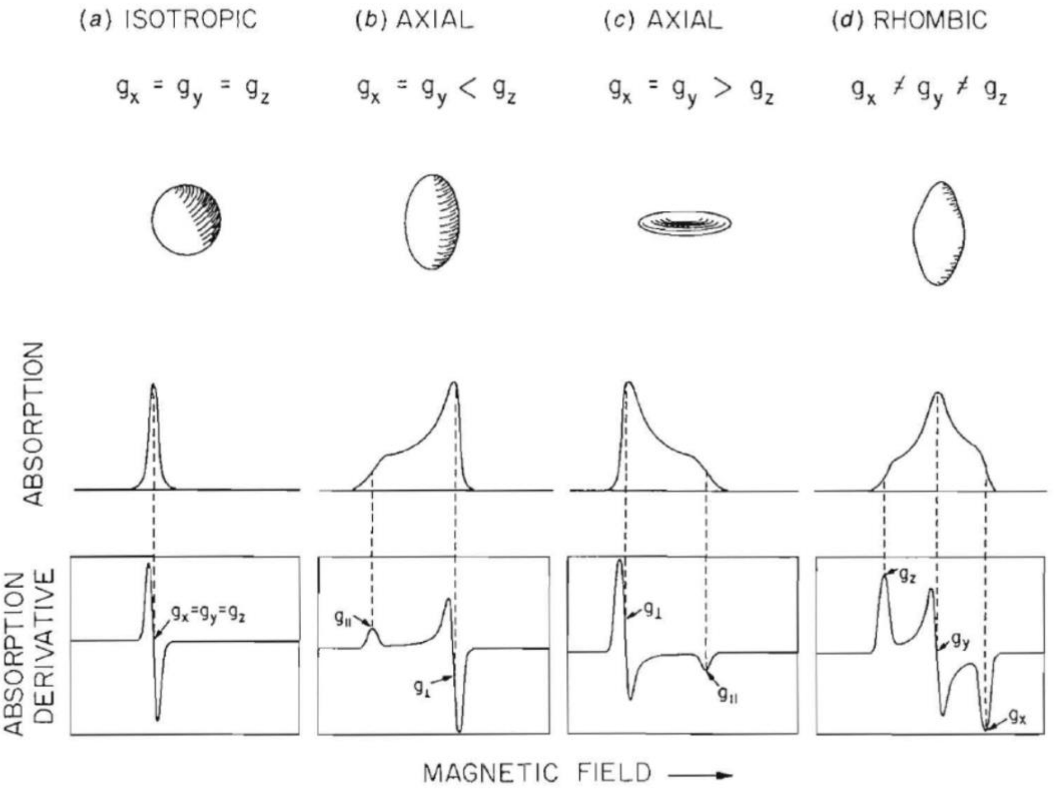

Fig. 2.9 Idealized powder EPR spectra of paramagnetic species.| Spin-spin, spin-orbit, and hyperfine interactions dictate the shape of the valence electron cloud (a-d), which in turns affects the molecule's EPR absorption spectrum. The EPR signal is in fact the derivative of the MW absorption spectrum. Adapted from G.Palmer, *Physical Methods in Bioinorganic Chemistry*, L. Que (ed) 2000.

$$H_{zfs} = D\left[S_z^2 - \frac{1}{3}S(S+1) + \frac{E}{D}\left(S_x^2 - S_y^2\right)\right] \qquad (2.6)$$

Here, E and D are the rhombic and axial zero-field splitting parameters respectively and the E/D ratio, which varies from 0 to 1/3, is obtained by fitting the EPR absorption spectrum.

Prior to investigating the spin-state of iron in FLPM6A, we first tested a sample of Equine horse-spleen ferritin (HSF), and assayed its iron and protein concentration using ferrozine and BCA assays respectively. We then prepared purified FLPM6A at an equivalent iron-protein ratio and flash froze the suspension to carry out comparative EPR measurements. As a reference, we also measured the EPR spectrum of a solution of 10 mM Fe(III)-citrate.

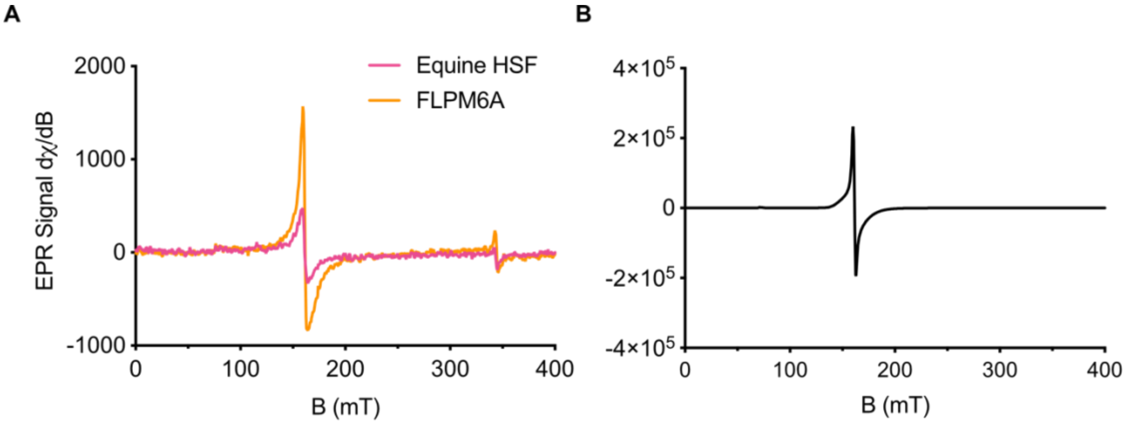

Fig. 2.10 X-band EPR Spectra of HSF, FLPM6A, and Fe(III) | A. 5K perpendicular mode X-band EPR spectroscopy of Equine HSF and FLPM6A at equivalent iron to protein ratios. **B.** EPR spectroscopy of 10 mM Fe(III) at 5K using the same parameters.

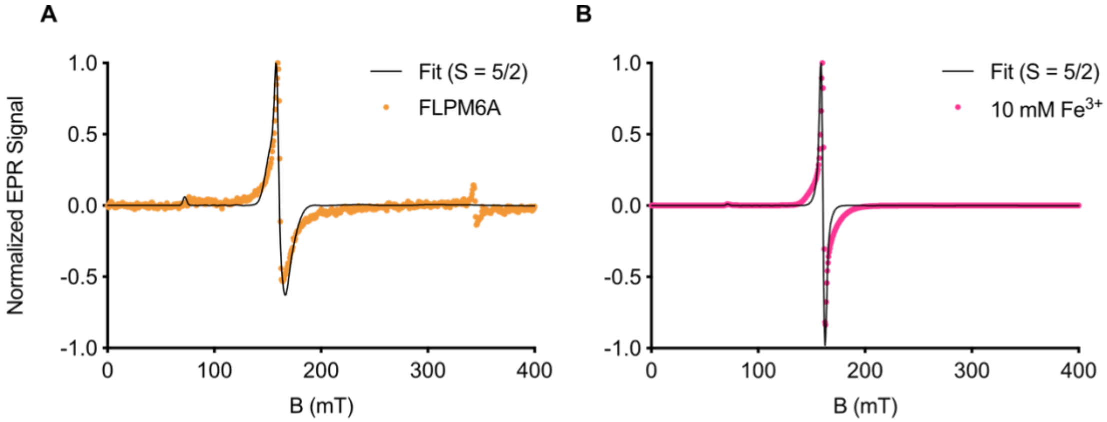

Fig. 2.11 Fit to EPR spectra of FLPM6A | A. Fit to normalized EPR signal of FLPM6A at equivalent iron to protein ratio as HSF. The data is well explained by high spin Fe3+ (S = 5/2) with rhombicity (E/D) of ~ 0.28. **B.** Fit to normalized EPR signal of 10 mM Fe(III)-Citrate solution for reference, which also indicates a high-spin Fe3+ (S = 5/2) with rhombicity (E/D) of ~ 0.32.

Consistent with previous reports on ferrihydrite and ferritins, we observed a small signal at $g_{eff} = 2.0$ ($\mathbf{B} \sim 344\ \mathrm{mT}$) and a larger signal at $g_{eff} = 4.3$ ($\mathbf{B} \sim 160\ \mathrm{mT}$) in HSF.[35,36] We observed the same EPR line shape with FLPM6A, albeit the signal was approximately 4 times stronger (ratio of the double-integral of the respective EPR lines). Both EPR signals were characteristic of high-spin Fe3+ (S=5/2) with highly rhombic zero-field splitting, as expected for adventitiously bound ferric iron (Fig. 2.10B). Interestingly, we observed the same effective improvement in per-iron paramagnetism using KappaBridge susceptibility measurements on UPMAG cells, which independently corroborates our hypothesis that FLPM6A stores iron in a much more paramagnetic spin state.

2.3.3 CEST spectroscopy of UPMAG cells

As discussed in Chapter 1, Chemical Exchange Saturation Transfer (CEST) is a powerful MRI technique which enables non-invasive discrimination of metabolites. Because CEST measures the diminishment of the bulk water signal as a consequence of exchange with a saturated proton pool, signal contrast is directly proportional to both the exchange rate, as well as the concentration of the secondary proton pool. Although they are genetically encoded, current generation of diamagnetic CEST (diaCEST) contrast agents, such as protamine sulfate or lysine rich peptide (LRP), require a local concentration of several mM in order to observe a detectable signal; the sensitivity of diaCEST contrast agents is fundamentally limited by the fact that their frequency offset is close to the water resonance ($\delta < 3.69\ \mathrm{ppm}$).[37–39] On the other hand, paramagnetic CEST (paraCEST) contrast agents, such as those based on chelated lanthanide ions, are sensitive and routinely achieve chemical shifts as large as several hundred ppm, but must be delivered exogenously.[40] If paraCEST agents could be genetically encoded, they would significantly expand the opportunities for CEST imaging *in vivo* given their enhanced sensitivity. Since UPMAG cells alter their intracellular magnetic susceptibility through the synthesis of ultraparamagnetic protein nanostructures, we asked if UPMAG cells can be employed as paraCEST contrast agents.

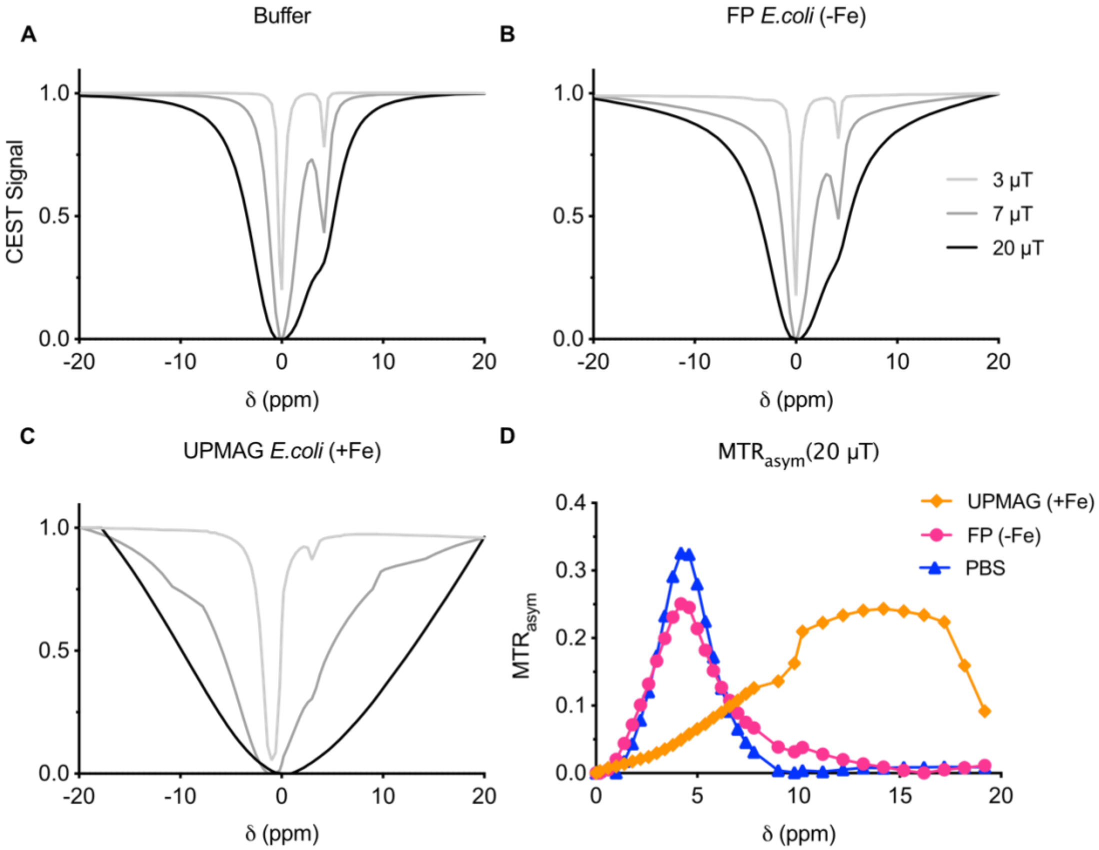

Fig. 2.12 CEST Spectroscopy |**A.** Z-spectra of the culture medium, and of **B.** Non-magnetic *E. coli* expressing a fluorescent protein at OD40, and of **C.** UPMAG *E. coli* at OD40, acquired at increasing $\mathbf{B}_1$ saturation field strengths. **D.** The asymmetry in magnetization transfer ratio ($\mathrm{MTR}_{\mathrm{asym}}$) shows maximal ^{1}H CEST contrast for UPMAG cells around 15 ppm.

To test our hypothesis, we resuspended ~ 3×10^{10} cfu/ml of *E. coli* expressing either fluorescent protein (FP) or UPMAG in M9 growth medium containing OptiPrep (50% v/v), a density medium. FP cells were cultured in iron-free media whereas UPMAG cells were grown in 1 mM Fe(II) (see Methods). Meanwhile, the purpose of the density medium was to prevent cells from settling during the course of the CEST measurement. The Z-spectra demonstrates unambiguous line broadening of the proton signal for UPMAG cells relative to non-magnetic FP cells at all saturation field ($\mathbf{B}_1$) strengths tested. The signal at approximately 4 ppm, which is present in the buffer and samples containing bacteria, originates from amide protons adjacent to the iodine moieties in the OptiPrep density reagent. The effect of a more paramagnetic intracellular magnetic susceptibility is evident in the magnetization transfer ratio asymmetry (Fig. 2.12D), which is calculated as follows:

$$\mathrm{MTR}_{\mathrm{asym}} = \left|S_{(+\Delta\omega)} - S_{(-\Delta\omega)}\right| / S_0 \tag{2.7}$$

Here, S_0 refers to water signal in the absence of any saturation, whereas $S_{(+\Delta\omega)}$ and $S_{(-\Delta\omega)}$ refers to the proton signal in the presence of $\mathbf{B}_1$, at frequency offsets given by $\pm\Delta\omega$. At the highest saturation field tested, we observed the clearest contrast in MTR asymmetry between UPMAG cells and non-magnetic FP cells. As expected, we observed maximal paraCEST contrast over a broad range of frequency offsets for UPMAG cells (10 – 17 ppm). The CEST line broadening results from (1) fast water exchange between intracellular and extracellular water molecules[41], and (2) the fact that iron in FLPM6A is stored as ferrihydrite, which is an intrinsically disordered mineral hydrate.[42] A previous study in which the CEST contrast properties of a tumor homing bacteria (Clostridium novyi-NT) was explored, found that maximal CEST contrast was produced at a frequency offset of 2.6 ppm.[43] Given that this frequency offset is well within the expected frequency shifts for common organic moieties such as amides and imines, high local concentrations of *C. novyi* are necessary for selective discrimination. Although the chemical shifts introduced by UPMAG cells are small when compared with synthetic paraCEST agents, our preliminary results suggest that UPMAG cells could potentially be discriminated more sensitively than previously reported bacCEST agents.

2.3.4 Monte-Carlo (MC) models of UPMAG driven MRI contrast

Monte-Carlo (MC) simulations of nuclear spin relaxation qualitatively and quantitatively agree with experimentally measured spin-spin relaxation rates for UPMAG cells. The observation that intracellular exchange is necessary and sufficient to explain the observed R2 trend corroborates the CEST measurements of proton line-broadening due to the presence of intracellular ferrihydrite. As covered in Chapter 1, the mechanism of spin-spin relaxation by ferrihydrite is predominantly through proton exchange driven dephasing, unlike SPIONs which relax nuclear spin primarily through outer-sphere relaxation.[44,45]

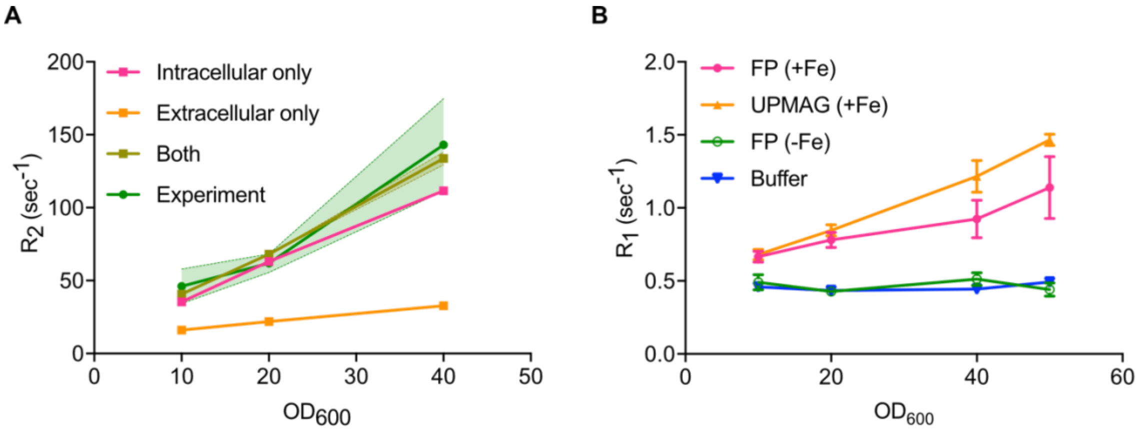

Fig. 2.13 Monte Carlo simulations of relaxation by UPMAG cells | A. Simulated transverse relaxation rates (R_2) for UPMAG expressing *E. coli* for different cell densities. Exchange of water between compartments with a difference of + 4.68 ppm in bulk susceptibility accounts for the bulk of the observed transverse relaxation rates. **B.** Spin-lattice relaxation rates (R_1) for *E. coli* expressing either FP or UPMAG grown under various conditions.

While the linearity of R_2 with increasing cell density is therefore unsurprising, we were nonetheless surprised by the poor spin-lattice relaxation rates. We suspect that at the high field strengths used (500 MHz), molecular motions are not resonant with the proton Larmor frequency, which may explain the low R_1 rates observed here.[46] Additionally, it is also likely that the spin-spin relaxation induced by the ultraparamagnetic mineral destroys spin-coherence well before T_1 relaxation. Further studies at low-fields are needed to test whether UPMAG cells can also act as spin-lattice contrast agents, analogous to synthetic paramagnetic nanoparticles.[47]

2.3.5 Bulk fitness profiling of UPMAG cells

One common technique for assessing the fitness of an engineered microbe is to quantify its growth-rate and saturation density. Given that UPMAG cells contain high intracellular concentrations of iron, we were interested in determining whether these high concentrations would deleteriously affect the health of the microbe.

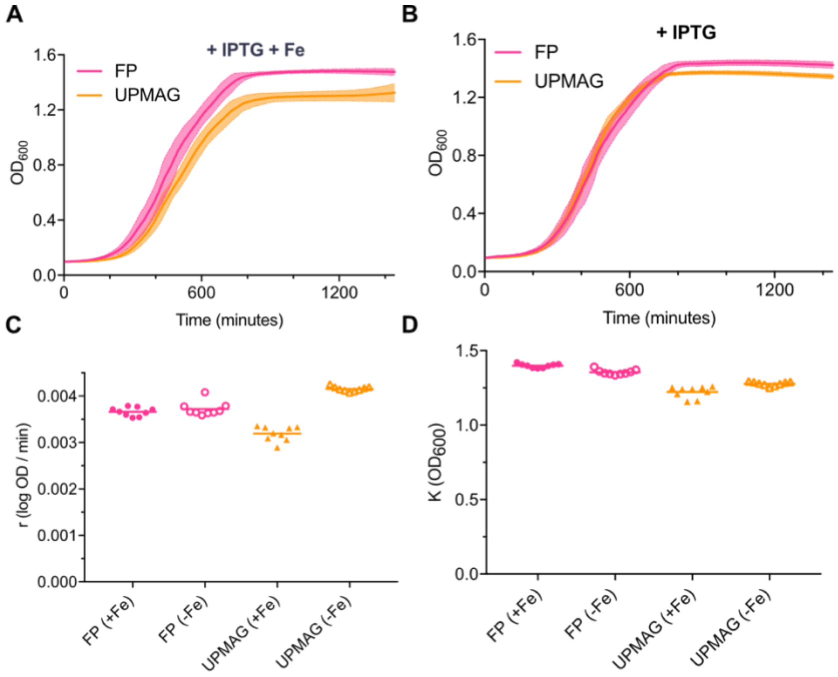

Fig. 2.14 Growth curves | A. Growth curves for *E. coli* expressing either FP or UPMAG in the presence of both inducer (0.1 mM IPTG) and iron (1 mM Fe(II)). **B.** Growth curves for *E. coli* expressing either FP or UPMAG in the presence of inducer (0.1 mM IPTG) alone **C.** Growth rates were obtained by fitting the modified Gompertz equation for the various conditions described in the text. **D.** Saturation OD as extracted from fits of the growth curves to the modified Gompertz equation.[48]

2.3.6 Magnetic separation of UPMAG cells from complex mixtures

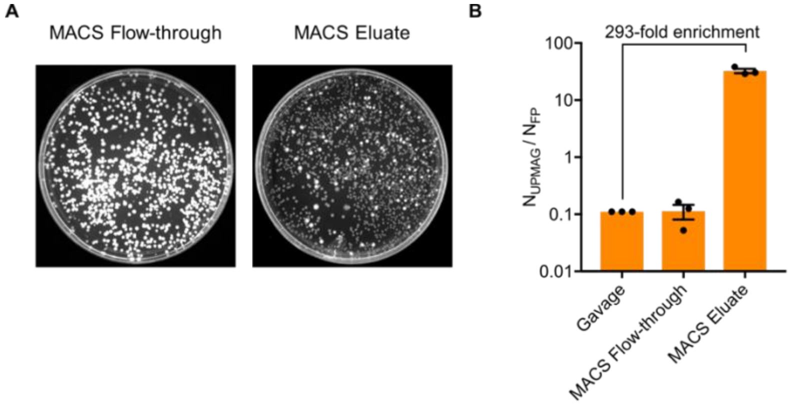

Fig. 2.15 MACS Separation from complex mixtures | A. Representative image of plates containing the flow-through and eluted fractions. **B.** Ratio of UPMAG to FP cells in the respective MACS fractions. UPMAG *E. coli* were enriched 293 ± 45.0 fold in the MACS eluate.

The magnetic force on a cell with different magnetic susceptibility relative to surrounding medium is $\vec{F}_m = \frac{V_{cell}\Delta\chi}{\mu_0}(B \cdot \nabla)B$ where V_{cell} is the cell volume, $\Delta\chi$ is the bulk susceptibility difference between the cell and the medium, μ_0 is the permeability of free space, B is the magnetic field, and ∇B is the magnetic field gradient. A MidiMACS separator produces a permanent field of $B \approx 0.45\ \mathrm{T}$, and MACS LD columns produce field gradients of $10^4\ \mathrm{T/m}$ according to the manufacturer.[2,3] From our measurements of UPMAG cells, $\Delta\chi \approx 4.8 \times 10^{-6}$ relative to water. This results in a magnetic force of $F_m \approx 19.8$ fN. By comparison, the sedimentation force acting on a single *E. coli* cell is approximately $\vec{F}_g = \frac{4}{3}\pi {r_{cell}}^3 g(\rho_{cell} - \rho_{fluid}) \approx 1.18$ fN, using r_{cell} = 0.65 μm, and where ρ_{fluid} is the density of water and ρ_{cell} is $1105\ \mathrm{kg/m^3}$.[1]

2.7.7 Additional biophysical characterization of FLPM6A

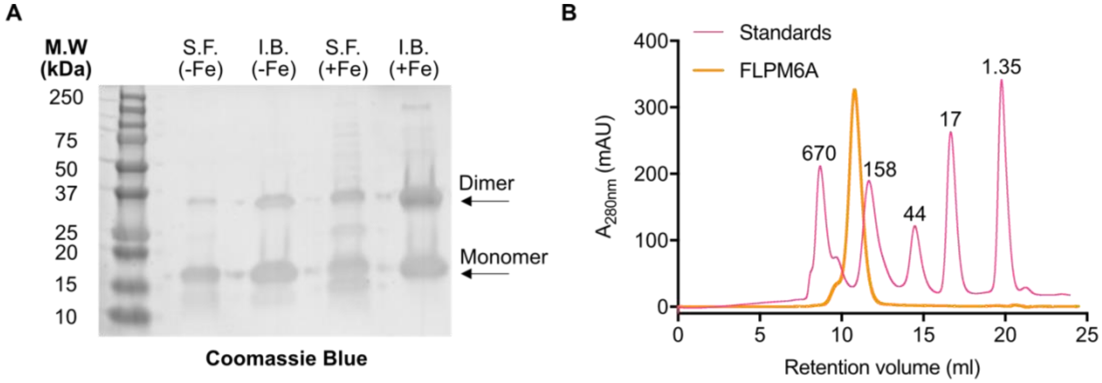

Fig. 2.16 Gel chromatography of FLPM6A| A. SDS-PAGE of purified 6xHis-FLPM6A from the soluble and inclusion body fractions when cells were cultured either with or without iron. The I.B. (-Fe) and S.F. (+Fe) fractions were concentrated 5-fold prior to SDS-PAGE. The monomer and dimer molecular weights are 16 and 32 kDa respectively. **B.** Size-exclusion of FLPM6A purified from *E. coli* BL21 DE3. The molecular weights of standards are indicated above their respective peaks in the chromatogram.

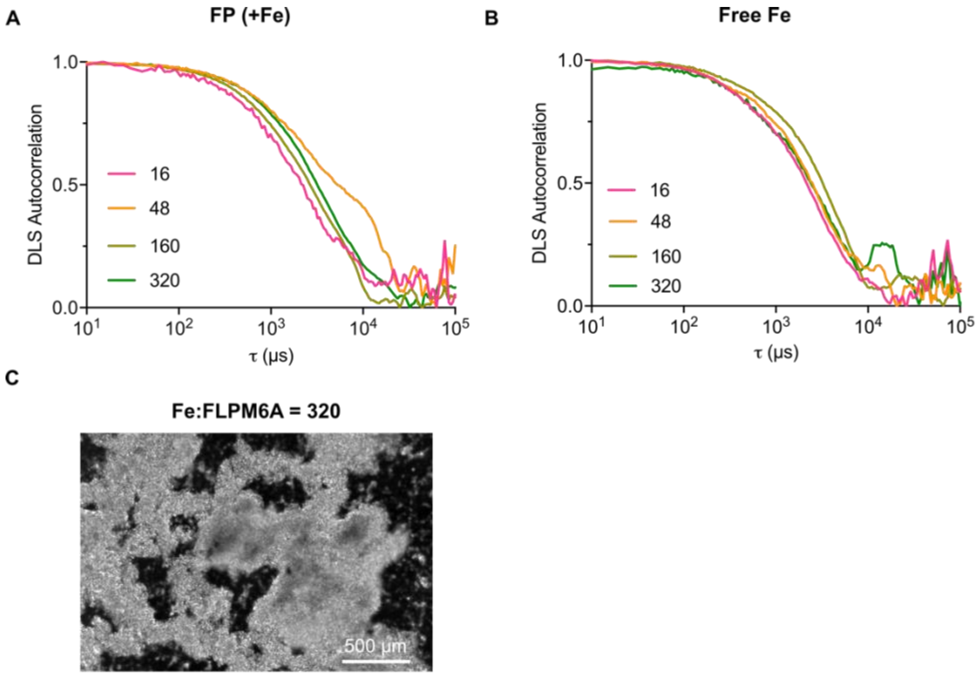

Fig. 2.17 DLS Spectroscopy | A. DLS spectra for a hexa-histidine tagged fluorescent protein that was incubated with iron at varying molar ratios **B.** DLS spectra for equivalent concentrations of free iron **C.** Brightfield images of the "ferrogel". FLPM6A was mixed with free iron at a ratio of 1:320 respectively in a glass bottom petri-dish. Unlike free iron which precipitates to the bottom of the dish, the ferrogel floats and no precipitates of iron were observed at the bottom when FLPM6A was present.

2.3.8 Iron source and its impact on intracellular iron loads

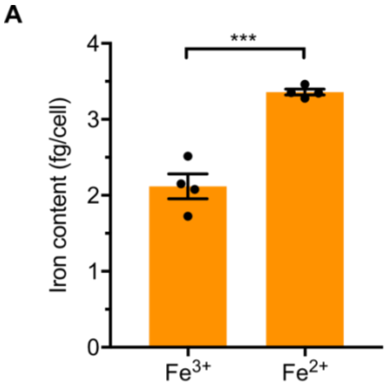

Fig. 2.18 Iron source | A. Intracellular Iron content of UPMAG *E. coli* cultured in protein expression medium with either 1 mM Fe(III) or 1 mM Fe(II) as the iron source.

Given that the UPMAG gene circuit contains a ferrous iron transporter, we expected diminished intracellular iron concentrations when UPMAG cells were grown in Fe^{3+} only growth medium. Nonetheless, iron levels are elevated since *E. coli* also express several siderophores and other ferric iron uptake pathways. Our construct, however, requires ferrous iron, since ferric iron is unlikely to be freely available in the cytoplasm.

2.3.9 Circular-dichroism spectroscopy of FLPM6A

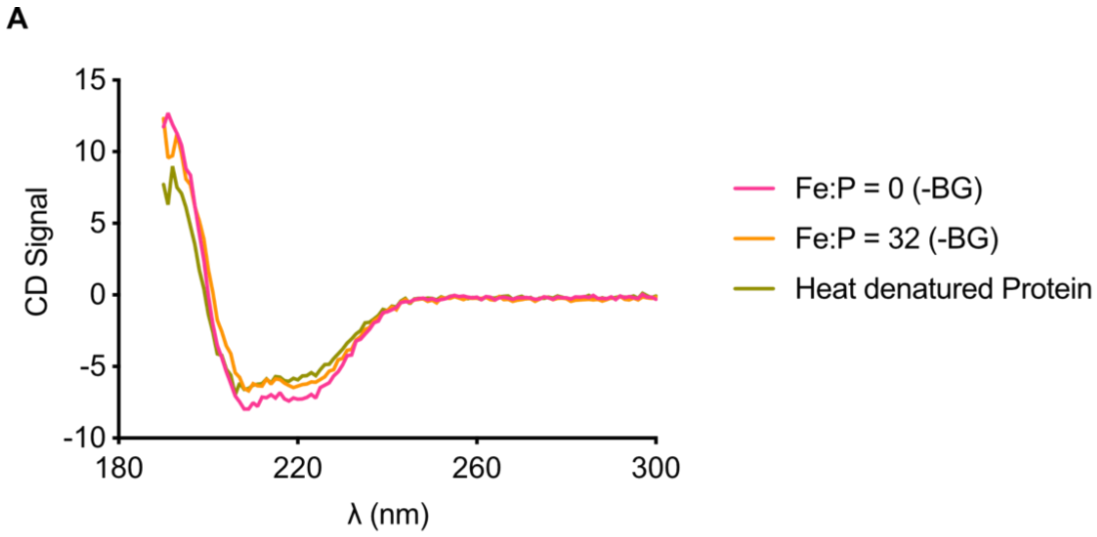

Fig. 2.19 CD Spectroscopy| A. Circular dichroism spectroscopy of purified His-FLPM6A with and without iron. Separately, the protein was heat denatured and allowed to cool back to room-temperature before being measured.

To investigate the secondary structure of FLPM6A in the presence and absence of iron, we turned to circular-dichroism (CD) spectroscopy. In brief, CD spectroscopy measures differential absorption between left – and right – circularly polarized light. Peptide bonds and amino-acid sidechains, which make up all proteins, preferentially absorb light between 180 nm – 260 nm. The tertiary structure of proteins, consisting of some combination of coils, α-helices, β-sheets, and disordered loops, in turn dictates optical dichroism, which refers to the differential absorption of polarized light as a function of its wavelength.[49]

We acquired CD spectra of FLPM6A in the absence and presence of 32 molar equivalents of iron, which is the iron-to-protein ratio that we previously used in our earlier EPR studies. Furthermore, this iron-to-protein ratio is also approximately equivalent to that of horse-spleen ferritin, which is a well-studied model protein whose tertiary structure and corresponding CD spectrum are known.[50] As expected, FLPM6A folds as a thermostable α-helical protein, given that we observed the same spectra on a heat denatured sample that was allowed to cool to room temperature before measurement. The addition of iron does not appear to affect its fold, although we were unable to obtain a signal at the iron-to-protein ratios found within the cell, due to precipitation within the cuvette. That said, the result that FLPM6A folds as an α-helix is unsurprising given that the structure of FLP alone was previously found to be α-helical.[16] The addition of M6A peptide to its C-terminus changes the overall isoelectric point of the protein and its mobility in a size-exclusion column but does not appear to affect its fold. The conclusions drawn from the CD measurement is independently corroborated by the fact that FLPM6A functions as a ferroxidase, in which the active site spans two α-helical monomers of the oligomeric complex.

2.3.10 Electron micrographs of FLPM6A in the presence of iron show a disordered mineral *in vitro* and *in cellulo*

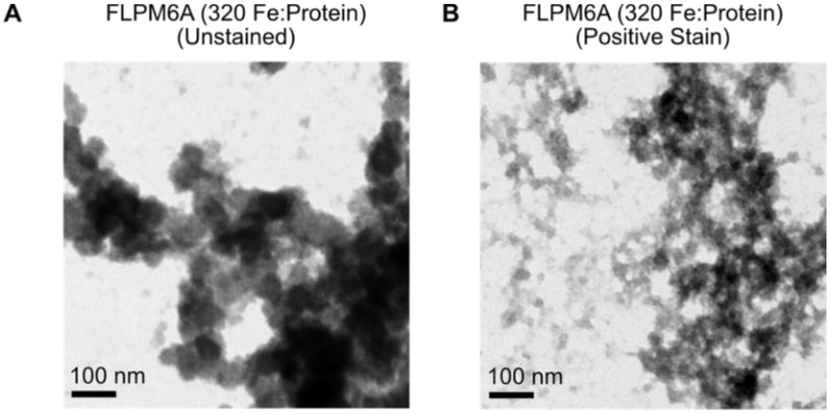

Fig. 2.20 TEM images of FLPM6A| A. Unstained TEM (120 keV) of FLPM6A incubated with 320 Fe:FLPM6A **B.** Positive stained TEM (120 keV) of the same sample indicating the presence of protein in the ferrogel.

Purified FLPM6A was incubated at an iron:protein ratio of 320, which is what we expect within the cell. A ferrogel was observed 1 hr after incubating the protein sample with ferrous iron under atmospheric oxygen. Unstained TEM images of the ferrogel show an amorphous material with variable electron density. UA staining of the ferrogel indicates that protein is intercalated with iron and does not appear to have any regular size distribution.

2.4 Outlook for ultraparamagnetic cells

Taken together, our results demonstrate that the expression of a three-component genetic circuit renders a model bacterial cell ultraparamagnetic at room temperature. The 8-fold increase in the total paramagnetic moment of the cell is sufficient to not only enable more sensitive detection using MRI relative to BFR, but also to facilitate magnetic capture and enrichment from complex biological samples.[21] These capabilities could enable new applications in chemical and synthetic biology, such as the tracking and rapid isolation and subsequent phenotyping of genetically engineered GI probiotics. The fact that the ultraparamagnetism is genetically encoded provides an advantage over previously reported approaches requiring cellular labeling with synthetic materials, which would become diluted during cell proliferation. While many previous efforts have focused on genetically mimicking the superparamagnetism or ferromagnetism of synthetic materials and magnetotactic bacteria, our work shows that paramagnetism is a viable alternative paradigm to achieving magnetic behavior under the field conditions employed in many envisioned applications (e.g. MACS and MRI). The experiments performed in this study provide the rudimentary proofs-of-concept for the capabilities provided by maximizing the paramagnetic moment of an engineered cell. Future studies are needed to evaluate the performance of the UPMAG circuit or similar constructs in more complex settings, such as cells residing in an animal host and in additional microbial species.[52] Furthermore, additional insights on the composition of the iron complexes from electron microscopy could further the development and optimization of the UPMAG approach.[53,54] Since the construct described in this work provides only 50.7% of the paramagnetism theoretically possible for the measured quantity of intracellular iron, there is considerable room to make UPMAG more “ultra”.

2.5 Experimental methods

2.5.1 Preparation of cell culture for *in vitro* NMR and *in vivo* MRI.

The following culture media were used for all experiments with *E. coli*. All reagents, unless otherwise specified, were purchased from Millipore-Sigma.

Table 2: Culture media used in experiments

Media	Composition
Overnight growth	M9 base salts + 0.4% (w/v) Glucose + 0.2% (w/v) CAS + 2 mM $MgCl_2$ + 0.1 mM $CaCl_2$ + 10 μM 2,2-Bipyridyl
Protein expression	M9 base salts + 0.4% (w/v) Glucose + 0.2% (w/v) CAS + 2 mM $MgCl_2$ + 0.1 mM $CaCl_2$
Cell maintenance	M9 base salts + 2 mM $MgCl_2$ + 0.1 mM $CaCl_2$

Prior to all experiments, *E. coli* were freshly chemically transformed with 1 ng of plasmid DNA and grown to saturation overnight in growth medium containing 10 μM of 2-2 bipyridyl, in order to starve the cells of iron and thus trigger RhyB mediated silencing of endogenous ferritins.[55] Overnight cultures of Novagen BL21 R2 DE3 *E. coli* expressing UPMAG, as well as controls, were inoculated (1:100) into fresh protein expression medium (100mL in a 500 mL Erlenmeyer flask) and grown at 37℃ with vigorous shaking at 250 RPM to OD 0.1, at which point IPTG and Fe(II) ammonium sulfate were added to final concentrations of 0.1 mM and 1 mM respectively. We found that the supplementation with Fe(II) led to more iron accumulation in cells than supplementation with Fe(III) (Supporting Data Fig. 2.17). The temperature was then reduced to 30℃ and cultures were grown for 36 hrs before harvest. Cultures were pelleted at 3500 g for 10 mins and subsequently resuspended in an equivalent culture volume of 1X PBS + 2 mM EDTA to wash away any extracellular iron. Cells were then pelleted at 3500 g for 10 mins and resuspended in 1/5 culture volume of cell maintenance medium. OD_{600} was measured in a 1:100 dilution of the resuspended cultures, and all cultures were normalized to the same OD_{600} by addition of cell maintenance medium. Subsequently, 0.3 mL PCR tubes with *E. coli* at a desired

OD_{600} were prepared by mixing stock suspensions with Optiprep, thus creating a uniformly suspended mixture. The total amount of Optiprep was kept constant across the different densities in order to ensure that the buffer relaxation rates were constant. PCR tubes were placed in a precast 1% agarose phantom to minimize magnetic susceptibility artifacts, and the phantom was subsequently imaged using a 7 Tesla horizontal bore Bruker MRI scanner. The same cell culture harvest and wash procedures were followed for preparing samples to be analyzed using a Bruker 500 MHz NMR spectrometer, with the only difference being that the total volume of sample analyzed was 0.8 mL. Data analysis for calculating relaxation rates was done using a custom Matlab script that fit mono-exponentials to the first 6 echoes in an echo train.

2.5.2 Protein purification and concentration measurements

Novagen BL21 DE3 *E. coli* were freshly transformed with 1 ng of plasmid containing an N-terminal hexa-histidine (with TEV protease cleavage site-tagged FLPM6A under a T7 promoter, and subsequently cultured in protein expression media (100 mL) containing 50 μg/ml kanamycin in a baffled flask at 37°C with constant shaking at 250 RPM. At OD_{600} 0.1, cells were induced with 100 μM IPTG, either with or without supplementation of 1 mM ferrous ammonium sulfate. The temperature was lowered to 30℃ to allow for protein expression for 36 hrs. 100 ml cultures of control *E. coli* expressing 6xHis-TEV-mRuby2 were likewise cultured in protein expression medium for downstream harvest and purification using Ni-NTA affinity chromatography. All cells were again harvested as previously described. Upon washing, cultures were centrifuged and frozen at –80℃ for 1 hr prior to thawing at room temperature for 10 mins. Pellets were lysed with a cocktail of SoluLyse (1 mL SoluLyse/ 10 mL cell culture), protease-inhibitor EDTA free (1X), lysozyme (50 μg/ml), and DNAse (10 μg/ml). Cells were lysed at 4℃ overnight on a slow rotator and subsequently clarified by centrifugation at 16,000 g for 15 mins. The supernatant was then mixed with Ni-NTA superflow resin (1 ml resin/100 ml cell culture) and again incubated overnight at 4℃. Protein was purified using gravity flow Polyprep (Biorad) columns and eluted with 1M imidazole (pH 8.0). Proteins were then dialyzed into 1X PBS using spin filters (10 kDa cutoff), and protein concentration was measured using both Pierce 660 nm and Pierce BCA assay. The insoluble fraction in the clarified cell lysate was first diluted 10-fold (by volume) in a SoluLyse buffer containing 1% Triton X-100, 0.1% Tween 20, and 0.1% NP-40 and incubated overnight at $4°\mathrm{C}$ on a rotator in order to completely solubilize all lipids. The mixture was subsequently centrifuged at 16,000g for 15 mins. The supernatant was decanted and the remaining dark pellet was resuspended in PBS containing 6M urea and sonicated for 2 mins (25% duty cycle, 35% amplitude). The mixture was then mixed with Ni-NTA superflow resin and the same procedure was followed as before for affinity purification with the exception that all wash and elution buffers contained 6M urea.

Protein purified from inclusion bodies when cells were grown in iron-poor media and protein purified from the soluble fraction when cells were grown in iron-rich media were both concentrated ~ 5 fold. All fractions (S.F. +/- Fe; I.B. +/- Fe) were mixed 1:1 with Laemmli buffer containing SDS, β-mercapatoethanol and 0.1 mM L-ascorbic acid, and boiled at $95°\mathrm{C}$ for 10 mins prior to SDS-PAGE analysis (Supplementary Fig. S3A).

Intracellular iron: protein ratio was computed by taking a ratio of the measured intracellular iron concentrations with the measured soluble protein yield when cultures were grown in the absence of iron in the growth media. *E. coli* volume was set to $1.2\ \mathrm{fl}$ and a cell density of $\mathrm{OD}_{600}1 = 21.9 \pm 2.2 \times 10^8\ \mathrm{cfu/ml} \cdot \mathrm{OD}_{600}$ was used in all calculations, consistent with literature values. The saturation cell-culture density for UPMAG cultures grown in protein expression medium was measured to be $\mathrm{OD}_{600} = 6.5 \pm 0.8$.

2.5.3 SQUID Magnetometry and KappaBridge Susceptibility

Cells were grown and washed as described above. Washed cells were pelleted at 3500 g for 10 minutes in 50 mL sterile polypropylene tubes, and the supernatant was aspirated. The cell pellet was subsequently frozen at $-80°\mathrm{C}$ for 1 hour, then lyophilized for 24 hours in order to completely remove any water. Care was taken to minimize dried pellet contact with any steel-containing materials, which are sources of ferromagnetic contaminants. The dried pellet was homogenized by vortexing. 10 – 15 mg of dried powder was placed in gelatin capsules, which were then analyzed using a SQUID MPMS (Quantum Design). All SQUID magnetization (field sweep) curves were acquired at 30 K. An empty capsule was also measured for reference. The data shown in the figures are the raw SQUID curves and do not include any background subtraction. The magnetization versus temperature data fit well to the Curie-Weiss law, $\chi = \frac{C}{T-T_c}$, as expected for purely paramagnetic materials. 80 – 120 mg of dried cell powder was also packed into acid-cleaned glass NMR tubes for susceptibility measurements using an Agico KappaBridge Susceptometer. The cell powder was packed into the tube such that it completely covered the probe's sensing volume, thus ensuring a homogeneous magnetic environment throughout the measurement process. The tube was purged with argon gas prior to measurements in order to remove any paramagnetic oxygen, and all measurements were done at 19°C. An empty glass tube was identically measured in order to obtain a reference susceptibility, which was then subtracted from all subsequent measurements to obtain the final bulk volume susceptibility.

To compute the maximum achievable volume susceptibility from an iron loaded cell, we first assumed that all iron atoms were high-spin ferric ions $[\mathrm{Ar}]3d^5$, with a spin of $S = 5/2$, using the Afbau principle. The effective magnetic moment of a single ion is $m_{\mathrm{Fe}^{3+}} = g_e\mu_B\sqrt{S(S+1)}$, where $g_e$is the Landé electronic g-factor and μ_B is the Bohr magneton. Assuming ideal paramagnetic behavior, the bulk volume susceptibility follows the Curie law, $\chi = \frac{\mu_0 N(m_{\mathrm{Fe}^{3+}})^2}{3k_B T}$, where *N* is the number of ferric ions per cubic meter within the cell (assuming a cell volume of 1.2 fl), μ_0 is vacuum permeability constant, k_B is the Boltzmann constant, and *T* is the temperature in Kelvin, which for our calculations was set to 293K (room temperature).

2.5.4 Intracellular measurements of iron

Washed cells were concentrated to a final OD_{600} of 80. Serial dilutions were plated concomitantly with ferrozine measurements to get precise colony counts. 20 μL of concentrated suspension was boiled in 180 μL of trace-metal free grade pure nitric acid (~ 70%) at 56°C for 6 hours to ensure complete dissolution of intracellular iron in a sterile 2 ml polypropylene Eppendorf tube. A blank tube containing 20 μL of maintenance media was treated identically for reference.

Ferrous ammonium sulfate hexahydrate standards (1 μg/ml to 200 μg/ml) were also prepared and treated identically to be used for absorbance measurements. Boiled samples were serially diluted in sterile miliQ water. A previously described ferrozine assay was subsequently used to measure iron concentrations across the dilutions.[56] Iron content per cell was obtained by dividing the total iron measured by the colonies counted.

To measure the quantity of iron in the soluble and insoluble fractions respectively, 150 mL of BL21 DE3 *E. coli* expressing 6xHis-FLPM6A was cultured in protein expression media supplemented with 1 mM Fe(II). Washed cells were lysed with 10 mL of lysis buffer, as described above and the lysate was clarified by centrifugation. The insoluble fraction was resuspended in 10 mL of inclusion body lysis buffer containing 6M Urea. A ferrozine assay was performed using 20 μL of both the soluble and resuspended insoluble fractions as described above. Iron contents were quantified per volume of the sample.

2.5.5 *In vitro* MACS experiments

Washed bacteria were resuspended in M9 base media to a final OD_{600} of 0.5, then poured over a MACS LD column (Miltenyi Biotech), which was sandwiched between neodymium rare earth magnets (B_0 = 0.45 T). The column was then washed with degassed PBS containing 0.5% BSA, and trapped microbes were eluted with degassed M9 medium. Dilutions of the eluate were plated, and colonies were subsequently counted for both the eluate and wash fractions. Magnetic fields were simulated using Gmsh, a finite element simulator, using values for magnetic coercivity taken from K&J magnetics.[57] N52 NdFeB magnets (BX084BR) from K&J magnetics were used in the petri-dish magnetic capture experiments.

2.5.6 *In vivo* experiments with NU/J mice and BALB/cJ mice

Mouse experiments were conducted under a protocol approved by the California Institute of Technology's Institutional Animal Care and Use Committee. For *in vivo* imaging experiments, *E. coli* were once again prepared as before. Washed microbes were resuspended in cell-maintenance media to a final OD_{600} of 20. 100 μL of microbes were then mixed with an equal volume of

Matrigel at 4°C and immediately injected subcutaneously into the hind flanks of nude mice. Mice were allowed to rest for 15 mins in order to set the matrigel-bacteria mixture, then imaged using a Bruker 7 Tesla small animal scanner. An M2M Quadrature coil was used to excite and receive RF signals, and isofluorane anesthesia was kept at 1.5% for the duration of imaging. Body temperature was recorded using a rectal fiber optic probe and kept constant at 37°C using a PID controlled hot-air blower.

For gavage experiments, *E. coli* were cultured and washed as previously described. Bacteria were then resuspended in cell maintenance media to a final OD_{600} of 1. A mixture of FP and UPMAG expressing cells were prepared in a 10:1 ratio. 200 μL of the mixture was then gavaged into female 8-week-old BALB/cJ mice. Mice were then returned to cages with access to food and water. Feces was freshly collected and weighed from mice 3-4 hours after gavage and homogenized in cell-maintenance medium (50 mg/ml) using a bead beater. Fecal samples were subsequently clarified through a 75 μm filter (BD Falcon) to remove large insoluble aggregates, then poured over 0.5% BSA-equilibrated MACS LD columns. Trapped microbes were eluted, and serial dilutions of the eluate were plated on LB Agar plates containing ampicillin (100 μg/ml) and IPTG (100 μM). Colonies were grown and allowed to express at 30°C for 36 hrs prior to imaging using a BioRad ChemiDoc gel imager. Fluorescence images were acquired using the Alexa546 filter set with exposure time fixed at 0.1 seconds. Colonies (fluorescent and non-fluorescent) were counted manually and the enrichment ratio was calculated. A sub-sampling of 20 non-fluorescent colonies were sequenced to confirm their identity as carriers of the UPMAG plasmid.

2.5.7 *In-vitro* DLS Experiments

Purified 6xHis-FLPM6A was diluted to 100 μg/ml (~ 6.5 μM monomer) in PBS and then aerobically incubated with freshly prepared Fe(II) ammonium sulfate at molar ratios of 0, 8, 16, 32, 48, 64, 80, 160, and 320 at 37°C in sterile 2 ml polypropylene Eppendorf tubes (total reaction volume 300 μL in 100 mM HEPES, pH 7.0) for 1 hour. Control experiments consisted of Ni-NTA affinity purified 100 μg/ml of 6xHis-mRuby2 and free iron at the same concentrations.

Photos were taken using a Google Pixel2 camera. 200 μL of each sample was used for the DLS measurement (Brookhaven Instruments) as per the manufacturer's protocol. Briefly, autocorrelation spectra were acquired for 10 seconds at 22 °C, and measurements were repeated with no dust filtering for 6 trials. Samples were mixed by pipetting between trials to avoid settling. Aliquots of the same samples were then mixed 1:1 with Native sample buffer (Bio-Rad) and loaded into a precast TGX gel (Bio-Rad), which was subsequently run at 80V for 70 mins. The gel was first treated with Prussian blue (Sigma) stain to visualize iron deposits and then treated with Coomassie blue stain (Thermo Fisher) to visualize protein.

2.5.8 Growth Curves

9 separate colonies of *E. coli* expressing either UPMAG or FP were picked and inoculated overnight in cell-growth media. Subsequently, cultures were diluted 1:100 with fresh protein expression medium containing both IPTG and/or Fe, and cultured in square 96 well plates sealed with breathable tape (200 μL total volume) for 26 hrs at 30℃ with maximum linear shaking. Growth curves were obtained by recording OD_{600} every 7 minutes and subsequently fitted to the modified Gompertz equation to obtain growth rates and carrying capacities.[48]

2.5.9 Monte Carlo Simulations

Nuclear spin relaxation was simulated using an adaptation of previously described code by randomly distributing spherical *E. coli* cells with $\chi = +4.68\ \mathrm{ppm}$ inside a $1000\ \mu\mathrm{m}^3$ cubic simulation volume using periodic boundary conditions.[58,59] Cell radius was set to $0.65\ \mu\mathrm{m}$ to match previously reported equivalent cell volumes of *E. coli*.[60] The number of cells in the simulation volume was set to match the OD of our experimental data using the Agilent estimate of $N_{\mathrm{cells}} = \mathrm{OD}_{600} \cdot V_{E.coli} \cdot 8 \times 10^{11}$, where V is the simulation volume in cubic meters. The magnetic moment of each *E. coli* cell was calculated as $\mathrm{m} = \chi \cdot V \cdot \mathbf{H}$ where χ is the bulk magnetic susceptibility, V is the volume of the cell, and $\mathbf{H}$ is the bias field in the NMR spectrometer (11.7 Tesla). The magnetic field B in the extracellular space was explicitly calculated for each water molecule based on the sum contribution from each *E. coli* cell. 4032 water molecules were randomly assigned initial 3D spatial coordinates $(\mathbf{r} = [x, y, z])$ in the simulation volume with phase $\phi(t_0) = 0$ and allowed to diffuse according to previously established cellular diffusion models.[58,59] The phase in the rotating reference frame evolves according to $\delta\phi(t) = -\gamma \cdot \mathbf{B}(\mathbf{r}) \cdot \delta t$ for water in the extracellular space, where γ is the proton gyromagnetic ratio and $\mathbf{B}$ is the total magnetic field in the rotating reference frame as experienced by the water molecules. For water in the intracellular space, phase evolves according to $\delta\phi(t) = \Delta\omega \cdot \delta t$, where $\Delta\omega$ is the shift in the Larmor frequency due to the difference in intracellular bulk magnetic susceptibility relative to external media. Re-focusing pulses were simulated by setting $\phi(t) = -\,\phi(t - \delta t)$. Cell membranes were modeled as semi-permeable boundaries with a permeability of $2\,\frac{\mathrm{\mu m}}{\mathrm{ms}}$, in accordance with previously measured values for *E.coli* cells.[41] Intracellular and extracellular water diffusivity were set to 1 and $2\,\frac{\mathrm{\mu m}^2}{\mathrm{ms}}$ respectively, in accordance with previous studies of cellular diffusion and established values for water diffusivity at the temperature of our spectrometer bore $(20\ ^\circ\mathrm{C})$. Bulk spin magnetization in the sample was calculated as $\mathbf{M}(t) = \sum_i cos[\phi_i(t)]$, where *i* is the index of simulated water molecules and the magnetic moment of a single molecule is normalized to 1. T_2 values were extracted from each simulated sample with a mono-exponential fit to the first 10 echoes. Background relaxation from buffer was accounted for by multiplying all simulated exponential decays with a mono exponential decay whose rate constant was equal to the experimentally measured relaxation rate of pure buffer.

We simulated three different diffusion models to determine the dominant relaxation mechanism for UPMAG expressing *E. coli.* In the combined model, both intracellular and extracellular contributions to relaxation were allowed as described above. In the “intracellular only” case, membrane permeability was as described above, but the $\delta\phi$ for extracellular water was set to zero. In this way, we were able to isolate the intracellular relaxation that arises solely from water molecules transiting through a compartment with different magnetic susceptibility. In the “extracellular only” case, water molecules were initialized only in the extracellular space, and the cell membranes were modeled as impermeable to water. In this way, we were able to isolate the effect of the outer-sphere dipolar relaxation due to the net magnetic moment of the *E. coli* cells. All simulations were written in CUDA and performed on two NVIDIA K40 GPUs.

2.5.10 Mössbauer Spectroscopy

Samples for Mössbauer measurements were prepared identically to those for magnetometry measurements. In brief, 100 ml of *E. coli* cultures expressing either UPMAG or BFR were grown in iron-rich media (1mM Fe(II)) and subsequently washed with PBS-EDTA to chelate any extracellular iron. Washed cell pellets were then snap frozen and lyophilized for 24 hours. 70 – 80 mg of dried cell powder was then placed in Teflon Mössbauer sample holders.

Mössbauer spectra were recorded on a spectrometer from SEE Co. (Edina, MN) operating in the constant acceleration mode in a transmission geometry. The sample was kept in an SVT-400 cryostat form Janis (Wilmington, MA). The quoted isomer shifts are relative to the centroid of the spectrum of a metallic foil of α-Fe at room temperature (RT). Data were collected at 80 K with a 50 mT magnet applied parallel to the gamma rays. Data analysis was performed using version 4 of the program WMOSS (www.wmoss.org) and quadrupole doublets were fit to Lorentzian line shapes.

2.5.11 Circular-Dichroism Spectroscopy

300 μl of 3.3 μM of purified FLPM6A in 20 mM Tris pH 7 was loaded into quartz cells with a 1 mm optical path length for CD measurements at room temperature. CD spectra were recorded using an Aviv Model 430 CD spectrometer at room temperature between wavelengths of 190 – 300 nm and averaged across 4 measurements. A buffer blank consisting of 20 mM Tris pH 7 was likewise recorded in the same manner and subsequently subtracted from the spectrum with protein.

2.5.12 Size-Exclusion Chromatography

Ni-NTA affinity purified FLPM6A was desalted into PBS and loaded onto a Superdex-200 10/300 gel-chromatography column (GE Healthcare, Little Chalfont, UK) with a flow rate of 0.25 ml/min.

2.5.13 Transmission Electron Microscopy

4 μl of protein-iron mixtures were spotted onto carbon-coated copper grids that were pre-treated with glow-discharge for 2 mins and blotted with Whatman paper. For stained samples, 4 μl of 2% Uranyl Acetate was added to the grids for 30 s before blotting. Grids were subsequently washed and rapidly blotted three times with 4 μl of miliQ water to thoroughly remove any salts and residual stain and allowed to air-dry for 10 mins before imaging. For unstained samples, grids were washed and rapidly blotted three times with 4 μl of miliQ water after sample was spotted and likewise allowed to air dry for 10 mins before imaging. All imaging was done using a 120 keV Tecnai T12 LaB6 TEM equipped with a Gatan Ultrascan 2k X 2k CCD.

Additional TEM imaging and *in situ* elemental analysis on thin-sections was done using a FEI Tecnai F30ST (300kV) field-emission TEM, equipped with a high angle annular dark field detector (HAADF-STEM), an Oxford ultra-thin window EDS detector, and a Gatan Ultra Scan 1000XP camera. Cells were fixed using Gluteraldehyde and resin embedded prior to sectioning and staining with Osmium tetroxide and Lead citrate. Sections were placed on holey carbon grids to minimize copper formvar signal artefacts in EDS.

2.5.14 EPR Spectroscopy

Perpendicular- and parallel-mode X-band (9.4-9.6 GHz) CW EPR spectra were acquired using a Bruker EMX spectrometer equipped with an ER 4116DM Dual-mode resonator. Temperatures were maintained using liquid helium as the coolant with an Oxford Instruments

ESR900 flow cryostat and an ITC-503 temperature controller. Spectra were simulated using the EasySpin simulation toolbox[61] (release 5.2.12) with Matlab R2016b.

2.5.15 CEST Spectroscopy

All NMR measurements were performed at room temperature (22°C) using a Bruker DSX-500 spectrometer and a Bruker solution NMR probe. About 800 μL of samples were loaded into Norell 5 mm glass NMR tubes and thoroughly shaken using a Vortex Mixer (Fisher Scientific) before transporting into the NMR probe. T_2 measurements were carried out using 40-μs $\pi/2$ and 80 μs π pulses, employing the Carr-Purcell-Meiboom-Gill (CPMG) pulse sequence. The echo delay time was varied from 0.5 ms to 5 ms range. The same pulse lengths were employed for T_1 measurements in the inversion recovery pulse sequence. The Z-spectra (CEST Signal) were acquired using a rectangular pre-saturation pulse with RF power of 0.3 kHz (~ 7 μT) and a duration time of 10 s, followed by a 40- μs $\pi/2$ pulse to initiate a free induction decay (FID) that is recorded. The frequency of the pre-saturation pulse (subsequently offset from the water peak) was varied from + 3 kHz to -3 kHz off the water resonance frequency.

2.5.16 Western Blotting

FLPM6A was purified from the soluble fraction of crude cell lysates for cells grown either with or without 1 mM Fe(II) using Ni-NTA affinity purification (Qiagen). All samples, including the insoluble fractions, were mixed with Laemmli sample buffer (BioRad) and 2-mercaptoethanol (BioRad) and boiled at 56°C for 10 mins before being loaded onto BioRad Mini-TGX 4-20% Precast gels and run at 80V for 65 mins. The gel was then transferred onto nitrocellulose membrane using a Trans Blot Turbo cassette and blocked with 5% Milk in TBS-Tween for 1 hr at room temperature. The blot was subsequently incubated with Mouse anti hexa-histidine-HRP conjugate antibody (1:100, Santa Cruz Biotechnology) at room temperature for 6 hrs before being washed twice with TBS-Tween and subsequently developed for chemiluminescent imaging (BioRad).

2.5.17 Genetic construction of UPMAG

All protein sequences were codon optimized for expression in *E. coli* and the vector map is provided below:

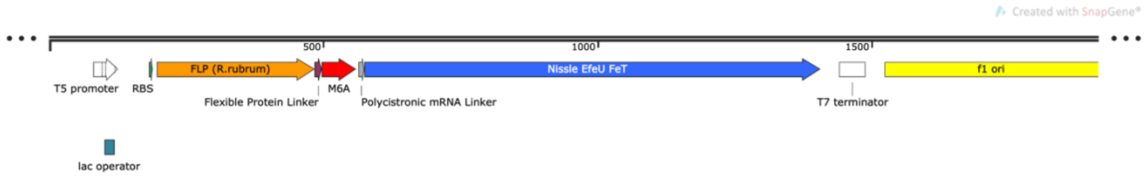

Amino-acid sequence of FLPM6A where the N-terminal truncated FLP from *R. rubrum* is indicated in orange and M6A from *M. magneticum* is indicated in red, separated by a short flexible linker.

MAQSSNSTHEPLEVLKEETVNRHRAIVSVMEELEAVDWYDQRVDASTDPELTAILAHNRDEEKEHAAMTLEWLRRNDAKWAEHLRTYLFTEGPITAGSGGKSRDIESAQSDEEVELRDALA*

Amino-acid sequence of His-FLPM6A with a TEV protease cleavage site in green:

MHHHHHHENLYFQGAQSSNSTHEPLEVLKEETVNRHRAIVSVMEELEAVDWYDQRVDASTDPELTAILAHNRDEEKEHAAMTLEWLRRNDAKWAEHLRTYLFTEGPITAGSGGKSRDIESAQSDEEVELRDALA*

Amino-acid sequence of the ferrous iron transporter EfeU from *E. coli* Nissle 1917:

MFVPFLIILREGLEAALIVSLIASYLKRTQRGRWIGVMWIGVLLAAALCLGLGIFINETTGEFPQKEQELFEGIVAVIAVVILTWMVFWMRKVSRNVKVQLEQAVDSALQRGNHHGWALVMMVFFAVAREGLESVFFLLAAFQQDVGIWPPLGAMLGLATAVVLGFLLYWGGIRLNLGAFFKWTSLFILFVAAGLAAGAIRAFHEAGLWNHFQEIAFDMSAVLSTHSLFGTLMEGIFGYQEAPSVSEVAVWFIYLIPALVAFVLPPRAGATASRSM*

Amino-acid sequence of the fluorescent protein, mRuby2 with a C-terminal histidine tag:

MVSKGEELIKENMRMKVVMEGSVNGHQFKCTGEGEGNPYMGTQTMRIKVIEGGPLPFAFDILATSFMYGSRTFIKYPKGIPDFFKQSFPEGFTWERVTRYEDGGVVTVMQDTSLEDGCLVYHVQVRGVNFPSNGPVMQKKTKGWEPNTEMMYPADGGLRGYT

HMALKVDGGGHLSCSFVTTYRSKKTVGNIKMPGIHAVDHRLERLEESDNEMFVV
QREHAVAKFAGLGGGMDELYKPWLEHHHHHH*

2.5.18 Statistical Analysis

Data were analyzed using GraphPad Prism version 7.0d for Mac. Unpaired parametric t-tests (two-tailed) were used throughout the manuscript. Asterisks indicate p-values below 0.05 (*), 0.002 (**), 0.0002 (***) and 0.0001 (****).

BIBLIOGRAPHY

1. Kolinko, I. *et al.* Biosynthesis of magnetic nanostructures in a foreign organism by transfer of bacterial magnetosome gene clusters. *Nat. Nanotechnol.* **9,** 193–197 (2014).
2. Kim, T., Moore, D. & Fussenegger, M. Genetically programmed superparamagnetic behavior of mammalian cells. *J. Biotechnol.* **162,** 237–45 (2012).
3. Murat, D., Quinlan, A., Vali, H. & Komeili, A. Comprehensive genetic dissection of the magnetosome gene island reveals the step-wise assembly of a prokaryotic organelle. *Proc. Natl. Acad. Sci. U. S. A.* **107,** 5593–8 (2010).
4. Nishida, K. & Silver, P. a. Induction of biogenic magnetization and redox control by a component of the target of rapamycin complex 1 signaling pathway. *PLoS Biol.* **10,** e1001269 (2012).
5. Piraner, D. I. *et al.* Going Deeper: Biomolecular Tools for Acoustic and Magnetic Imaging and Control of Cellular Function. *Biochemistry* **56,** 5202–5209 (2017).
6. Donaldson, G. P., Lee, S. M. & Mazmanian, S. K. Gut biogeography of the bacterial microbiota. *Nat. Rev. Microbiol.* **14,** 20–32 (2015).
7. Baumgartner, J. *et al.* Nucleation and growth of magnetite from solution. *Nat. Mater.* **12,** 310–314 (2013).
8. Rahn-Lee, L. & Komeili, A. The magnetosome model: insights into the mechanisms of bacterial biomineralization. *Front. Microbiol.* **4,** 352 (2013).
9. Matsumoto, Y., Chen, R., Anikeeva, P. & Jasanoff, A. Engineering intracellular biomineralization and biosensing by a magnetic protein. *Nat Commun* **6,** 8721 (2015).
10. Radoul, M. *et al.* Genetic manipulation of iron biomineralization enhances MR relaxivity in a ferritin-M6A chimeric complex. *Sci. Rep.* **6,** 1–9 (2016).
11. Liu, X. *et al.* Engineering Genetically-Encoded Mineralization and Magnetism via Directed Evolution. *Sci. Rep.* **6,** 1–10 (2016).
12. Melville, D., Paul, F., Roath, S. & Cells, R. E. D. B. High Gradient Magnetic Separation of Red Cells from Whole Blood. *IEEE Trans. Magn.* **11,** 1701–1704 (1975).
13. Schenck, J. F. The role of magnetic susceptibility in MRI. *Med. Phys.* **23,** (1996).
14. García-Prieto, A. *et al.* On the mineral core of ferritin-like proteins: structural and magnetic characterization. *Nanoscale* **8,** 1088–1099 (2016).
15. Harris, J. G. E., Grimaldi, J. E., Awschalom, D. D., Chiolero, a. & Loss, D. Excess Spin and the Dynamics of Antiferromagnetic Ferritin. **60,** 4 (1999).
16. He, D. *et al.* Structural characterization of encapsulated ferritin provides insight into iron storage in bacterial nanocompartments. *Elife* **5,** 1–31 (2016).
17. Rawlings, A. E. *et al.* Ferrous Iron Binding Key to Mms6 Magnetite Biomineralisation: A Mechanistic Study to Understand Magnetite Formation Using pH Titration and NMR Spectroscopy. *Chem. - A Eur. J.* **22,** 7885–7894 (2016).

18. Lau, C. K. Y., Krewulak, K. D. & Vogel, H. J. Bacterial ferrous iron transport: The Feo system. *FEMS Microbiol. Rev.* **40,** 273–298 (2016).
19. Tanaka, M., Mazuyama, E., Arakaki, A. & Matsunaga, T. MMS6 protein regulates crystal morphology during nano-sized magnetite biomineralization in vivo. *J. Biol. Chem.* **286,** 6386–6392 (2011).
20. Wang, L. *et al.* Self-Assembly and Biphasic Iron-Binding Characteristics of Mms6, A Bacterial Protein That Promotes the Formation of Superparamagnetic Magnetite Nanoparticles of Uniform Size and Shape. *Biomacromolecules* **13,** 98–105 (2012).
21. Hill, P. J. *et al.* Magnetic Resonance Imaging of Tumors Colonized with Bacterial Ferritin-Expressing Escherichia coli. *PLoS One* **6,** e25409 (2011).
22. Dyar, M. D., Agresti, D. G., Schaefer, M. W., Grant, C. A. & Sklute, E. C. Mössbauer Spectroscopy of Earth and Planetary Materials. *Annu. Rev. Earth Planet. Sci.* **34,** 83–125 (2006).
23. Miltenyi, S., Müller, W., Weichel, W. & Radbruch, A. High gradient magnetic cell separation with MACS. *Cytometry* **11,** 231–8 (1990).
24. Leong, S. S., Yeap, S. P. & Lim, J. Working principle and application of magnetic separation for biomedical diagnostic at high- and low-field gradients. *Interface Focus* **6,** 20160048 (2016).
25. Volkmer, B. & Heinemann, M. Condition-Dependent cell volume and concentration of Escherichia coli to facilitate data conversion for systems biology modeling. *PLoS One* **6,** 1–6 (2011).
26. McHugh, J. P. *et al.* Global Iron-dependent Gene Regulation in Escherichia coli. *J. Biol. Chem.* **278,** 29478–29486 (2003).
27. Seo, S. W. *et al.* Deciphering Fur transcriptional regulatory network highlights its complex role beyond iron metabolism in Escherichia coli. *Nat. Commun.* (2015). doi:10.1038/ncomms5910.Deciphering
28. Andrews, S. C., Robinson, A. K. & Rodri-guez-Quinones, F. Bacterial iron homeostasis. *FEMS Microbiol. Rev.* **27,** 215–237 (2003).
29. Riglar, D. T. *et al.* Engineered bacteria can function in the mammalian gut long-term as live diagnostics of inflammation. *Nat. Biotechnol.* **35,** 653–658 (2017).
30. Junk, M. J. N. Electron Paramagnetic Resonance Theory. *Assess. Funct. Struct. Mol. Transp. by EPR Spectrosc.* 7–52 (2012). doi:10.1007/978-3-642-25135-1_2
31. Yoshida, Y. & Langouche, G. *Mössbauer spectroscopy: Tutorial book. Springer* (2013). doi:10.1007/978-3-642-32220-4
32. Murad, E. & Schwertmann, U. The Mössbauer spectrum of ferrihydrite and its relations to those of other iron oxides. *Am. Mineral.* **65,** 1044–1049 (1980).
33. Jr, E. L. *et al.* Magnetic characterization of ferrihydrite nanoparticles synthesized by hydrolysis of Fe metal-organic precursor. **403,** 4156–4159 (2008).
34. Minaev, B. F., Ågren, H. & Minaeva, V. O. Spin-Orbit Coupling in Enzymatic Reactions and the Role of Spin in Biochemistry. in *Handbook of Computational Chemistry* 1–2381

(2016). doi:10.1007/978-3-319-27282-5

35. Aime, S. *et al.* EPR investigations of the iron domain in neuromelanin. *Biochim. Biophys. Acta - Mol. Basis Dis.* **1361,** 49–58 (1997).

36. Murphy, D. M. EPR Spectroscopy of Polycrystalline Oxide Systems. in *Metal Oxide Catalysis* (2009). doi:10.1002/9783527626113.ch1

37. Airan, R. D. *et al.* MRI biosensor for protein kinase A encoded by a single synthetic gene. *Magn. Reson. Med.* **68,** 1919–1923 (2012).

38. Bar-Shir, A. *et al.* Human protamine-1 as an MRI reporter gene based on chemical exchange. *ACS Chem. Biol.* **9,** 134–8 (2014).

39. McMahon, M. T. *et al.* New 'multicolor' polypeptide Diamagnetic Chemical Exchange Saturation Transfer (DIACEST) contrast agents for MRI. *Magn. Reson. Med.* **60,** 803–812 (2008).

40. Sinharay, S. & Pagel, M. D. Advances in Magnetic Resonance Imaging Contrast Agents for Biomarker Detection. *Annu. Rev. Anal. Chem.* **9,** 95–115 (2016).

41. Persson, E. & Halle, B. Cell water dynamics on multiple time scales. *Proc. Natl. Acad. Sci. U. S. A.* **105,** 6266–71 (2008).

42. Michel, F. M. *et al.* Ordered ferrimagnetic form of ferrihydrite reveals links among structure, composition, and magnetism. *Proc. Natl. Acad. Sci. U. S. A.* **107,** 2787–2792 (2010).

43. Liu, G. *et al.* Noninvasive imaging of infection after treatment with tumor-homing bacteria using Chemical Exchange Saturation Transfer (CEST) MRI. *Magn. Reson. Med.* **70,** 1690–1698 (2013).

44. Gossuin, Y., Roch, A., Muller, R. N., Gillis, P. & Lo Bue, F. Anomalous nuclear magnetic relaxation of aqueous solutions of ferritin: An unprecedented first-order mechanism. *Magn. Reson. Med.* **48,** 959–964 (2002).

45. Michel, F. M. *et al.* The Structure of Ferrihydrite, a Nanocrystalline Material. *Science.* **316,** 1726–1729 (2007).

46. Bloch, F. Nuclear Induction. *Phys. Rev. Lett.* **70,** 127–127 (1946).

47. Vuong, Q. L. *et al.* Paramagnetic nanoparticles as potential MRI contrast agents: Characterization, NMR relaxation, simulations and theory. *Magn. Reson. Mater. Physics, Biol. Med.* **25,** 467–478 (2012).

48. Zwietering, M. H., Jongenburger, I., Rombouts, F. M. & Van't Riet, K. Modeling of the bacterial growth curve. *Appl. Environ. Microbiol.* **56,** 1875–1881 (1990).

49. Greenfield, N. J. Using circular dichroism spectra to estimate protein secondary structure. *Nat. Protoc.* **1,** 2876–2890 (2007).

50. Cheesman, M. R. *et al.* E.p.r. and magnetic circular dichroism spectroscopic characterization of bacterioferritin from Pseudomonas aeruginosa and Azotobacter vinelandii. *Biochem. J.* **286,** 361–367 (1992).

51. Ngo, P. D. Energy Dispersive Spectroscopy. in *Wagner L.C. (eds) Failure Analysis of Integrated Circuits* 205–215 (Springer, Boston, MA, 1999).

52. Riglar, D. T. & Silver, P. A. Engineering bacteria for diagnostic and therapeutic applications. *Nat. Rev. Microbiol.* **16,** 214–225 (2018).
53. Wang, Q., Mercogliano, C. P. & Löwe, J. A ferritin-based label for cellular electron cryotomography. *Structure* **19,** 147–154 (2011).
54. Fdez-Gubieda, M. L. *et al.* Magnetite Biomineralization in Magnetospirillum gryphiswaldense: Time-Resolved Magnetic and Structural Studies). *ACS Nano* **7,** 3297–3305 (2013).
55. Seo, S. W. *et al.* Deciphering Fur transcriptional regulatory network highlights its complex role beyond iron metabolism in Escherichia coli. *Nat. Commun.* **5,** 4910 (2014).
56. Riemer, J., Hoepken, H. H., Czerwinska, H., Robinson, S. R. & Dringen, R. Colorimetric ferrozine-based assay for the quantitation of iron in cultured cells. *Anal. Biochem.* **331,** 370–5 (2004).
57. Geuzaine, C. & Remacle, J.-F. Gmsh: a three-dimensional finite element mesh generator with built-in pre-and post-processing facilities. *Int. J. Numer. Methods Eng.* **79,** 1309–1331 (2009).
58. Mukherjee, A., Wu, D., Davis, H. C. & Shapiro, M. G. Non-invasive imaging using reporter genes altering cellular water permeability. *Nat. Commun.* **7,** 1–9 (2016).
59. Davis, H. C. *et al.* Mapping the microscale origins of magnetic resonance image contrast with subcellular diamond magnetometry. *Nat. Commun.* **9,** 1–9 (2018).
60. Kubitschek, H. E. & Friske, J. A. Determination of Bacterial Cell Volume with the Coulter Counter. *J. Bacteriol.* **168,** 1466–1467 (1986).
61. Stoll, S. & Schweiger, A. EasySpin, a comprehensive software package for spectral simulation and analysis in EPR. *J. Magn. Reson.* **178,** 42–55 (2006).

C h a p t e r 3

CELLULAR LOCALIZATION USING MAGNETIC FIELDS

Ramesh, P.† Buss, M.† et. al. "Remote Control of Cellular Localization in the G.I. Tract Assisted by Magnetic Particles." *In preparation.*

† Equal contribution

P.R. and M.G.S conceived the study. P.R. and M.B. designed the experiments, as well as collected and analyzed the resulting data. P.R developed the *in silico* model of magnetic capture. P.R., M.B., and M.G.S prepared the manuscript.

3.1 Motivation

Remote control of cellular localization in deep tissue has been a long-standing goal of synthetic biology, with the aim of directing therapeutic cells to specific sites of interest noninvasively, in a deterministic manner. While light-actuated proteins have enabled robust, optogenetic control of cellular function in living cells, the poor penetrance of light through optically scattering tissue, limits the utility of such techniques largely to *in vitro* and *ex vivo* studies.[1,2] On the other hand, since magnetic fields can easily penetrate deep tissue, there has been considerable interest in leveraging this fundamental property of magnetic fields for non-invasive control of cell motility. To date, magnetic fields have been successfully used to localize therapeutic cells to tumors, in order to enhance existing anti-cancer therapies[3–5], as well as enhance site-specific cellular uptake of therapeutics, such as viral vectors or drug containing liposomes, in order to improve cellular transduction *in vivo*.[6,7]

While extremely promising, remote control of cellular localization using magnetic fields is fundamentally limited by the rapid attenuation of magnetic fields and field gradients from their source. The force on a magnetized (i.e. paramagnetic or superparamagnetic) particle or cell (Eq. 3.1) is a product of the magnetic field and magnetic field gradients acting on the subject[8], which decay as $1/r^3$ and $1/r^4$ respectively.

$$\mathbf{F}_{\mathbf{mag}} = \frac{V\Delta\chi}{\mu_0}(\mathbf{B}\cdot\nabla)\mathbf{B} \tag{3.1}$$

Here, $\Delta\chi$ represents the difference in magnetic susceptibility between the magnetic cell and its surrounding medium. Since the magnetic force decays as $\frac{1}{r^7}$, previous efforts to maximize the localization and capture of magnetized cells *in vivo* have largely focused on increasing $\Delta\chi$ and $\nabla\mathbf{B}$ through the use of strong magnetic labels, and minimizing the distance between the external magnet and the desired target.[4–6,9] While these methods are successful in enhancing targeting to tissues that are near the surface ($d < 1$ mm), they are insufficient for controlling the localization of engineered cells in deep tissue such as the gastrointestinal (GI) tract, which spans approximately 3 – 13 mm from the abdominal surface in mice.[10] New strategies to remotely target either therapeutic microbes or drug-carrying vehicles in the GI tract using magnetic fields would be invaluable for advancing therapy and basic studies, given the broad role of the GI microbiota in regulating animal physiology.[11–14]

To date, the most successful methods for achieving site-specific cellular localization in the GI tract employ endogenous microbes that have a fitness advantage relative to others at a particular GI locale.[15] Given that the GI tract spans a range of pH, osmolarity, mucosal thickness, and microbial densities, there exist species-specific niches that confer ecological advantages to their cognate microbes over others.[16] That said, we are critically limited by the number of endogenous microbial species that are amenable to genome engineering – which in turn diminishes our ability to engineer and deploy therapeutic probiotics across a broader region within the GI tract.

To overcome these challenges, we developed a simple approach by which the retention of therapeutic microbes or drug-vehicles can be enhanced within the small intestines, where the majority of absorption takes place[17], using an external magnetic field. Inspired by the design of magnetic separation columns[18], our cellular localization assisted by magnetic particles (CLAMP) approach provides a facile, non-genetic approach that is broadly generalizable. We observed that commercially obtained magnetic separation columns and microfluidic magnetic sorting chips overcome the challenge of rapid field attenuation from the source through the use of a ferromagnetic matrix that consists of a tightly packed slurry of ferromagnetic beads, with an average interparticle spacing of approximately $30\ \mu\mathrm{m}$. The permanent magnet in these systems saturates the magnetization of its matrix (ferromagnetic beads) using relatively low fields ($B_{MACS} \approx 0.45$ T), which in turn produces strong local fields and field gradients of up to $10^4\ \mathrm{T/m}$ within the matrix mesh.[18] By locally amplifying the field and field gradients through a factor of 10^4, magnetic separation columns can effectively capture sparsely labeled and even paramagnetic cells.[19–22]

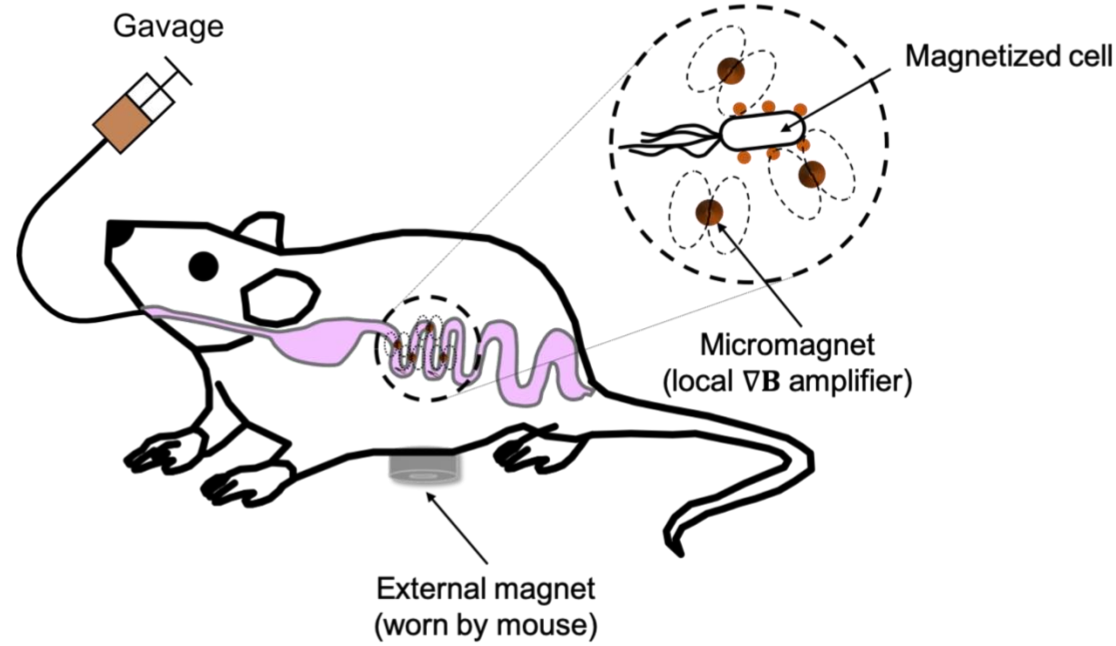

Fig. 3.1 Concept of Cellular Localization Assisted by Magnetic Particles (CLAMP). | Mice are gavaged a slurry consisting of magnetized cells, as well as small micromagnetic beads. An external magnet captures the micromagnets deep in the GI tract, which concomitantly produce strong local field gradients that subsequently assist in the capture of magnetized cells.

Given the success of this 'local amplifier' strategy *in vitro*, we hypothesized that this magnetic slurry approach could be extended towards the capture of magnetically labeled cells at distances where the field and field gradients are too weak to facilitate appreciable capture. If successful, the distal capture and enhanced retention of magnetized cells using CLAMP will enable new synthetic biology applications in the study of the gut microbiome (Fig. 3.1).

3.2 Results

3.2.1 Design of an *in vitro* model of the mouse GI tract

To test the hypothesis that magnetized cells can be effectively CLAMPed at distal positions, we first constructed an *in vitro* model of the murine GI tract. Histological studies on whole GI tracts isolated from mice found that the average length and diameter of the murine GI tract was $56 \pm 1.8\ \mathrm{cm}$ and $3.2 \pm 0.76\ \mathrm{mm}$ respectively.[23] Meanwhile, peristaltic rates in the mouse GI tract were found to be approximately $30\ \mu\mathrm{l/min}$.[7,24] Furthermore, the entirety of the mouse GI tract lies within 13 mm of the abdominal surface according to previous photoacoustic studies, as well as our X-ray CT imaging studies.[10]

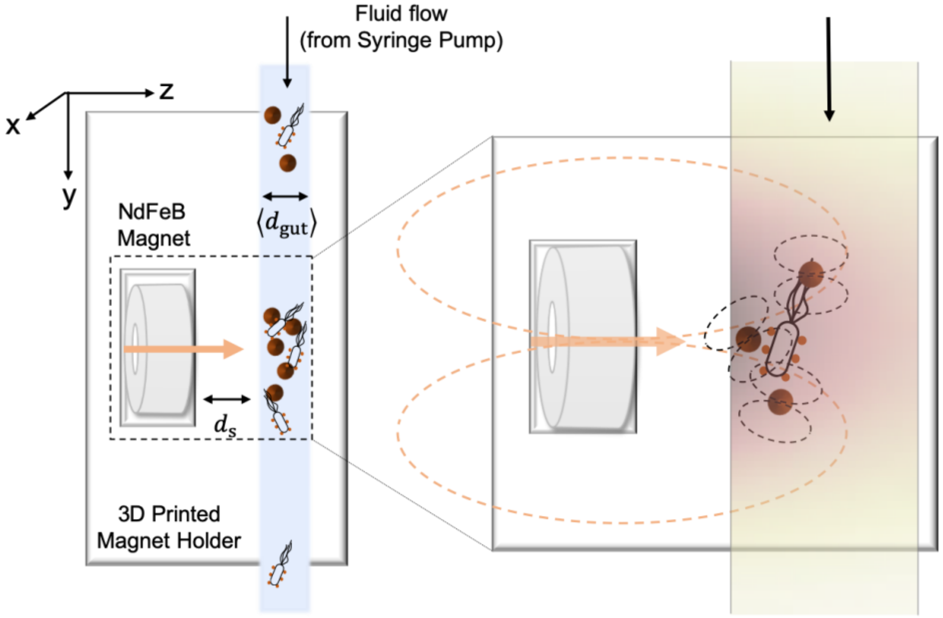

Fig. 3.2 *In vitro* model of the mouse GI tract. | Magnetized cells express mScarlet to facilitate downstream counting using flow cytometry, and the color variation within the tube in the right inset represents the simulated magnetic field strength at a distance of z = 10 - 13 mm from the magnet surface. The orange arrow indicates the direction of magnetization for the permanent magnet, while the dotted orange ellipses denote the magnetic field lines produced by the external magnet, as well as by the micromagnets within the tube. The coordinate frame is oriented such that gravity acts in the +y direction and the center of the magnet is at ($y = 40, z = 0$).

Accordingly, to simulate the transport and enhanced retention of magnetized cells in the mouse GI tract using CLAMP, we first connected a non-stick tubing whose inner-diameter matches the average diameter of a mouse GI tract to a syringe pump set to a volumetric flow rate (Q) of $100\ \mu\text{l/min}$. We specifically chose a fast flow-rate, compared with average peristaltic rates, in order to conservatively assess the feasibility and efficacy of CLAMP. Next, a syringe containing a solution of micromagnets, SPION-labeled 0.5 μm Nile-red beads (magnetized synthetic cells), and 0.5 μm Yellow-green non-magnetic control beads, was connected to the tubing. Here, the micromagnets (1.5 μm BioMag-NH_2 and 1 μm Silica-OH) act as the local magnetic field and field gradient amplifiers. Meanwhile, the magnetic and non-magnetic 0.5 μm synthetic cells are flowed concurrently in order to assess the effects of sharp local field-gradients, as well as surface charges, on the efficacy of CLAMP. Additionally, a 3D-printed holder was used to stably maintain the external magnet at a predetermined radial distance from the tubing for the duration of the experiment, which consisted of an injection step, followed by an extensive washing step. Finally, the complete setup was vertically oriented to prevent settling of micromagnets during experiments (Fig. 3.2).

3.2.2 Numerical simulations of micromagnet capture in the *in vitro* setup

Since CLAMP fundamentally requires effective capture and retention of micromagnets at arbitrary offset distances from the external magnet, we numerically simulated the relevant magnetic fields and forces acting on the micromagnets within our *in vitro* setup to assess concept feasibility. First, the magnetic field produced by the permanent magnet was simulated using FEMM. Briefly, Maxwell's equations were numerically solved using a $25\ \mu\text{m}$ mesh in the positive r-z half-plane, using values for coercivity and magnetization provided by the manufacturer. Since the magnet in our experiments is axially symmetric, we used the principle of superposition to obtain the magnetic field over the full r-z space (Fig. 3.3). Due to axial symmetry, $\mathbf{B}$ is nonzero only for its axial (z) and radial (r) components. For simplicity, we constrained the problem to the 2D y-z plane, corresponding to $\mathbf{B}_r\left(\phi = \frac{\pi}{2}\right) = \mathbf{B}_y$.

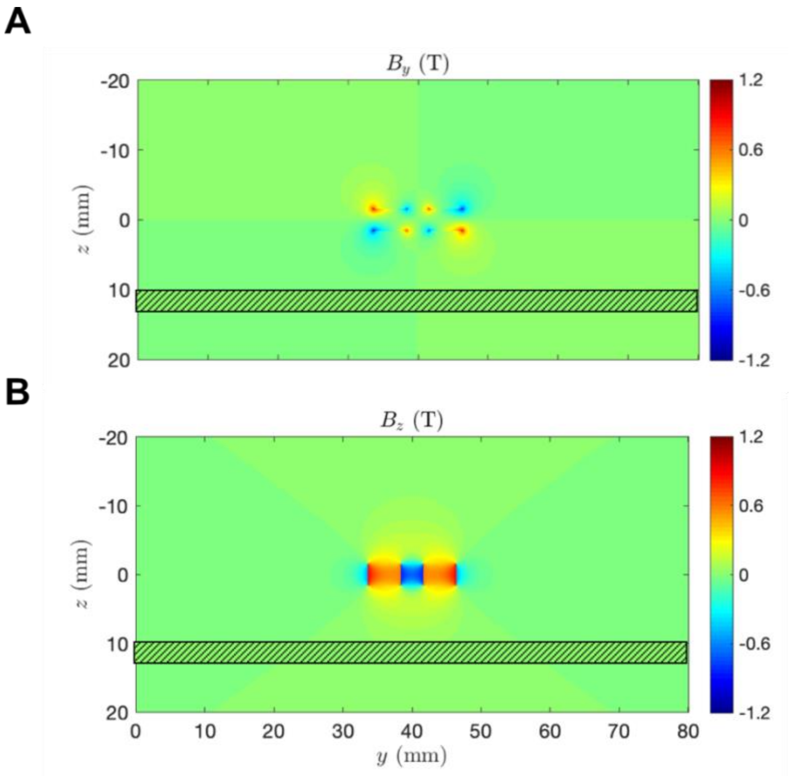

Fig. 3.3 Simulated 2D field of the external magnet used for CLAMP | A. Radial component of the magnetic field in the *y*-*z* plane. **B**. Axial component of the magnetic field in *y*-*z* plane. The hashed rectangle indicates the position of the tube used in the *in vitro* experiments (10 – 13 mm from the magnet surface).

Given that the majority of the murine GI tract lies within 10 – 13 mm from the abdominal surface, we chose to evaluate the efficacy of CLAMP at this separation distance; if magnetized cells could be captured at this distance, then this automatically implies capture at distances closer to the magnet surface (*z* < 10 mm). To gain insight into the fields and field gradients at this large offset, we conducted a 'high-resolution' (5 μm) simulation of the field within the tube used in the *in vitro* experiments (Fig. 3.4). These simulations revealed that the magnetic fields and field gradients within the tube are relatively weak, and their magnitudes do not exceed 60 mT or 16 T/m respectively. As such, these field strengths are not optimal for the capture of sparsely labeled or weakly magnetized cells.

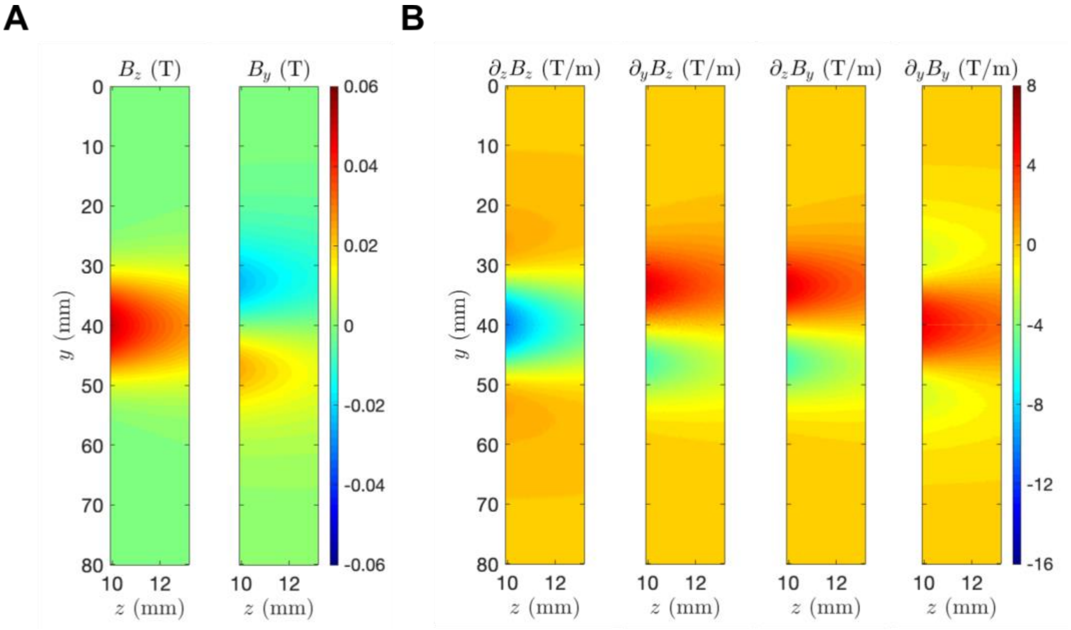

Fig. 3.4 Simulated 2D field and field gradients in the *in vitro* setup | A. B_z (left) and B_y (right). **B.** From left to right $\frac{\partial B_z}{\partial z}, \frac{\partial B_z}{\partial y}, \frac{\partial B_y}{\partial z}, \frac{\partial B_y}{\partial y}$. The magnet is centered at (*y = 40*, *z = 0*).

To understand whether these bias fields are sufficient to magnetize the local amplifiers, we used the mass magnetization curves for the micromagnetic beads to numerically calculate their magnetic field profiles within the tube (Fig. 3.5). By fitting the classical Langevin function (Eq. 3.2) to the manufacturer supplied SQUID magnetization curve, we were able to estimate the particle's magnetic moment (Eq. 3.3) at any arbitrary magnetic field.

$$\mathbf{M}(B) = M_{sat}\left[\coth(\alpha \cdot B) - \frac{1}{\alpha \cdot B}\right] \tag{3.2}$$

$$\mathbf{m}(B) = \frac{4}{3}\pi r_{bead}^{3}\mathbf{M}(B) \tag{3.3}$$

We were then able to simulate the field and field gradients produced by these micromagnets in the *y-z* plane using well-known dipole field equations. We specifically focused on the 1.5 μm BioMag micromagnets since these are >90% magnetite by volume, and consequently expected to produce the strongest local field and field gradients.

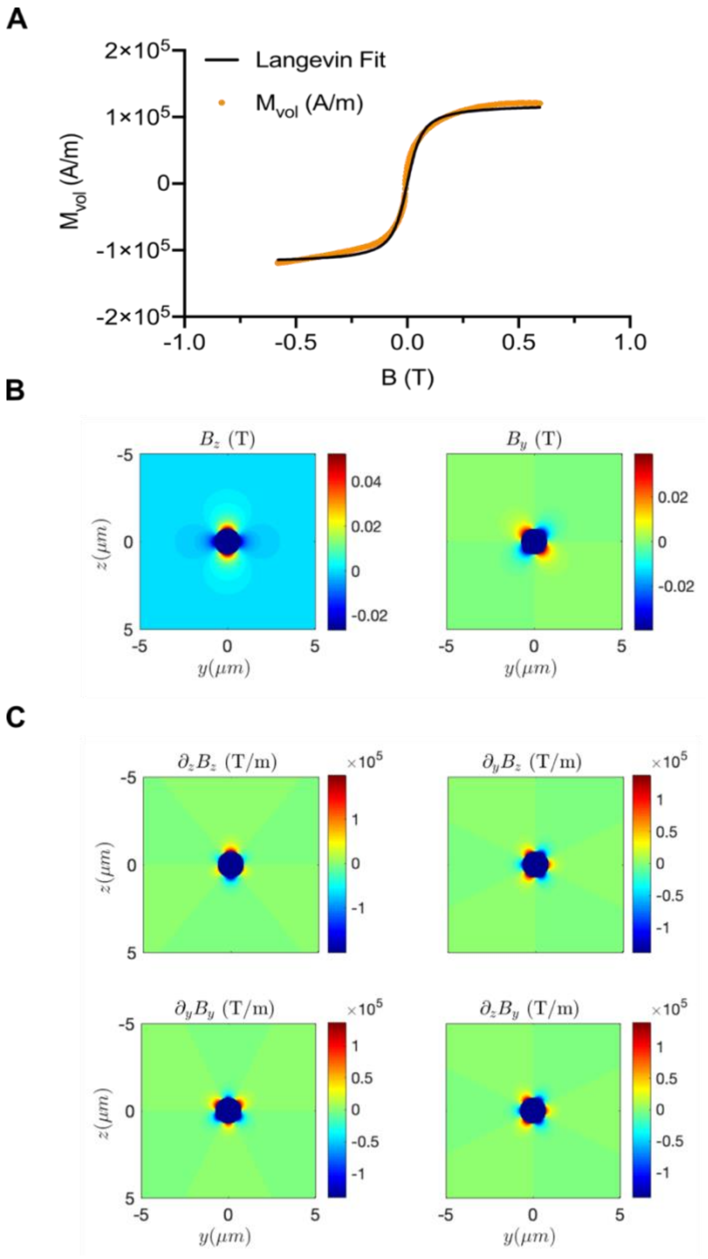

Fig. 3.5 Magnetic properties of the micromagnets used for CLAMP | A. Room temperature SQUID magnetization curve of the micromagnets used in our experiments, as well as a fit to the data using the Langevin function (Chapter 1). **B.** Magnetic fields (B_z, B_y) produced by the micromagnets in the *y*-*z* plane, when magnetized by a 50 mT external field. **C.** Field gradients produced by the micromagnets: top row $\frac{\partial B_z}{\partial z}, \frac{\partial B_z}{\partial y}$, and bottom row $\frac{\partial B_y}{\partial z}, \frac{\partial B_y}{\partial y}$ respectively.

While the local fields produced by the $1.5\ \mu\text{m}$ BioMag micromagnets are comparable to the fields produced by the external magnet within the tube, the field gradients are up to 10^4 fold stronger within $5\ \mu\text{m}$ of the micromagnet surface. This suggests that the field gradients produced by these micromagnets are sufficient for capturing magnetized cells within the tube.

To conclude our *in-silico* studies on the feasibility of CLAMP, we investigated whether the external magnet was capable of capturing the $1.5\ \mu\text{m}$ BioMag micromagnets at a 10 mm offset distance. Accordingly, we conducted a Monte Carlo simulation wherein the $1.5\ \mu\text{m}$ BioMag beads were flown into the channel at the same volumetric flow-rate used in our *in vitro* experiments (Fig. 3.6). In addition, given that the dynamic viscosities of GI mucus[25] deviate significantly from that of water, we explored the effect of increasing viscosity on magnetic capture in our simulations. Micromagnet centroids were randomly initialized at the entrance of the tube ($y = 0$), and their corresponding trajectories were calculated from the combined action of magnetic forces, hydrodynamic drag forces, and Brownian motion. Particle-particle interactions were neglected for simplicity, as well as lift forces and inertial forces. Particles achieve equilibrium rapidly in the conditions we simulated, and consequently a steady state ($m\frac{d}{dt}\dot{\mathbf{r}} = 0$) treatment is appropriate and sufficient for calculating particle trajectories. We also included a 'washing' step in the simulation by maintaining a simulated flow for 30 mins and discarding any particles that were no longer within the influence of the external magnet ($30\ \text{mm} \le y \le 50\ \text{mm}$).

Retention was defined as particles whose centroids were within 100 μm of the inner surface (z = 10 mm), to mimic retention within the mucosal layer in the mouse GI tract (whose average thickness is 0.1 mm). Additionally, we observed that the $1.5\ \mu\text{m}$ BioMag-NH_2 beads are prone to aggregation *in vitro*, even in the absence of a magnetic field. Since aggregates experience significantly different drag forces, we also investigated the effect of aggregate size of retention. Future Dynamic Light Scattering studies will yield greater insight into the size distribution of these aggregates.

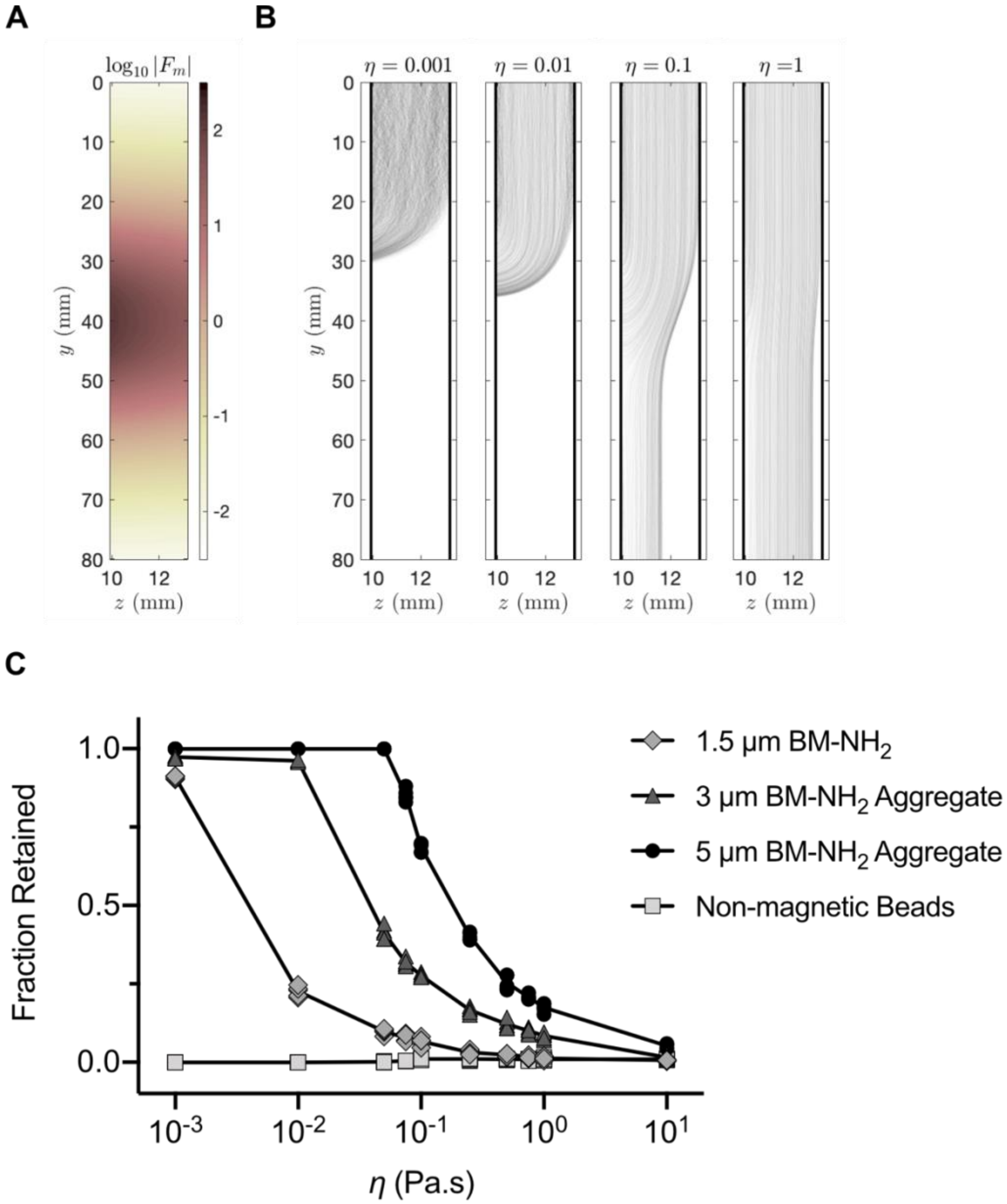

Fig. 3.6 Monte Carlo simulations of micromagnet capture *in vitro*. | A. Magnetic force acting on the 1.5 µm BM (BioMag)-NH$_2$ micromagnets within the tube. For clarity, the log$_{10}$ of the magnetic force (in pN) is plotted. **B.** Simulated 2D trajectories of N = 1000 5 µm micromagnet aggregates in the tube at viscosities ranging from 10^{-3} Pa·s to 10^{1} Pa·s. The walls of the tube are demarcated using black lines for clarity. **C.** Fraction of magnetic and non-magnetic beads retained at the end of the simulation run as a function of solution viscosity and aggregate size (N = 5). Retention rates are considerably enhanced for 5 µm aggregates of 1.5 µm BM-NH$_2$ beads compared with a colloidal solution of the 1.5 µm micromagnets alone.

Even at a distance of 10 mm from the magnet surface, the magnetic forces acting on the 1.5 μm magnetic beads are substantial (Fig. 3.6A) along the axis of the external magnet ($y = 40$ mm, $z = 10$ mm). Given these strong magnetic forces, all of the BM-NH$_2$ 1.5 μm micromagnets were captured in our simulation (Fig. 3.6B, C), when the viscosity of the solution matched that of water (10^{-3} Pa s). However, unaggregated beads could not be captured when solution viscosities exceeded $\eta = 10^{-2}\ \mathrm{Pa \cdot s}$ (Fig. 3.6C).

At high viscosities ($\eta \geq 10^{-1}\ \mathrm{Pa \cdot s}$), the 5 μm aggregates were not captured, but instead experienced reduced mobilities. This enhanced *retention* of the aggregates is due to the fact that the magnetic force scales as $\sim r^3$, whereas the Stokes drag force scales as $\sim r$. As such, approximately 18% of the 5 μm aggregates could still be retained within the tube after 30 mins of flow, even at solution viscosities of $\eta = 1\ \mathrm{Pa \cdot s}$, which are comparable to those found *in vivo*. Taken together, these first-order simulations suggest that aggregation of the small 1.5 μm BM-NH$_2$ is critical for achieving enhanced retention at high viscosities. This suggests that the surface charge of the micromagnet and its corresponding tendency to aggregate is an additionally important parameter to be optimized for enhancing the efficacy of CLAMP.

3.2.3 Small micromagnets enable CLAMP *in vitro*

Having ascertained that 1.5 μm BioMag micromagnets can be retained *in silico* and that its aggregation propensity is important, we proceeded to test the efficacy of CLAMP using our *in vitro* setup. Initially, we used 150 nm SPION-labeled 0.5 μm Nile-red polystyrene particles as our synthetic ‘ magnetized cells’ , since these are approximately the same size as *E. coli,*[26] and more generalizable for pharmaceutical drug delivery. 0.5 μm Yellow-green carboxyl beads were used as the synthetic ‘non-magnetic cells’ , which were flowed concurrently to test the specificity of CLAMP mediated retention. To evaluate the maximum achievable retention of these synthetic ‘magnetized cells’ using CLAMP, we tested a standoff distance of 10 – 13 mm from the magnet surface, since these distances constitute the maximum possible depth of the GI tract *in vivo*. Lastly, we also tested micromagnets of different surface-charge and aggregation propensity, in order to deduce the optimal composition of the micromagnetic slurry distances (Fig. 3.7).

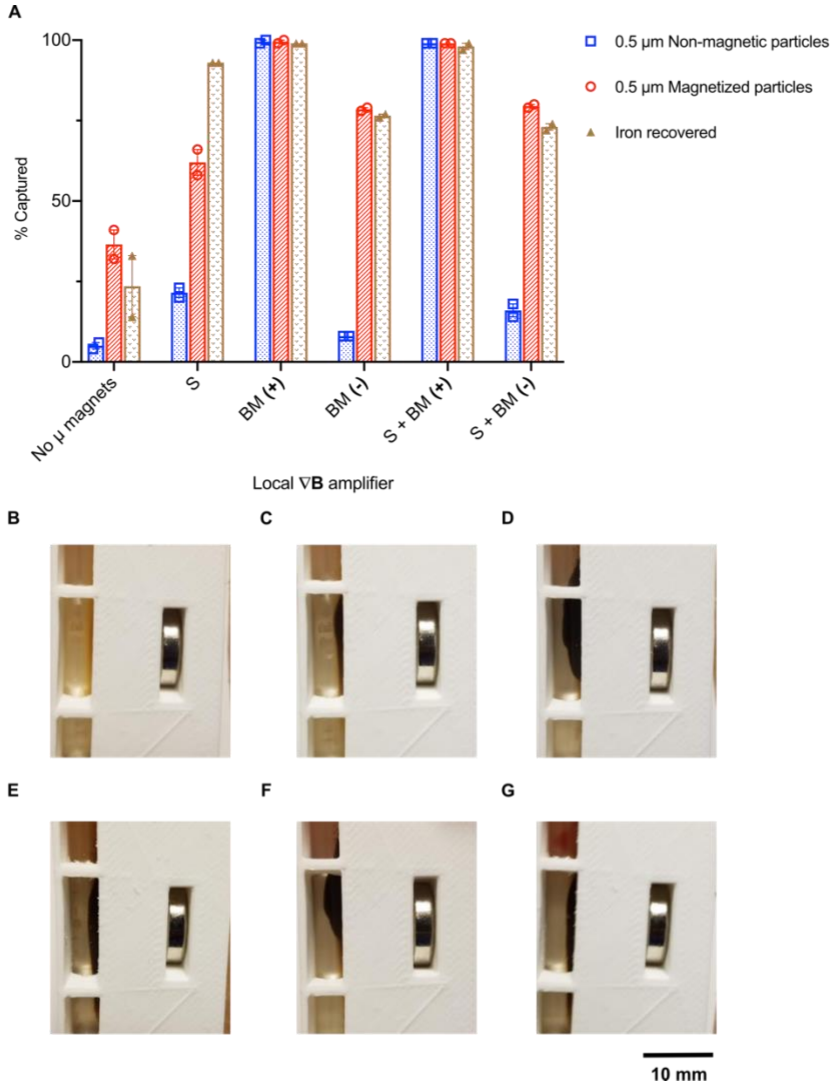

Fig. 3.7 *In vitro* efficacy of CLAMP. | A. Capture of magnetized and non-magnetized particles assisted by micromagnets *in vitro* at 10 mm, plotted as a percentage of the input quantity (*N*= *2*). The particles in these experiments are the magnetized Nile-red and non-magnetic Yellow-green beads. S refers to 1 μm Silica-OH magnetic particles, whereas BM (+) indicates the positively charged 1.5 μm BioMag-NH_2 micromagnets and BM (-) denotes the negatively charged 1.5 μm BioMag-COOH beads respectively. Photographs of the tube upon extensive washing at various local field-amplifier combinations **B.** 0.5 μm magnetic and non-magnetic particles (No μ-magnets) or in combination with **C.** 1 μm Silica-OH micromagnets, **D.** 1.5 μm BioMag-NH_2 micromagnets, **E.** 1.5 μm BioMag-COOH micromagnets, **F.** both 1 μm Silica-OH and 1.5 μm BioMag-NH_2 micromagnets, or **G.** both 1 μm Silica-OH and 1.5 μm BioMag-COOH micromagnets. The solution retained in the tube upon washing was subsequently analyzed for its iron content using the ferrozine assay.

When magnetized particles were flown into the channel without any accompanying micromagnets, we found that approximately 37% could be captured compared with 7% of non-particles of equivalent size. However, when the magnetized particles were co-administered with either 1.5 μm BM-NH_2 magnetic beads, or a combination of both 1.5 μm BM-NH_2 magnetic beads and 1 μm Silica magnetic beads, we observed almost complete capture of the test particles (Fig. 3.7). Unexpectedly, we also observed equivalent capture of non-magnetic particles using the positively-charged micromagnets, whereas this non-specific effect was effectively eliminated using the negatively charged micromagnets.

The photographs (Fig. 3.7 D-F) show appreciable micromagnet aggregation when positively charged micromagnets are used, which is beneficial for capture of both magnetic and non-magnetic particles. These positively charged micromagnets accorded approximately 3-fold improvement in magnetized particle capture, compared with no micromagnet controls. Furthermore, although we did not observe any significant differences in capture between the 1.5 μm BM-NH_2 beads alone, and the combination of 1.5 μm BM-NH_2 beads and 1 μm Silica-OH beads *in vitro*, we hypothesized that a combinatorial micromagnetic slurry likely enhances cellular capture *in vivo* by creating multiple field gradients.

Having observed enhanced retention of synthetic cells in the presence of micromagnets, we tested the capture efficacy of SPION-labeled *E. coli.* Analogous to our experiments using synthetic 'cells,' we observed that the surface charge of the 1.5 μm BioMag micromagnet had a significant impact on specificity, as well as magnetic capture. While the negatively charged 1.5 μm BioMag beads conferred a ~ 3-fold improvement in magnetized *E. coli* retention over no micromagnet controls, their overall capture rates (~ 40%) were significantly less than the aggregation prone and positively charged 1.5 μm BioMag beads (~ 95% captured). These positively charged beads however did not discriminate between magnetized and non-magnetized cells *in vitro*.

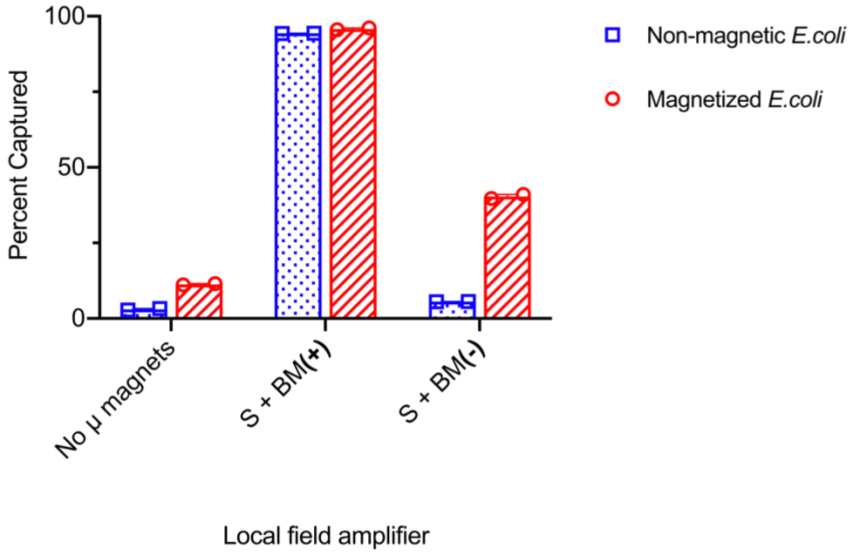

Fig. 3.8 *in vitro* capture of magnetized *E. coli* using CLAMP. | (*N = 2*) S refers to 1 µm Silica-NH_2 magnetic particles, whereas BM (+) indicates the positively charged 1.5 µm BioMag-NH_2 micromagnets and BM (-) denotes the negatively charged 1.5 µm BioMag-COOH beads. The addition of negatively charged 1.5 µm BioMag-COOH to the solution conferred an approximately 3 fold increase in magnetic capture, whereas the addition of positively charged 1.5 µm BioMag-NH_2 beads enabled complete capture of magnetized *E. coli*. Non-magnetic *E. coli* were equivalently captured using these aggregation prone micromagnets.

Taken together, we concluded that the positively-charged 1.5 µm micromagnets in combination with the 1 µm Silica-NH_2 magnetic beads, constitute the most optimal micromagnetic slurry for cellular capture *in vivo*.

3.2.4 Development of an animal protocol to optimize micromagnet capture *in vivo* and detection *ex vivo*.

Having confirmed the efficacy of CLAMP *in vitro* for enhancing cell capture, we proceeded to test its efficacy *in vivo* using a specially developed animal protocol. To overcome the confounding effects of coprophagy which might obfuscate the true kinetics of particle transport, all mice were singly housed in wire-floor cages after gavage.[27] Secondly, to minimize dissolution of the magnetic slurry in the stomach, 10% (w/v) sodium bicarbonate was introduced into the gavage mixture in order to transiently neutralize stomach pH.[28] Finally, to clear the GI tract of feces which might otherwise interfere with optical detection of the micromagnetic slurry *ex vivo* as well as capture *in vivo*, all mice were fasted for 18 hours with access to water prior to oral gavage. 75 minutes after gavage with the test mixture, magnets or non-magnetic washers of equivalent weight (2.8 g) were glued onto mice using tissue glue, and additionally secured using adhesive tape. 75 minutes was chosen to facilitate gastric transit and avoid trapping the micromagnetic slurry in the stomach, consistent with previous studies on gastric transit of magnetic pills.[7,24,29,30] Once the magnets or washers were secured onto animals, mice were kept on a 5% sucrose diet for the remainder of the experiment. A sucrose-only diet was maintained to avoid bead aggregation effects caused by fibers which are common components of solid rodent diets, and could potentially accelerate particle transit out of the GI tract.[31]

To test the impact of these animal protocol modifications on particle integrity, as well as fluorophore brightness, we used 6 μm Dragon-green COMPEL polystyrene beads as tracer particles. Accordingly, mice were first fasted for 18 hours and subsequently gavaged with either PBS, 6 μm Dragon-green beads in PBS, or 6 μm Dragon-green beads in PBS containing both BSA and sodium bicarbonate. Additionally, mice were kept on a sucrose-only diet or normal rodent chow, 75 mins after gavage. Mice were then euthanized at 4 hours post gavage and their GI tracts were dissected and imaged (Fig. 3.9).

The fluorescence images confirmed that the addition of BSA and sodium bicarbonate to the gavage mixture ensured particle integrity during gastric transit. Meanwhile, keeping mice on a 5% sucrose only diet kept the intestines free of feces, thus facilitating sensitive optical detection of tracer particles. Lastly, the wire-floor cages were successful in minimizing coprophagy. Armed with an improved animal protocol, we proceeded to test the efficacy of CLAMP *in vivo*.

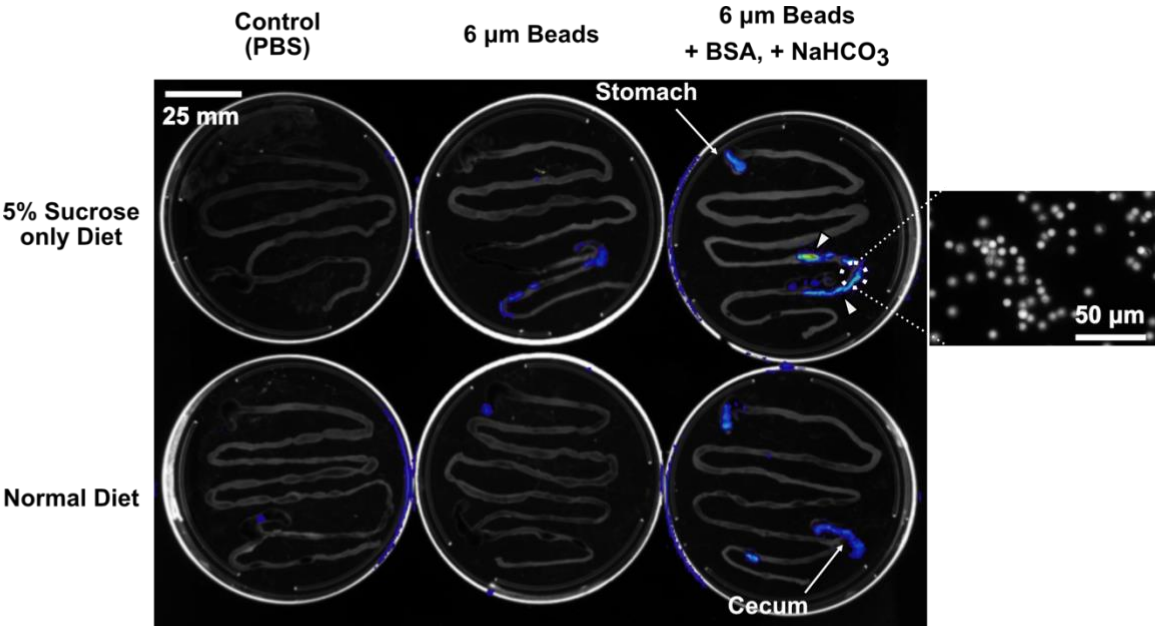

Fig. 3.9 Optimization of the animal protocol for CLAMP| (*N* = 6). These are false color fluorescence images overlaid on a brightfield image. Hotter (red) colors indicate greater intensity. Tracer 6 µm Dragon-green fluorescent polystyrene beads were gavaged into mice to understand the kinetics of particle transit through the GI tract, as well as the stability of fluorophores upon gastric transit. All other parameters held constant, the brightest signals (indicated with arrows) were observed in the 5% sucrose only diet, with the combined addition of BSA and sodium bicarbonate. The inset shows a fluorescence image of the tracer particles in the *ex vivo* specimen.

3.2.5 Small micromagnets promote enhanced retention of cells *in vivo*

To confirm that the mouse GI tract was within 10-13 mm of the abdominal surface, we first gavaged one mouse with 200 µl of Isovue-370, an Iodine-based X-ray contrast agent, in order to non-invasively visualize the entirety of its GI tract (Fig. 3.10A-B). Concordant with previous photoacoustic studies, the entirety of the mouse GI tract could be found within 10 - 13 mm of the abdominal surface, and the intestinal network spanned a lateral area of approximately $22\ \mathrm{mm} \times 20\ \mathrm{mm}$ – which was adequately covered by our cylindrical magnet (diameter ~ 12 mm).[10]

Following our modified animal protocol, mice were subsequently gavaged with a mixture of the optimized micromagnetic slurry and magnetized particles. Magnets or non-magnetic washers of equivalent weight were attached onto the abdomen of animals 75 mins after gavage. At 6- and 9-hours post-gavage, their respective GI tracts (*N = 4*) were dissected and imaged using optical microscopy.

Representative images are shown in Fig. 3.10. Interestingly, we observed a punctate distribution of micromagnets in mice that wore magnets (Fig. 3.10D), suggesting accumulation near field gradient hot-spots. That said, the spatial distribution of micromagnets were significantly different at 9 hours in mice that wore magnets, relative to control mice that only had non-magnetic washers. In mice that wore magnets and were euthanized 9 hours after gavage, we observed that the majority of beads were adjacent to the walls of the intestine. The preponderance of optical density was found in the cecum and large-intestines of control mice at 9 hours post-gavage, whereas optical density was primarily found to be in small-intestines for mice that had magnets (Fig. 3.10E).

The presence of magnetized particles in the intestines were confirmed by fluorescence imaging of the optically dense puncta that were squeezed out from the intestines. Furthermore, since micromagnets are expected to produce strong T_2 MRI contrast, we subsequently embedded the intestines (9h samples) from this experiment in 1% Agarose and acquired anatomical (T_1) and spin-echo (T_2) weighted 3D images (Supporting Data Fig. 3.14). As expected, micromagnets in the intestine taken from the mouse that had a magnet produced strong T_2^* blooming artefacts, which were not observed in the controls.

The presence of micromagnets in the puncta (Fig. 3.10E) were additionally confirmed by recording movies (Fig. 3.11) of aggregate displacement, when a magnet was brought in close proximity to the *ex vivo* specimen. Beads rapidly moved through the mucosal network towards the magnet and returned to their equilibrium positions when the magnet was removed. Additionally, bulk movement of intestinal segment towards the magnet was also observed during instances where intestinal segments had large areas of optical density.

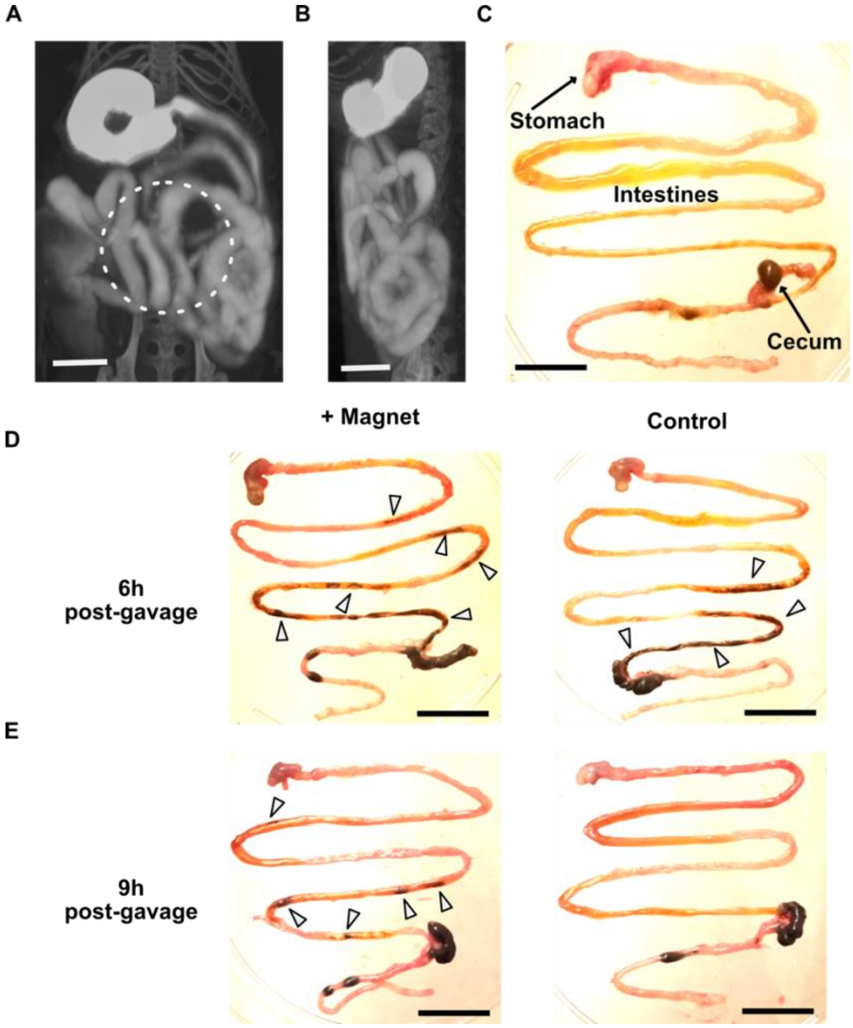

Fig. 3.10 Representative *in vivo* CLAMP results. | A and **B**. Representative X-ray CT images of the mouse GI tract upon administration of a CT contrast agent. Scale bar is 5 mm and the hashed circle indicates the approximate loci of the external magnet. **C**. Representative *ex vivo* image of a mouse GI tract after the mouse was gavaged with saline and euthanized. Positions of the relevant regions are indicated. Scale bar is 25 mm. **D**. Representative *ex vivo* images of mouse GI tracts after mice were gavaged with micromagnets and magnetized particles. A magnet was placed on the abdomen of the experimental mouse (left) and a non-magnetic washer of equivalent weight was placed on the control mouse (right). Animals were euthanized and dissected 6 hours after gavage. **E.** Representative *ex vivo* images of mouse GI tracts at 9 hours after gavage with micromagnets and magnetized 'cells.' Mice that had magnets on their abdomen had enhanced retention of micromagnets and magnetized 'cells' in the upper intestines, compared with mice that only had non-magnetic washers. Arrows indicate the presence of micromagnets as confirmed by recording movies of bead displacement when a small magnet was brought into proximity (Fig. 3.10).

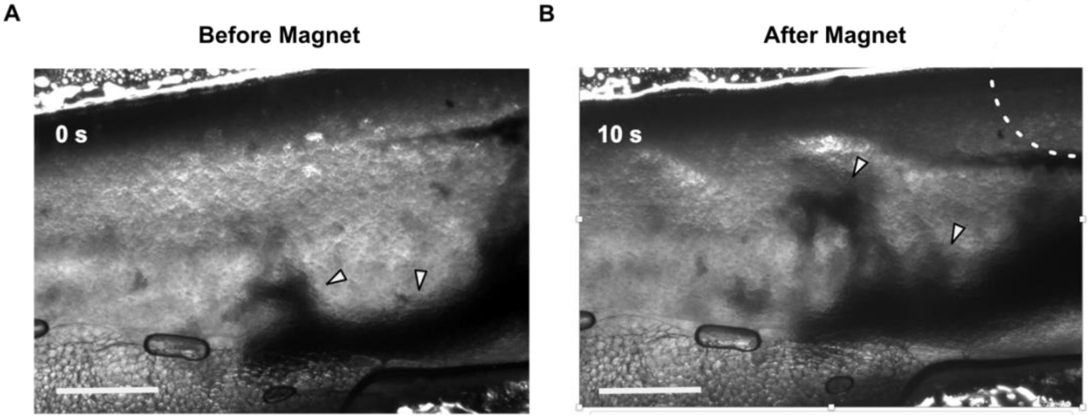

Fig. 3.11 Brightfield images of micromagnet displacement in an *ex vivo* specimen. | A. At 0 sec and **B.** 10 sec after exposure to a small NdFeB magnet. The hashed circle indicates the approximate placement of the magnet. Scale bar is 0.5 mm and arrows indicate an aggregate of beads.

Collectively, these data suggested that the external magnet functions as intended, and successfully enhances the retention of micromagnets and associated magnetized cells in the mouse intestine *in vivo*.

3.2.6 Enhanced retention of magnetized particles *in vivo* using CLAMP

To quantify the efficacy of cellular capture *in vivo*, we repeated the aforementioned *in vivo* experiment. Mice were gavaged with a mixture consisting of 1.5 μm BioMag-NH_2 beads, 1 μm Silica-NH_2 magnetic beads, ~ 10^7 0.5 μm magnetized (red) particles, and ~ 10^7 0.5 μm non-magnetic carboxyl (yellow-green) particles. Magnets or non-magnetic washers of equivalent weight were attached onto the abdomen of mice 75 mins post-gavage, and animals were singly-housed in wire-floor cages with access to 5% sucrose. 9 hours after gavage, animals were euthanized, and their GI tracts were removed. The intestines, starting from the stomach up to the cecum, were subsequently cut into 4 cm segments and their contents were squeezed out for downstream analysis. The luminal contents were weighed and homogenized into PBS at a concentration of 50 mg/ml and filtered using a 40 μm filter, prior to analysis by flow-cytometry.

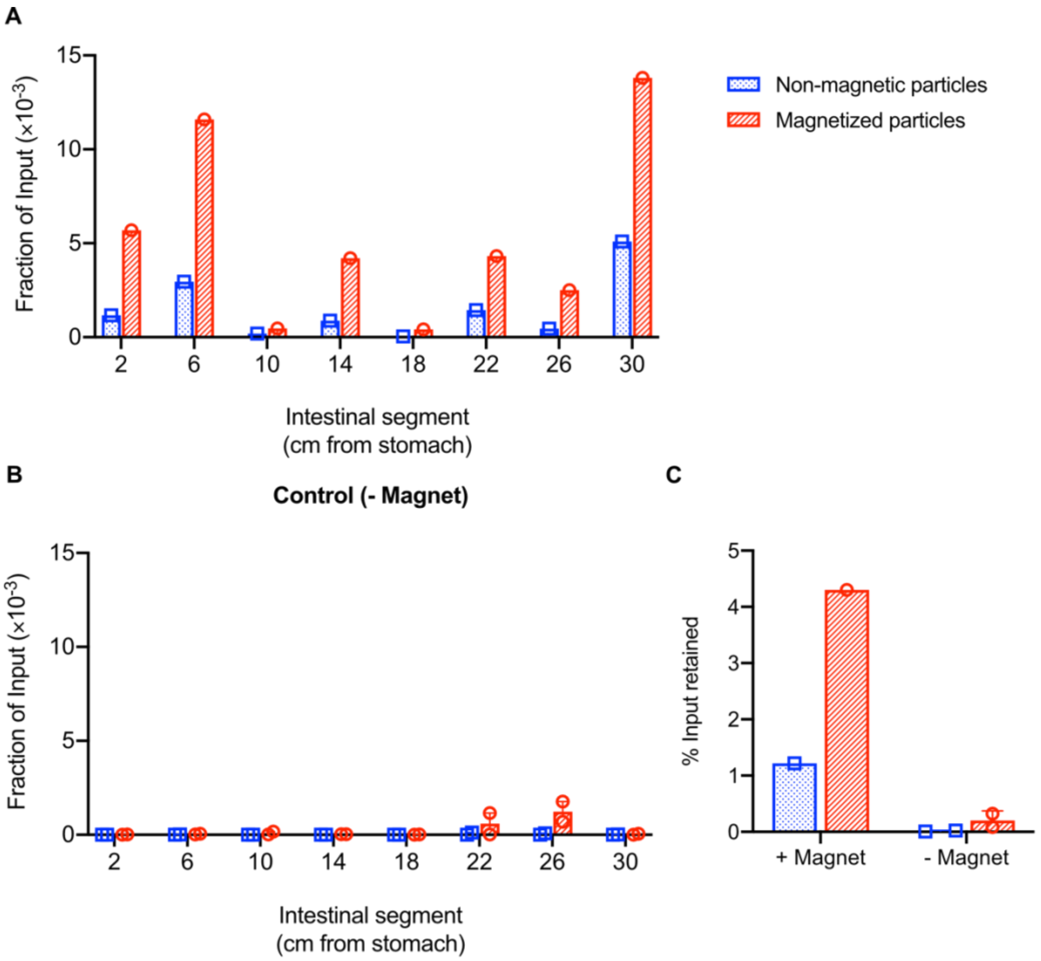

Fig. 3.12 Efficacy of CLAMP *in vivo.* | A. Fraction of magnetic and non-magnetic particles (relative to quantity gavaged) retained in each intestinal segment when mouse wore a magnet for 9 hours ($N = 1$). For clarity, the y-axis is plotted in parts per thousand. The x-axis contains the midpoint of a given intestinal segment, and the origin is taken to be the stomach. The particles in these experiments are the magnetized Nile-red and non-magnetic Yellow-green beads. **B.** Fraction of magnetic and non-magnetic particles in each intestinal segment when mouse wore a non-magnetic washer of equivalent weight for 9 hours ($N = 2$). **C.** Total quantity of magnetized and non-magnetic particles retained in the entirety of the intestine 9 hours after gavage, which is plotted as a percentage of the input gavage quantity.

Consistent with our previous *in vivo* experiments, we observed a punctate distribution of micromagnets in the intestines of the mouse that wore a magnet (Fig. 3.10E). We also observed that the magnetized and non-magnetized particles were clustered around the micromagnet puncta, suggesting localized retention of particles. Meanwhile, the spatial distribution of magnetized and non-magnetic particles in the control (washer) intestine was heavily biased towards the posterior end, proximal to the cecum and large-intestine. We also observed non-specific retention of non-magnetic particles in the intestine of a mouse that wore a magnet, as expected based on our *in vitro* results; however, magnetized particles were approximately 3-4 times more likely to be captured *in vivo*. More replicates are needed to assess the significance of this result, but these initial data are quite promising. Taken together, these data suggest that our two-stage amplification approach, coupled with a judicious choice of micromagnets can enable enhanced retention of magnetized particles in the intestine.

3.3 Supporting Data

3.3.1 Whole animal images confirm surface localization of micromagnets

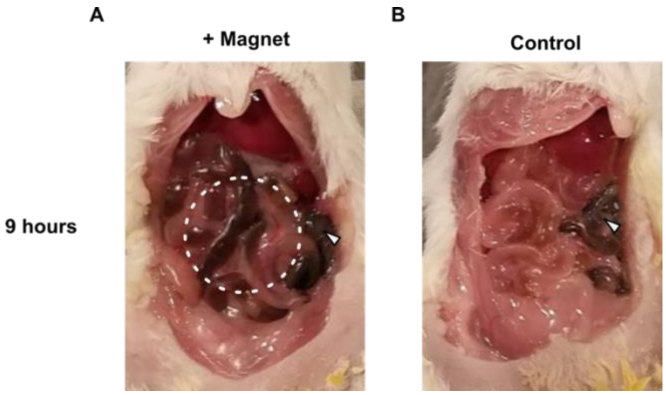

Fig. 3.13 Photographs of euthanized mice post-gavage with micromagnets. | Gavage mixture consists of 1 μm Silica-OH beads, 1.5 μm BM-NH_2 beads, and 0.5 μm magnetized particles. **A.** Image of a mouse that wore a magnet, with the hashed circle indicating the approximate position of the external magnet. **B.** Image of a mouse that wore a washer of equivalent weight. The arrows indicate the cecum, which always appears dense, due to the accumulation of beads. No optical density is observed in the upper intestines in the control mouse.

3.3.2 *Ex vivo* MRI on mouse intestines confirm enhanced retention of micromagnets and synthetic cells

Small intestines were dissected out from mice that were euthanized 9h post-gavage. Mice either had a magnet or non-magnetic washer of equivalent weight placed on their abdomen 75 mins after gavage with the experimental mixture consisting of the 1.5 μm BM-NH$_2$ beads and 1 μm Silica-OH beads and SPION labeled 0.5 μm Nile-red particles. A 3D FLASH was used to acquire the anatomical T_1 weighted image, whereas a 3D UTE was used to acquire the T_2 weighted image. Projections of the 3D cube along the x-z plane are shown.

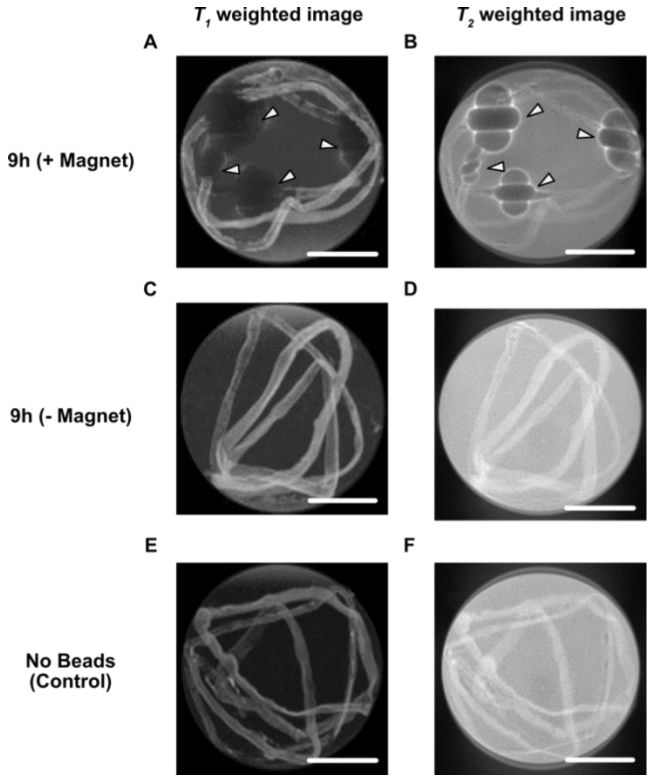

Fig. 3.14 Representative *ex vivo* MRI on mouse GI tracts. | A. T_1 weighted anatomical image alongside **B.** T_2 weighted image of a mouse SI, with arrows indicating regions of susceptibility artefacts which are caused by the presence of micromagnets. The SI was isolated from a mouse 9h post-gavage. A magnet was placed on the mouse abdomen 75 mins after gavage with the micromagnet and synthetic-cell mixture. **C.** T_1 weighted anatomical image alongside **D.** T_2 weighted image of a mouse SI 9h post gavage. A non-magnetic washer of equivalent weight was placed on the mouse abdomen 75 mins after gavage with the same experimental mixture as in A. No susceptibility artefacts were observed in the SI as evidenced by the lack of T_2^* blooming

in the T_2 weighted image. **E.** T_1 and **F.** T_2 weighted images of a control mouse SI respectively. The mouse was not gavaged with any beads but was maintained under the same experimental conditions as in A and C. The SI was dissected from the GI tract and placed within an agarose matrix to minimize susceptibility artefacts during imaging. Scale bars are 20 mm.

3.3.3 Efficacy of CLAMP using large micromagnets

In addition to testing small micromagnets, we were also interested in exploring the efficacy of larger micromagnets, since these are expected to have larger field and field-gradient profiles. Accordingly, we fluorescently labeled 8 µm BM-NH_2 beads and 50 µm Silica-OH beads with green and red fluorophores respectively. Upon conducting an *in vivo* experiment akin to our previous experiments with smaller micromagnets, *ex vivo* fluorescence imaging of the GI tracts did not demonstrate any appreciable difference in transit profiles between mice that had magnets and mice that had non-magnetic washers of equivalent weight (Fig. 3.15). Although the experiment was repeated multiple times, we did not observe any differences in micromagnet kinetics between the experimental and control subjects.

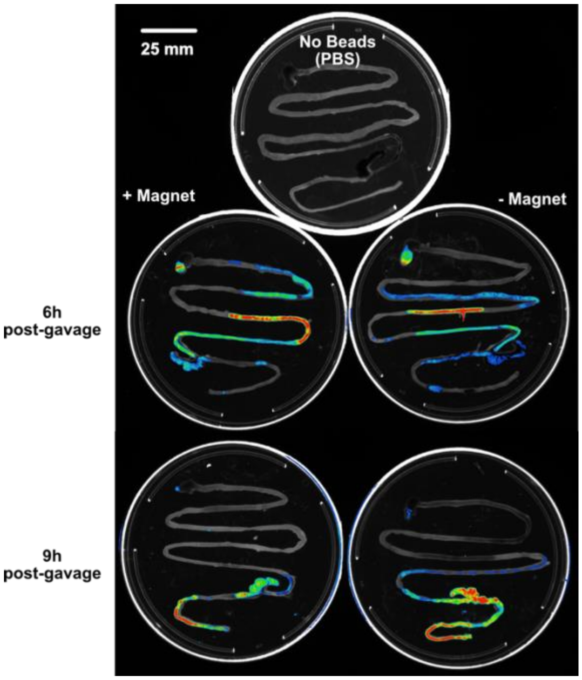

Fig. 3.15 Kinetics of large micromagnets *in vivo*. | Mice were gavaged with a slurry consisting of NHS conjugated 8 µm BM-NH_2 beads and 50 µm Silica-OH beads. Fluorescence

images in the green channel was combined with a brightfield image. Here, red indicates highest intensity. The red fluorescence image of the Silica beads is not shown since it exhibits the same trend. No differences in transit kinetics were observed between the experimental (left) subjects wearing magnets and the control (right) subjects wearing non-magnetic washers at 6 and 9 hours after gavage.

To gain insight into why the large micromagnets do not appear to be trapped *in vivo*, we first took high resolution brightfield images of the micromagnets within the mouse GI tracts.

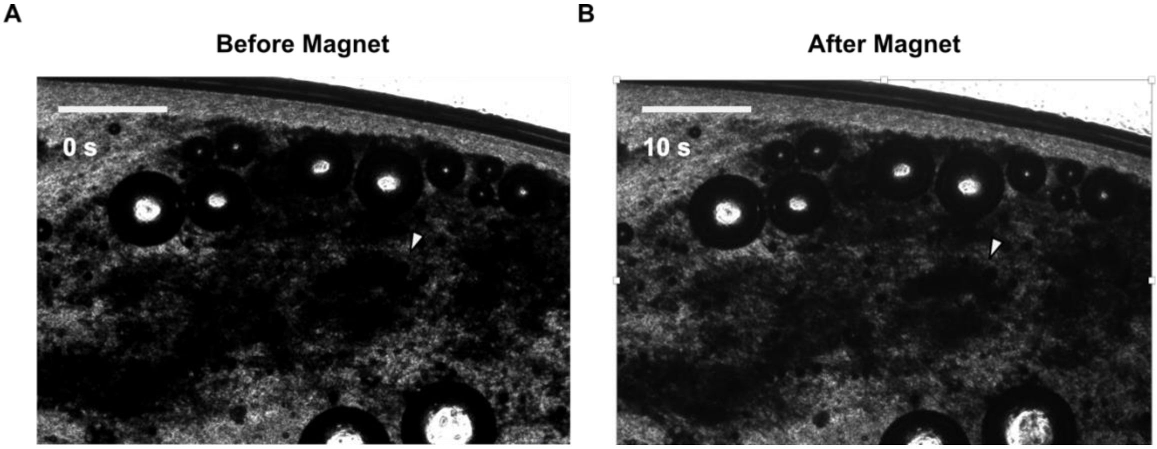

Fig. 3.16 Brightfield images of micromagnet displacement *ex vivo*. | A mouse was gavaged with 8 μm BM-COOH beads and 50 μm Silica-OH beads and euthanized 3 hours after gavage. **A** and **B** correspond to frames before and 10 s after magnet exposure (from the right). Scale bar is 0.5 mm and arrows indicate a subtle, hardly discernible displacement of micromagnets when a small magnet is placed proximal to the intestinal segment.

Contrary to what we observed with small micromagnets, we only observed a slow, collective motion of the micromagnets towards the walls of the GI tract when a magnet was placed immediately adjacent to the tissue sample (Fig. 3.16). These data suggest that the large micromagnets are adhered to mucins, which constitute the bulk of the GI lumen and are drive aggregation of particulates in the intestine.[31–33] Since these beads are considerably larger than the average mesh size of the mucosal network, their motion towards the walls of the intestine is significantly retarded; consequently, beads were not observed next to the intestinal walls, unlike the smaller micromagnets. As such, these large beads are unsuitable for CLAMP in the GI tract.

3.4 Summary and Outlook for CLAMP

Remote control of cellular localization is a long sought-after goal within the synthetic biology community, which if successful would enable unprecedented new applications in synthetic biology and therapy. One area of research where such noninvasive control would be particularly beneficial is the study of the GI microbiome. Current methods to localize microbes in the GI tract rely on species that are naturally suited to colonizing a desired niche, as opposed to any external methods to alter local microbiome composition – a strategy that is not broadly generalizable for advancing synthetic biology or therapy. On the other hand, while deeply penetrant forms of energy such as magnetic fields can enable remote control of cellular function, to date most applications involving magnetic control or actuation of cellular function require that the cells be immediately adjacent (< 1mm) to the magnetic source.

Inspired by decades-old magnetic separation columns which enable capture of weakly magnetized cells, we developed a new strategy for extending magnetic control up to depths of 13 mm from the surface of the skin. Our cellular localization strategy uses a two-stage field-gradient amplification approach, in which micromagnets that are orally administered, are first magnetized by the external magnet and captured. Thereafter, these micromagnets produce 10^4-fold stronger local field gradients, which significantly enhances the capture of small, magnetized particles or cells. Using *in silico* Monte Carlo models, we confirmed that small micromagnets, such as those used in our study, can be reliably captured in solution viscosities of up to 1 Pa.s. Our *in silico* models also revealed the importance of micromagnet aggregation for capture *in vivo*. Furthermore, using our *in vitro* GI tract model, we established that the same micromagnets confer an approximately 3-fold enhancement in magnetized cell capture, relative to no micromagnet controls, at distances between 10-13 mm offset from the magnet surface. When tested *in vivo*, the positively charged micromagnet slurry conferred an approximately 4-fold enhancement in magnetized particle capture, compared with non-magnetic particle controls.

Further studies are needed to deduce the statistical significance of our *in vivo* results, as well as test the efficacy with which magnetized microbes can be similarly retained *in vivo*. Additional CT studies would yield insight on the kinetics of micromagnet transport and enable quantification of micromagnet abundance *in vivo*. One significant challenge we have encountered thus far in our *in vivo* experiments is that intestinal positions vary considerably between mice, and our approach for magnet positioning currently assumes that we are covering the intestines. One strategy that we are considering going forward is to first image the mouse non-invasively using Ultrasound in order to deduce the location of its intestines. We will then use this information to adjust magnet position on the abdomen. Another open question of interest is to determine micromagnet retention at 12 hours post gavage and beyond; our current *in vivo* data suggests that we have enhanced the retention of micromagnets by approximately 3 hours, and it remains to be seen whether this is sufficient for some of the synthetic biology applications being considered.

Finally, if preliminary studies using probiotic microbes are successful, then our novel approach would foster new strategies for controlled therapy *in vivo*. Furthermore, given that CLAMP is orthogonal to other non-invasive imaging modalities such as Ultrasound, one can use CLAMP to selectively enrich engineered cells at a desired locus, while reading out relevant information about their local environment non-invasively.

3.5 Experimental Methods

3.5.1 Materials

NEB Turbo *E. coli* were used for all cloning and stable plasmid maintenance. BL21(DE3) *E. coli* and *E. coli Nissle* 1917 were both used for *in vitro* and *in vivo* experiments. LB Broth (Lennox) and LB-agar (Lennox) plates were prepared according to the manufacturer's instructions (Millipore-Sigma). M9-glucose media was prepared by combining M9 Minimal Salts (6.78 g Na_2HPO_4, 3 g KH_2PO_4, 1 g NH_4Cl, 0.5 g NaCl), D-glucose (4 g), $MgSO_4$ (2 mmol), $CaCl_2$ (100 μmol), and miliQ water to 1 L, and subsequently sterile filtering using a 0.22 μm bottle top vacuum filter. Magnets (R822-N52) were obtained from K&J Magnetics and non-stick plastic tubing was obtained from McMaster-Carr. The following nano- and micro-particles were used (manufacturer indicated in parentheses): Hi-Sur Mag 150 nm Streptavidin Beads (Ocean Nanotech), 8 μm carboxyl-modified undyed COMPEL Magnetic (Bangs Laboratories), 6 or 8 μm carboxyl-modified Dragon Green COMPEL Magnetic (Bangs Laboratories), 8 μm carboxyl-modified Flash Red COMPEL Magnetic (Bangs Laboratories), 8 μm non-magnetic PS/DVB Dragon Green (Bangs Laboratories), 1.5 μm or μm 3-12 μm BioMag Maxi Carboxyl or Amine (Bangs Laboratories), 50 μm or 1 μm Colloidal Magnetic Silica Microspheres (Alpha Nanotech), 0.5 μm Biotin Coated Fluorescent Nile Red Particles (Spherotech), 0.5 μm yellow-green carboxylate-modified FluoSpheres (ThermoFisher), and 1 μm yellow-green amine-modified FluoSpheres (ThermoFisher). All beads were washed 3 times in PBS and re-suspended at the appropriate concentration in PBS before use. All chemicals were of analytical grade and commercially available.

3.5.2 *In vitro* model of the mouse GI tract

To test capture of SPION-labeled *E. coli* and SPION-labeled 0.5 μm particles in vitro, a syringe pump was used to flow a suspension of fluorescently-stained SPION-labeled BL21(DE3) *E. coli* or SPION-labeled 0.5 μm nile red particles and magnetic beads (1 μm or 50 μm Silica-OH magnetic beads, 1.5 μm or 3-12 μm carboxyl or amine BioMag beads, or a combination of these) at 100 μL/min through non-stick tubing (1/8" ID x 3/16" OD). The tubing was held vertically and flow was in the direction of gravity to avoid issues with beads settling and bubbles being introduced while changing the syringe. A 1/2" OD x 1/8" ID x 1/8" thick ring magnet (D822-N52) with the axial direction pointing toward the tube was held at distances ranging from 0 to 15 mm away from the surface of the tubing using a 3D-printed holder. For each run, first 1 mL of 4 mg magnetic beads and ~10^8 fluorescently-stained SPION-labeled *E. coli* or ~10^8 SPION-labeled Nile red particles in PBS + 0.5% (w/v) BSA was flowed at 100 µL/min; unlabeled *E. coli* or unlabeled or non-magnetic particles were used as controls where indicated. Next, 5 mL of PBS + 0.5% (w/v) BSA at 100 µL/min was used to wash away beads that were not trapped and the flow through + wash was collected (~5.1 mL); during changing the syringe before the wash, care was taken not to introduce bubbles and a stopcock valve was used to prevent the fluid from flowing out the bottom due to gravity. Then the magnets were removed from the holder and the remaining liquid in the tubing was collected as the eluate (~0.9 mL). The mass of each fraction (flow through + wash and eluate) was measured to get an estimate of the volume assuming the density is approximately that of water. Capture of the SPION-labeled *E. coli* or SPION-labeled particles was quantified by counting the number of cells/particles in each fraction with flow cytometry (described below). Capture of the magnetic beads was quantified by measuring the iron content in each fraction by dissolving the magnetic beads in at least 5x volume excess of 70% HNO_3 at 65°C overnight and performing a ferrozine assay according to the manufacturer's instructions (Total Iron Reagent Set, Pointe Scientific). Percent capture was calculated by dividing the number of cells/particles or iron content in the eluate by the total number of cells/particle or total iron content in the two fractions.

3.5.3 Animal procedures

All animal experiments were approved by the Caltech Institutional Animal Care and Use Committee (IACUC). All mice were 7-11 week-old female Balb/c mice obtained from Jackson Labs and were gavaged using a 20 gauge 1.5" length animal feeding needle. Gavage volume was 200 µl and consisted of a mixture of magnetic beads (4 mg), SPION-labeled *E. coli* or SPION-labeled 0.5 µm Nile red particles (~10^8), 50% (w/v) $NaHCO_3$, and 0.5% (w/v) BSA. Prior to gavage, mice were fasted for 18 hours on wire bottom cages in groups of 2-3 with access to water only and kept on wire bottom cages throughout the experiment to prevent coprophagy. Their abdominal fur was also removed with Nair prior to gavage. At 75 minutes after gavage, a

1/2" OD x 1/8" ID x 1/8" thick ring magnet (R822-N52) or non-magnetic washer of similar size and weight (3.2 g) was glued onto their abdomens with GLUture Topical Tissue Adhesive (Abbott Laboratories) while they were sedated with isoflurane. Adhesive tape was wrapped around their abdomens to further secure the magnet/weight and prevent it from hanging off the skin. Water with 5% (w/v) sucrose was provided and mice were housed individually for the remainder of the experiment.

For dissection experiments, mice were euthanized at various time points after gavage by sedating with isoflurane and performing cervical dislocation. Intestines were removed and placed on petri dishes. Connective tissue and mesenteric fat were carefully removed from the intestines with forceps, and a wet Kimwipe was used to remove any blood. Intestines were then analyzed with a gel imager, microscopy, MRI, and/or flow cytometry as described below.

3.5.4 Flow-cytometry

A MACSQuant VYB flow cytometer (Miltenyi Biotec) was used for all flow cytometric analysis with the following settings: low flow rate, medium mixing, 25 uL uptake volume, standard mode, chilled 96 rack, and a trigger by SSC with a threshold of 4.00. For analyzing *in vitro* samples, appropriate dilutions in PBS + 0.5% (w/v) BSA were prepared to target 10^5 – 10^6 particles/mL. For analyzing *in vivo* samples, the small intestines were divided into 4 cm segments and the contents were carefully squeezed out using forceps. The contents were suspended in PBS at a concentration of 50 mg/mL and homogenized by vortexing and sonicating. The resulting homogenates were filtered through 40 μm Cell Strainers (VWR) and diluted in PBS + 0.5% (w/v) BSA to a concentration of 10 mg/mL before being run. The Y1 channel (561 nm laser, 586/15 nm filter) was used to quantify nile red particles and the B1 channel (488 nm laser, 525/50 nm filter) was used to quantify yellow-green particles. Gains and thresholds were set based on control fluorescent samples.

3.5.5 Particle labeling

To label 0.5 μm biotin-coated fluorescent Nile red particles with Hi-Sur Mag 150 nm streptavidin beads, 10^8 biotin-coated Nile red particles were first suspended in 850 μL PBS with vortexing.

A mixture of 0.05 mg Neutravidin DyLight633 (ThermoFisher) and 0.5 mg Hi-Sur Mag 150 nm streptavidin beads in PBS (150 μL) was then added to the suspension. The suspension was immediately vortexed and incubated at room temperature with rotation for 90 minutes. The excess dye and unlabeled biotin-coated particles were removed by magnetic separation and washed twice with PBS + 0.5% (w/v) BSA.

To label silica magnetic particles with fluorescent dyes, the particles were washed four times with 100% ethanol and suspended in 100% ethanol at a concentration of 5 mg/mL. 3-(Aminopropyl)triethoxysilane (Sigma-Aldrich) was added for a final concentration of 20 mg/mL and the suspension was incubated at room temperature with rotation for 24 hours. The resulting amine-functionalized silica magnetic particles were washed 3 times with PBS pH 8.1 and the appropriate NHS dye ester (Alexa Fluor 488 NHS ester or Alexa Fluor 568 NHS ester) was added for a final concentration of 0.02 mg/mL. The mixture was incubated at room temperature overnight with rotation, and then the reaction was quenched with PBS + 100 mM glycine. The fluorescently labeled particles were washed four times in PBS to remove excess dye. BioMag Maxi Amine particles (3-12 μm) were labeled by suspending at a concentration of 1 mg/mL in PBS (pH 8.1). DyLight550 NHS ester was added at a concentration of 100 μM and the suspension was incubated at room temperature overnight with rotation. The reaction was quenched with PBS + 100 mM glycine and the particles were washed four times in PBS to remove excess dye.

3.5.6 SPION labeling of *E. coli*

The appropriate strain of BL21(DE3) or *E. coli* Nissle 1917 was used to inoculate 2 mL of LB medium with the appropriate antibiotic (50 μg/mL kanamycin or 100 μg/mL ampicillin). This starter culture was grown overnight at 37°C and 250 rpm and sub-cultured into 25 mL or 50 mL of LB medium + antibiotic in 250 mL baffled shake flasks at a 1:100 dilution ratio. The subculture was grown at 37°C and 250 rpm until the OD_{600} reached 0.5 to 0.7. If the cultures were to be induced, at this point 0.2% (w/v) arabinose or 0.5 mM IPTG was added and the cultures were grown at 37°C and 250 rpm for an additional 6 hours to allow for expression.

Subsequently, 10 mL of culture was spun down at 3500 x g and 4°C, washed four times with PBS (pH 8.1), and re-suspended in 1 mL of PBS (pH 8.1). One mg of EZ-Link Sulfo-NHS-X-Biotin (Thermo Fisher Scientific), where X = SS for in vitro experiments or X = LC or LC-LC for in vivo experiments, was added and the suspension was incubated with rotation at 4°C for 60 to 90 min. The biotinylation reaction was quenched by adding 1 mL of PBS + 100 mM glycine and mixing. The suspension was then pelleted at 3500 x g and 4°C, and re-suspended in 400 μL routine PBS. Next, 100 μL of 5x (5 mg/mL) Hi-Sur Mag 150 nm Streptavidin Beads (SPIONs) were added and the cells + beads mixture was incubated overnight at 4°C with rotation. The next day directly before use in subsequent experiments, the cells + beads mixture was magnetically separated by holding a magnet to the side of the tube, allowing the beads and labeled cells to migrate towards the magnet, and pipetting off the supernatant. The pellet containing excess beads and SPION-labeled *E. coli* was washed twice in PBS + 0.5% (w/v) BSA and re-suspended in the appropriate amount of PBS + 0.5% (w/v) BSA for use in subsequent experiments. Unlabeled *E. coli* was prepared the same as labeled *E. coli* except that no EZ-Link Sulfo-NHS-X-Biotin or Hi-Sur Mag 150 nm Streptavidin Beads were added.

3.5.7 Microscopy and gel imager settings

Immediately after dissection, intact intestines were imaged using a BioRad ChemiDoc gel imager for fluorescence (blue epifluorescence and 530/28 filter for Dragon Green and Alexa Fluor 488 particles; green epifluorescence and 605/50 filter for Nile red, DyLight 550, and Alexa Fluor 568 particles) and optical density (white epifluorescence, 605/50 filter). ImageJ was used to threshold and colorize the fluorescence images, and GIMP was used to overlay them on top of the white-light images. Shortly after, intestines were imaged using a Zeiss AxioCam microscope for both bright-field microscopy and epifluorescence microscopy. Intestines were either intact or compressed between a glass slide and a coverslip, or intestinal contents were removed by squeezing with forceps and placed on a glass slide with a coverslip, where indicated.

3.5.8 X-ray CT imaging

CT images of the abdominal area (45 x 45 mm field-of-view) were acquired using 3D micro-CT (Rigaku) with a resolution of 90 μm, tube potential peaks of 90 kV, tube current of 88 μA, and imaging duration of approximately 5 min. Mice were sedated during imaging using isoflurane (1%) at various time points after gavage. The magnets/non-magnetic washers were removed prior to imaging and immediately re-attached afterwards. Thresholding and 3D image reconstruction was performed using ImageJ.

3.5.9 MRI

Shortly after dissection, mouse intestines were fixed using 10% formalin at room temperature for 20 minutes. Fixed intestines were washed using cold PBS + 0.1 mM L-ascorbic acid and stored at 4°C until imaging. Before imaging, intestines were cast in a 1% (w/v) agarose gel phantom to minimize susceptibility artifacts. A Bruker 7 T small-animal scanner was used for all MR imaging, with a Rat volume coil (70 mm inner diameter) supplying the RF for ^{1}H spin-excitation and subsequent readout. Given the high relaxivity of the micromagnets gavaged, we used a 3D UTE sequence ($T_E = 20$ μs, $T_R = 8$ ms, $N_{avg} = 2$) to localize micromagnets within the intestines, using an isotropic voxel size of 234 μm. A 3D FLASH sequence, with an isotropic voxel size of 325 μm, was used to obtain anatomical images of the *ex vivo* GI tract specimens.

3.5.10 Ferrozine assay

For feces experiments, feces were collected every 2 hours until 16 hours after gavage. Magnets and non-magnetic weights were either removed after 8 hours or kept on for the duration of the experiment. To analyze the iron content from the magnetic beads, feces were homogenized in PBS and aliquots of the suspension were added to excess 70% HNO_3. The acid + feces mixtures were incubated at 65°C and 600 rpm overnight and then dried down leaving behind a yellow pellet. The pellet was suspended in 2% HNO_3 and the iron content was measured with a ferrozine assay according to the manufacturer's instructions (Total Iron Reagent Set, Pointe Scientific).

3.5.11. Monte Carlo Simulations

The magnetic field of the R822-N52 magnet was numerically calculated using FEMM. Given that the magnet is cylindrically symmetric, we calculated the field it produces in the positive *r-z* half-plane using an axi-symmetric magnetostatics problem with Dirichlet boundary conditions and obtained $\mathbf{B}_r$ and $\mathbf{B}_z$ respectively. $\mathbf{B}_z$ is identical about rotations of *z*, whereas $\mathbf{B}_r(\phi = \pi) = -\mathbf{B}_r(\phi = 0)$ by symmetry. Due to axial symmetry, $\mathbf{B}_\phi = 0$, and the field has no azimuthal components (i.e. $\mathbf{B(r}, \phi, \mathbf{z)} = \mathbf{B(r, z)}$). The magnetic field over the complete *r-z* plane was obtained using superposition of the two half-plane solutions. For simplicity, we chose to model the field within the *y-z* plane (at *x = 0*) since this is sufficient for understanding the relevant force-scales and bead kinetics within the tube ($\mathbf{B}_y = \mathbf{B}_r\left(\phi = \frac{\pi}{2}\right)$ and $\mathbf{B}_z = \mathbf{B}_z$). The calculated magnetic field within the tube was obtained by interpolating the original solution to a step-size of 5 μm, using a spline interpolant across 4 neighboring points in either direction. The volume magnetization of a bead and its resulting magnetic susceptibility were obtained by fitting the manufacturer supplied SQUID magnetometry data to a Langevin function. Given some bias field (B_{bias}), the magnetic field produced by a magnetized bead in the *y-z* plane was numerically calculated at a step-size of 10 nm over a region spanning 5 μm × 5 μm using the dipole field relations (Eq. 3.4 – 3.5).

$$\mathbf{B}_z(i,j) = \frac{\mu_0 \mathbf{m}(B_{bias})}{4\pi r_{i,j}^3} \cdot \left(\frac{3\left(z_j - z_0\right)^2}{r_{i,j}^2} - 1 \right) \tag{3.4}$$

$$\mathbf{B}_y(i,j) = \frac{\mu_0 \mathbf{m}(B_{bias})}{4\pi r_{i,j}^3} \cdot \left(\frac{3\left(z_j - z_0\right)(y_i - y_0)}{r_{i,j}^2} \right) \tag{3.5}$$

The force acting on a magnetic bead in the channel midplane is the vector expansion of Eq. 3.1 and we neglect the contribution from the bead's remnant magnetization since this was not provided by the manufacturer. In doing so, our simulations offer a conservative estimate of magnetic force ($\mathbf{F}_m$) acting on the particle.

$$\mathbf{F}_m(i,j) = \frac{\chi_{bead} V_{bead}}{\mu_0} \left[\left(\mathbf{B}_y \partial_y \mathbf{B}_y + \mathbf{B}_z \partial_y \mathbf{B}_z \right) \hat{y} + \left(\mathbf{B}_y \partial_z \mathbf{B}_y + \mathbf{B}_z \partial_z \mathbf{B}_z \right) \hat{z} \right] \tag{3.6}$$

Here, $\mathbf{B}_z$ and $\mathbf{B}_y$, as well as their corresponding gradients, are evaluated at each point *(i,j)* in the simulated tube. Given the small size of the micromagnets, we can neglect inertial forces and consider only the effects of hydrodynamic drag.

$$\mathbf{F_d} = 6\pi\eta r_{bead}\left(\mathbf{u}_{flow} - \mathbf{v}_{bead}\right) \tag{3.7}$$

The Brownian motion acting on the bead can be computed using the Stokes-Einstein-Sutherland relation.

$$\langle \mathbf{r^2} \rangle = 2D_{bead}t \tag{3.8}$$

Here $\mathbf{r} = (\mathrm{y}, \mathrm{z})$ is the coordinate pair corresponding to the position of the particle in the channel. The diffusion coefficient, as usual is $D_{bead} = \frac{k_B T}{6\pi\eta r_{bead}}$. We can then simulate the time evolution of beads in the channel as follows:

$$m\frac{d}{dt}\mathbf{v}_{bead} = 0 = \mathbf{F_d} + \mathbf{F}_m \tag{3.9}$$

$$y(t+\Delta t) = y(t) + \frac{\Delta t}{6\pi\eta r_{bead}}\left[6\pi\eta r_{bead}\mathbf{u}_{flow}(z) + \mathbf{F}_m\hat{y}\right] + \xi \tag{3.10}$$

$$z(t+\Delta t) = z(t) + \frac{\Delta t}{6\pi\eta r_{bead}}[\mathbf{F}_m z] + \xi \tag{3.11}$$

The flow velocity in the tube follows the Hagen-Poiseuille flow profile, wherein the pressure drop across the length of the tube (*L*), with volumetric flow rate *Q* as set by the syringe pump, is given by:

$$\Delta P_{tube} = \frac{8\eta L Q}{\pi r_{tube}^4} \tag{3.12}$$

$$\mathbf{u}_{flow}(z) = \frac{\Delta P_{tube}}{4\eta L}[r_{tube}^2 - (z - z_{mid})^2] \tag{3.13}$$

To avoid singularities, the minimum fluid flow was set to the random Brownian velocity of the bead ($\mathbf{u}_{min} = \sqrt{\frac{2D}{t}}$). Additionally, ξ is a gaussian distributed random variable with width $\sigma = \sqrt{2D_{bead}t}$. For simplicity, lift forces and particle-particle interactions were neglected in the simulation. A time step (Δt) of 100 ms was chosen for all runs, and a fixed number (1000) of particles were initialized at $y = 0$, but with z positions spanning the full diameter of the tube. To simulate a washing step, the simulation time was extended to 1600 s. Beads were magnetically captured if they ended up (z coordinate) along the wall of the tube (within 0.1 mm of $z = 10$ mm) and if their final y position was within the bounds of the tube at the end of the simulation. In instances where the drag-forces are stronger than the magnetic forces, any 'retention' in the tube is simply the result of reduced mobility through the fluid. This isn't true magnetic capture, but rather 'enhanced' retention due to the force provided by the external magnet. Accordingly, any beads whose final y positions were between $y = 30$ mm and $y = 50$ mm were treated as 'retained.'

BIBLIOGRAPHY

1. Valon, L., Marín-Llauradó, A., Wyatt, T., Charras, G. & Trepat, X. Optogenetic control of cellular forces and mechanotransduction. *Nat. Commun.* **8,** (2017).
2. Buckley, C. E. *et al.* Reversible Optogenetic Control of Subcellular Protein Localization in a Live Vertebrate Embryo. *Dev. Cell* **36,** 117–126 (2016).
3. Muthana, M. *et al.* Directing cell therapy to anatomic target sites in vivo with magnetic resonance targeting. *Nat. Commun.* **6,** 8009 (2015).
4. Felfoul, O. *et al.* Magneto-aerotactic bacteria deliver drug-containing nanoliposomes to tumour hypoxic regions. *Nat. Nanotechnol.* **11,** 941–947 (2016).
5. Chiang, C. *et al.* Combination of fucoidan-based magnetic nanoparticles and immunomodulators enhances tumour-localized immunotherapy. *Nat. Nanotechnol.* **13,** 746–754 (2018).
6. Zhu, H. *et al.* Spatial control of in vivo CRISPR–Cas9 genome editing via nanomagnets. *Nat. Biomed. Eng.* **3,** 126–136 (2019).
7. Chen, H. & Langer, R. Magnetically-responsive polymerized liposomes as potential oral delivery vehicles. *Pharm. Res.* **14,** 537–540 (1997).
8. Shevkoplyas, S. S., Siegel, A. C., Westervelt, R. M., Prentiss, M. G. & Whitesides, G. M. The force acting on a superparamagnetic bead due to an applied magnetic field. *Lab Chip* **7,** 1294–1302 (2007).
9. Kang, J. H. *et al.* An extracorporeal blood-cleansing device for sepsis therapy. *Nat. Med.* **20,** 1211–1216 (2014).
10. Zhang, Y. *et al.* Non-invasive multimodal functional imaging of the intestine with frozen micellar naphthalocyanines. *Nat. Nanotechnol.* **9,** 631–638 (2014).
11. Hsiao, E. Y. *et al.* Microbiota Modulate Behavioral and Physiological Abnormalities Associated with Neurodevelopmental Disorders. *Cell* **155,** 1451–1463 (2013).
12. Yano, J. M. *et al.* Indigenous Bacteria from the Gut Microbiota Regulate Host Serotonin Biosynthesis. *Cell* **161,** 264–276 (2015).
13. Mimee, M. *et al.* An ingestible bacterial-electronic system to monitor gastrointestinal health. *Science (80-.).* **360,** 915–918 (2018).
14. Abramson, A. *et al.* An ingestible self-orienting system for oral delivery of macromolecules. *Science (80-.).* **363,** 611–615 (2019).
15. Riglar, D. T. *et al.* Engineered bacteria can function in the mammalian gut long-term as live diagnostics of inflammation. *Nat. Biotechnol.* **35,** 653–658 (2017).
16. Donaldson, G. P., Lee, S. M. & Mazmanian, S. K. Gut biogeography of the bacterial microbiota. *Nat. Rev. Microbiol.* **14,** 20–32 (2015).
17. Masaoka, Y., Tanaka, Y., Kataoka, M., Sakuma, S. & Yamashita, S. Site of drug absorption after oral administration: Assessment of membrane permeability and luminal

concentration of drugs in each segment of gastrointestinal tract. *Eur. J. Pharm. Sci.* **29,** 240–250 (2006).

18. Miltenyi, S., Müller, W., Weichel, W. & Radbruch, A. High gradient magnetic cell separation with MACS. *Cytometry* **11,** 231–8 (1990).
19. Ramesh, P. *et al.* Ultraparamagnetic Cells Formed through Intracellular Oxidation and Chelation of Paramagnetic Iron. *Angew. Chemie - Int. Ed.* **57,** 12385–12389 (2018).
20. Matsumoto, Y., Chen, R., Anikeeva, P. & Jasanoff, A. Engineering intracellular biomineralization and biosensing by a magnetic protein. *Nat Commun* **6,** 8721 (2015).
21. Liu, X. *et al.* Engineering Genetically-Encoded Mineralization and Magnetism via Directed Evolution. *Sci. Rep.* **6,** 1–10 (2016).
22. Kim, T., Moore, D. & Fussenegger, M. Genetically programmed superparamagnetic behavior of mammalian cells. *J. Biotechnol.* **162,** 237–45 (2012).
23. Casteleyn, C., Rekecki, A., Van der Aa, A., Simoens, P. & Van den Broeck, W. Surface area assessment of the murine intestinal tract as a prerequisite for oral dose translation from mouse to man. *Lab. Anim.* **44,** 176–183 (2010).
24. Teply, B. A. *et al.* The use of charge-coupled polymeric microparticles and micromagnets for modulating the bioavailability of orally delivered macromolecules. *Biomaterials* **29,** 1216–1223 (2008).
25. Yang, P. J., Lamarca, M., Kaminski, C., Chu, D. I. & Hu, D. L. Hydrodynamics of defecation. *Soft Matter* **13,** 4953–5088 (2017).
26. Volkmer, B. & Heinemann, M. Condition-Dependent cell volume and concentration of Escherichia coli to facilitate data conversion for systems biology modeling. *PLoS One* **6,** 1–6 (2011).
27. Ebino, K. Y., Yoshinaga, K. & Saito, T. R. A simple method for prevention of coprophagy in the mouse. *Lab. Anim.* **22,** 1–4 (1988).
28. Sang Yoo, H. & Gwan Park, T. Biodegradable nanoparticles containing protein-fatty acid complexes for oral delivery of salmon calcitonin. *J. Pharm. Sci.* **93,** 488–495 (2003).
29. Laulicht, B., Gidmark, N. J., Tripathi, A. & Mathiowitz, E. Localization of magnetic pills. *Proc. Natl. Acad. Sci.* **108,** 2252–2257 (2011).
30. Cheng, J. *et al.* Magnetically responsive polymeric microparticles for oral delivery of protein drugs. *Pharm. Res.* **23,** 557–564 (2006).
31. Preska Steinberg, A. *et al.* High-molecular-weight polymers from dietary fiber drive aggregation of particulates in the murine small intestine. *Elife* **8,** 1–33 (2019).
32. Ensign, L. M., Cone, R. & Hanes, J. Oral drug delivery with polymeric nanoparticles: The gastrointestinal mucus barriers. *Adv. Drug Deliv. Rev.* **64,** 557–570 (2012).
33. Maisel, K., Ensign, L., Reddy, M., Cone, R. & Hanes, J. Effect of surface chemistry on nanoparticle interaction with gastrointestinal mucus and distribution in the gastrointestinal tract following oral and rectal administration in the mouse. *J. Control. Release* **197,** 48–57 (2015).

Chapter 4

OPTICAL MAGNETIC FIELD IMAGING USING NV DIAMONDS

4.1 Motivation

An array of living organisms, spanning from prokaryotes to eukaryotes, sense and utilize magnetic fields in their environment for essential functions such as navigation. Numerous such organisms biosynthesize magnetically sensitive minerals, including nanostructured magnetite and greigite, which facilitate their interaction with external magnetic fields.[1] In addition to their fundamental biological relevance, magnetic fields are actively exploited by bioengineers to both image and perturb cellular function noninvasively in living animals.[2–6]

One major challenge in the study of biological magnetism thus far has been sensitively correlating changes in cellular biochemistry to changes in cellular magnetization, which is necessary for mapping the genetic pathway that enables biosynthesis of intracellular superparamagnetic nanostructures.[7,8] A more complete understanding of such natural magnetite biosynthesis pathways will aid in the development of more sensitive genetically encoded contrast agents for MRI and CT, which are currently limited to paramagnetic metalloproteins.[9–11] Moreover, this challenge is compounded by the fact that current-day technologies for magnetic field imaging are fundamentally limited in scope and ability.

While spectroscopic techniques such as NMR, Mössbauer, and X-ray absorption near edge structure (XANES) are chemically sensitive, they a) require large quantities of purified sample, b) cannot be used to study live cells or animals, c) cannot be multiplexed with common molecular tools such as fluorescent tags, and d) do not provide information about the spatial distribution of magnetically responsive minerals.[12,13] Meanwhile, spatial field mapping technologies such as superconducting quantum interference device (SQUID) magnetometers and spin-exchange relaxation free (SERF) cells, offer modest spatiotemporal resolution but require cryogenic temperatures for maximum sensitivity and are low in throughput.[14–16]

Additionally, noninvasive imaging modalities such as MRI are fundamentally unable to image at the cellular and sub-cellular level due to the diffusion of nuclear spins within the acquisition window and comparatively slower gradient slew rates.[17] Consequently, there is a critical unmet need for technologies that facilitate sub-cellular magnetic field imaging under ambient conditions with high sensitivity *and* throughput. Doing so would not only bring new insight on biomagnetism but would also enable new experimental studies on MRI contrast agents and their mechanisms of action.

4.2 Nitrogen-vacancy (NV) diamond magnetometry

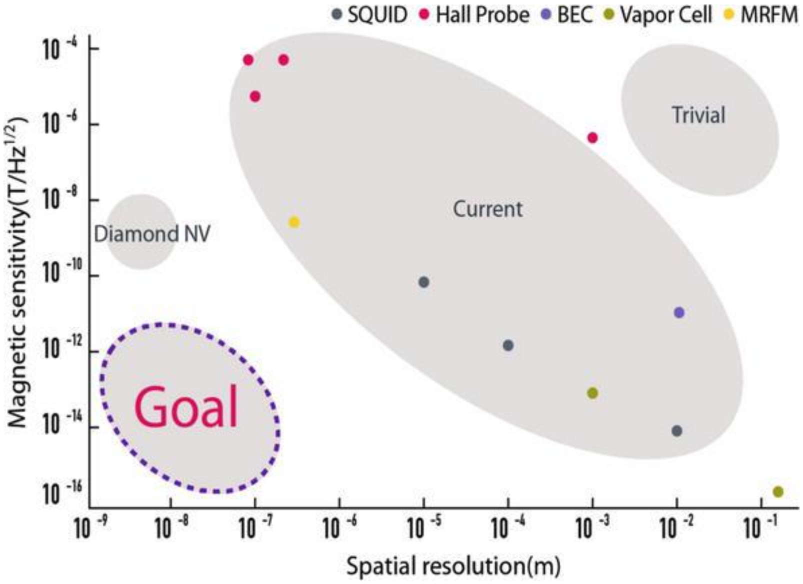

Fig. 4.1 Comparison of various magnetometers. | Spatial resolution and magnetic field sensitivity of various magnetometers. Adapted from Ref.[18]

Nitrogen-vacancy (NV) diamond magnetometry is an emergent imaging technology that is ideally suited to address the aforementioned challenge (Fig. 4.1). NV diamonds are engineered crystals that contain paramagnetic lattice defects whose electronic spin can be optically manipulated. As such, NV diamonds enable optical imaging of magnetic fields at ~ 300 nm resolution with $\mathrm{pT}/\sqrt{\mathrm{Hz}} - \mathrm{nT}/\sqrt{\mathrm{Hz}}$ sensitivity at room temperature. Additionally, the remarkable properties of NV diamonds have also enabled unprecedented new technologies for optical NMR[19] in living cells, intracellular thermometry[20], and magnetic field sensing.[21–26]

4.2.1 Electronic structure of NV color centers in a diamond lattice

All naturally colorful diamonds owe their color to impurities within their crystal lattice, which create point defects in the local electronic structure of carbon.[27] NV diamonds use unique, chemically synthesized diamond crystals which are grown using either high-pressure high-temperature (HPHT) synthesis or chemical vapor deposition (CVD). In HPHT diamond synthesis, graphite is compressed at high temperatures ($1300-2300\ ℃$) and pressures ($5-10\ \mathrm{GPa}$) in the presence of molten metal catalysts (Ni, Co, Fe) until diamond crystallizes from solution. On the other hand, CVD synthesis of diamond occurs by first activating a carbon containing gas mixture (CH_4, C_2H_2, H_2) at low pressures using a hot filament; the radicalized gas particles subsequently interact with a substrate consisting of diamond dust and nucleate on the exposed surfaces while maintaining the original tetrahedral geometry of diamond.[28]

While diamonds for industrial use have historically been synthesized using HPHT, NV diamonds today are increasingly synthesized using CVD, since this synthesis route allows for more tunable synthesis of diamonds, which is necessary for magnetic field imaging applications.[29] Nitrogen, which is one of the most common impurities in naturally occurring diamonds, is introduced into the diamond either during epitaxial CVD crystal growth, or through ion beam implantation. Nitrogen ion implantation is often favored since it allows for precise control of NV layer thickness, as well as lateral patterning on diamond substrates, both of which are critical for determining the field sensitivity of the resulting NV diamond.[30] Accordingly, an epitaxially grown diamond is first bombarded with N^+ or N_2^+ ions, which creates substitutional nitrogen ions and lattice vacancies (holes) in the crystal. Baking the ion implanted crystal at high temperatures ($\geq 400\ ℃$) causes the vacancies to diffuse through the crystal and subsequently accumulate near the substitutional nitrogen ions, thus forming a Nitrogen-Vacancy (NV) center; this is thought to occur because substitution of carbon with any other element introduces high strain into the diamond crystal, which is minimized when lattice defects are co-localized.[31,32] The resulting NV center (Fig. 4.1) can be thought of as an artificial atom that exists in either a neutral (NV^0) or charged (NV^-) state, and transitions between these two states are driven by photon-induced interconversions.[33] For the remainder of this thesis, we will focus the discussion on the negatively charged state.

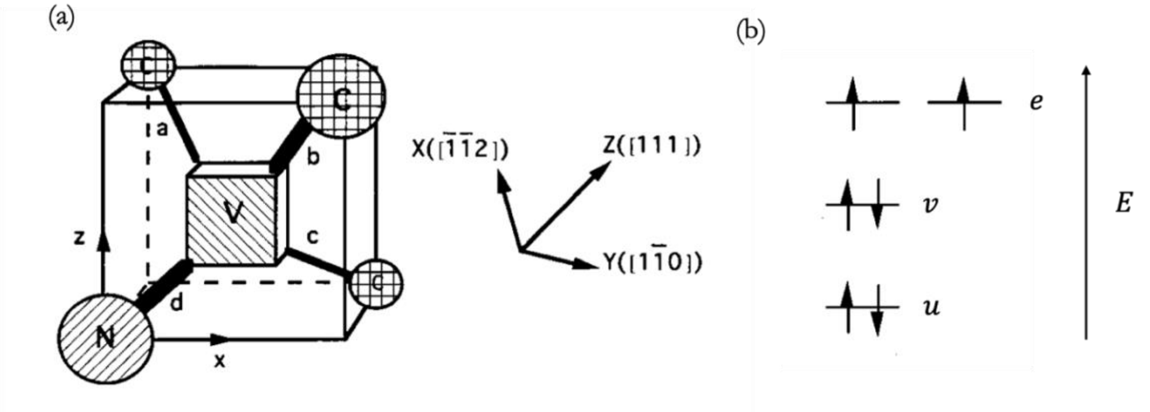

Fig. 4.2 Physical structure of the NV center | A. Physical structure of the N-V center, consisting of a substitutional nitrogen impurity (N) adjacent to a carbon vacancy (V). Both constituents are tetrahedrally coordinated to one another and three carbon atoms (C). **B.** Ground spin-state configuration for 6 active electrons in the NV^- center, consisting of low energy (but high symmetry) *u* and *v* molecular orbitals and doubly-degenerate *e* orbitals (with low symmetry and highest energy).[34] *u, v,* and *e* represent the orbital wavefunctions for the respective molecular orbitals (see Eqn. 1-6). The dipole pointing from the nitrogen into its adjacent vacancy sets the NV spin-quantization axis. Adapted from Ref.[34]

The negatively charged state (NV^-) is the most relevant electronic state for magnetic field imaging applications, and consists of 6 electrons, two of which are contributed by the lone-pair on the nitrogen ion, three of which are contributed by adjacent carbon ions, and the last of which is thought to be donated from adjacent nitrogen defects within the lattice.[34] The electronic structure of the NV^- center is calculated using linear superpositions of one nitrogen and three carbon sp^3 orbitals (Eq. 4.1-4.6), and results in a set of molecular orbitals with C_{3v} symmetry (120 ° rotation).[35,36] The lowest energy level (Fig. 4.2B) is localized on the nitrogen ion (*u*), whereas the next lowest energy eigenstate is localized between the nuclei of the carbon centers (*v*). The doubly-degenerate (*e* = [e_x,e_y]) orbitals occupy the highest energy levels in the NV center. It is immediately apparent from the electronic structure (Fig. 2b) that the NV center ground-state can be effectively modeled as a *S = 1* triplet with two unpaired electrons that can exist in either the $m_s = 0$ or $m_s = \pm 1$ spin eigenstates. The complete wavefunctions that describe the triplet and singlet (S=0) spin states of the NV center are a direct product of the symmetric and anti-symmetric orbital and spin wavefunctions (Table 4.1).

$$u = d - \lambda v \tag{4.1}$$

$$v = (a + b + c)/\sqrt{3 + 6S} \tag{4.2}$$

$$e_x = (2c - a - b)/\sqrt{6 - 6S} \tag{4.3}$$

$$e_y = (a - b)/\sqrt{2 - 2S} \tag{4.4}$$

$$S = \int ab \; d\tau \tag{4.5}$$

$$\lambda = \int dv \;\; d\tau \tag{4.6}$$

Configuration	**Wavefunction** ($\|\boldsymbol{\psi}\rangle = \textbf{Orbital}\ \|\boldsymbol{\varphi_O}\rangle \otimes \textbf{Spin}\ \|\boldsymbol{\varphi_S}\rangle$)		
	$\|\varphi_O\rangle$	$\|\varphi_S\rangle$	
Triplet **($S = 1$)**	$\|e_x e_y - e_y e_x\rangle$	$\|\downarrow\downarrow\rangle$ $\|\uparrow\downarrow + \downarrow\uparrow\rangle$ $\|\uparrow\uparrow\rangle$	$m_s = -1$ $m_s = 0$ $m_s = +1$
Singlet **($S = 0$)**	$\|e_x e_x - e_y e_y\rangle$ $\|e_x e_y + e_y e_x\rangle$ $\|e_x e_x - e_y e_y\rangle$	$\|\uparrow\downarrow - \downarrow\uparrow\rangle$	$m_s = 0$

Table 4.1 Wavefunctions of NV$^-$ ground state molecular orbitals. | The orbital and spin components are constructed from linear combinations of *sp*^{3} molecular orbitals of carbon and nitrogen within the NV center (Fig. 4.1 and Eqn. 4.1 – 4.6).

Spin-spin interactions naturally split the triplet state into high-energy ($m_s = \pm 1$) and low-energy ($m_s = 0$) eigenstates with an energy difference of (zero-field splitting) of $D_{zfs} \sim 2.87$ GHz. Exposure to an external magnetic field (**B**) breaks the degeneracy between the high-spin ($m_s = \pm 1$) eigenstates with a Zeeman shift given by $\Delta E = \gamma_e m_s \mathbf{B}$, where the electron gyromagnetic ratio (γ_e) is ~ 2.8 MHz/G. It turns out that transitions between the ground and excited states of a NV center can be optically excited and readout, which underpins the basis for all optical imaging using NV centers (Fig. 4.3). Furthermore, the long electronic spin relaxation time of NV centers ($T_{1e} \sim 1 - 10$ ms) at room temperature enables sensitive magnetometry using an array of NV pulsing schemes; this unusual property of NV diamonds is due in part to the low density of magnetically active nuclear spins (^{13}C, ^{14}N), which produce local magnetic field inhomogeneities that accelerate the decoherence of NV spins. Using isotopically pure (0.01% ^{13}C) diamonds, researchers have achieved NV coherence times approaching 1 second, which has enabled new and exciting applications in sensing.[37]

4.2.2 Optically detected magnetic resonance (ODMR) using NV centers

Transitions between the ground ($|g\rangle$) and excited electronic states ($|e\rangle$) of an NV center are optically mediated, which forms the basis of all optical magnetic field imaging. In the NV ground state, electrons exist in either the low- ($m_s = 0$) or high- ($m_s = \pm 1$) spin eigenstates.

Illumination with green (514 or 532 nm) light of a NV$^-$ center in the $m_s = 0$ state, transiently excites the spins into the $m_s = 0$ excited state, from which the system cycles back to the $m_s = 0$ ground state through broadband radiative decay within 25 ns ($\lambda_{emission} \sim 637 - 800$ nm; Fig. 3a).[33] Illumination of a NV$^-$ center in the $m_s = \pm 1$ ground state likewise excites the spins into the $m_s = \pm 1$ excited state, from which they cycle into $m_s = 0$ ground state with $\approx 70 - 80$ % probability through radiative decay. However, with $\approx 20 - 30\%$ probability, the excited $m_s = \pm 1$ state can also decay into a metastable singlet state through non-radiative ISC (Fig. 4.3A). This singlet state is long-lived (~ 300 ns) compared to the excited-state $|e\rangle$ lifetime, and the spins subsequently cycle into $m_s = 0$ ground state through a combination of radiative ($\lambda_{emission} \sim 1043$ nm) and non-radiative processes. Although the excited $m_s = 0$ can also decay into the metastable single state with some low probability, this pathway has significantly slower ISC rates which effectively results in spin transitions dominated through radiative decay.

Continuous illumination with green light (532 nm) optically polarizes NV centers into the $m_s = 0$ eigenstate, which illustrates the utility of NV diamonds as macroscopic quantum materials whose quantum states can be precisely prepared with 80 – 95% NV polarization efficacy.[38] Subsequent application of a microwave (MW) whose frequency matches the energy gap between the $m_s = 0$ and $m_s = \pm 1$ ground states, enables transitions between these two energy eigenstates which manifests itself as a drop in NV PL intensity (Fig. 4.3D). It is therefore this *state-dependent* PL contrast which serves as the basis for all optically detected magnetic resonance (ODMR) in NV magnetometry. External magnetic fields split the NV $m_s = \pm 1$ levels, thus altering the energy gap between transitions ($|0\rangle \rightarrow |1\rangle$); consequently, the microwave (MW) frequency must be concomitantly altered to match the energy difference, in order to achieve resonant population cycling. The effect of external magnetic fields on NV PL is summarized in Fig. 4.3 D-E, which demonstrates the shift in MW frequency as the external magnetic field is increased from 0 T.

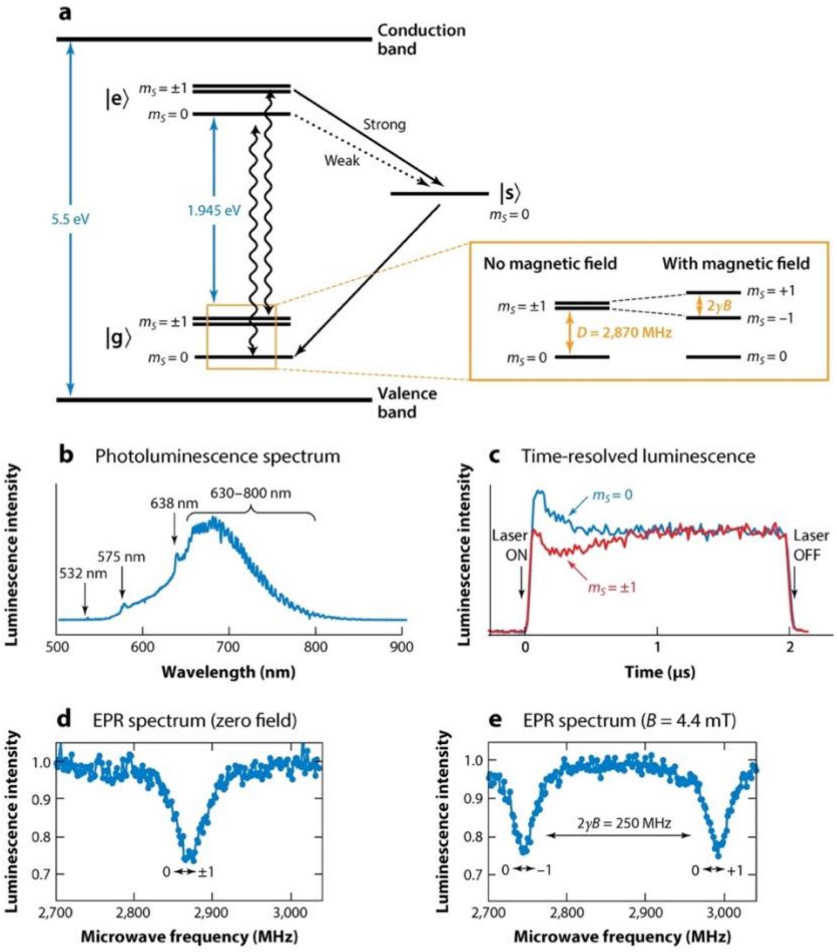

Fig. 4.3 Characteristics of the NV center. | A. Energy-level diagram of NV$^-$. $|\text{g}\rangle$ denotes the electronic ground state as discussed in the text, $|\text{e}\rangle$ denotes the electronic excited state, and $|\text{s}\rangle$ denotes the metastable, excited singlet state. There is a radiative transition within the singlet state at $\lambda = 1043\ \text{nm}$ which is not shown for simplicity. Wiggly arrows indicate radiative transition, and black arrows indicate strong and weak nonradiative decay via the metastable singlet state. The inset shows the three spin sublevels within the triplet state consisting of $m_s = 0$ and $m_s = \pm1$ at zero and nonzero magnetic field **B**. *D* is the zero field splitting as discussed in the text, and $\Delta E = 2\gamma_e B$ is the Zeeman splitting, where the pre-factor of 2 is a result of two $s = 1/2$ electrons. By convention, the lower energy transition is associated with $|0\rangle \rightarrow |-1\rangle$. **B.** Photoluminescence (PL) spectrum of a bulk NV diamond, showing the green excitation laser (532 nm), the NV^0 phonon line (575 nm), the NV$^-$ zero phonon line (638 nm), and NV- vibrational side bands (630 – 800 nm). In typical NV experiments, a non-resonant 532 nm excitation is used, and luminescence is integrated across 630 – 800 nm. **C.** Time-resolved luminescence during a 2 μs laser pulse. The curves show

histograms of photon counts excited out of the (blue) $m_s = 0$ ground state, and (red) $m_s = \pm 1$ ground state. Note that the PL contrast between the two spin states decays as a function of time since the $m_s = \pm 1$ ground states are depopulated as a result of continuous excitation. (D-E) Electron paramagnetic resonance (EPR) spectrum of a single NV center at zero and non-zero magnetic field, recorded using the optically detected magnetic resonance technique discussed in the main text. The small splitting observed at the trough of the Lorentzian even at zero magnetic field is a result of strain ($\mathbf{E}$) fields within the NV diamond. Adapted from Ref.[39]

An ODMR spectra (Fig 4.3 D-E and Fig. 4.4A) is obtained by first optically polarizing a NV diamond with green light and subsequently sweeping across MW frequencies while recording the PL spectra; if the MW frequency is resonant with spin transitions ($|0\rangle \rightarrow |\pm 1\rangle$), then a drop in PL intensity is observed at the resonant MW frequency (Fig. 4.4A). The magnitude and direction of external magnetic fields and internal electric fields is recovered by fitting the ODMR spectra to the spin-Hamiltonian of the NV center (Eq. 4.7).[40]

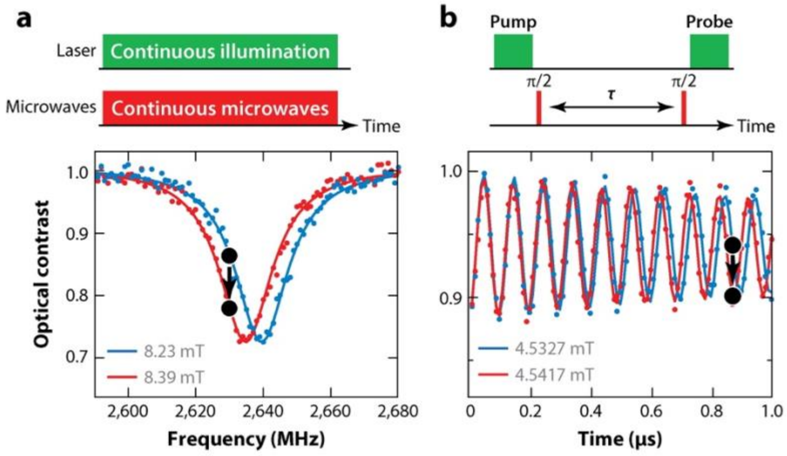

Fig. 4.4 Sensing techniques and protocols for NV magnetometry. | (Top) pulse-timing diagrams and (bottom) example measurements. **A.** Continuous-wave detection of the spectral line shift. The frequency difference between curves is 4.7 MHz, corresponding to a magnetic field difference of 0.16 mT **B.** Pulsed detection of electron spin precession in a pump probe experiment. The frequency difference between the two curves is 0.25 MHz, corresponding to a magnetic field difference of 9.0 μT. Oscillations are shown relative to a 2753 MHz carrier frequency. Adapted from Ref.[39]

$$\frac{1}{\hbar}\mathcal{H} \approx D_{zfs}\left(S_z^2 - \frac{2}{3}\right) + \gamma_e \mathbf{B}\cdot\mathbf{S} + \epsilon_z E_z\left(S_z^2 - \frac{2}{3}\right) + A_{hf}\mathbf{S}\cdot\mathbf{I} \tag{4.7}$$

Here, D_{zfs} is the zero-field splitting as before, $\mathbf{B}$ is a magnetic field vector, $\mathbf{E}$ is an electric field (strain) vector and ϵ_z is its corresponding axial (*z*) coupling constant. Additionally, A_{hf} represents the hyperfine coupling constant between the NV electron spins and the nuclear magnetic moments of ^{14,15}N and ^{13}C nuclei within the diamond lattice. Lastly, this Hamiltonian can be made more accurate by incorporating lateral (*xy*) strain, which is given by $\epsilon_{xy}\left[E_x\left(S_xS_y + S_yS_x\right) + E_y\left(S_x^2 + S_y^2\right)\right]$. In most NV experiments, a weak bias field is applied along the NV axis (Fig. 4.1) in order to quantize spins along a specific direction.

The simplest NV magnetic field sensing scheme is based on continuous wave (CW) EPR (Fig. 4.4A), whereas pulsed EPR techniques wherein the duration and temporal spacing of MW pulses are varied, enable more sensitive 'lock-in' detection of alternating magnetic fields. Since the diamond lattice has a tetrahedral geometry (Fig 4.5A), NV centers can be formed along any one of the crystallographic axes. Consequently, a bulk NV diamond, such as those used in our experiments, has NV centers along all four axes. An external magnetic field therefore has different projections along any given direction, which proportionally splits the ODMR spectrum (Fig. 4.5B). By fitting the ODMR spectrum over all NV projections, one can deduce both the magnitude and direction of the external magnetic field (Eq. 4.8-4.11).[41]

$$\boldsymbol{\delta}\mathbf{B_x} = \left(\frac{3}{2}\right)^{1/2}\frac{(\mathbf{B}_\mathrm{B} - \mathbf{B}_\mathrm{D})}{2} \tag{4.8}$$

$$\boldsymbol{\delta}\mathbf{B_y} = \left(\frac{3}{2}\right)^{1/2}\frac{(\mathbf{B}_\mathrm{A} - \mathbf{B}_\mathrm{C})}{2} \tag{4.9}$$

$$\boldsymbol{\delta}\mathbf{B_z} = (3)^{1/2}\frac{(-\mathbf{B}_\mathrm{A} - \mathbf{B}_\mathrm{B} - \mathbf{B}_\mathrm{C} - \mathbf{B}_\mathrm{D})}{4} \tag{4.10}$$

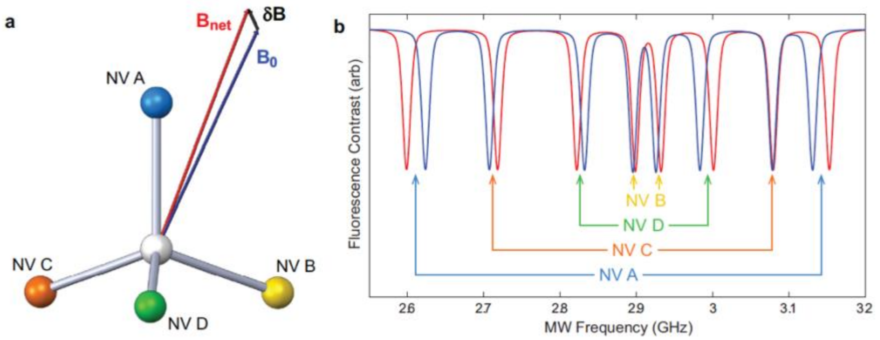

Fig. 4.5 DC vector magnetometry with bulk NV diamonds. | **A.** Diagram showing the known static field $\mathbf{B_0}$, the measured net magnetic field $\mathbf{B_{net}}$, and the extracted unknown static field ($\boldsymbol{\delta}\mathbf{B}$) in relation to the four NV crystallographic axes. **B.** Modeled ODMR spectrum of an NV ensemble in the presence of the known magnetic field $\mathbf{B_0}$ (blue) and the net magnetic field $\mathbf{B_{net}}$ (red). By measuring the resonance shifts between these two spectra, the unknown magnetic field ($\boldsymbol{\delta}\mathbf{B}$) can be extracted. Adapted from Ref.[42]

4.2.3 Factors affecting the sensitivity of NV DC magnetometry

While CW magnetometry is the simplest sensing scheme to implement for imaging static (DC) fields, it does not approach the field sensitivity conferred by pulsed ESR schemes (Fig. 4.4B).[43–46] The sensitivity of an ensemble NV EPR measurement for a DC magnetic field was previously derived (Eq. 4.11).[42,47]

$$\eta_{ESR} = \mathcal{P}_{\mathcal{F}} \frac{h}{g\mu_B} \frac{\Delta\nu\sqrt{t_m}}{\alpha\sqrt{\beta}} \tag{4.11}$$

Here, $\mathcal{P}_{\mathcal{F}}$ is a numerical pre-factor which is a function of the NV resonance line-shape (~ 0.77 for a typical Lorentzian NV profile), α is single-shot EPR contrast, β is the number of photons collected per EPR measurement, $\Delta\nu$ is the spectral linewidth of each NV resonance, and t_m is the measurement duration. While single-shot contrast (α) can be improved upon through the use of high MW powers, doing so broadens the resonance linewidth ($\Delta\nu$) because of RF energy absorption. In practice, the linewidth ($\Delta\nu$) is primarily controlled by modulating laser excitation power.[48] However, any gain in linewidth sharpness is offset by reduced photon counts in each measurement (β), which must be overcome through longer integration times (t_m). The single-shot EPR contrast (α) is also a function of NV density within the diamond, although this cannot be arbitrarily increased past a critical threshold due to increased strain in the diamond lattice, as well as spurious NV-NV couplings which decrease NV coherence lifetimes (T_{1e}, T_2^*).

Furthermore, the thickness of the NV layer and its distance from the sample also affects the sensitivity of the measurement. Although thicker NV layers are brighter and produce stronger single-shot EPR contrast, they are not suitable for imaging weak (< nT) fields due to the rapid decay of magnetic fields from their source($\mathbf{B} \sim \frac{1}{r^3}$); consequently, NVs closest to the sample experience a significantly different field than NVs farther away. Since the field sensitivity of any NV diamond pixel is the integrated EPR contrast across all NVs within its column, the EPR signal would be dominated by NVs insensitive to the source field. This explains why all nanotesla imaging demonstrations thus far have relied on shallow NV layers ($\sim 10 - 20\ \text{nm}$).[41] To compensate for reduced NV density ($\sim 10^{10} - 10^{11}\ \text{NVs/cm}^2$), integration times have to be extended for several minutes to hours to achieve satisfactory signal-to-noise ratios and optimal field sensitivity.

4.3 Technological bottlenecks with current DC magnetometry

For the purposes of live-cell imaging, such as imaging magnetotactic bacteria and engineered cells, integration time (t_m) is fundamentally constrained by cell viability. The pioneering NV studies on magnetic field imaging of live magnetotactic bacteria by the Walsworth group at Harvard achieved $\sim\ \mu\text{T}/\sqrt{\text{Hz}}$ sensitivity with their setup and were able to detect biomagnetic fields of $\sim 10^{-4}\ \text{T}$ and magnetic moments of $\sim 10^{-17}\ \text{A}\cdot\text{m}^2$ at 400 nm resolution after nearly 10 minutes of signal integration.[41] However, cell-viability was compromised during magnetic field imaging partially due to heat transfer from diamond. Since a shallow NV layer was used for imaging, high optical power densities ($I_{peak} \sim 1\ \text{kW/cm}^2$) were needed to achieve sufficient NV polarization and EPR signal. Since diamond has an extremely high thermal conductivity ($\sim 25\ \mathrm{W/cm\cdot K}$ at 300K), energy deposited into the diamond is rapidly transferred to its neighboring substrates. In the case of biological substrates, this heat transfer can drastically alter and reduce cell viability unless adequate steps are taken to thermally insulate cells from the NV diamond. In principle, one can reduce the measurement time (and exposure to thermal gradients) by using strongly magnetized cells, but fundamental improvements are necessary for imaging weakly paramagnetic cells and mapping the behavior of commonly used MRI contrast agents.[49]

Additionally, the high refractive index of diamond ($n_{diamond} \sim 2.42$) necessitates the use of high NA (> 0.9) objectives for PL capture upon NV excitation with 532nm light. One significant challenge with such high NA objectives is that their working distances are quite small to allow for wide-angle light capture. While small working distances are not problematic for imaging monolayers of magnetized cells, they are not suitable for imaging *ex vivo* tissue slices.

We were motivated to build a NV imager not only to image the magnetism of paramagnetic cells (Chapter 2), but also to understand how the distribution of magnetic materials within a cell affects its MRI contrast on the macroscopic scale. We hypothesized that taking a super-resolution approach to MRI would yield new insight on how to better design MRI contrast agents. As such, we improved on current state-of-the-art DC imaging techniques from the Walsworth group in order to build a NV imager capable of rapidly imaging cultured mammalian cells at high-sensitivity without compromising cell viability.

BIBLIOGRAPHY

1. Lefèvre, C. T. & Bazylinski, D. a. Ecology, diversity, and evolution of magnetotactic bacteria. *Microbiol. Mol. Biol. Rev.* **77,** 497–526 (2013).
2. Ramesh, P. *et al.* Ultraparamagnetic Cells Formed through Intracellular Oxidation and Chelation of Paramagnetic Iron. *Angew. Chemie - Int. Ed.* **57,** 12385–12389 (2018).
3. Mohr, A. *et al.* Wireless magnetothermal deep brain stimulation. *Science.* **347,** 1477–1480 (2015).
4. Meldrum, F. C., Heywood, B. R. & Mann, S. Magnetoferritin: in vitro synthesis of a novel magnetic protein. *Science* **257,** 522–523 (1992).
5. Louie, a Y. *et al.* In vivo visualization of gene expression using magnetic resonance imaging. *Nat. Biotechnol.* **18,** 321–325 (2000).
6. Matsumoto, Y., Chen, R., Anikeeva, P. & Jasanoff, A. Engineering intracellular biomineralization and biosensing by a magnetic protein. *Nat Commun.* **6,** 8721 (2015).
7. Greene, S. E. & Komeili, A. Biogenesis and subcellular organization of the magnetosome organelles of magnetotactic bacteria. *Curr. Opin. Cell Biol.* **24,** 490–5 (2012).
8. Murat, D., Quinlan, A., Vali, H. & Komeili, A. Comprehensive genetic dissection of the magnetosome gene island reveals the step-wise assembly of a prokaryotic organelle. *Proc. Natl. Acad. Sci. U. S. A.* **107,** 5593–8 (2010).
9. Sigmund, F. *et al.* Bacterial encapsulins as orthogonal compartments for mammalian cell engineering. *Nat. Commun.* **9,** 1990 (2018).
10. Radoul, M. *et al.* Genetic manipulation of iron biomineralization enhances MR relaxivity in a ferritin-M6A chimeric complex. *Sci. Rep.* **6,** 1–9 (2016).
11. Martell, J. D. *et al.* Engineered ascorbate peroxidase as a genetically encoded reporter for electron microscopy. *Nat. Biotechnol.* **30,** 1143–8 (2012).
12. Dyar, M. D., Agresti, D. G., Schaefer, M. W., Grant, C. A. & Sklute, E. C. Mössbauer Spectroscopy of Earth and Planetary Materials. *Annu. Rev. Earth Planet. Sci.* **34,** 83–125 (2006).
13. Fdez-Gubieda, M. L. *et al.* Magnetite Biomineralization in Magnetospirillum gryphiswaldense: Time-Resolved Magnetic and Structural Studies). *ACS Nano* **7,** 3297–3305 (2013).
14. Shah, V. K. & Wakai, R. T. A compact, high performance atomic magnetometer for biomedical applications. *Phys. Med. Biol.* **58,** 8153–8161 (2013).
15. Allred, J. C., Lyman, R. N., Kornack, T. W. & Romalis, M. V. High-Sensitivity Atomic Magnetometer Unaffected by Spin-Exchange Relaxation. *Phys. Rev. Lett.* **89,** 4–7 (2002).
16. Qian, L. Quantitative Magnetic Characterization of Single Cells. (Stanford, 2013).
17. Xu, J., Does, M. D. & Gore, J. C. Sensitivity of MR diffusion measurements to variations

in intracellular structure: effects of nuclear size. *Magn. Reson. Med.* **61,** 828–33 (2009).

18. Lee, M., Yoon, J. & Lee, D. Atomic Scale Magnetic Sensing and Imaging Based on Diamond NV Centers. in *Magnetometers - Fundamentals and Applications of Magnetism* (2019).
19. Aslam, N. *et al.* Nanoscale nuclear magnetic resonance with chemical resolution. *Nat. Nanotechnol.* **357,** 67–71 (2017).
20. Kucsko, G. *et al.* Nanometre-scale thermometry in a living cell. *Nature* **500,** 54–8 (2013).
21. Hall, L. T., Cole, J. H., Hill, C. D. & Hollenberg, L. C. L. Sensing of Fluctuating Nanoscale Magnetic Fields Using Nitrogen-Vacancy Centers in Diamond. *Phys. Rev. Lett.* **103,** 220802 (2009).
22. Arai, K. *et al.* Fourier magnetic imaging with nanoscale resolution and compressed sensing speed-up using electronic spins in diamond. *Nat. Nanotechnol.* **10,** 859–864 (2015).
23. Gould, M., Barbour, R., Thomas, N., Arami, H. & Kannan, M. Room-temperature detection of a single 19 nm super-paramagnetic nanoparticle with an imaging magnetometer. *Appl. Phys. Lett.* **105,** (2014).
24. Barry, F. *et al.* Optical magnetic detection of single-neuron action potentials using quantum defects in diamond. *Proc. Natl. Acad. Sci.* **114,** E6730–E6730 (2017).
25. Steinert, S. *et al.* Magnetic spin imaging under ambient conditions with sub-cellular resolution. *Nat. Commun.* **4,** 1607 (2013).
26. Schäfer-Nolte, E. *et al.* Tracking Temperature-Dependent Relaxation Times of Ferritin Nanomagnets with a Wideband Quantum Spectrometer. *Phys. Rev. Lett.* **113,** 217204 (2014).
27. Aharonovich, I., Greentree, A. D. & Prawer, S. Diamond photonics. *Nat. Photonics* **5,** 397–405 (2011).
28. Angus, J. C. & Hayman, C. C. Low-Pressure, Metastable Growth of Diamond and 'Diamondlike' Phases. *Science (80-.).* **241,** 913–921 (1988).
29. Edmonds, A. M. *et al.* Production of oriented nitrogen-vacancy color centers in synthetic diamond. *Phys. Rev. B - Condens. Matter Mater. Phys.* **86,** 1–7 (2012).
30. Meijer, J. *et al.* Generation of single color centers by focused nitrogen implantation. *Appl. Phys. Lett.* **87,** 1–3 (2005).
31. Pezzagna, S., Naydenov, B., Jelezko, F., Wrachtrup, J. & Meijer, J. Creation efficiency of nitrogen-vacancy centres in diamond. *New J. Phys.* **12,** (2010).
32. Nadolinny, V., Komarovskikh, A. & Palyanov, Y. Incorporation of Large Impurity Atoms into the Diamond Crystal Lattice: EPR of Split-Vacancy Defects in Diamond. *Crystals* **7,** 237 (2017).
33. Aslam, N., Waldherr, G., Neumann, P., Jelezko, F. & Wrachtrup, J. Photo-induced ionization dynamics of the nitrogen vacancy defect in diamond investigated by single-shot charge state detection. *New J. Phys.* **15,** (2013).
34. Lenef, A. & Rand, S. C. Electronic structure of the N- V center in diamond: *Phys. Rev. B* **53,** 13441–13455 (1996).
35. Maze, J. R. *et al.* Properties of nitrogen-vacancy centers in diamond: the group theoretic

approach. *New J. Phys.* **13,** 025025 (2011).

36. Manson, N., Harrison, J. & Sellars, M. Nitrogen-vacancy center in diamond: Model of the electronic structure and associated dynamics. *Phys. Rev. B* **74,** 104303 (2006).
37. Bar-Gill, N., Pham, L. M., Jarmola, A., Budker, D. & Walsworth, R. L. Solid-state electronic spin coherence time approaching one second. *Nat. Commun.* **4,** 1743–1746 (2013).
38. Pham, L. M. *et al.* Magnetic field imaging with nitrogen-vacancy ensembles. *New J. Phys.* **13,** 045021 (2011).
39. Schirhagl, R., Chang, K., Loretz, M. & Degen, C. L. Nitrogen-Vacancy Centers in Diamond: Nanoscale Sensors for Physics and Biology. *Annu. Rev. Phys. Chem.* **65,** 83–105 (2013).
40. Schirhagl, R., Chang, K., Loretz, M. & Degen, C. L. Nitrogen-Vacancy Centers in Diamond: Nanoscale Sensors for Physics and Biology. *Annu. Rev. Phys. Chem.* (2013). doi:10.1146/annurev-physchem-040513-103659
41. Le Sage, D. *et al.* Optical magnetic imaging of living cells. *Nature* **496,** 486–489 (2013).
42. Pham, L. M. Magnetic Field Sensing with Nitrogen-Vacancy Color Centers in Diamond. (Harvard, 2013).
43. Lovchinsky, I. *et al.* Nuclear magnetic resonance detection and spectroscopy of single proteins using quantum logic. *Science (80-.).* **351,** 836–842 (2016).
44. Staudacher, T. *et al.* Nuclear Magnetic Resonance Spectroscopy on a (5-Nanometer)3 Sample Volume. *Science (80-.).* **339,** 561–563 (2013).
45. Rugar, D. *et al.* Proton magnetic resonance imaging using a nitrogen-vacancy spin sensor. *Nat. Nanotechnol.* 1–12 (2014). doi:10.1038/nnano.2014.288
46. Mamin, H. J. *et al.* Nanoscale Nuclear Magnetic Resonance with a Nitrogen-Vacancy Spin Sensor. *Science (80-.).* **339,** 557–560 (2013).
47. Acosta, V. M. Optical Magnetometry with Nitrogen-Vacancy Centers in Diamond. (University of California, Berkeley, 2011).
48. Dréau, A. *et al.* Avoiding power broadening in optically detected magnetic resonance of single NV defects for enhanced dc magnetic field sensitivity. *Phys. Rev. B* **84,** 1–8 (2011).
49. Glenn, D. R. *et al.* Single-cell magnetic imaging using a quantum diamond microscope. *Nat. Methods* **12,** 736–738 (2015).

Chapter 5

MAPPING THE MICROSCALE ORIGINS OF MRI CONTRAST

Davis, H.†, **Ramesh, P.**† et al. (2018). "Mapping the microscale origins of MRI contrast with sub-cellular NV magnetometry". In: Nature Communications 9, 131. doi: 10.1038/s41467-017-02471-7
(†Equal contribution)

P.R. and H.D. co-conceived and planned the NV study. H.D. and P.R. built the magneto-microscope and prepared the *in vitro* and *in vivo* specimens. H.D. acquired and processed the NV data, and conducted the *in silico* studies on relaxation. P.R. and H.D. performed the MRI measurements and analyzed the resulting data. P.R. also participated in the preparation of the manuscript.

5.1 Motivation

Magnetic resonance imaging (MRI) is a widely used biomedical imaging modality with millions of scans performed each year for medical diagnosis, human neuroscience research and studies in animal models. The contrast seen in MRI images is strongly influenced by microscale magnetic field gradients in cells and tissues, produced by endogenous substances such as blood, cellular iron deposits[1, 2], or molecular imaging agents such as iron oxide nanoparticles (IONs).[3-6] The precise dependence of voxel-scale (~ 0.5 mm) MRI contrast on the microscale magnetic field has been a topic of intense theory and simulation due to its importance for disease diagnosis and contrast agent design.[2, 7-10] These studies predict, for example, that the spatial frequency of the local magnetic field can significantly impact the T_2 relaxation rate of a tissue, and that optimizing contrast agent size can maximize T_2 contrast for a given set of material and imaging parameters. However, despite its significance for biological imaging, the relationship between microscopic magnetic field patterns in tissue and T_2 relaxation has not been studied experimentally due to a lack of effective methods to map magnetic fields at the microscale under biologically relevant conditions.

Here, we establish a new method to study the connection between subcellular magnetic fields and MRI contrast using nitrogen vacancy (NV) magnetometry, a recently developed technique that enables the imaging of magnetic fields with optical resolution using the electronic properties of fluorescent NV quantum defects in diamond.[11] The electronic structure of an NV center forms a ground-state triplet, with the $m_s = \pm 1$ states separated from the $m_s = 0$ state by 2.87 GHz, making ground-state spin transitions addressable by standard electron spin resonance (ESR) techniques. The Zeeman energy difference between the +1 and -1 states leads to the splitting of the 2.87 GHz resonance into two distinct energy levels, whose separation from each other increases linearly with magnetic field strength. Upon green laser excitation (532 nm), the $m_s = \pm 1$ states are more likely to undergo non-radiative relaxation than the zero-spin state, so that microwave-induced transitions from $m_s = 0$ to $m_s = \pm 1$ cause a drop in NV fluorescence. Thus, the local magnetic field of an NV center can be extracted from the optically reported ground-state spin transition frequency. Diamonds densely doped with NV centers make it possible to optically image this resonant transition frequency over a wide field of view, thus providing an Abbe-limited image of the magnetic field at the diamond surface.[12]

NV magnetometry has recently been used in proof-of-concept biological applications such as imaging the magnetic fields produced by magnetotactic bacteria[13], detecting magnetically labeled cancer cells[14], visualizing paramagnetic ions bound to cells[15], and measuring magnetic fields produced by neuronal action potentials.[16] However, to date this technology has not been used to map subcellular magnetic fields in living mammalian cells or to connect these maps to *in vivo* diagnostic imaging modalities such as MRI. Doing so requires adapting NV magnetometry for high-sensitivity imaging of sparse magnetic fields in cells and tissues, developing methods to convert 2-D NV data into the 3-D distribution of magnetic field sources and simulating the behavior of nuclear spins in the resulting magnetic fields. In addition, monitoring the evolution of magnetic fields in live cells requires operating under non-damaging optical and thermal conditions with reduced available signal. In this work, we address these challenges to enable the mapping of sub-cellular magnetic fields in an *in vitro* model of macrophage iron oxide endocytosis and histological samples from a mouse model of liver iron overload, connecting both to MRI contrast.

5.2 Results

5.2.1 Mapping sub-cellular magnetic fields using our magneto-microscope

Our home-built NV magneto-microscope (Fig. 5.1A) was optimized for both high-resolution magnetic field imaging of fixed samples and dynamic imaging of living cells. By virtue of a relatively thick NV layer in our diamond (~ 4 μm), we were able to significantly reduce the applied laser power compared to shallower surface-implanted NV diamond microscopes, while maintaining a strong NV fluorescent signal for rapid imaging. We used a total internal reflection geometry to minimize phototoxicity[13, 16] and bonded a silicon carbide wafer to the diamond base to improve thermal dissipation.[16] For cell imaging experiments, we applied a moderate bias field (~ 10 mT) to magnetize cell-internalized superparamagnetic IONs. While a larger bias field would increase the magnetization of the sample, it would also produce stronger off-axis magnetic fields for each NV axis, which significantly reduces the sensitivity of NV magnetometry.[17]

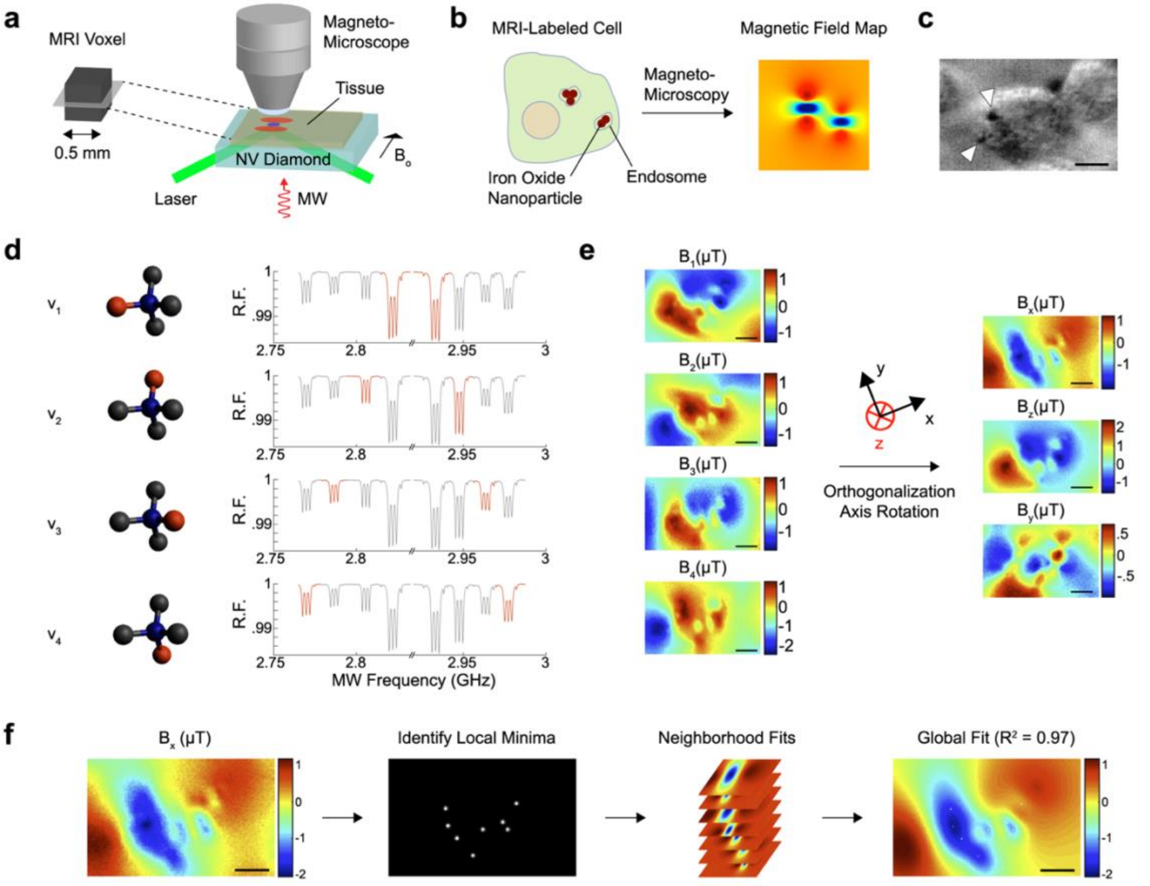

Fig. 5.1 Subcellular mapping of magnetic fields in cells labeled for MRI. | A. Schematic of sub-voxel magnetic field mapping using a NV magneto-microscope. **B.** Illustration of a cell labeled with IONs and its expected magnetic field pattern. **C.** Brightfield image of RAW 264.7 macrophage labeled with 200 nm IONS. White arrows point to internalized IONs. A brightfield imaging artifact also appears as black in the upper right corner of the cell. **D.** Cartoon representation of each NV orientation and corresponding representative spectra from fixed cell experiments. The blue ball represents the nitrogen and the red ball represents the adjacent lattice vacancy. Highlighted peaks in each relative fluorescence (RF) spectrum show the transition corresponding to each of the 4 orientations. **E.** Magnetic field images of the field projections along each of the 4 NV axes of macrophages 2 hours after initial exposure to 279 ng/ml 200 nm IONs (left). These images are converted via Gram-Schmidt orthogonalization and tensor rotation to field maps along 3 Cartesian coordinates with the z-axis defined perpendicular to the diamond surface and the x-axis defined as the projection of the applied bias field onto the diamond surface plane (right). The y-axis is defined to complete the orthogonal basis set. **F.** Representative example of the procedure for dipole localization in cellular specimens. This

procedure comprises three steps: first the local minima in the field map are identified and ranked; next, in decreasing order of magnitude, the neighborhood of each local minimum is fit to a point dipole equation and the resulting field is subtracted from the field map to reduce the fit-deleterious effect of overlapping dipole fields; finally, the results of these fits are used as guess parameters for a global fit over the full field-of-view. The fit shown has a degree-of-freedom-adjusted R^2 of 0.97. Scale bars are 5 μm.

As a first test of our method, we imaged the magnetic fields resulting from the endocytosis of superparamagnetic IONs by murine RAW 264.7 macrophages. Magnetic labeling and *in vivo* imaging of macrophages is under development for a variety of diagnostic and therapeutic applications, which could benefit from an improved understanding of the resulting MRI contrast.[4, 18-20] In particular, although labeling is typically done with dispersed particles of sizes ranging from a few nanometers to several microns[21-23], their internalization and subsequent compaction by the cell (Fig. 5.1, B-C) could produce radically different magnetic field profiles, which cannot be directly observed by conventional electron microscopy or iron staining techniques.[8-10] We performed vector magnetometry on fixed macrophages after incubating them for one hour with 200 nm, multi-core IONs and allowing one additional hour for internalization. After measuring the magnetic field along each of the four NV orientations (Fig. 5.1D), we projected the field maps along Cartesian axes convenient for magnetic dipole localization via orthogonalization and tensor rotation (Fig. 5.1E).

5.2.2 Connecting microscale fields to bulk MRI contrast

To connect microscale magnetic field measurements to MRI contrast, we first converted our 2-D images to 3-D maps of magnetic field sources in the sample, then simulated the behavior of aqueous nuclear spins in the corresponding 3-D field. To convert 2-D vector maps imaged at the diamond surface into a 3-D model of magnetic fields in cells above the diamond, we developed an algorithm for iterative localization of magnetic dipoles (Fig. 5.1F, Supplementary Fig. 5.5). First, the in-plane coordinates of putative dipole field sources (e.g., clusters of magnetic particles) were identified from local minima in the x-component of the vector field, chosen parallel to the projection of the bias field onto the diamond surface. Then, the off-diamond height (z) and magnetic moment of each cluster were determined by fitting the local dipole field profile. After fitting the dipole at the strongest local minimum, the resulting magnetic field pattern was subtracted, and the next strongest local minimum fitted, with this process repeated until all local minima were exhausted. A global fit was then performed using the results from the local fits as starting parameters. The degree-of-freedom-adjusted R^2 for all the global fits made to 6 representative particle-containing cells was greater than 0.90. Magnetic localization of nanoparticle clusters was confirmed in a separate set of cells using fluorescently labeled nanoparticles (Supplementary Fig. 5.12). In addition, independent measurements of intracellular iron concentration using inductively coupled plasma mass spectroscopy, 1.09 ± 0.10 pg Fe per cell, corroborated the estimated iron content inferred from NV measurements, which was 1.126 pg Fe per cell. The final dipole values were scaled from the 10 mT bias field of the NV instrument to the 7 T field of our MRI scanner using the bulk magnetization curve of the IONs (Supplementary Fig. 5.6).

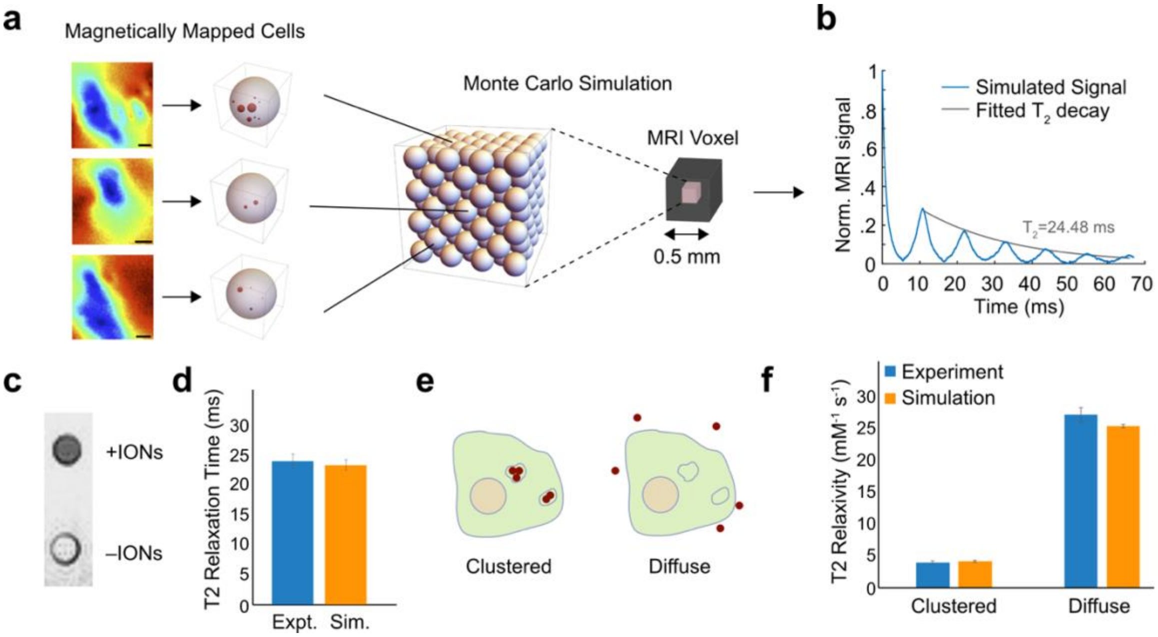

Fig. 5.2 Predicted and experimental MRI behavior in cells. | A. Schematic of Monte Carlo modeling of spin relaxation using NV-mapped magnetic fields. A library of 11 cells mapped with vector magnetometry (three representative cells shown) in a 1:1 mix with unlabeled cells, was used to randomly fill a 108 cell FCC lattice with periodic boundary conditions and run a Monte

Carlo simulation of spin echo MRI to predict T_2 relaxation behavior. **B.** Representative simulated MRI signal. **C.** T_2-weighted MRI image of cell pellets containing a 1:1 mixture of supplemented and un-supplemented cells (top) or 100% unlabeled cells (bottom). **D.** Simulated and experimentally measured T_2 relaxation times for the 1:1 mixture. **E.** Illustration of the same quantity of magnetic particles endocytosed or distributed in the extracellular space. **F.** Simulated and experimentally measured relaxivity for endocytosed and extracellular distributions of IONs. Measurements and simulations have N=5 replicates. All error bars represent ± SEM.

To translate sub-cellular magnetic field maps into predictions about MRI contrast, we performed Monte Carlo simulations of nuclear spin T_2 decoherence in lattices of representative cells. These cells contained magnetic dipole distributions and magnitudes derived from NV magnetometry of a representative cellular library (Fig. 5.2A, Supplementary Fig. 5.7). The resulting lattice thereby contains information about the spatial frequencies of the magnetic field present in the pellet tissue, a critical parameter for T_2 contrast. Importantly, since this information can be obtained from NV measurements performed on a representative sampling of cells or tissues, this obviates the need for NV evaluation of the exact individual sample imaged with MRI, enhancing the versatility of this approach.

Our simulation predicted a bulk MRI T_2 relaxation time of 24.3 ms for a 1:1 mixture of supplemented and unsupplemented cells (Fig. 5.2B). Mixing was done to obtain a sufficiently long T_2 for accurate measurement with our MRI system. When compared to an experimental MRI measurement of T_2 in macrophages prepared as in the NV experiment and pelleted in a 1:1 mixture with unsupplemented cells, the Monte Carlo prediction was accurate to within 2.8% (Fig. 5.2, C-D). Importantly, the T_2 relaxation time of the cell pellets could not have been predicted solely from the concentration of IONs in the sample, as previous simulations have suggested a major influence of packing geometry on contrast agent relaxivity.[8-10] To establish that this relationship also holds for our model system, we performed MRI measurements and Monte Carlo simulations with IONs distributed in the extracellular space (Fig. 5.2E). Per iron mass, we found that this diffuse extracellular arrangement produces approximately 6.63-fold faster T_2 relaxation than do endocytosed particles (Fig. 5.2F), underlining the importance of the microscale magnetic field patterns mapped with our method. Simulations of additional particle distributions, shown in Supplementary Fig. 5.11, examine the relative influence of particle clustering and confinement inside cells and endosomes.

5.2.3 Mapping magnetic fields in histological specimens

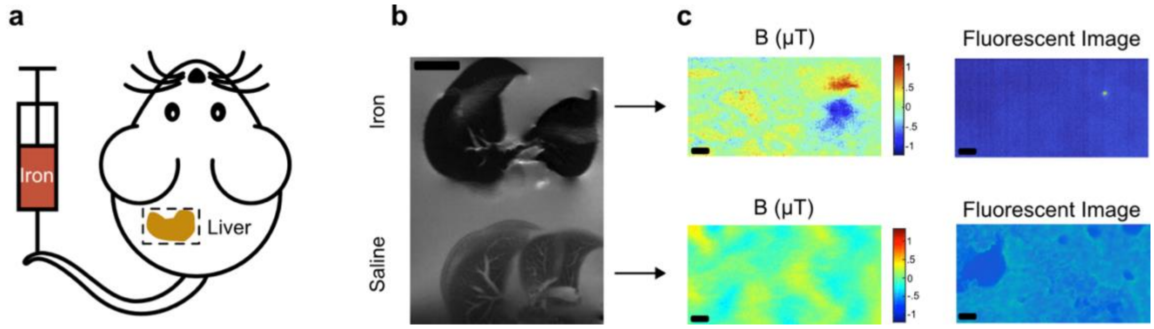

Fig. 5.3 Magnetometry of histological samples. | A. Diagram of mouse model of iron overload, as prepared by injecting 10 mg/kg of 900 nm iron oxide nanoparticles into the tail vein. **B.** 7T T_2-weighted MR image of fixed, excised mouse livers from mice injected with IONs or saline. **C.** NV magnetic field maps and fluorescence images of 10 μm liver sections obtained from the mice in B. Fluorescent images were taken with auto-gain to reduce the necessary exposure time, resulting in the visibility of the autofluorescence of the tissue in the saline control. Magnetometry scans were taken with a fixed gain. This experiment was repeated a total of three times, with data from two additional experiment shown in Supplementary Fig. 5.8. Scale bars in A, B, and C are 2.5 μm, 5 mm, and 10 μm respectively.

To extend this technique to diagnostic imaging, we performed NV magnetometry on liver specimens from a mouse model of hepatic iron overload. The spatial distribution of iron deposits in the liver and other tissues has been a topic of interest in clinical literature as an indicator of disease state, including efforts to discern it noninvasively using MRI.[2] Iron overload was generated through intravenous administration of 900 nm IONs to C57bl/6 mice (Fig. 5.3A) to produce efficient iron loading of the liver detectable by MRI. Livers were harvested 18 hours after injection and imaged with 7 T MRI, showing enhanced macroscale T_2 relaxation compared to controls (Fig. 5.3B). To investigate the microscale nature of this contrast enhancement, we cryo-sectioned the livers of saline- and iron-injected mice and imaged the magnetic field profiles of these tissue sections on our NV magneto-microscope. We measured the projection of the magnetic field along a single NV orientation, probing the $|0\rangle \rightarrow |1\rangle$ and $|0\rangle \rightarrow |-1\rangle$ transitions. The magnetic particle clusters were relatively sparse, resulting in a punctate distribution of magnetic dipoles within the liver tissue of the iron-overloaded mouse (Fig. 5.3C, Supplementary Fig. 5.8). We confirmed that these magnetic fields resulted from IONs using fluorescent imaging, for which purpose the IONs were labeled with a fluorescent dye. These results suggest that NV magnetometry could be used to map sub-voxel magnetic field patterns within histological specimens, increasing the diagnostic power of MRI by correlating magnetic field distributions to disease state.

5.2.4 Magnetic imaging of endocytosis

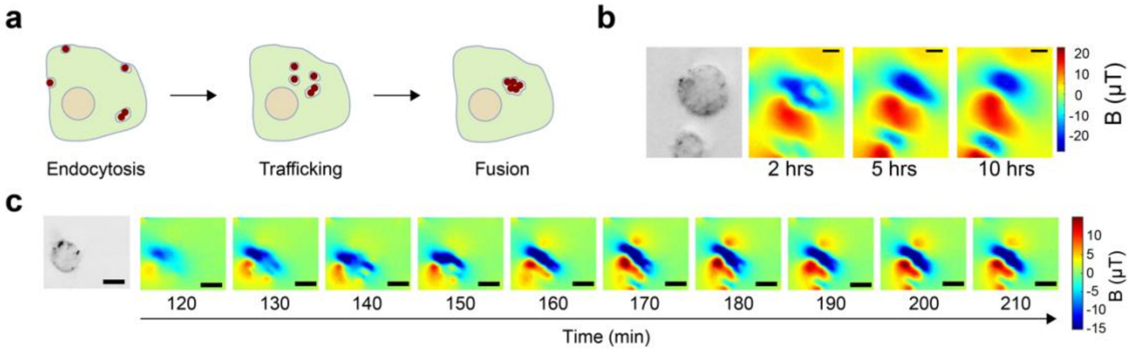

Fig. 5.4 Dynamic magnetic microscopy in live mammalian cells. | A. Cartoon showing the typical progression of endocytotic uptake of IONs. **B.** Brighfield (left) and series of time-lapse magnetic field images of RAW macrophages over 10 hours. Three additional replicates are shown in Supplementary Fig. 6. **C.** Brightfield (left) and series of time-lapse magnetic field images of a RAW macrophage with 10 min between magnetic field images. Two additional replicates of this experiment are shown in Supplementary Fig. 5.9. Scale bars are 5 μm.

Finally, we tested whether NV magnetometry could be used to follow the magnetic consequences of the dynamic redistribution of magnetic material in living mammalian cells. Macrophages endocytosing IONs go through several stages of internalization, gradually reconfiguring diffuse particles into compacted lysosomal clusters (Fig. 5.4A). This process could be relevant to interpreting MRI data from labeled macrophages and to the development of clustering-based magnetic nanoparticle contrast agents.[24, 25] To image living cells, we adjusted our NV methodology to minimize optical and thermal energy deposition. We sub-sampled the NV spectrum to probe only the $|0\rangle \rightarrow |1\rangle$ transition of one NV orientation and limited laser illumination to 5 minutes per image. This allowed us to generate time-lapse images of magnetic fields coalescing inside macrophages after ION internalization (Fig. 5.4**,** B-C, Supplementary Figs. 5.9-5.10), at the expense of precise 3-D source localization, which requires vector magnetometry using multiple NV orientations. Cell viability (assessed via a Trypan Blue exclusion assay) was ~90%. To our knowledge, this represents the first magnetic field imaging of a dynamic process in living mammalian cells and could aid the development of dynamic contrast agents for MRI.

5.3 Supporting Data

5.3.1 Verification that a Live Cell Process was required for nanoparticle trafficking

To ensure that the nanoparticle motion observed in the live cell experiments was due to a live cellular process, we also analyzed particle motion in fixed cells. Supplementary Fig. 5.10D shows that there was no observable change in the nanoparticle fields over the relevant time-course in fixed cells (~10 hours).

5.3.2 SQUID Magnetometry and Saturation Field Scaling

Strong off-axis fields shift the eigenbasis of the NV spin Hamiltonian from along the NV axis to along the applied field. In this condition, m_s is no longer an eigenstate of the spin Hamiltonian, leading to mixing of the $|0\rangle$ and $|\pm 1\rangle$ states. This effect significantly reduces the sensitivity of NV vector magnetometry at bias fields above 10 mT.[1] Therefore, all our vector magnetometry experiments were conducted with a 10 mT bias field. To translate these measurements to the 7 T field strength of MRI in Monte Carlo simulations, we scaled the measured magnetic moments from the 10 mT bias field to 7 T using the results of SQUID magnetometry performed on a dried sample containing $\sim 3 \times 10^9$ IONs (Supplementary Fig.

5.6A). This scaling works well for large pseudo-spherical clusters but does not fully account for the difference in inter-particle effects between small clusters of nanoparticles and the dried SQUID sample in a non-saturated field. As has been previously demonstrated, bulk mass magnetization of continuum nanoparticle assemblies $\mathbf{M}_{Bulk}$ is reduced from the mass magnetization of a single nanoparticle or a small nanoparticle cluster (**M**) due to magnetic dipole coupling [2] such that:

$$\mathbf{M}_{Bulk} = (1-\alpha)\mathbf{M} \tag{5.1}$$

To assess the potential impact of dipole-dipole interactions on the accuracy of our dipole scaling, we estimated it using a Monte Carlo model of magnetic coupling in nanoparticle clusters (Supplementary Fig. 5.6B). Since we used multi-core particles, we assumed that each nanoparticle has many domains and is in thermal equilibrium, allowing us to neglect the complex time-dependence of Neel relaxation for single domains. We spline-interpolated the SQUID magnetization curve in MATLAB, and solved the following many-body problem employing a similar method to one used previously to simulate magnetic dipole coupling.[3] Our governing equations are as follows:

$$\mathbf{m}_i = S[\mathbf{H}_{\mathbf{ef,i}}] = S\left[\mathbf{H}_\mathbf{0} + \sum_{j\neq i} \mathbf{H}_\mathbf{j}\right] \tag{5.2}$$

$$\mathbf{H}_\mathbf{j} = \frac{1}{4\pi}\left(\frac{3\mathbf{r}_\mathbf{ij}(\mathbf{m}_\mathbf{j}\cdot\mathbf{r}_\mathbf{ij})}{r_{ij}^5} - \frac{\mathbf{m}_\mathbf{j}}{r_{ij}^3}\right) \tag{5.3}$$

Here $\mathbf{m}_\mathbf{i}$ is the magnetic moment of the *i*th nanoparticle in the cluster, S[$\mathbf{H}_\mathbf{ef,i}$] is the splined approximation of the SQUID M vs H curve for the effective field at the location of the *i*th nanoparticle, $H_0 = 7958\frac{A}{m} = 100\text{ Oe}$ is the initial bias field applied to all nanoparticles in the lattice, and $\mathbf{r_{ij}}$ separating the *i*th and the *j*th nanoparticle. The effect on the mass magnetization of clusters due to dipole coupling is calculated as follows:

1) Nanoparticles are randomly dispersed into a pseudo-spherical arrangement with packing fraction $\eta = .33$. This value is equal to the packing fraction from our Monte Carlo simulation and is within the range of measured values in literature.[4-5]
2) The magnetic moment of each nanoparticle is calculated based on the bias field $\mathbf{H_0}$.
3) The field at each nanoparticle is calculated as the superposition of the dipole fields from the other nanoparticles in the cluster.
4) In order to enforce a smooth process, the magnetic moment magnitude and orientation of each nanoparticle are adjusted to a weighted average of their value in the previous step and the value calculated from (5.2).
5) Steps 3 and 4 are repeated until the effective applied field and the magnetic moment of each nanoparticle are aligned such that $\max\limits_{i\epsilon[1,N]}\{\frac{\|\mathbf{m_i}\times\mathbf{H_{ef,i}}\|}{\|\mathbf{m_i}\|}\} < 10^{-12}$ and the fractional change of each nanoparticle's magnetic moment is less than 10^{-15}.
6) The dipole-coupling induced magnetization's deviation from the bulk measurement is quantified as:

$$\alpha(N) = \frac{\left(\mathbf{m}_{mc}(N) - \mathbf{m}_{Bulk}(N)\right)}{\mathbf{m}_{mc}(N)} \tag{5.4}$$

Here $\mathbf{m}_{mc}(N)$ is the simulated magnetic moment of a cluster with *N* particles and $\mathbf{m}_{Bulk}(N)$ is the predicted magnetic moment for that cluster applying the bulk mass-magnetization. We assume that a 100 nanoparticle cluster behaves as bulk.

The results of this simulation are shown in Supplementary Fig. 5.11. The expected difference relative to the bulk measurement is largest for small clusters, where the dipole interaction is not in the continuum limit. However, in all cases it is below 25%, and for the mean cluster size of ~28 nanoparticles measured with our NV magnetometer it is 7.5%. The curve flattens above *N*=80, validating our treatment of *N*=100 as a bulk material. Overall, this represents a modest under-estimation of the mass magnetization, meaning that NV measurements would slightly over-estimate the mass of particles in a given cluster at 10 mT, which in turn would cause an over-estimation of the magnetic moment of a given cluster at saturation (7 T). This in turn could help to account for our simulation's ~3% over-estimation of the relaxivity of our "clustered" samples. Future work mapping magnetic fields of nanoparticles could use the presented simulations to better estimate the relaxivity from pseudo-spherical and anisotropic particle clusters.

5.3.3 Packing and Distribution Effects on T2 Relaxivity

In Fig. 5.2 of the main text we evaluated the ability of NV measurement-based Monte Carlo modeling to predict the effect of nanoparticle clustering patterns in cells on T_2 relaxivity compared to un-clustered particles distributed in the extracellular space. While these two cases enabled experimental validation of our method, we performed additional *in silico* trials of hypothetical particle geometries to better understand the parameters driving the measured difference in relaxation (Supplementary Fig. 5.11).

One hypothetical condition (Supplementary Fig. 5.11A) addresses the significance of extracellular confinement for un-clustered nanoparticles by randomly placing un-clustered nanoparticles throughout the whole lattice, including intracellular space. Dispersing the particles throughout the entire lattice slightly increases their relaxivity compared to extracellular confinement, from 25.6 ± .3 $mM^{-1}s^{-1}$ to 27.8 ± .8 $mM^{-1}s^{-1}$. However, this effect is small compared to that caused by endocytosis and clustering (Supplementary Fig. 5.11D).

Two additional hypothetical conditions utilized clusters drawn from the NV-measured cell library described in the main text. One condition (Supplementary Fig. 5.11C) examined clustered nanoparticles placed in the extracellular, rather than intracellular, space. Clusters obtained from the NV measurement library were randomly distributed throughout the extracellular space of the cell lattice. This increased T_2 relaxivity from 4.1 ± 0.20 $mM^{-1}s^{-1}$ to 6.7 ± .3 $mM^{-1}s^{-1}$ compared to the cell-confined intracellular clusters analyzed in the main text. This 63% increase can be understood as arising from a more homogeneous distribution of particles in the lattice, compared to confinement within a subset of cells. This result supports the significance of using NV magnetometry to visualize the sub-tissue and sub-cellular distribution of magnetic fields.

The final condition analyzed the effect of confining intracellular clusters in a lipid compartment (Supplementary Fig. 5.11E). We simulated the effect of such a compartment by creating an impermeable 5 nm diffusion barrier surrounding the nanoparticle clusters. This decreased the relaxivity from 4.1 ± 0.20 $mM^{-1}s^{-1}$ to 3.8 ± 0.16 $mM^{-1}s^{-1}$, within statistical error, indicating that the majority of the contrast from these large nanoparticle clusters does not come from water molecules in close proximity to the cluster surface.

5.3.4 Fluorescent Colocalization

To assess the accuracy of NV-based localization of magnetic particles in cells in the *x-y* plane, we performed vector magnetometry and fluorescent imaging on the same cellular specimens. To enable fluorescent visualization, the same nanoparticles used in the main text were labeled at their amino groups with Alexa 488 NHS (ThermoFisher Scientific). Before labeling, nanoparticles were diluted to 1 mg/ml in 0.1M sodium bicarbonate at pH = 8.2. Alexa 488 dye was dissolved in DMSO at 10 mg/ml and added in 10 times molar excess to the nanoparticle surface amino groups. Fluorescent images were taken before the NV magnetometry commenced to avoid photobleaching due to NV illumination. We then performed a 2-hour vector magnetometry scan and localized the magnetic field sources using the algorithm depicted in Fig. 5.1F**.** Alexa 488 fluorescent signal was Wiener filtered to remove background speckle and then Gaussian blurred. Local maxima of the Gaussian blurred image were designated the centroids of the fluorescent signal. The average discordance between NV and fluorescent localization was 790 ± 105 nm. In one case we were unable to establish a fluorescent centroid corresponding to a dipole that was visible on the NV magnetometry scan. Fitting of this magnetic source predicted a magnetic moment corresponding to a single nanoparticle, which may explain its weak fluorescent signal.

5.3.5 Uniqueness of Fit for Dipole Magnetization and Height off the Diamond

Here, we seek to demonstrate that for a given (*z*, **M**) value pair, there does not exist another (*z'*, **M'**) value pair such that $\mathbf{B_x}(x, y, z, \mathbf{M}) = \mathbf{B_x}(x, y, z', \mathbf{M}')$ for all values of *x* and *y*. This can be proven by contradiction. The coordinate system is set such that the point dipole is at the origin and the measurement plane is below the point dipole and is parallel to the *x-y* plane.
Assume there exists:

$$(z, \mathbf{M})\ and\ (z', \mathbf{M}')\ \text{such that}\ \ \mathbf{B_x}(x, y, z, \mathbf{M}) = \mathbf{B_x}(x, y, z', \mathbf{M}')\ \forall\ (x, y)$$

Let $(x, y) = (0, y_1)$ with $y_1 > 0$. From the equation for $B_x$provided in the main text,

$$\frac{\mathbf{M} \cdot \hat{x}}{r^3} = \frac{\mathbf{M}' \cdot \hat{x}}{r'^3} \tag{5.5}$$

Where $r_1 = \sqrt{{y_1}^2 + z^2}\ and\ r_1' = \sqrt{{y_1}^2 + z'^2}$. Simplifying

$$\frac{\mathbf{M_x'}}{\mathbf{M_x}} = \frac{r_1'^3}{r_1^3} \tag{5.6}$$

Now take $(x, y) = (0, y_2)$ with $y_2 > 0$. By similar logic:

$$\frac{\mathbf{M_x'}}{\mathbf{M_x}} = \frac{r_2'^3}{r_2^3} \tag{5.7}$$

Where $r_2 = \sqrt{y_2^2 + z^2}\ and\ r_2' = \sqrt{y_2^2 + z'^2}$. Substituting from equation 5.6

$$\frac{r_2'^3}{r_2^3} = \frac{r_1'^3}{r_1^3} \tag{5.8}$$

Plugging in the definitions and simplifying gives

$$\frac{y_1^2 + z'^2}{y_1^2 + z^2} = \frac{y_2^2 + z'^2}{y_2^2 + z^2} \tag{5.9}$$

Cross-multiplying and simplifying gives

$$z^2(y_1^2 - y_2^2) = z'^2(y_1^2 - y_2^2) \tag{5.10}$$

As the measurement plane is always below the magnetic source in our system, this implies either $z = z'$ or $y_1 = y_2$, both of which violate assumptions in the proof. Thus, sampling any two points with y>0 along x=0 on the measurement plane uniquely specifies both **M** and *z*. (It is trivial to demonstrate that this also holds for any two points with $y < 0$. The degeneracy from $y_1 = -y_2$ makes sense given the symmetric shape of the dipolar field.) Due to SNR constraints and the need to localize the (x, y) position of the dipole source, we fit to many more than two points per dipole source.

5.3.6 Supplementary Figures

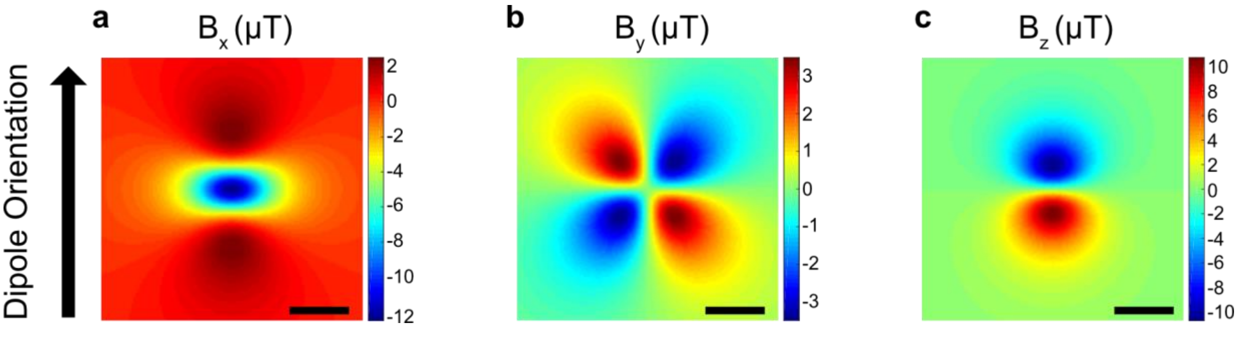

Fig. 5.5 Simulated dipole fields. | Simulated **A. B_x**, **B. B_y**, and **C. B_z** field projections for a point dipole oriented towards the top of the image with a magnetic moment of $10^{-15} A \cdot m^2$. The x and y coordinates of the dipole are fixed at the center of the image and the dipole is spaced two μm above the plane of projection. As in the main text, x is defined along the dipole

axis, *z* is defined out of the page, and *y* is defined to complete the normal basis. Scale bars are 2.5 μm.

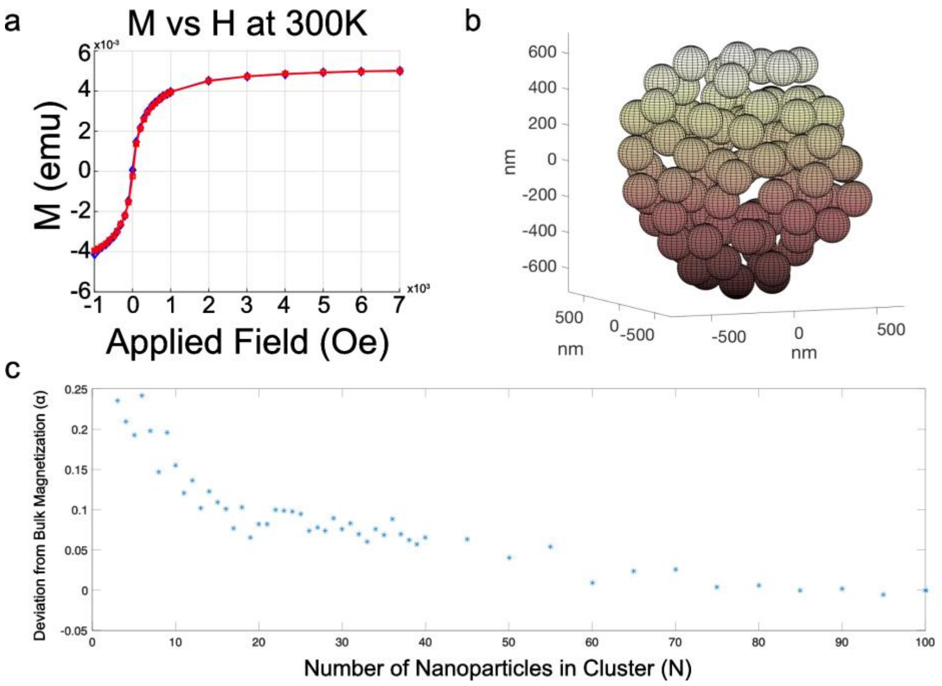

Fig. 5.6 SQUID magnetometry and saturation of IONs. | A. SQUID magnetometry of a 100 μg stock of our IONs at 300K. **B.** A representative pseudo-spherical cluster ($N = 100$ nanoparticles) used in our Monte Carlo magnetization simulations. **C.** Approximate error α of our bulk approximation for clusters containing varying numbers of nanoparticles. Each point represents the mean value from 60 random particle arrangements.

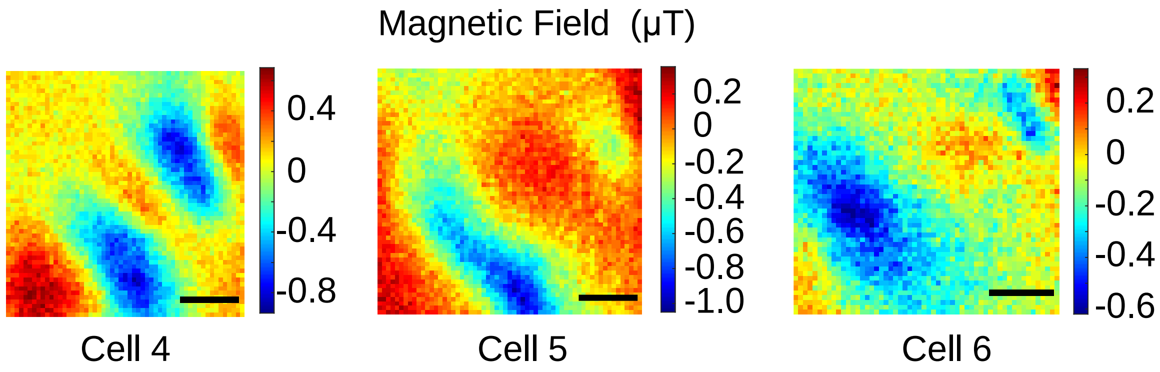

Fig. 5.7 Additional cells for Monte Carlo library. | Vector magnetometry results from three additional cells. These cells were measured as described in Fig. 5.1 with the exception that the imaging time was cut to 2 hours. Scale bars are 2.5 μm.

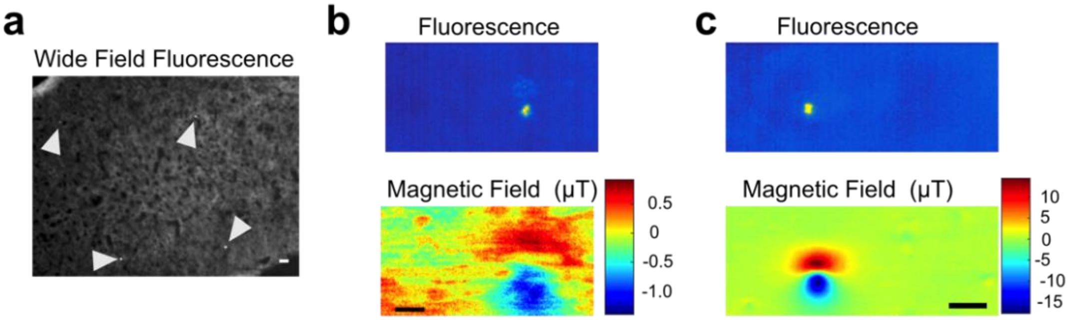

Fig. 5.8 Additional tissue sections. | A. Fluorescent image of a wide field of view of a representative liver tissue section from an iron-injected mouse. Punctate fluorescent spots from the fluorescently labeled 900 nm ION are sparsely visible in the fluorescent image. (**B., and C**) Field profile of two additional clusters measured using our NV microscope, measured as in Fig. 5.2. Scale bars are 20 μm.

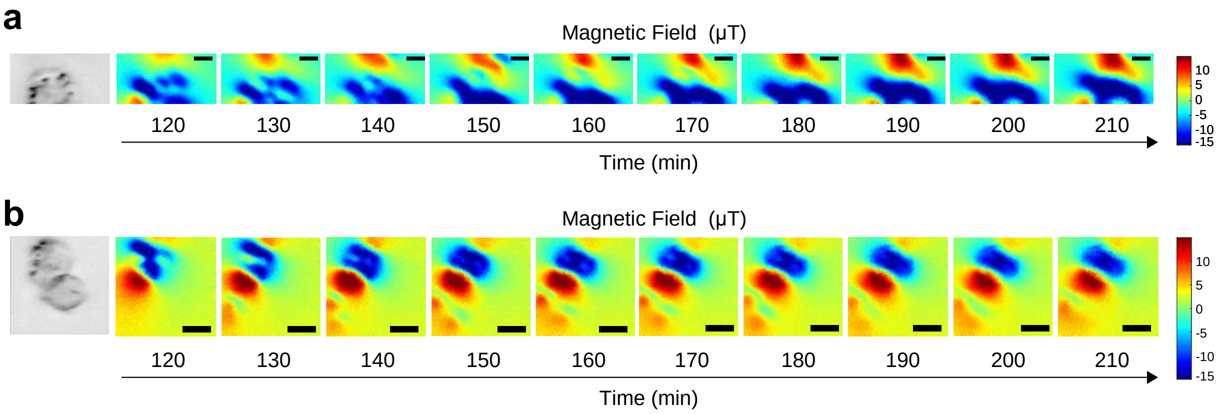

Fig. 5.9 Additional live cells. | A. and **B.** Two additional live cell replicates matching Fig. 5.3b. Cells were confirmed alive with trypan blue after NV imaging. Scale bars are 5 μm.

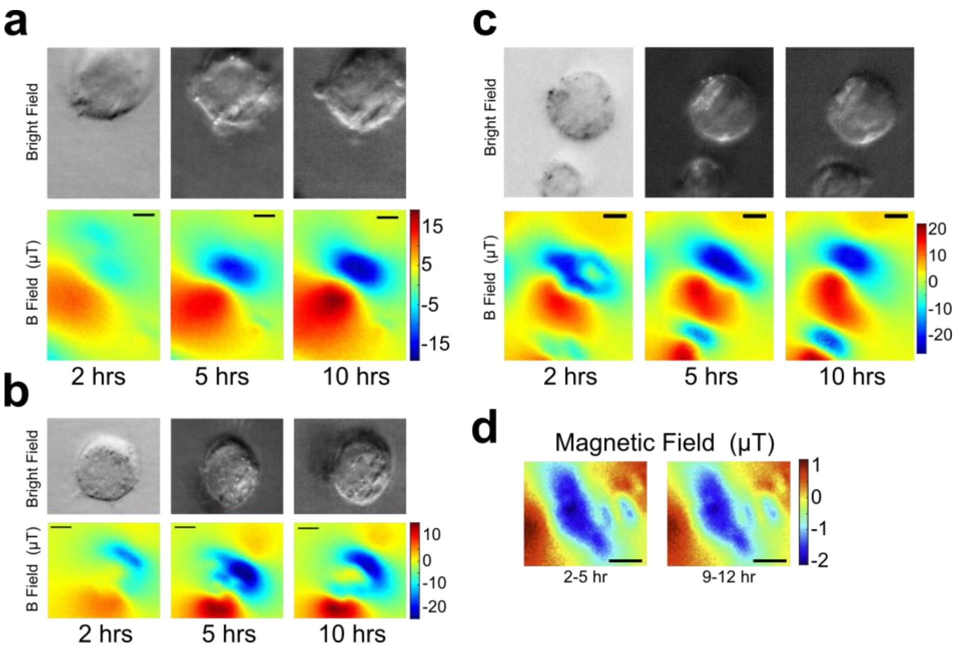

Fig. 5.10 Live cell imaging with extended time course. | A., B., and C. Bright field and magnetic images of ION endocytosis in RAW cells acquired 2, 5, and 10 hours after initial nanoparticle exposure to 279 ng/ml 200 nm IONs. Trypan blue assay revealed an ~70% viability for these imaging studies. All displayed cells were still alive after imaging. Bright field illumination was provided by a hand-positioned LED source that was repositioned between images. **D.** Magnetic field map from fixed cell acquired 7 hours apart to show the absence of dynamic changes in the magnetic field. Scale bars are 5 μm.

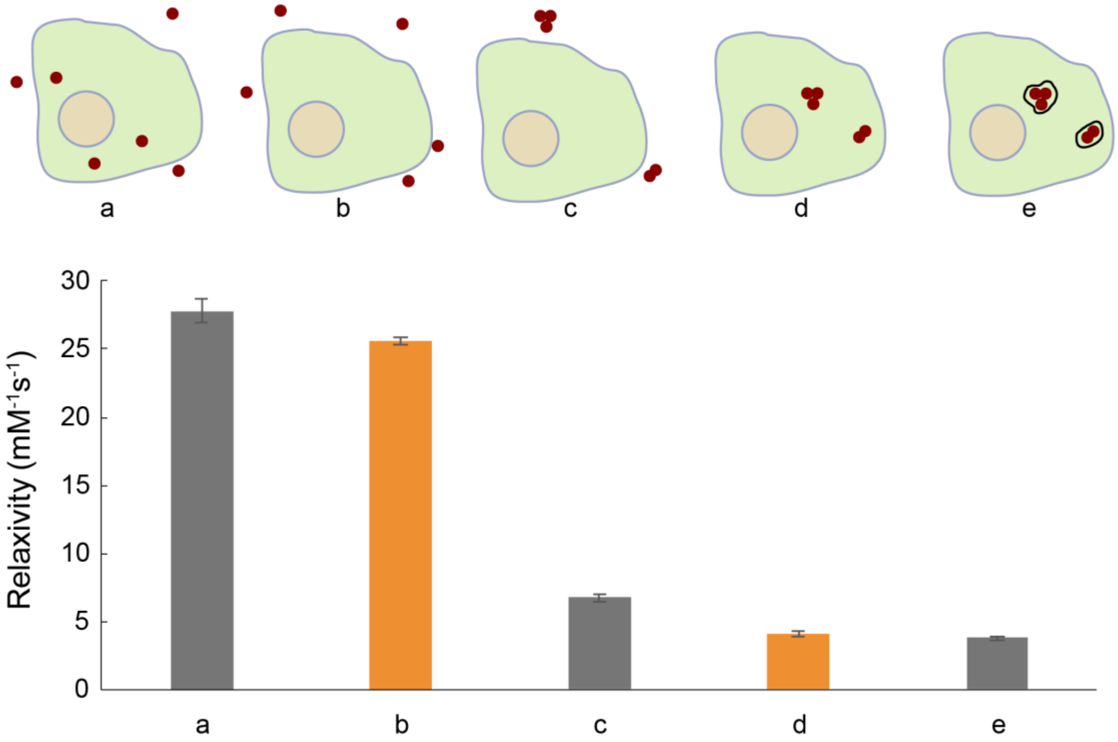

Fig. 5.11 Supplementary *in silico* models of T_2 relaxation. | In order to further assess the predicted effect of spatial frequency and cellular confinement on nanoparticle relaxivity, we simulated several additional particle distribution scenarios using the same Monte Carlo algorithm described in the main text. The scenarios are illustrated on top, with corresponding T_2 relaxivities below. Orange bars correspond to data in the main text. **A.** Diffuse (unclustered) nanoparticles were randomly placed throughout the lattice. As this geometry minimized clustering, it maximized relaxivity for our IONs. **B.** Unclustered particles randomly placed in the extracellular space in the lattice. This is the same as the diffuse condition that was experimentally verified in Fig. 5.2 of the main text. As the particles are still unclustered, the partial refocusing effect is small, maintaining the high nanoparticle relaxivity **C.** Clusters from NV-established cell library randomly dispersed throughout the extracellular space of the lattice. The clustering of the particles significantly reduces their relaxivity relative to the unclustered condition, but the large distances between the clusters significantly increase relaxivity compared to clusters spatially confined in "host" cells, as shown in (D). **D.** Cells from the NV library were randomly placed in the lattice, and clustered nanoparticles were confined inside of their host cells. This is the same condition as the "clustered" case that was experimentally verified in Fig. 5.2 of the main text. **E.** In order to determine the effect of confinement in an intracellular compartment, we added an impermeable 5 nm diffusion barrier around the clusters and randomly placed them inside their host cells as in condition (D). There

was a statistically insignificant decrease in the nanoparticle relaxivity, supporting the hypothesis that the majority of the relaxivity of these particles comes from is outer-sphere effects on aqueous protons.

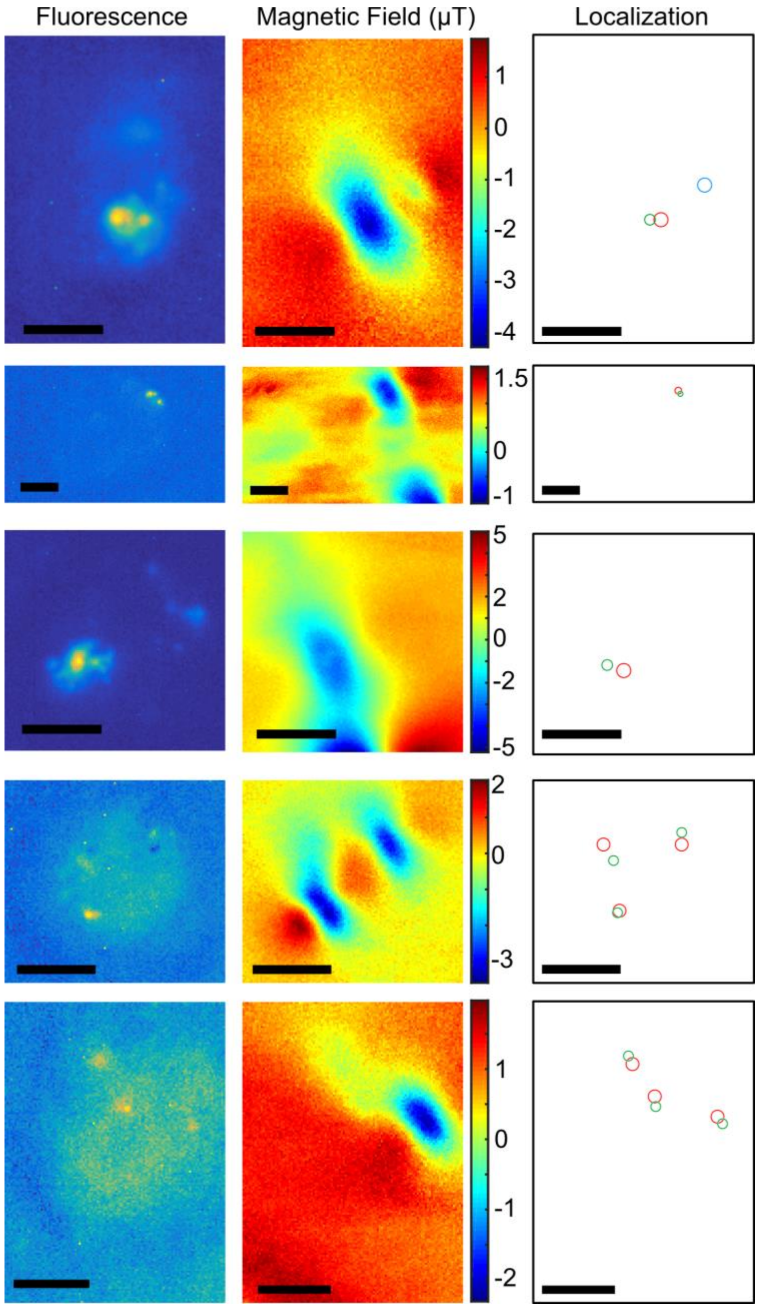

Fig. 5.12 Magnetic–fluorescent colocalization. | Fluorescence and magnetic images of fixed cells after the uptake of 200 nm IONs labeled with Alexa 488 fluorescent dye. NV localization (red circles) show strong fidelity to centroids of fluorescent images (green circles) with a mean

offset of < 800nm. Circle diameters are fixed to the diffraction limit for the NV and Alexa 488 dye fluorescence respectively. The sole mismatch occurred in the top cell, where a second dipole was visible in the NV image and localization, but there was no corresponding centroid in the Alexa 488 fluorescent image. NV localization of this dipole is marked with blue. Fitting of this dipole revealed that it possessed the magnetic moment of ~1 nanoparticle, perhaps explaining the weak fluorescent signal. Scale bars are 5 μm.

5.4 Summary and outlook for subcellular NV magnetometry

In summary, this work establishes the capability of subcellular NV diamond magnetometry to map microscale magnetic field patterns in mammalian cells and tissues and introduces computational methods to connect these patterns to MRI contrast. The ability to make this connection experimentally will facilitate the interpretation of noninvasive images through microscopic analysis of matching histological specimens and aid the development of magnetic contrast agents for molecular imaging and cellular tracking. Alternative methods for magnetic measurement, such as scanning SQUID microscopy[26, 27] and magnetic force microscopy[28, 29], are more difficult to apply to tissue-scale biological specimens due to the need to raster scan samples, the spatial offsets required for thermal insulation of SQUID magnetometers from biological materials, and the need to penetrate samples with probe tips for force microscopy. Meanwhile, methods such as electron microscopy or iron staining, which can also reveal the *in vitro* locations of putative magnetic materials based on their density or atomic composition, contain no information about the magnetic properties of such materials and their resulting fields, limiting the utility of these methods to examining the distribution of known magnetic field sources.

Although the present study also used known particles to enable direct experimental validation of our methods, NV magnetometry can in principle be used to measure magnetic field profiles arising from unknown sources, such as biomineralized iron oxide. To enable such measurements, NV imaging could be performed with a variable, electromagnet-driven bias field to first map the locations of magnetic field sources at low field (where vector magnetometry is possible), then apply a ramping field along a single NV axis to assess the M *vs.* H behavior of each field source. Such *in situ* saturation curves would provide the information needed to model MRI relaxation in samples with unknown saturation behavior.

Additional improvements in this technique may be needed to reconstruct the location and magnetization of more diffuse magnetic materials that are less easily detected as point dipoles. The sensitivity of our current instrument, established by computing the variance between 3 sequential magnetic measurements of the identical sample, was 17 nT at 1 μm in-plane resolution. This sensitivity corresponds to the field produced by a 92 nm particle situated 10 μm above the diamond surface (assuming the same volumetric magnetization as the IONs used in this study), or a 10 nm particle located immediately on top of the diamond. This sensitivity was more than sufficient to detect the 200 nm IONs used in our proof-of-concept experiments. While these particles are within the size range used in MRI contrast agents [21-23], future work should focus on improving the sensitivity of NV magnetometry and demonstrating detection of smaller sources. Sensitivity could be improved by employing diamonds with thinner NV layers, which would allow detection of significantly smaller magnetic sources near the diamond surface and would reduce the point spread function of NV-imaged magnetic fields, increasing the precision of source localization. Combined with improved methods for positioning tissue sections flatter on the diamond surface, this would allow the mapping of fields produced by smaller, endogenous magnetic inclusions and ultra-small superparamagnetic nanoparticles.

The study of microscale sources of T_2 contrast could be complemented by methods to map the concentrations of T_1 contrast agents using alternating current (AC) NV magnetometry.[15] In particular, adapting this technique to measure the 3-D distribution of T_1 agents inside of the cell using nanodiamonds[30, 31] could enable Monte Carlo modeling of T_1 relaxation in contrast-labeled cells and tissues. In addition to mapping the distribution of contrast agents and resultant magnetic fields, recent advances in NV magnetometry could allow for *in situ* imaging of water-bound proton relaxation, enabling a direct measurement of the effect of contrast agents on the relaxation of surrounding water molecules.[32]

Besides contributing to the study of MRI contrast, the methods presented for mapping magnetic field sources in 3-D from planar optical data will enable biological imaging applications directly using NV diamonds and magnetic labels. Because the optical readout in this technique is confined to the diamond surface, this method can be used to study opaque tissues inaccessible to conventional microscopy. To this end, our demonstration that time-resolved wide-field NV magnetic imaging can be performed on living cells increases the utility of this technique for monitoring dynamic biological processes.

5.5 Experimental Methods

5.5.1 Nitrogen Vacancy Magneto-Microscope

The NV magneto-microscope was constructed from a modified upright Olympus microscope and a 532 nm laser source. The diamond used in this work is an electronic grade (N < 5ppb) single crystal substrate with nominal rectangular dimensions of 4.5 mm x 4.5 mm x 500 μm, grown using chemical vapor deposition (CVD) by Element Six. The top-surface NV sensing layer is measured to be 3.87 μm thick, consists of 99.999% isotopically pure ^{12}C with 21.4 ppm ^{14}N (3.77 x 10^{17} cm^{-3}) incorporated into the layer during growth. Layer thickness and nitrogen concentration were determined by secondary ion mass spectroscopy. The diamond was irradiated with a 4.5 MeV electron source with an irradiation dose of 9 x 10^{18} cm^{-2}. The samples were subsequently annealed at 400°C for 2 hrs, 800°C for 16 hrs and 1200°C for 2 hrs. This diamond was affixed to a silicon carbide wafer (for enhanced heat dissipation), which was in turn affixed to a pair of triangular prisms to facilitate a total internal reflection excitation path. The prisms, silicon carbide wafer and diamond were fused using Norland Optical Adhesive (NOA 71). The diamond assembly was removable to allow live cell culture on the diamond surface in a cell culture incubator. Light was collected from the top of the diamond through a water-immersion objective. Images were acquired on a Basler acA2040-180kmNIR - CMV4000 CCD camera with 2048x2040 5.5 μm pixels (we used 256x1020 pixels to increase frame rate). For high-resolution vector magnetometry and tissue imaging, NV fluorescence was excited using a 100 mW Coherent OBIS LS 532 nm optically pumped semiconductor laser. For live cell imaging, we used an attenuated 2 W 532 nm laser from Changchun New Industries Optoelectronics. When necessary, focal drift was adjusted for using a piezo-driven stage (Thorlabs). Microwave radiation was applied through a single turn copper loop immediately surrounding the diamond. The microwave signal was generated by a Stanford Research Systems

Inc. SG384 signal generator and amplified by a ZHL-16W-43-S+ amplifier from MiniCircuits. Experimental timing was controlled by a National Instruments USB 6363 X Series DAQ. A bias magnetic field was generated by two NeFeB grade N52 magnets (1"x2"x.5", K&J Magnetics) positioned on opposite sides of the NV diamond. The NV setup was controlled by custom software written in LabView.

5.5.2 Cell Culture

RAW 264.7 cells (ATCC) were cultured at 37° C and 5% CO_2 in DMEM (Corning Cellgro) and passaged at or before 70% confluence. For particle labeling, media was aspirated and replaced with phenol red-free DMEM supplemented with 279 ng/ml IONs (200 nm Super Mag Amine Beads Ocean Nanotech, MHA). After one hour, the ION solution was aspirated, and cells were washed twice with PBS to remove unbound particles. For fixed-cell magnetometry, the cells were trypsinized quenched with DMEM and deposited on the diamond surface at 40-70% confluency. After a 1-hour incubation on the diamond under ambient conditions, the cells were fixed with 4 % paraformaldehyde-zinc fixative (Electron Microscopy Services) and washed twice with PBS.

For live cell imaging, the cells were cultured as above until trypsinization and spotting on the diamond. Their media was supplemented with 0.1 mM ascorbic acid to mitigate phototoxicity.[33] For extended imaging (Supplementary Fig. 5.10A), the cells were maintained on the diamond in DMEM supplemented with 10 mM HEPES to stabilize pH at 7.4 under ambient atmosphere.

5.5.3 Vector Magnetometry

The bias magnetic field was aligned close to in-plane with the diamond surface while having sufficient out-of-plane field strength to resolve the resonance of each NV axis, and the full NV optically detected magnetic resonance (ODMR) spectrum was probed. The out-of-plane component was necessary because a purely in-plane bias field did not provide each NV axis with a unique parallel B-field, causing absorption lines to overlap. The microwave resonance for each pixel in the image was set as the center of the middle hyperfine peak of the transition. Spectra were swept at 0.5 Hz with 2000 images acquired per spectrum (0.9 ms exposure time). Images were acquired with an Olympus 60x water immersion objective (NA 1.0). Magnetometry spectra were acquired for 2 hours each. For a sub-set of measurements, this time was extended to 6 hours to improve SNR.

Projection field maps for each NV orientation were generated from the corresponding peaks in the NV ODMR spectrum, and the background magnetic gradient from the bias magnets (32 μT/mm in a representative scan) was subtracted out by fitting the background to a 2D quadratic function and subtracting the fit from the signal. Projection field maps were combined to form 3 orthogonal field maps with $\mathbf{B}_z$ oriented normal to the diamond sensing surface. $\mathbf{B}_x$ is defined as the projection of the applied field onto the diamond plane and $\mathbf{B}_y$ is defined along the vector that completes the orthogonal set. Pixels were binned 2 x 2 in post-processing to boost SNR. (This does not cause a significant reduction in resolution as the binned pixels in the object plane are 92 nm on a side, which oversamples the Abbe limit of ~340 nm.)

5.5.4 Live Cell Magnetometry

For live cells, the bias magnetic field was aligned such that it was possible to resolve at least one NV resonance, and the magnetic field projection along a single NV orientation was probed using the $|0\rangle \rightarrow |+1\rangle$ transition. The microwave resonance for each pixel in the image was set as the center of the middle hyperfine peak of the transition. While probing only one NV transition allowed us to reduce the light dose to the sample while maintaining good SNR, it also limited our information to a projection of the field along one axis. This limitation precludes the source fitting performed on the fixed samples. Spectra were swept ~10 MHz at 1 Hz with 200 images acquired per spectrum (4 ms exposure time). In order to limit phototoxicity, each image was averaged for only 5 minutes and the laser was shuttered for five minutes in between images, resulting in a 50% duty cycle. Regions of interest were selected to include all relevant fields for a given cell. Optical power density was ~40 W/cm^2. Images were acquired with a Zeiss 40x near infrared water immersion objective (NA 0.8). Cell viability was assessed by performing a Trypan Blue exclusion assay after NV measurements.

5.5.5 Intracellular Iron Quantification

We performed inductively coupled plasma mass spectrometry (ICP-MS) to independently confirm the intracellular iron concentration estimated by NV magnetometry. RAW 264.7 cells were cultured and labeled with IONs as described above. After trypsinizing, the cells were counted using a disposable hemocytometer (InCYTO C-Chip). The cells were then pelleted at 400 g for 5 min, and the supernatant was aspirated. The cell pellet was first boiled in 2 mL of 70% nitric acid (ICP grade, Sigma) for 24 hrs to completely oxidize and dissolve any intracellular iron. The dried residue was then resuspended in 2% nitric acid and diluted 10-fold with deionized water for analysis using an Agilent ICP-MS quadrupole spectrometer. Un-supplemented cells contained 0.21 ± 0.04 pg Fe per cell. A procedural blank was included throughout the process to account for background iron contamination (~ 34 ppb), which was subtracted from measured samples.

5.5.6 Field Fitting and Dipole Localization

In-plane dipole coordinates were identified as local minima in the $\mathbf{B}_x$ field map. Before localization, the field map was spatially low-passed (2D Gaussian filter with σ = 0.5 pixels) to eliminate noise-generated local minima in the background. A pixel was identified as a local minimum if and only if its $\mathbf{B}_x$ field value was smaller than all of its immediate neighbors (including diagonals) in the spatially low-passed image.

Starting with the strongest local minimum, the measured magnetic field in a 10x10 pixel (~ 1.8 x 1.8 μm) square surrounding this minimum was fitted to a point dipole equation and averaged through the full NV layer depth (assuming uniform NV density), with the magnetic moment, height off of the diamond, and dipole orientation as free parameters.

$$\mathbf{B}_x(i,j) = \frac{\int_{-z}^{-(z+h)} \mathbf{B}_{xo}(i',j',b,M,\theta,\phi)\cdot db}{-h} \tag{5.11}$$

Where

$$\mathbf{B}_{xo}(i,j) = \frac{\mu_0}{4\pi} \cdot \left(\frac{3\,x\,(\mathbf{M} \cdot \mathbf{r})}{r^5} - \frac{\mathbf{M} \cdot \hat{x}}{r^3} \right) \tag{5.12}$$

Here i'=(i-i_0) and j'=(j-j_0) where (i_0,j_0) are the in-plane coordinates of the magnetic dipole, θ and ϕ correspond to the two rotational degrees of freedom available to a point dipole, $\mathbf{M}$ is the magnetic moment, *z* is the height of the dipole over the diamond, **r** is the displacement vector, $\hat{x}$ is the unit vector along the projection of the dipole axis onto the diamond surface plane, $x = i' \cos(\theta) - j' \sin(\theta)$, *b* is a dummy variable for integration through the NV layer, and *h* is the NV layer thickness. All parameters are free to fit other than the in-plane dipole coordinates, which are fixed by the local minimum of the $\mathbf{B}_x$ field map. While the *z* offset between the dipole and the diamond and the magnetic moment of the dipole both affect the strength of the detected field, they have distinguishable effects on the resultant field pattern. This is clear from the distinct dependence of the dipole function on **M** and **r**, as shown in the Supplementary Information.
After the strongest minimum has been fitted, the fitted field from the fit dipole (within the full field of view) was subtracted from the magnetic field image, to facilitate the fitting of weaker dipoles. The 10x10 pixel neighborhood of the second strongest dipole was then fitted in the subtracted image. The fitted field was subtracted, and the fitting continued until the list of local minima had been exhausted.

A global fit was then performed using the results from the neighborhood fits as starting parameters. The global fit function is the sum of *N* dipoles (where *N* is the number of local minima) with the in-plane dipole coordinates fixed at the local minima.

$$\mathbf{B}_{\mathbf{x_{tot}}}(i,j) = \sum_q \mathbf{B}_{\mathbf{x_q}}(i,j) \tag{5.13}$$

Here q is an index that runs from one to *N* and indicates the dipole field source. The precision of this technique is limited by the key assumption that the local minima are not significantly shifted in the *x-y* plane by neighboring dipoles. The degree of freedom-adjusted R^2 for each of the four global fits in the cell library was greater than 0.9. (For 3 of the 6 labeled cells, with image acquisition time increased from 2 to 6 hours, the R^2 was greater than 0.95). While this approach was able to produce a sufficiently precise magnetic field reconstruction to predict MRI relaxation, other methods are also available for analytic dipole localization and magnetic field reconstruction.[34]

5.5.7 Monte Carlo Simulations & Cell Library

Nuclear spin relaxation was simulated by assigning 11 representative cells from vector magnetometry to random positions in a repeating face-centered cubic (FCC) lattice containing a total of 108 spherical cells with periodic boundary conditions. The intracellular volume fraction of this packing geometry is 74%. While spherical cells in a periodic lattice represent a geometric simplification compared to real tissues, this and similar simplifications have been used previously to model diffusion in cell pellets and tissues.[35-37] Cell size was set to match previously measured values for RAW 264.7 cells.[38] Water molecules were randomly assigned initial x, y, and z coordinates in the lattice and allowed to diffuse while their phase in the rotating frame evolved from $\phi(0) = 0$ by $\delta\phi(t) = -\gamma\mathbf{B}(x, y, z)\delta t$, where $\mathbf{B}(x, y, z)$ is the local nanoparticle-induced field. This phase step does not account for inner-sphere effects from water coordinating to the nanoparticle surface. Re-focusing pulses were simulated at 5.5 ms Carr-Purcell time (11 ms echo time) by setting $\phi(t) = -\phi(t - \delta t)$. Adjusting the Carr-Purcell time has been demonstrated to significantly affect the efficacy of the refocusing pulses in T_2 sequences. We used an 11 ms echo time to match the echo time of our cell pellet MR measurements. The magnetic field was mapped within this 3D-volume using a finite mesh whose mesh size was inversely proportional to the local field gradient. If a water molecule moved within a distance equivalent to six nanoparticle cluster radii of a cluster, the field contribution from that cluster was calculated explicitly. Background RAW cell relaxation was accounted for by post-multiplying the simulated signal with an exponential decay with time constant set to the measured relaxation rate of an unlabeled RAW cell pellet. Cell membranes were modeled as semi-permeable boundaries with a permeability of .01 $\frac{\mu m}{ms}$ in accordance with previously measured values for murine macrophage-like cells, adjusted to the temperature in our magnet bore (12.9ºC).[39] Intracellular and extracellular water diffusivity were set, respectively, to 0.5547 and 1.6642 $\frac{\mu m^2}{ms}$ in accordance with previous studies of cellular diffusion[35, 36, 40] and established values for water diffusivity at 12.9 ºC[41], the temperature of our scanner bore. Bulk spin magnetization in the sample was calculated as $\mathbf{M}(t) = \sum_i \cos[\phi_i(t)]$, where i is the index of simulated water molecules and the magnetic moment of a single molecule is normalized to 1.

Nanoparticle clusters were modeled as spheres packed so as to occupy three times the volume of their constituent nanoparticles, within the range of measured literature values and grain packing theory.[42,43,44] To account for the increase in nanoparticle magnetizations at 7 T compared to our NV bias field, we scaled dipole magnetization using a SQUID-measured curve (Supplementary Fig. 5.6A). Magnetic dipole coupling effects between particles were neglected, as is valid for our average cluster size and geometry. (See Supplementary Information for further discussion.) Data presented in the manuscript represents the output of $N = 10$ simulations, each containing 20 random arrangements of cells and 2000 water molecules. The number of trials was chosen such that the SEM for our simulations was smaller than the SEM of our corresponding experiments.

To assess the impact of an alternative nanoparticle distribution (Fig. 5.2, E-F), we simulated the same 200 nm nanoparticles, unclustered and distributed randomly in the extracellular space. The presented data comprises $N = 10$ simulations, each containing 20 random arrangements of particles and 2000 water molecules.

5.5.8 MR Imaging and Relaxometry

Imaging and relaxometry were performed on a Bruker 7 T MRI scanner. A 72 mm diameter volume coil was used to both transmit and receive RF signals. To measure the T_2 relaxation rate of RAW cells after nanoparticle labeling, the cells were labeled identically to their preparation for NV magnetometry, then trypsonized, resuspended in 10 mL DMEM and pelleted for 5 min at 350 g. DMEM was aspirated and cells were resuspended in 150 μL PBS. The cells were mixed with an equal number of un-supplemented cells during resuspension in PBS to extend the T_2 time of the final pellet, improving the fidelity of the T_2 fit. After transferring the cells to a 300 µL centrifuge tube, the cells were pelleted for 5 min at 350 g. These tubes were embedded in a phantom comprising 1% agarose dissolved in PBS and imaged using a multi-echo spin echo (CPMG) sequence (TR = 4000 ms, TE = 11 ms, 2 averages, 20 echoes, 273x273x1000 µm voxel size). T_2 relaxation was obtained from a mono-exponential fit of the first 6 echoes. As an input into Monte Carlo simulations, we measured the "background" relaxation of 4 pellets of un-supplemented RAW cells using the same parameters as above, except that since the T_2 was significantly longer, we fitted the first 20 echoes.

For the scenario in which nanoparticles are un-clustered in the extracellular space, un-supplemented RAW cells were pelleted and re-suspended in PBS supplemented with 100 µg/ml IONs. This concentration was selected to ensure a measurable T_2 and allow both *in silico* and *in cellulo* comparisons between the per-iron relaxation rates of extracellular and internalized particle scenarios. The validity of a per-iron comparison was confirmed by previous studies of the linearity of relaxivity for this size of iron oxide nanoparticles when un-clustered.[45] To limit endocytosis, cells were moved to the cold MRI bore and imaged immediately after supplementation and pelleting. Imaging parameters were as described above.

5.5.9 Mouse Model of Iron Overload

Animal experiments were conducted under a protocol approved by the Institutional Animal Care and Use Committee of the California Institute of Technology. Female C57bl/6 mice were injected in the tail vein with 10 mg/kg of dragon green labeled 900 nm ION (Bangs) or saline. A total of three mice were used in this study. No randomization or blinding were needed given the design of the study. 16 hours after injection, the mice were perfused with 2 mL of 10% formalin, and their livers were harvested for MRI or NV magnetometry. MRI was performed on livers embedded in 1 % agarose using the 7 T scanner described above, using a spin-echo pulse sequence with T_R = 2500, T_E = 11 ms, 4 averages, and a 273x273x1000 µm voxel size. For NV magnetometry, the liver was frozen in OCT embedding media and sectioned into 10 µm slices. Sections were mounted in on glass coverslips. We inverted the glass cover slip and pressed the tissue sample against the NV diamond. Silicon vacuum grease was applied at the edge of the cover slip (away from the diamond) to hold the sample against the diamond. After this preparation was complete, PBS was added to the dish to wet the sample. We performed fluorescent imaging to locate magnetic sources in the tissue. As the sources were sparsely distributed, the camera was set to an auto-gain function to allow for short exposure time and rapid scanning. The camera was set back to fixed gain before NV imaging commenced. To compensate for magnetic field sources being further from the diamond due to tissue thickness and/or folds in the sections, NV imaging was performed with a strong (25 mT) bias field applied along a single NV axis. This strong bias field served to increase the magnetization of the magnetic inclusions in the liver. As it was applied along an NV axis, this bias field did not significantly reduce the contrast of the relevant ODMR spectral lines. However, such a strong bias field precludes the use of vector magnetometry. Future improvements to histological sample preparation should increase the sample flatness and bring the magnetic material closer to the diamond surface, allowing for a lower bias field and, as a result, vector magnetometry and source localization. Images were acquired with a Zeiss 40x near infrared water immersion objective (NA 0.8).

5.5.10 Software and Image Processing

All fits and plots were generated in MATLAB. Monte Carlo Simulations were performed in C++ on a Linux High Performance Computing Cluster.

5.5.11 Statistical Analysis

Sample sizes were chosen on the basis of preliminary experiments to have sufficient replicates for statistical comparison. Data are plotted, and values are given in the text, as mean ± S.E.M. Statistical comparisons assumed similar variance.

BIBLIOGRAPHY

1. Rouault, T.A. Iron metabolism in the CNS: implications for neurodegenerative diseases. *Nat. Rev. Neurosci.* **14**, 551-564 (2013).
2. Ghugre, N.R. & Wood, J.C. Relaxivity-iron calibration in hepatic iron overload: Probing underlying biophysical mechanisms using a Monte Carlo model. *Mag. Res. in Med.* **65**, 837-847 (2011).
3. Corot, C., Robert, P., Idée, J.-M. & Port, M. Recent advances in iron oxide nanocrystal technology for medical imaging. *Advanced Drug Delivery Rev.* **58**, 1471-1504 (2006).
4. Weinstein, J.S. *et al.* Superparamagnetic iron oxide nanoparticles: diagnostic magnetic resonance imaging and potential therapeutic applications in neurooncology and central nervous system inflammatory pathologies, a review. *Journal of Cerebral Blood Flow & Metabolism.* **30**, 15-35 (2010).
5. Kircher, M.F., Gambhir, S.S. & Grimm, J. Noninvasive cell-tracking methods. *Nat. Rev. Clin. Onc.* **8**, 677-688 (2011).
6. Shapiro, E.M., Sharer, K., Skrtic, S. & Koretsky, A.P. In vivo detection of single cells by MRI. *Mag. Res. in Med.* **55**, 242-249 (2006).
7. Vuong, Q.L., Gillis, P. & Gossuin, Y. Monte Carlo simulation and theory of proton NMR transverse relaxation induced by aggregation of magnetic particles used as MRI contrast agents. *J. Magnetic Resonance.* **212**, 139-148 (2011).
8. Bowen, C.V., Zhang, X., Saab, G., Gareau, P.J. & Rutt, B.K. Application of the static dephasing regime theory to superparamagnetic iron-oxide loaded cells. *Mag. Res. in Med.* **48**, 52-61 (2002).
9. Gossuin, Y., Gillis, P., Hocq, A., Vuong, Q.L. & Roch, A. Magnetic resonance relaxation properties of superparamagnetic particles. *Wiley Interdisciplinary Reviews: Nanomedicine and Nanobiotechnology.* **1**, 299-310 (2009).
10. Matsumoto, Y. & Jasanoff, A. Relaxation induced by clusters of superparamagnetic nanoparticles: Monte Carlo simulations. *Mag. Res. Imaging.* **26**, 994-998 (2008).
11. Balasubramanian, G. *et al.* Nanoscale imaging magnetometry with diamond spins under ambient conditions. *Nature.* **455**, 648-651 (2008).
12. Schirhagl R, C.K., Loretz M, Degen CL. Nitrogen-Vacancy Centers in Diamond: Nanoscale Sensors for Physics and Biology. *Annu. Rev. of Phys. Chem.* **65**, 83-105 (2014).
13. Le Sage, D. *et al.* Optical magnetic imaging of living cells. *Nature.* **496**, 486--489 (2013).
14. Glenn, D.R. *et al.* Single-cell magnetic imaging using a quantum diamond microscope. *Nat. Meth.* **12**, 736-738 (2015).

15. Steinert, S. *et al.* Magnetic spin imaging under ambient conditions with sub-cellular resolution. **4**, 1607 (2013).
16. J. F. Barry, M.J.T., J. M. Schloss, D. R. Glenn, Y. Song, M. D. Lukin, H. Park, R. L. Walsworth Optical magnetic detection of single neuron action potentials using quantum defects in diamond. *arXiv:1602.01056* (2016).
17. Tetienne, J.P. *et al.* Magnetic-field-dependent photodynamics of single NV defects in diamond: an application to qualitative all-optical magnetic imaging. *New Journal of Physics*. **14**, 103033 (2012).
18. Daldrup-Link, H.E. *et al.* MRI of tumor-associated macrophages with clinically applicable iron oxide nanoparticles. *Clinical Cancer Research*. **17**, 5695-5704 (2011).
19. Zanganeh, S. *et al.* Iron oxide nanoparticles inhibit tumour growth by inducing pro-inflammatory macrophage polarization in tumour tissues. *Nat. Nano.* (2016).
20. Corot, C. *et al.* Macrophage imaging in central nervous system and in carotid atherosclerotic plaque using ultrasmall superparamagnetic iron oxide in magnetic resonance imaging. *Investigative radiology*. **39**, 619-625 (2004).
21. Tarulli, E. *et al.* Effectiveness of micron-sized superparamagnetic iron oxide particles as markers for detection of migration of bone marrow-derived mesenchymal stromal cells in a stroke model. *J. Mag. Res. Imaging*. **37**, 1409-1418 (2013).
22. Shapiro, E.M. *et al.* MRI detection of single particles for cellular imaging. *Proceedings of the National Academy of Sciences of the United States of America*. **101**, 10901-10906 (2004).
23. McAteer, M.A. *et al.* In vivo magnetic resonance imaging of acute brain inflammation using microparticles of iron oxide. *Nature Medicine*. **13**, 1253-1258 (2007).
24. Perez, J.M., Josephson, L., O'Loughlin, T., Hogemann, D. & Weissleder, R. Magnetic relaxation switches capable of sensing molecular interactions. *Nat. Biotech.* **20**, 816-820 (2002).
25. Atanasijevic, T., Shusteff, M., Fam, P. & Jasanoff, A. Calcium-sensitive MRI contrast agents based on superparamagnetic iron oxide nanoparticles and calmodulin. *Proceedings of the National Academy of Sciences of the United States of America*. **103**, 14707-14712 (2006).
26. Kirtley, J.R. & Wikswo Jr, J.P. Scanning SQUID microscopy. *Annu. Rev. of Mat. Sci.* **29**, 117-148 (1999).
27. Finkler, A. *et al.* Self-aligned nanoscale SQUID on a tip. *Nano letters*. **10**, 1046-1049 (2010).
28. Hartmann, U. Magnetic force microscopy. *Annu. Rev. of Mat. Sci.* **29**, 53-87 (1999).
29. Sidles, J.A. *et al.* Magnetic resonance force microscopy. *Reviews of Modern Physics*. **67**, 249 (1995).
30. Maclaurin, D., Hall, L.T., Martin, A.M. & Hollenberg, L.C.L. Nanoscale magnetometry through quantum control of nitrogen–vacancy centres in rotationally diffusing nanodiamonds. *New Journal of Physics*. **15**, 013041 (2013).

31. Kucsko, G. *et al.* Nanometre-scale thermometry in a living cell. *Nature.* **500**, 54-58 (2013).
32. RugarD *et al.* Proton magnetic resonance imaging using a nitrogen–vacancy spin sensor. *Nat. Nano.* **10**, 120-124 (2015).
33. Wäldchen S, L.J., Klein T, van de Linde S, Sauer M. Light-induced cell damage in live-cell super-resolution microscopy. *Sci. Rep.* (2015).
34. Mosher, J.C., Lewis, P.S. & Leahy, R.M. Multiple dipole modeling and localization from spatio-temporal MEG data. *IEEE Trans. Biomed. Eng.* **39**, 541-557 (1992).
35. Mukherjee, A., Wu, D., Davis, H.C. & Shapiro, M.G. Non-invasive imaging using reporter genes altering cellular water permeability. *Nat. Commun.* **7**, 13891 (2016).
36. Szafer, A., Zhong, J. & Gore, J.C. Theoretical Model for Water Diffusion in Tissues. *Mag. Res. Med.* **33**, 697-712 (1995).
37. Imae, T. *et al.* Estimation of Cell Membrane Permeability and Intracellular Diffusion Coefficient of Human Gray Matter. *Mag. Res. Med. Sci.* **8**, 1-7 (2009).
38. Hevia, D. *et al.* Cell volume and geometric parameters determination in living cells using confocal microscopy and 3D reconstruction. (2011).
39. Loike, J.D. *et al.* Role of facilitative glucose transporters in diffusional water permeability through J774 cells. *The Journal of General Physiology.* **102**, 897-906 (1993).
40. Pfeuffer, J., Flögel, U., Dreher, W. & Leibfritz, D. Restricted diffusion and exchange of intracellular water: theoretical modelling and diffusion time dependence of 1H NMR measurements on perfused glial cells. *NMR in Biomedicine.* **11**, 19-31 (1998).
41. Holz, M., Heil, S.R. & Sacco, A. Temperature-dependent self-diffusion coefficients of water and six selected molecular liquids for calibration in accurate 1H NMR PFG measurements. *Phys. Chem. Chemical Phys.* **2**, 4740-4742 (2000).
42. Wilhelm, C., Cebers, A., Bacri, J.C. & Gazeau, F. Deformation of intracellular endosomes under a magnetic field. *Eur. Biophys. J.* **32**, 655-660 (2003).
43. Aubertin, K. *et al.* Impact of photosensitizers activation on intracellular trafficking and viscosity. *PLoS One.* **8**, e84850 (2013).
44. Huang, W., Liang, Y. Serial Symmetrical Relocation Algorithm for the Equal Sphere Packing Problem. *arXiv:1202.4149* (2012).
45. Thorek, D.L.J. & Tsourkas, A. Size, Charge and Concentration Dependent Uptake of Iron Oxide Particles by Non-Phagocytic Cells. *Biomaterials.* **29**, 3583-3590 (2008).